Exploring CVD Fabrication of Transition Metal Dichalcogenides for Nanoscrolling

MS53035

Nicole Burg

Delft University of Technology

TU Delft

Exploring CVD Fabrication of Transition Metal Dichalcogenides for Nanoscrolling

by

Nicole Burg

to obtain the degree of Master of Science in Materials Science and Engineering
at the Delft University of Technology,
to be defended publicly on Friday November 7, 2025 at 9:00 AM.

Student number:	6063446	
Project duration:	Jan 13, 2025 – November 7, 2025	
Thesis committee:	Dr. P. Dey,	TU Delft, Chair
	Dr. S. Conesa-Boj,	TU Delft, supervisor
	Dr. M. Blaauboer ,	TU Delft
	Dr. V. A. Popovich,	TU Delft

Cover:	Artist's interpretation of the evolution of MoO_3 beads to MoS_2 flakes and scrolls.
Style:	TU Delft Report Style, with modifications by Daan Zwaneveld

An electronic version of this thesis is available at http://repository.tudelft.nl

TU Delft

Acknowledgments

First and foremost, I would like to thank Dr. Sonia Conesa-Boj for her invaluable support and direction over the course of this thesis. Having a mentor who can not only guide but also encourage and inspire is a privilege. I will forever take with me the lessons I have learned from her and the memories of celebrating the little lab victories, even when experiments were not progressing as planned.

In addition to Sonia, I was lucky enough to have a second mentor, Dr. Poulumi Dey, who graciously took on the role of supervising a project outside her department and realm of study. I thank her for all of the help and support she has provided in keeping my graduation on track and frictionless.

To the PhD members of the group, Chris, Jeroen, and Onima, I cannot thank you enough for all of the help you have provided me in various ways throughout the project, including mentoring me in and out of the clean room, providing ideas and feedback when I was stuck, and performing tasks that I could not do myself. I wish you all success in completing your own theses and in your future endeavors as researchers.

I would also like to thank my student peers in the Conesa-Boj Lab, Zahra, Bart, Floris, Christian, David, and Alexandra, who became wonderful friends over the course of the last year and never failed to create fantastic lunchtime conversations, scientific or otherwise.

To my parents, I cannot express enough gratitude to them for raising me with love and always encouraging me to chase my dreams, even when they are on the other side of an ocean. Without their support, I would not be where I am today.

Finally, to my incredible partner, Martin. Thank you for always being there. Every late night, every busy weekend, you made sure I took care of myself and pushed me to be the best I could be. For this, I am forever grateful.

In the end, I am very proud of the work which is detailed in the following report, and performing it has allowed me to develop immensely as both a student and a researcher. Thank you again to everyone involved.

Nicole Burg
Delft, November 2025

Abstract

The continuous demand for smaller, faster, and more efficient electronic devices has driven research into two-dimensional (2D) materials that can overcome the physical limitations of Si brought on by quantum effects. Among these, transition metal dichalcogenides (TMDs) stand out due to their inherent bandgaps and highly tunable properties. In particular, the one-dimensional (1D) nanostructure formed by rolling up sheets of 2D materials, known as a nanoscroll, has immense potential for emergent optoelectronic properties brought on by its uniquely non-uniform strain field. Stacked and scrolled TMD heterostructures offer a promising route toward realizing novel optoelectronic phenomena driven by broken centrosymmetry and interlayer coupling. However, it is not well reported how the morphology of the initial 2D TMD sheet affects the final scrolled structure, which is a significant barrier to the deterministic control of nanoscrolls. This thesis explores the synthesis and morphological control of molybdenum-based TMDs, specifically MoS_2 and $MoSe_2$, using chemical vapor deposition (CVD), with an emphasis on understanding how 2D flake morphology governs the formation and properties of 1D nanoscrolls. Through systematic modification of CVD parameters, it was found that synchronizing temperature ramps between precursor zones greatly improved MoS_2 flake uniformity, yielding smaller, triangular monolayers with consistent morphology. Subsequent scrolling experiments demonstrated that flake shape and substrate adhesion critically influence scrolling yield and integrity, establishing a clear relationship between 2D precursor structure and final scroll geometry. In parallel, attempts to extend hydrogen-free CVD growth to $MoSe_2$ revealed significant challenges associated with selenium's low reactivity, resulting instead in dominant Mo oxidation processes. MoO_X phase evolution was investigated via these results, with a detailed structural study being carried out on novelly synthesized 2D α-MoO_3 nanobelts. Altogether, the findings advance the understanding of how CVD growth parameters dictate morphology and transformation pathways in molybdenum-based 2D materials, highlighting both the opportunities and challenges of fabricating non-hydrogen TMD heterostructures and strain-engineered nanoscrolls for future optoelectronic applications.

Contents

Acknowledgments i

Abstract ii

Nomenclature v

1 Introduction 1

2 Literature Review 3
2.1 Two Dimensional Materials . . . 3
2.2 Transition Metal Dichalcogenide Structure and Properties . . . 3
2.2.1 MoS_2 and $MoSe_2$ . . . 5
2.2.2 Edge Structure . . . 5
2.2.3 Optoelectronic Properties . . . 6
2.2.4 Manipulating the Properties of TMDs with Strain . . . 7
2.2.5 Moiré Superlattices . . . 8
2.2.6 Polarization . . . 10
2.3 TMD Nanoscrolls . . . 11
2.3.1 Structure of TMD Nanoscrolls . . . 11
2.3.2 Emergent Properties of TMD Nanoscrolls . . . 14
2.4 Motivation for the Thesis . . . 17

3 Methodology 18
3.1 2D Fabrication of TMDs . . . 18
3.1.1 Chemical Vapor Deposition . . . 18
3.2 Methodology of the Study . . . 26
3.2.1 Example Growth of MoS_2 as a Template for the Experimental Work . . . 27
3.3 Scrolling Flakes via Volatile Organic Solvents . . . 29
3.3.1 Technique for this Study . . . 29
3.4 Raman Spectroscopy for Characterization . . . 30

4 Optimization of CVD Grown MoS_2 for Nanoscrolling 33
4.1 Characterizing Flakes Grown with Unoptimized Procedure . . . 33
4.1.1 Raman Spectroscopy Thickness Analysis . . . 34
4.2 Increased Control Over Temperature Profile . . . 35
4.3 Optimization of MoS_2 Flakes . . . 37
4.3.1 Thickness Measurements . . . 37
4.3.2 Effects of Sulfurization Temperature . . . 40
4.3.3 Ideal flakes for scrolling . . . 40
4.4 Scrolling MoS_2 Flakes . . . 41
4.4.1 Scrolling Small Flakes . . . 42
4.4.2 Characterizing the Scrolls . . . 44
4.5 Conclusions Regarding MoS_2 Optimization . . . 46

5 Attempted CVD Fabrication of $MoSe_2$ 48
5.1 Developing a Vapor Phase CVD Recipe for $MoSe_2$ Flakes . . . 48
5.1.1 Selenization Temperature . . . 49
5.1.2 Argon Flow Rate . . . 52
5.1.3 Substrate Orientation . . . 53
5.2 Introducing NaCl as a Promoter . . . 54
5.2.1 Direct Placement on Substrate . . . 57
5.3 Mo-film Based Two-Step Growth Approach . . . 61

5.3.1 Characterization of Crystals 65
5.4 Discussion of Oxidation States and Failure of Growth 69

6 Self-Assembled α-MoO_3 Nanobelts: A Byproduct of $MoSe_2$ CVD 71
6.1 Synthesis of Unidentified Crystals 72
6.2 Determination of Chemical Composition and Characterization 73
6.3 Electronic Properties of α-MoO_3 Nanobelts 75
6.4 Discussion 76

7 Conclusion and Outlook 77

References 80

A Supplementary Data & Images 95
A.1 $MoSe_2$ CVD Parameters and Temperature Profiles 95

Nomenclature

Abbreviations

Abbreviation	Definition
1D	One-Dimensional
2D	Two-Dimensional
AC	Armchair
AFM	Atomic Force Microscopy
APCVD	Atmospheric Pressure CVD
CVD	Chemical Vapor Deposition
EDX	Energy-Dispersive X-Ray Spectroscopy
HR-TEM	High Resolution Transmission Electron Microscopy
OM	Optical Microscopy
PL	Photoluminescence
SAD	Selected Area Diffraction
SEM	Scanning Electron Microscopy
STEM	Scanning Transmission Electron Microscopy
TEM	Transmission Electron Microscopy
TMD	Transition Metal Dichalcogenide
vdW	van der Waals
XRD	X-Ray Diffraction
ZZ	Zigzag
ZLP	Zero-Loss-Peak

1

Introduction

Due to the immense growth and dominance of semiconductor transistor technologies in the last century, further advancement in this domain has become a significant driver of scientific study. The miniaturization of traditional silicon-based transistor technologies is now facing a bottleneck brought on by the physical limitations of the element itself. Thus, the search for smaller, faster, and more efficient electronic and photonic materials is an extremely present and important field of research. This is especially true in the context of fundamental materials science and condensed matter physics, where quantum effects observable at the nanoscale can be exploited in novel ways. Low-dimensional nanostructures are an exciting avenue for focused research. This is because the confinement of physics to two or fewer dimensions not only allows for miniaturization below the limit of silicon, but also gives rise to interesting and exploitable effects not present in three-dimensional structures [1].

The first isolation of a two-dimensional (2D) material, graphene, in 2004 opened the door to the study of materials with weakly connected atomic layers that can be reduced to just a single atomic plane [2]. With its incredible electrical and thermal conductivity, strength, and flexibility, graphene has quickly become the most studied 2D material. However, it has no bandgap, limiting its potential use in semiconductor devices. As a result of this handicap, transition metal dichalcogenides (TMDs) have emerged as a versatile class of 2D materials that can possess inherent bandgaps while maintaining unique and promising properties at low dimensionality. While TMDs possess great potential across a range of applications, their semiconducting nature and tunable nanoscale electronic properties have made them particularly attractive for optoelectronic devices [3].

Tunability is an important aspect to the successful application of TMDs in the context of optoelectronic devices, since controlling material parameters, such as bandgap, directly influences the properties of produced devices [4]. It has been known for some time that the number of layers in TMDs directly affects their bandgap and photoluminescence [5]. However, recently, it has been found that the strain profile within the lattice of TMDs also exhibits significant effects on their electronic properties and is the key to unlocking powerful effects such as lattice reconstruction, unintuitive bandgap changes, and even the induction of pseudo-ferroelectric polarization within the material [6, 7, 8].

One particularly promising avenue of strain-engineered TMD morphology is nanoscrolls, a 1D structure formed by rolling up monolayer sheets into spiral, cross-sectioned tube-like morphologies. These structures, due to their unevenly curved cross-sections, have intrinsically non-uniform strain fields in the lattice of their constituent materials [9]. Combining this with the interaction between the layers of the scroll creates a highly exciting platform for investigating emergent optoelectronic effects. However, TMD nanoscrolls are not yet widely studied, particularly in regard to how their structure is tied to properties such as strain and bandgap. Even more critically, the tie between the 2D and 1D domains is not well understood and forms the first major research question of this work: **How does 2D flake morphology govern the formation and final structure of the resulting nanoscroll?**

To address this, a popular technique for growing high-quality TMD flakes with controlled morphology, chemical vapor deposition (CVD), will be used to fabricate the material MoS_2 under different conditions.

After which, the effects this has on scrolling (with a facile and well-studied method) will be assessed.

However, in isolation, MoS_2 is not a strong candidate for one of the novel emergent effects of strained TMDs; in-plane polarization fields. This is due to the inversion symmetry it possesses in its most stable form [8, 10]. One method for addressing this is combining MoS_2 with other TMDs in stacks known as heterostructures. In this configuration, inversion symmetry can be broken. This has the serendipitous result of introducing enhanced strain fields due to the lattice mismatch between the materials. Among TMDs, $MoSe_2$ stands out as a candidate for this pairing due to its structural similarities with MoS_2 [11]. The well-studied CVD methodology for MoS_2 should also apply to 2D $MoSe_2$ growth. However, the relatively low reactivity of Se presents a challenge to the growth of $MoSe_2$, often requiring the use of high-risk H_2 reducing gas [12]. This reasoning motivates the second research question of the thesis: **How do the parameters of hydrogen-free atmospheric pressure CVD affect the growth of $MoSe_2$?**

This work is structured in the following way. Chapter 2 introduces the fundamental structure and properties of TMDs, how they have been manipulated, and the current work on rolling them into nanoscrolls. The emergent properties of these materials will also be addressed, highlighting the immense potential for nanoscrolls to unlock new effects not yet seen in other TMD structures. Chapter 3 covers the theory of CVD and how it is implemented in this thesis, as well as the scrolling and characterization techniques that will be used. Chapter 4 presents the results and discussion of changing the CVD growth parameters on the structure of the obtained MoS_2 flakes and scrolls. This is followed by Chapter 5, which reviews the attempts to grow 2D $MoSe_2$ flakes via non-hydrogen methods and analyzes the root cause of growth failure. Finally, Chapter 6 introduces a van der Waals oxide material which was discovered via the growth process of $MoSe_2$. This material is characterized to determine its nature. Additionally, its structural and electronic properties are discussed.

2

Literature Review

To lay the foundations of the thesis and further provide the motivation behind the methodology used for this study, a literature review is presented in the following chapter. Firstly, the fundamental structure and properties of TMDs are introduced along with an examination of the state-of-the-art with regard to the control of their properties. From there, nanoscrolls are presented with a focus on their formation mechanisms and structural characterization.

2.1. Two Dimensional Materials

Two-dimensional (2D) materials are an important group of nanomaterials characterized by their ability to exist in few- or single-layer sheets of atoms [13]. Their structure arises as a result of anisotropic bonding, where the atoms within each layer are covalently bonded. The layers themselves are only held together by weak van der Waals (vdW) forces, allowing them to be easily separated from the bulk in sheets [14]. This is visualized in Figure 2.1. These materials rose in prominence with the discovery of graphene, single-layered carbon graphite, a material which has since found wide application thanks to its remarkable strength, electron mobility, thermal conductivity, and optical transparency [15]. Its lack of an electronic bandgap, however, limits graphene's potential application in electronics [16]. This has naturally led to great interest in exploring other 2D materials, which may possess unique and tunable electronic properties.

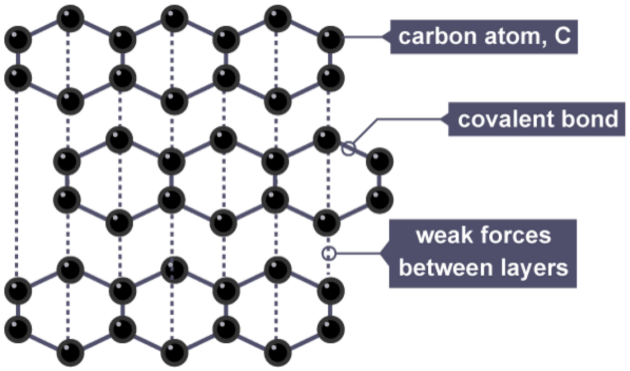


Figure 2.1: Basic structure of 2D materials modeled by graphite [17].

2.2. Transition Metal Dichalcogenide Structure and Properties

Transition metal dichalcogenides (TMDs) are one class of 2D materials that have garnered interest recently due to their often semiconductor nature and highly promising electrical and optical properties [18]. As seen in Figure 2.2, they are chemically composed of a transition metal, M, such as Mo, W,

or V, and a chalcogen, X, such as S, Se, or Te, in the composition of MX_2 [19]. These atoms arrange themselves in a three-layer structure, with two layers of the chalcogen atom sandwiching a layer of transition metal atoms, forming in either a trigonal prismatic (H), octahedral (T), or distorted octahedral (T') phase [20]. Each of these can be seen from both the side and top-down view in Figure 2.3. When the atoms are arranged in the trigonal prismatic structure, they give rise to a hexagonal lattice, as viewed from the top down. This is reminiscent of the single-layer hexagonal structure of graphene and is valuable for characterizing the material at the atomic scale. As layers are added, the overall bulk crystal symmetry can be 2H (trigonal), 1T (octahedral), or 3R (rhombohedral), where the numbers refer to the amount of layers that make up one unit cell [21]. The resulting stacking configurations are visualized in Figure 2.3b.

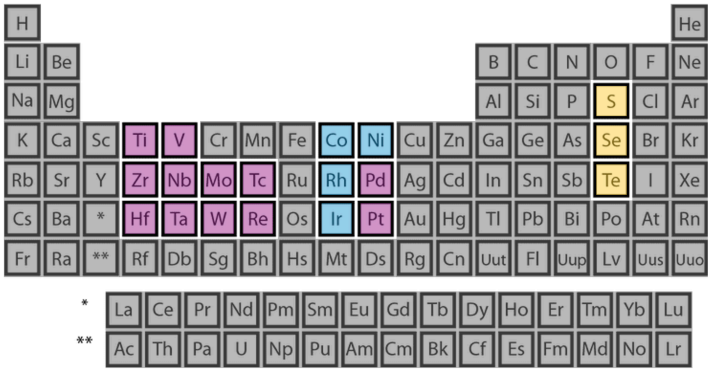


Figure 2.2: Periodic table where the constituent elements of TMDs are highlighted. Yellow represents chalcogens, and purple indicates transition metals. The blue highlights in groups 9 and 10 indicate that only some of the MX_2 combinations involving this atom result in a 2D-layered structure [20].

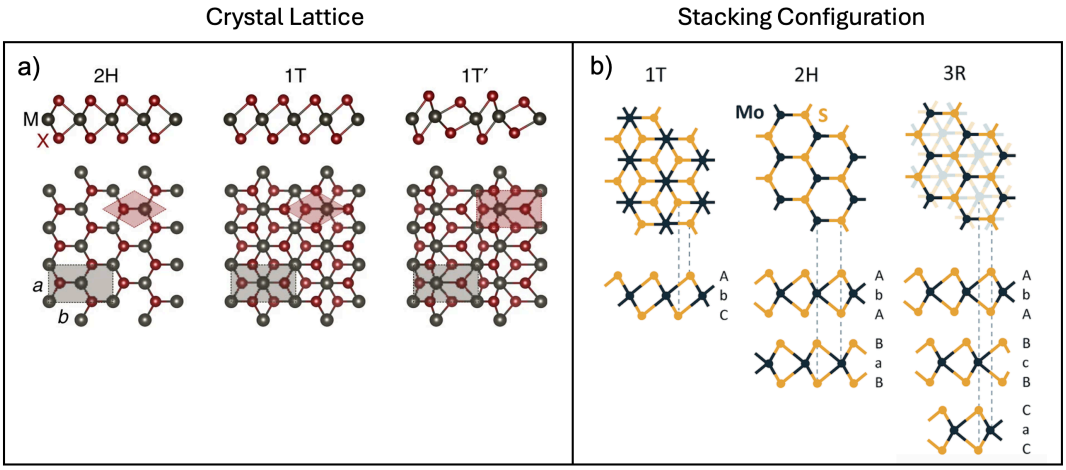


Figure 2.3: a) Structural monolayer phases of TMDs. b) Stacking phases of MoS_2. Adapted with permission from [21] and [22].

Among the TMDs, those formed from Mo and W have garnered the most attention for their semiconducting properties. These include MoS_2, $MoSe_2$, and WS_2. The 2H stacking phase is the most stable for these TMD crystals, both in bulk and when simple mechanical layer isolation is performed. As seen in Figure 2.3b, in this configuration, the transition metal atom is in full alignment with the chalcogen atoms of the layer above and below it. This creates an AB structure or, more technically, an "AbA BaB" where upper and lower case letters signify the chalcogen and metal atoms, respectively. Its unit cell is thus composed of two layers and has the space group P63/mmc. This structure allows for a uniform charge density and eliminates the lack of inversion symmetry found in the single-layer material [23].

The next most stable phase, that of 3R (space group R3m), consists of three layers in an "AbA BcB CaC" sequence and, as can be seen in Figure 2.3b, leads to a lack of inversion symmetry in the bulk. This symmetry difference from the 2H phase found in nature implies notable changes in the expected

properties of the bulk crystal and makes synthesizing MoS_2 and other TMDs with this phase highly interesting for research [23].

Finally, when the crystal structure of atoms is octahedral, a one-layer unit cell is formed. It generally creates a metallic material, but is unstable and must be formed in lab settings using various methodologies [24, 25]. Since this work is mainly concerned with semiconducting phases of TMDs and their application, the 1T structure will not be investigated in more depth.

2.2.1. MoS_2 and $MoSe_2$

As mentioned, some of the most studied TMDs are those formed from molybdenum, specifically MoS_2, which is found in nature as molybdenite and has been well described since the end of the 18th century [26]. Each layer consists of a Mo sublayer sandwiched between two S sublayers, and it is easily isolated in few and single layers via simple exfoliation. As a result, MoS_2 is by far the most researched TMD and the most commercially used (due to its application as a dry lubricant) [27]. While both 3R and 2H polytypes of MoS_2 can be found in nature, 2H is by far the most common. A single layer of MoS_2 is 3.15 Å thick with an interlayer distance of 6.15 Å [22]. The lattice parameters of 2H MoS_2 (space group P63/mmc) are a = 3.15 Å and c = 12.30 Å [28]. It is also important to note that the crystal has a hexagonal Brillouin zone, which is visible in 2D diffraction patterns.

$MoSe_2$, a material which is not found isolated in nature, shares the same lattice structure as MoS_2, that of 2H in bulk, with only about a 3% lattice mismatch [11]. Its lattice constants are a = 3.32 Å and c = 13.54 Å with a single layer being about 7 Å thick with an interlayer distance of 6.46 Å [29, 30, 31]. It is also a semiconductor and acts similarly to MoS_2 in many contexts. These immense similarities in structure allow MoS_2 and $MoSe_2$ to not only be researched for related applications, but also encourages their combination into material heterostructures [32, 33]. However, there are subtle differences in their optoelectronic properties, such as different bandgap sizes, vibrational modes, photoluminescence, and carrier mobility [34, 35]. Additionally, $MoSe_2$ tends to have slightly stronger spin-orbit coupling than MoS_2 due to the presence of the heavier Se atom, which can affect the potential for each material in spintronic applications [36, 37, 38]. MoS_2 is additionally used as a catalyst in multiple applications, including the removal of sulfur from natural gas and the production of hydrogen gas from water in the hydrogen evolution reaction [39, 40]. However, MoS_2 is not the most effective catalyst for these applications and others due to its 2D structure, limiting the number of dangling bonds it possesses to only the edges [41]. This has raised interest in developing techniques to reduce the dimensionality of MoS_2 and other TMDs in order to increase the edge-to-surface ratio, thus improving their potential as a catalyst [42].

2.2.2. Edge Structure

Due to their multilayer hexagonal lattice, MoS_2 and $MoSe_2$ possess multiple possible edge terminations. In the 2D morphology, these are zigzag (ZZ) and armchair (AC), shown in Figure 2.4. In the case of the ZZ, only one type of atom (Mo or S/Se) forms the edge, while in AC, the atoms alternate. ZZ edges exhibit metallic behavior and are the most stable. AC edges, however, are semiconducting and in line with the properties of the bulk material [43]. As illustrated in Figure 2.4, the type of termination also dictates the angles between adjacent edges, which are 60º or 120º when identical terminations meet, and 30º or 90º when different ones intersect.

Generally, these edge structures are thought of as low-dimensional defects and are present in other layered materials, such as graphene [45]. While the term defect often indicates a structure that acts as a hindrance to the possession of desirable properties, these various edge structures have been shown to be of use for tailoring such properties, specifically electronic and chemical [46, 47].

For example, the hydrogen saturation of TMD nanoribbons can increase the stability of their magnetic states while simultaneously reintroducing an electronic bandgap, effectively removing their metallic properties [48]. Consequently, ”edge-rich” TMD structures and methods for controlling their edge terminations are of great interest for property engineering.

Experimentally, achieving uniform AC edges via chemical vapor deposition remains highly challenging due to their intrinsic instability [49], making ZZ edge formation more thoroughly understood. For MoS_2 and $MoSe_2$, ZZ edges may terminate with either Mo or S(Se) atoms, and their formation strongly

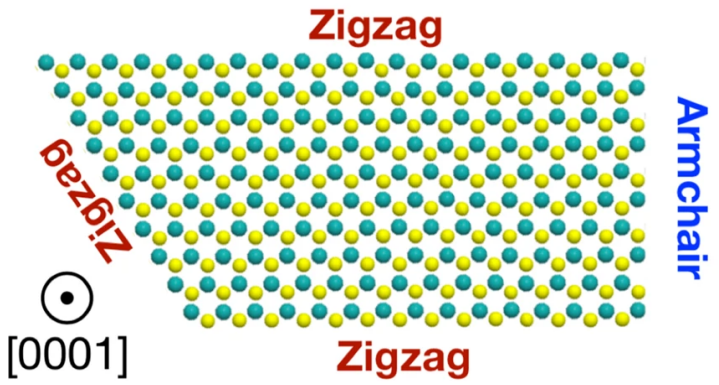


Figure 2.4: Edge structures of 2D MoS_2. Reproduced with permission from [44].

depends on the Mo:S(Se) ratio [50]. As shown in Figure 2.5, S(Se)-rich conditions (ratios <1:2) favor S(Se)-ZZ terminations, while Mo-rich environments (>1:2) favor Mo-ZZ terminations. Near stoichiometric conditions (≈1:2), both edges grow equally, producing hexagonal flakes with alternating Mo- and S(Se)-ZZ edges [51].

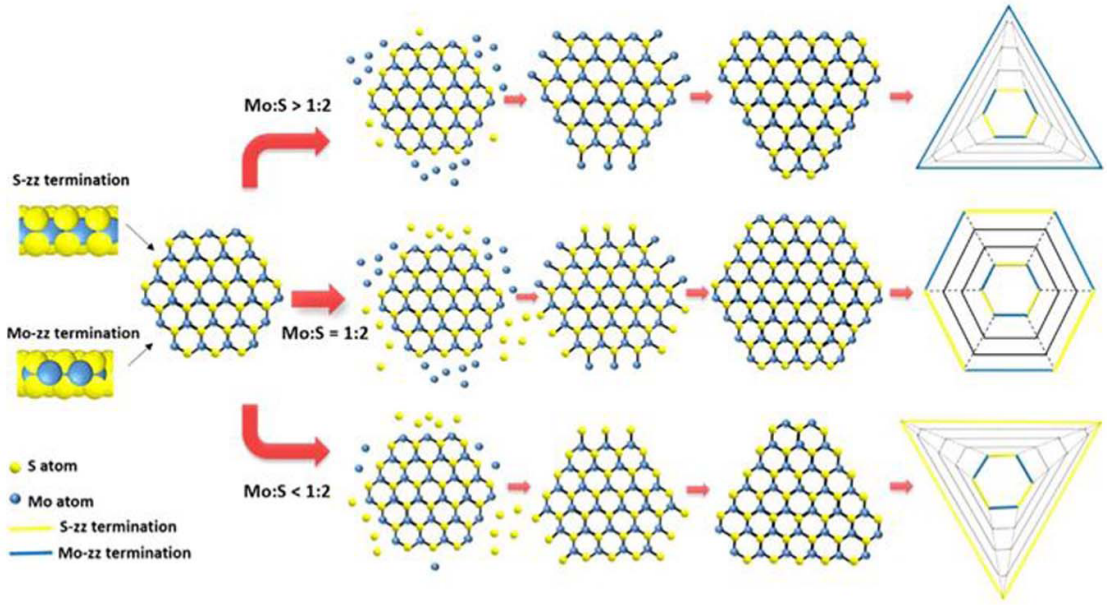


Figure 2.5: Edge development of 2D MoS_2 as a result of varying Mo:S ratios [51]. Reprinted with permission from [51]. Copyright 2014 American Chemical Society.

2.2.3. Optoelectronic Properties

In addition to the atomic configuration within layers, TMD properties are also affected by the stacking between layers. For the TMDs MoS_2 and $MoSe_2$, which are semiconductors in the 2H structure, their bandgap changes as the number of van der Waals layers decreases from bulk to monolayer [33]. Specifically, while these materials have an indirect bandgap in the bulk, this becomes a direct bandgap when there is only one layer. In the case of MoS_2 (seen in Figure 2.6a), when calculated using density functional theory, the bulk bandgap is 0.88 eV, whereas the monolayer bandgap shifts to 1.71 eV [5]. This jump is less significant in experiments, however, with a change from about 1.2 eV in the bulk to 1.8 eV in single-layer [38]. Looking again at Figure 2.6a, one can also notice how the minimum of the conduction band is located between the K and Γ points of the Brillouin zone, while the maximum of the valence band is centered at the Γ point [52]. As layers are reduced, the minimum of the conduction band moves towards the K point. As mentioned, this layer-dependent bandgap change is also

present in $MoSe_2$, for which the experimental values for bandgap are 1.1 eV and 1.5 eV in the bulk and monolayer, respectively [38].

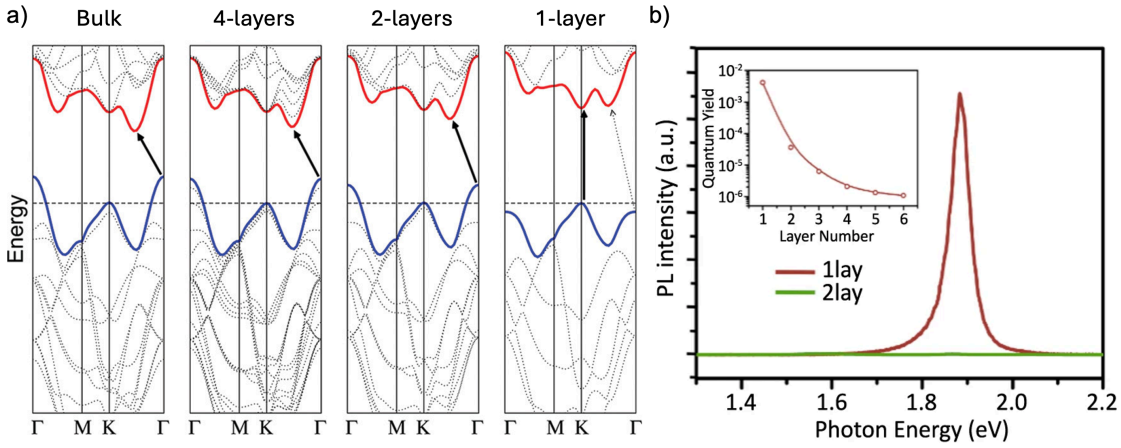


Figure 2.6: a) Band structure of MoS_2 ranging from bulk to monolayer. b) PL spectrum of mono- and bilayer MoS_2. Figure a) is adapted with permission from [53]. Copyright 2010 American Chemical Society. Figure b) reproduced with permission from [54].

In the context of electronic applications, MoS_2 has a very high On/Off ratio and theoretical electron mobility, 10^8 and 410 $cm^2V^{-1}s^{-1}$, respectively [55]. This makes it highly interesting for use in transistors and other switching-based technologies, though the electron mobility is still lower than that of silicon (1400 $cm^2V^{-1}s^{-1}$). $MoSe_2$, on the other hand, has only been demonstrated to achieve an On/Off ratio of between 10^5 and 10^5. In the case of mobility, due to the significantly less research on $MoSe_2$ transistors, it is hard to say the best case scenario value, however, the literature generally reports values less than 100 $cm^2V^{-1}s^{-1}$ and even as low as 7 $cm^2V^{-1}s^{-1}$ [56, 57].

In the monolayer, MoS_2 and $MoSe_2$ exhibit strong photoluminescent (PL) properties due to their previously mentioned transition to a direct bandgap [1, 58]. In fact, upon moving from the bulk to monolayer, MoS_2 shows a three order of magnitude increase in PL yield, seen in Figure 2.6b. As a result, these TMDs have great potential in photonic applications. In $MoSe_2$ monolayers, the transition from indirect to direct bandgap similarly leads to a very large increase in PL [59]. Interestingly, the effect is exponential as thickness decreases, with 2- and 3-layer samples demonstrating only marginal increases in PL over bulk material [60]. Furthermore, there is a structural change in the PL spectrum as layer number is changed, with monolayer MoS_2 possessing only one strong peak at 1.84 eV, while in few-layer samples a second (less intense and broader) peak appears at 1.95 eV [61]. These peaks correspond to the A and B exciton transitions [60]. Because of their 2D nature, MoS_2 and $MoSe_2$ exhibit in-plane spatial confinement and reduced dielectric screening (a result of the electron wave functions extending outside the material) compared with their bulk counterparts, which have more neighboring atoms. Thus, there is a strong Coulomb interaction between charged particles within one layer of these materials, which leads to the formation of excitons (electron-hole pairs) when MoS_2 or $MoSe_2$ are photoexcited [33]. What is particularly interesting is the large binding energies of these excitons, which have been found in literature to be about 0.5 eV [54, 62]. This value is high enough that these excitons are measurable even at room temperature [63].

2.2.4. Manipulating the Properties of TMDs with Strain

One of the most intriguing aspects of TMDs for study is that layer number is not the only thing that can influence their bandgap. Strain, both theoretically and experimentally, has been demonstrated to have a significant effect on the bandgap of MoS_2 and other TMDs [64, 65]. From a theoretical perspective, strain should have a highly significant effect on the bandgap and electronic properties of MoS_2. According to first-principle calculations performed by Lu et al. [64], the direct bandgap semiconductor, monolayer MoS_2 can be modulated to possess an indirect bandgap with tensile strain, and bilayer MoS_2 (an indirect bandgap semiconductor) can be made to have a direct bandgap with the application of compressive strain. Additionally, strain can, in principle, be used to change the bandgap size of few-layer

MoS_2. While monolayer MoS_2 experiences a reduction in bandgap regardless of strain type, isotropic compressive strain on bilayer MoS_2 can actually increase the bandgap [64]. These theoretical findings emphasize what a crucial role deterministically engineering strain into nanoscale TMD structures can have on their usability in practice. In particular, the ability to create a direct bandgap semiconductor out of multilayered material has the potential to vastly increase the ease of fabrication for future devices.

These theoretical findings were supported by the work of Hui et al. [66], who performed biaxial strain experiments on trilayer MoS_2. As seen in Figure 2.7a, as strain was increased, both the valence band maximum and conduction band minimum shifted to higher energies. The conduction band minimum, however, shifted more for the same amount of strain, resulting in the enlargement of both the indirect bandgap (E_{id}) and the direct bandgap (E_{dir}). E_{id} was shown to widen faster per percentage of strain than E_{dir} (Figure 2.7b), indicating that the material could potentially transition to a direct bandgap semiconductor with further applied strain. This covers just one form of strain and thus leaves out the complexities of combining multiple strain directions at various degrees or mixing tensile and compressive strain along differing axes.

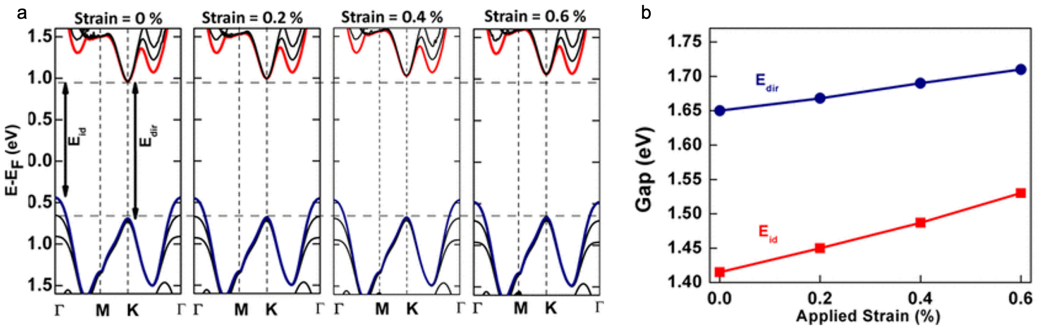


Figure 2.7: a) Band structure evolution of MoS_2 as biaxial compressive strain is applied. b) Plot of bandgap energy with respect to applied strain percentage. Figure a) is adapted with permission from [66]. Copyright 2013 American Chemical Society.

2.2.5. Moiré Superlattices

Due to the 2D nature and similar structure of various TMDs, they are ideal candidates for stacking multiple layers to build functional materials [1]. In fact, van der Waals heterostructures have the unique potential to include materials with diverse properties, combining the best properties of each without the epitaxial constraints of more conventional heterostructures [67].

When TMD layers are stacked with a slight rotational misalignment, the atomic lattices interfere to form a larger periodic pattern known as a Moiré superlattice, which can be seen for a simple hexagonal lattice in Figure 2.8 [67]. In the field of 2D materials, Moiré superlattices have emerged as an incredibly rich playground for investigating new functionalities and previously unknown phenomena, as, in their presence, homo- and heterostructures can exhibit not just the properties of their constituents, but new, unique properties of their own. For example, ”magic-angle” bilayer graphene at a twist of $\tilde{1}.1^{o}$ exhibits flat electronic bands and even superconductivity, properties which are otherwise absent in untwisted graphene [68].

Since this review is mostly focused on the materials MoS_2 and $MoSe_2$, a closer look will be taken at the mechanisms of Moiré superlattices for the same or highly similar materials. The 2H phase of these two TMDs have a hexagonal lattice structure (similar to graphene), thus there exists an in-plane radial symmetry every 60^{o}. This means that when a bilayer of a 2H-TMD is stacked and twisted, the offset between a fully aligned state and its current configuration is maximized at 30^{o}. Furthermore, the layers are once again in alignment every 60^{o}. When it comes to the size of the new lattice constant, it is understood that the smaller the relative twist angle, the larger the new superlattice unit cell will be (see Figure 2.8b). However, the interaction between layers forming a Moiré superlattice is not the same for all angles. Instead, there are two domains that arise depending on the size of the angle [6].

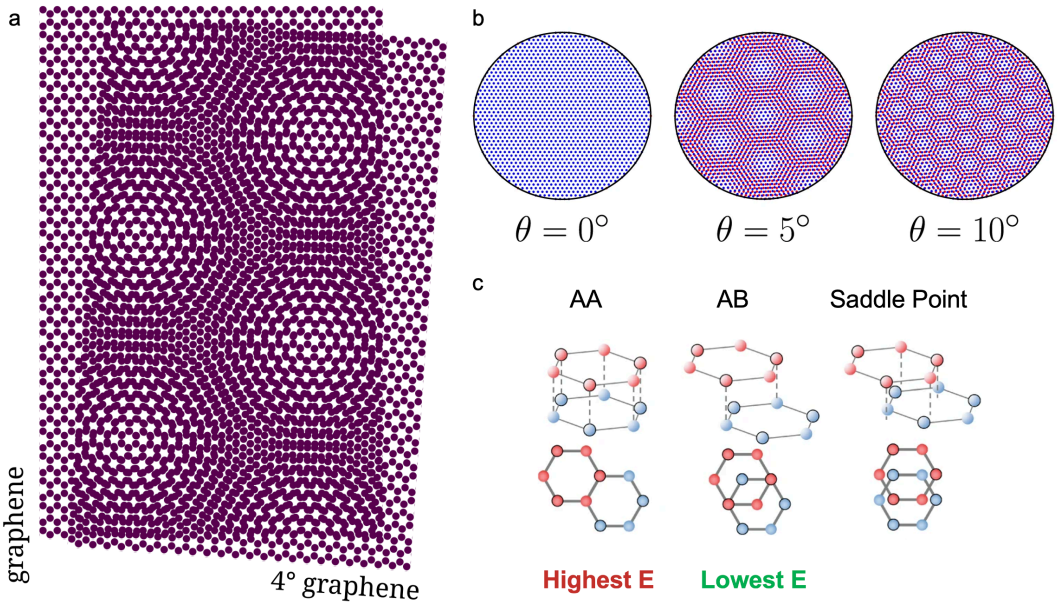


Figure 2.8: a) Visualization of Moiré superlattice interference pattern [69]. b) Evolution of Moiré periodicity as a result of different twist angles [70]. c) Possible stacking alignments during lattice reconstruction of stacked 2H MoS_2 and $MoSe_2$ [6]. Figure b) is reproduced with permission via Creative Commons Attribution 4.0 International License. Figure c) is adapted with permission from [6]. Copyright 2020 Nature.

Lattice Reconstruction

The idea of lattice reconstruction arises from the energetic favorability of different stacking configurations. Figure 2.8c shows the three possible arrangements with respect to hexagonal lattices like 2H MoS_2 and $MoSe_2$. The most energetically costly configuration is that of AA, where two like atoms are positioned directly on top of one another. The most energetically favorable configuration is AB aligned, as the bulk 2H structure would be. Finally, there exists the stacking known as “saddle point” which exists as a gradient in between AA and AB [6]. In a twisted configuration, these regions all exist to varying degrees across the Moiré.

In the smallest twist angles of bilayer MoS_2 or $MoSe_2$ (below about 2º), the lattices of the two layers are relaxed. The favorable AB and BA stacking is present as triangular domains with only defect points of AA stacking. When the angle is greater than about 6º, the material enters a rigid regime where the alignment created naturally remains. In between these angles of twist, however, large domains of AA and saddle point stacking are highly energetically unfavorable, but interlayer coupling is still strong. This coupling drives the atoms to reconfigure to reduce the interlayer stacking fault energy [71]. This effect was robustly modeled by Quan et al. for a 2.5º twisted bilayer of MoS_2. As can be seen in Figure 2.9a & b, the bilayer Moiré lattice reconstructs to maximize the area of AB stacking domains and minimize AA. Figure 2.9c highlights the preferable interlayer energy of the new configuration. It is important to note that the exact degrees of twist that define the lines of these regimes are not well agreed upon. Specifically, some references agree that there should be no reconstruction below 2º [6], while others regard this reconstruction as occurring even at very small angles [71]. It is thus good practice not to predetermine the lattice physics of a stacked structure purely based on its angle. Instead, other methods should be used to further probe the resulting structure.

The energetic benefit of reconstruction, however, comes at the cost of introducing substantial in-plane strain. As atoms shift to form the lowest-energy configurations, strain accumulates periodically across the Moiré superlattice, particularly within the saddle-point regions between AB and AA domains as visualized in Figure 2.10 [71]. This intrinsic non-uniform strain not only alters local electronic and optical properties but also provides a natural platform for strain engineering in 2D materials.

Recent work by van Heijst et al. [7] on WS_2 demonstrates the importance of this effect. They found that twisted multilayers exhibited a reversed relationship between bandgap and thickness compared to conventional stacked flakes, i.e., twisted flakes had increased bandgap with increased thickness, a

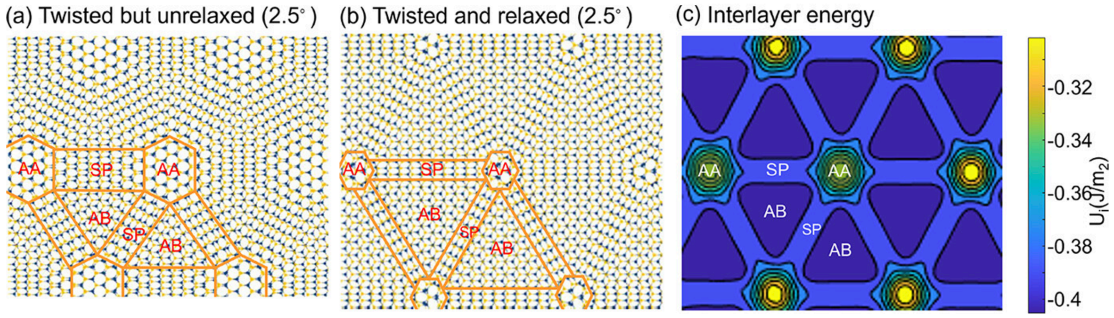


Figure 2.9: Visualization of lattice reconstruction of MoS_2 at 2.5º from a) unrelaxed to b) relaxed and c) the resulting energy of the reconstructed lattice. Figure is adapted with permission from [71]. Copyright 2023 American Chemical Society.

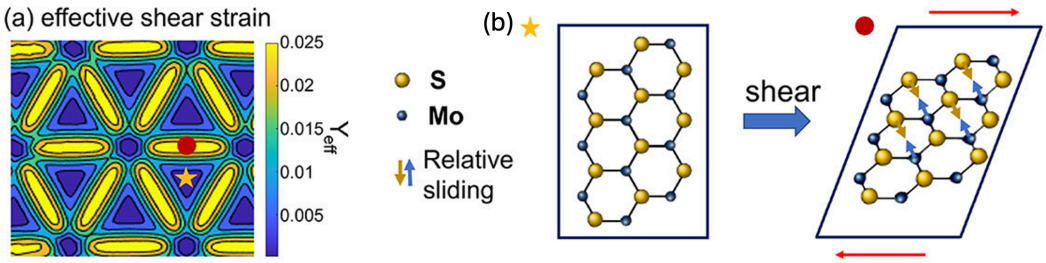


Figure 2.10: Visualization of strain as a result of lattice reconstruction of a MoS_2 bilayer with 2.5º twist angle. Figure is adapted with permission from [71]. Copyright 2023 American Chemical Society.

result attributed to the non-uniform strain distribution in the spiral structure. These findings emphasize that Moiré-driven reconstruction and strain are deeply intertwined phenomena, and that understanding their interplay is crucial for exploiting twisted TMDs in future optoelectronic and quantum applications.

2.2.6. Polarization

Another unique property of 2D material stacks is their ability to exhibit ferroelectricity [70]. This has been observed in bilayers such as hBN, GaSe, ZnO, and MoS_2, where interlayer translation induces spontaneous out-of-plane polarization fields [72]. These vdW heterostructures have an advantage over traditional ferroelectrics due to their tunability via control of stacking parameters like offset and twist [8]. As shown in Figure 2.11, polarization arises from interlayer charge transfer caused by a lateral offset between two layers, where the magnitude is 0 in AA stacking and maximized in AB stacking [70]. Consequently, materials such as MoS_2 and $MoSe_2$ can display out-of-plane polarization even in bulk due to their 2H structure [72].

Furthermore, because twisted bilayers naturally form distinct stacking domains (Section 2.2.5), Moiré superlattice TMDs exhibit alternating out-of-plane polarization patterns depending on local stacking [10]. Recently, however, the possibility of in-plane polarization for Moiré superlattices has been considered. Through the lens of hBN, the development of in-plane polarization due to strain from twisted bilayers was proven theoretically [70]. Even more importantly, though, within this past year, multiple experimental papers have been published which show evidence for Moiré-induced in-plane polarization in TMD material stacks [8, 73]. It has been found that in bilayer systems, an alternating in-plane texture arises with AA regions possessing polarization and AB regions not [74]. In TMD multilayers, however, unique uniform polarization vortices have been observed that closely align with the strain induced by the Moiré superlattice reconstruction, something which can be seen in Figure 2.12 [8].

Despite these exciting results, the field remains underexplored, and contradictions are present. Most notably, polarization vortices should not theoretically be possible in centrosymmetric bilayer MoS_2 [70], but one paper has claimed to have observed them [73]. Additionally, few controlled experiments have systematically linked morphology, strain, and polarization, leaving a large area of unexplored research.

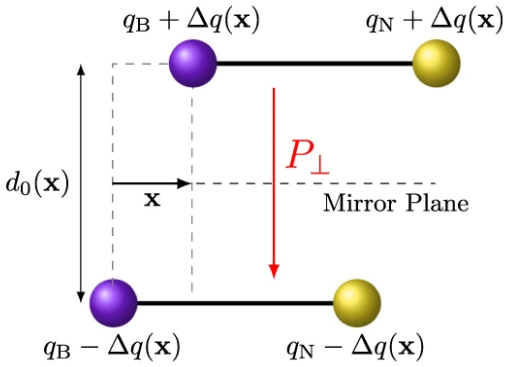


Figure 2.11: Diagram of how out-of-plane polarization arises in stacked van der Waals materials. Figure b) is reproduced with permission from [70].

In the context of this thesis, because of the link already found to non-uniform strain, 1D morphologies such as nanotubes and nanoscrolls offer an especially compelling direction for study, as their intrinsic curvature provides a natural route for potentially generating in-plane polarization fields.

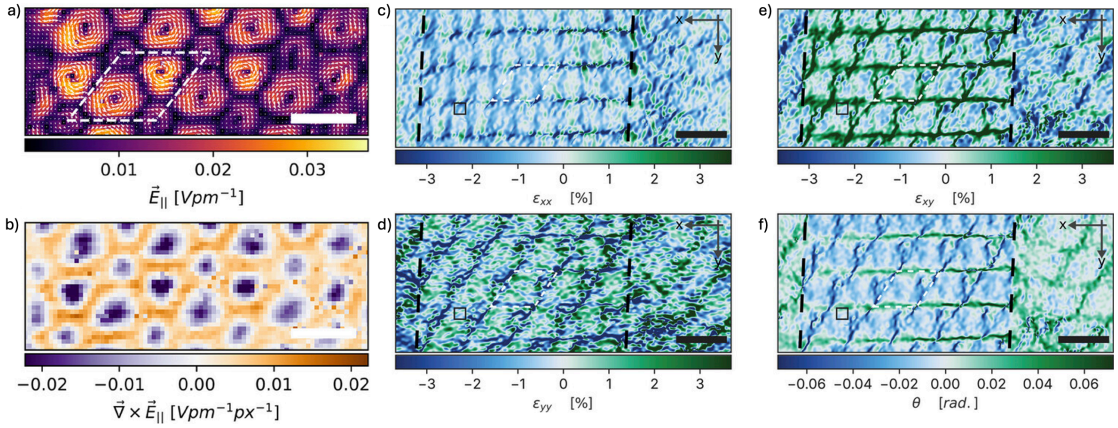


Figure 2.12: a) In-plane polarization field vector for a region of multilayer twisted WSe_2 b) Vorticity of the observed electric field for the same region (scale bars 5nm for a) & b)) c-f) Strain fields of the WSe_2 specimen (scale bar 10nm). For each image, a white dashed region highlights the Moiré unit cell [8]. Figure is adapted with permission from [8].

2.3. TMD Nanoscrolls

Since it has been seen through the literature that there is incredible potential for unique and tunable properties in TMDs, especially through the introduction of strain, it naturally raises the question of what structures can be specifically created with controlled strain. Even further, the incorporation of unique strain fields, such as those produced by twisted multilayers and non-uniform morphologies, can uncover properties that are not yet fully understood in the literature. While there are many ways to achieve unique strain fields in van der Waals materials, the 1D nanostructure known as the nanoscroll stands out as both a highly interesting and still underexplored candidate.

2.3.1. Structure of TMD Nanoscrolls

Due to the large amount of literature on the subject, one may already have familiarity with the 1D nanostructure known as a nanotube. However, nanoscrolls, seen in Figure 2.13, differ from nanotubes in that the rolled sheet does not reconnect at its edge to form a continuous cylinder. Instead, when forming a nanoscroll, one 2D material sheet is rolled up into itself, much like a historical writing scroll or modern-day tube of wrapping paper. This leads to a multiwalled structure with open edges at both the innermost and outermost layers [75]. The scroll can thus extend unconfined in a single direction,

creating a 1D structure. Nanoscrolls are a nanostructure that have been less discussed in literature than nanotubes. However, in the last decade, more attention has been given to their study [76, 77, 78, 79]. TMD nanoscrolls have been successfully fabricated with a number of different methods, which range from highly simplistic [78, 80, 81] to extremely complex [82, 83] and in between [81]. At their core, all methods take a 2D structure and roll it up to the 1D geometric structure discussed in this section.

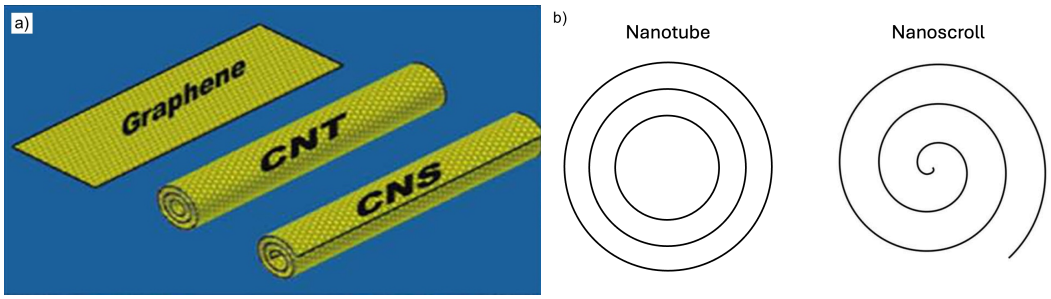


Figure 2.13: a) 3D comparison between nanotubes and nanoscrolls for graphene. b) Cross-section comparison of nanotubes versus nanoscrolls. Figure a) is adapted with permission from [76]. Copyright 2021 Elsevier.

Since nanoscrolls are formed with a spiral geometry and no closed ends, they have unique degrees of freedom that can be changed to adjust the final morphology of the scroll. These parameters are highlighted in Figure 2.14. The nanoscroll can be mathematically defined as a series of continuous Archimedean spiral shapes, and thus any point on the scroll can be described with the polar equation

$$r = r_{in} + \frac{d_{in}}{2\pi}\theta \tag{2.1}$$

where r_{in} is the core radius of the spiral, d_{in} is the interlayer spacing, and θ is the angle of the point, r, as seen in Figure 2.14b. The term θ can vary from 0 to $2\pi N_{turn}$ where N_{turn} is the number of turns made by the nanoscroll [76, 84]. The term R can also be used to represent the outermost diameter of the scroll.

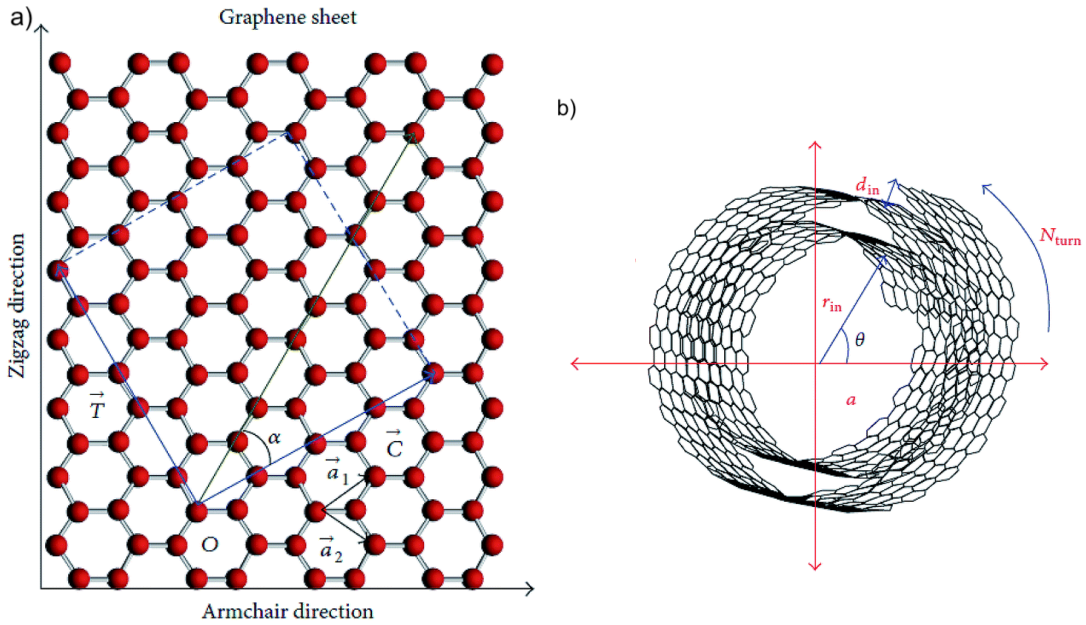


Figure 2.14: Diagram of the geometrical parameters of a nanoscroll [84]. Figure is adapted with permission from [84]. Copyright 2016 Royal Society of Chemistry.

Furthermore, there are parameters related to the 2D TMD sheet that define the resulting structure of the nanoscroll. These are shown in Figure 2.14a and consist of the chiral vector, $\vec{C}$, along which the

scroll is rolled and the translation vector, $\vec{T}$, that follows the length of the scroll. Recalling Section 2.2.2, it can be understood that various nanoscroll edge structures can result from the axis along which the TMD is rolled. When $\vec{C}$ is aligned with the AC edge, nanoscrolls will have an armchair edge as seen in Figure 2.15a, and when $\vec{C}$ is aligned with the ZZ edge, the scrolls will have a zig-zag edge (Figure 2.15c). However, any direction of rolling between these is considered "chiral" and leads to a mixed state edge.

In the case of MoS_2 nanoscrolls, both experiment and molecular dynamics simulations have been carried out to try to determine which of these scrolling directions is most favorable [80]. It has been found that MoS_2 flakes prefer to scroll from the Mo-ZZ edge, leaving the scroll with an armchair orientation. This is thought to be due to the reduced energy per atom achieved via $\vec{C}$ being parallel with the AC edge. It was also found through simulation that chiral scrolling is by far the least favorable energetically [80].

As mentioned, nanoscrolls have the geometry of an Archimedean spiral and, thus, there is an equation that specifies the length of the sheet in the $\vec{C}$ direction that forms the scroll [84].

$$L = \int_a^b \sqrt{r_{in}^2 + \frac{\mathrm{d}r_{in}}{\mathrm{d}\theta}^2}\,\mathrm{d}\theta \approx (2\pi r_{in} N_{turn} + \pi d_{in} N_{turn}^2) \tag{2.2}$$

By using this equation, one can determine the length of the flake/sheet that formed the scroll using a cross-sectional observation of it. This can help correlate scroll properties and their morphology pre-scrolling.

Generally, the ideal interlayer distance, d_{in}, for TMD nanoscrolls is close to or matches that which is found in the bulk materials (about 6.5 Å). This has been achieved regularly in the literature via various methodologies (a topic that will be returned to later). Some interlayer distances, however, are found to be much greater due to uncontrolled scrolling speed [78, 80]. Furthermore, theoretical work on graphene nanoscrolls has shown there is an equilibrium core radius, r_{in}, which arises from the core's role in force distribution [85]. Shi et al. [85] report that the equation for the virtual change in free energy of the core expanding/contracting with respect to the elastic strain, W, and surface energy, Γ, is

$$\frac{\mathrm{d}E_{tot}}{\mathrm{d}r_{in}} = \frac{\mathrm{d}W}{\mathrm{d}r_{in}} + \frac{\mathrm{d}\Gamma}{\mathrm{d}r_{in}} \tag{2.3}$$

This indicates that very small cores will experience strain energy domination and a driving force to expand. For very large cores, the surface energy will dominate, and there will be a force to contract. To solve for the equilibrium point, one must set $\mathrm{d}E_{tot} = 0$ and plug in the equations for the change in elastic strain of a scroll (Equation 2.4) and the change in total surface energy of the scroll (Equation 2.5).

$$\mathrm{d}W = -\frac{\pi D L}{d_{in}} \frac{R^2 - r_{in}^2}{R^2} \frac{\mathrm{d}r_{in}}{r_{in}} \tag{2.4}$$

where D is the bending stiffness.

$$\mathrm{d}\Gamma = 2\pi\gamma L(1 + \frac{r_{in}}{R})\,\mathrm{d}r_{in} \tag{2.5}$$

where γ is the surface energy per unit area. This results in the relationship

$$2\pi\gamma(1 + \frac{r_{in}}{R}) = \frac{DL}{r_{in}R^2} \tag{2.6}$$

so for a fixed L, D, γ, and d_{in}, the ideal core radius and outer radius can be determined [85]. However, it is not always possible to achieve this ideal, and research groups have encountered a wide range of results even using similar methodologies [9, 78, 80].

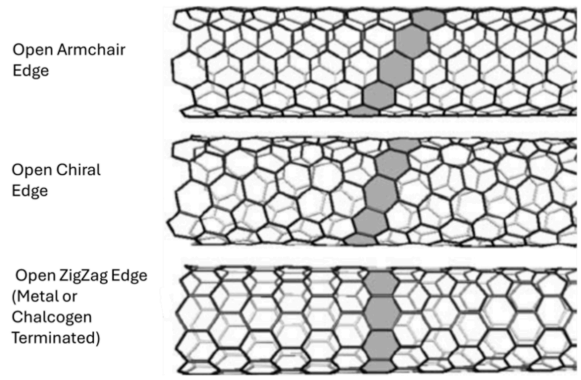


Figure 2.15: The possible edge structures of a nanoscroll. Adapted and reproduced from [75, 86].

2.3.2. Emergent Properties of TMD Nanoscrolls

As seen in Section 2.2.4, TMDs have highly tunable properties and can develop unique phenomena via the introduction of stacking, twisting, and strain. Nanoscrolls are thus a highly interesting structure as they incorporate all three. While it is self-explanatory how layering is present in a nanoscroll, the presence of the other two, twisting and strain, could use some additional discussion.

Geometric Strain in Nanoscrolls

Because of the spiral geometry of nanoscrolls, the 2D sheet of TMD, which is rolled into a nanoscroll, experiences a curvature strain. This strain, shown in Figure 2.16, is intrinsically non-uniform in cross section. The closer a layer is to the core of the scroll, the tighter it is rolled. This means that layers near the center have the highest curvature strain. Furthermore, within each layer, there are two directions of force. The layer of chalcogen atoms closer to the center experiences an in-plane compressive force. The other layer experiences a tensile force [75]. As a result, there is a lattice deformation that does not have inversion symmetry (something quite different than the Moiré-induced strain discussed earlier in 2D flakes). Combining these two effects (Figure 2.16b) creates a structure with a strain field not achievable in 2D structures.

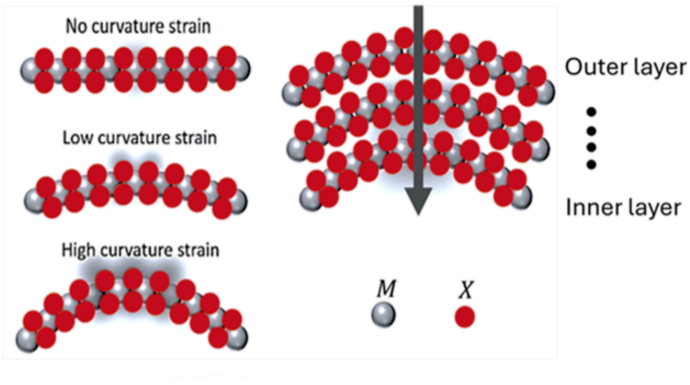


Figure 2.16: Diagram of the non-uniform strain caused by curvature in a nanoscroll. Reproduced with permission from [75].

Twist and Moire Formation

Since the rolling of TMD flakes creates a lattice distortion to their hexagonal structure, the periodic pattern of the lattice is lost. However, the non-uniformity of each layer stacking on top of one another can give rise to new interference patterns resulting in the Moiré superlattices as discussed in Section 2.2.5. Figure 2.17 demonstrates this process using a 3D model of a simple one-atom-thick hexagonal lattice (such as graphene). The regions highlighted in red represent the new Moiré patterns.

This Moiré formation has been demonstrated in TMDs such as MoS_2, however, few reports detail the

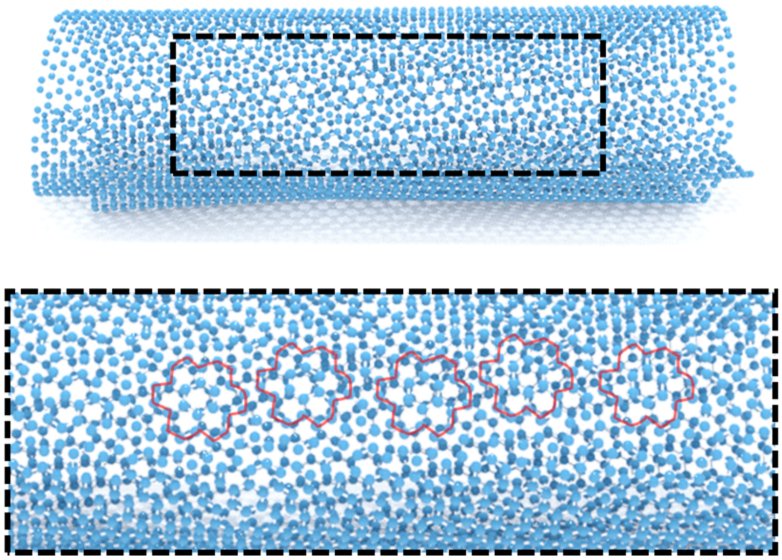


Figure 2.17: 3D model of a scrolled hexagonal lattice.

exact nature of their development [75, 87]. Chatterjee et al. [88] investigated the twist angle found in MoS_2 nanoscrolls. They found that the twist measured is a combination of the chiral angle of rolling and a slight twist between each layer. This twist has been reported before in the context of nanoscrolls and is thought to be unavoidable even in the case of a perfect AC or ZZ scrolling direction.

Similarly to graphene, one study has presented a computational-based argument for special angles in WS_2 which would arise from the chiral angle (ϵ_c) satisfying the formula [89]

$$\sin \epsilon_C = \frac{a}{2\pi d} n, n = 0, 1, 2, 3, ... \tag{2.7}$$

In this case, the lateral shift between layers (as seen in Figure 2.18b) would cause each one to coincide with the one underneath it and lead to an enhanced interference effect. The authors of this paper also argue that these special angles should be the most energetically favorable and will thus naturally arise in the scrolling process, but were not able to obtain a scroll with any of the possible values [89]. Additionally, no other papers report these angles in TMD scrolls, so it is not yet clear if this phenomenon is physical. Furthermore, if one recalls the discussion from Section 2.3.1, other reports find that AC-edge aligned scrolling should be the most favorable and chiral the least [80].

Interestingly, it should also be noted that the Moiré patterns formed in nanoscrolls share character with those caused by lattice mismatch in heterostructures, but instead are the result of the non-uniform lattice strain caused by the curvature differences between layers discussed earlier [90, 91]. This unique superlattice structure is widely agreed to be highly impactful on several properties, including photoluminescence, bandgap, electron mobility, and exciton phonon coupling.

Optoelectronic Effects

One of the first properties that comes to one's mind when imagining the effect of scrolling on TMDs is their electronic bandgap. Recalling the effects of stacking on 2D MoS_2 and $MoSe_2$, it is no surprise that TMD nanotubes are consistently found to possess indirect bandgaps which become smaller as the number of layers is increased [77, 80]. However, nanoscrolls present a more complicated and less understood story. While some literature reports the expected indirect bandgaps of multilayered TMDs in nanoscrolls [9], others have found a maintenance of the direct gap found in the original monolayers [92]. In the worst case, this means there is no clear consensus on the bandgap transition experienced from scrolling, but it could also indicate even more possible tunability in nanoscrolls than other 1D structures. The reasoning for this is theorized to be the result of morphology-dependent van der Waals interlayer

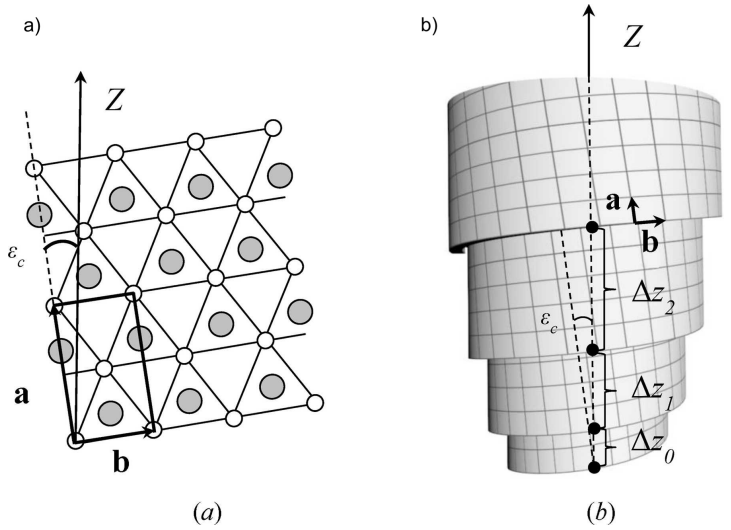


Figure 2.18: Diagram of the structure of a 2H TMD nanoscroll with a non-zero chiral angle. a) The unscrolled lattice structure b) Model of the scroll highlighting the lateral shift between layers. Figures reproduced with permission from [89]. Copyright 2014 International Union of Crystallography.

interaction [88, 92]. These interlayer interactions can be suppressed by widening the interlayer distance. So far, methodologies to increase this distance have been proposed (see Section 3.3), but no studies have successfully fabricated scrolls with a range of interlayer distances to directly compare their electronic bandgaps. This is a highly exciting avenue to explore, employing the reported techniques to attempt a study of direct controllability on interlayer distance.

Similarly to the bandgap, it can be recalled that PL is strongly connected to the layer number and van der Waal interlayer interaction. Thus, the effect of scrolling on this property reflects the discussion of the previous paragraph. One unique feature found in the decreased interlayer interaction scrolls was a significant increase in PL intensity, seen in Figure 2.19 [92]. The research group was able to replicate these results in part of a 2D bilayer by utilizing a similar fabrication to decrease the interlayer interaction in the stack. This increase in PL is, thus, most likely due to an effective combination of multiple monolayer PL emissions. Again, however, replication is needed to draw concrete conclusions from these findings.

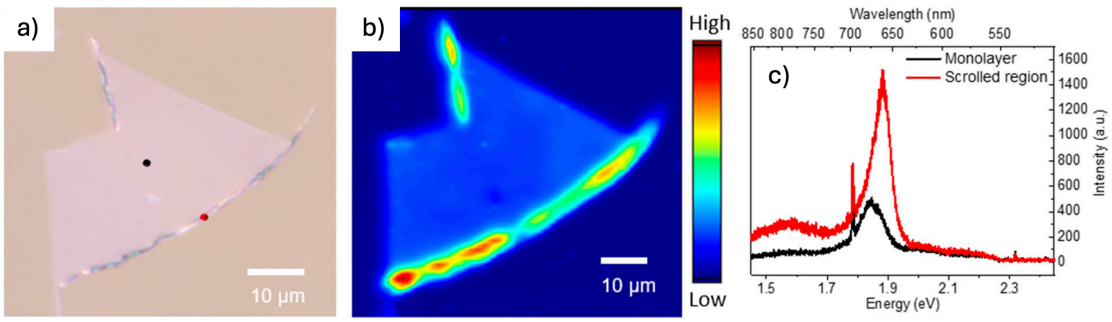


Figure 2.19: a) Optical image of partially scrolled monolayer MoS_2 flake, b) PL intensity map of a), c) PL spectra obtained from points labeled in a) Figured adapted with permission from [92], Copyright 2022 American Chemical Society.

Although nanoscrolls can clearly differ in emergent properties from nanotubes, they can still be valuable tools for estimating the effects of multilayered 1D structures in areas where little to no work has been done. For example, MoS_2 nanotubes have been found via first principle calculations to react to externally applied strain [64]. Depending on the strain direction and chirality of nanotubes, the bandgap can be decreased or enhanced by uniaxial strain along the axial direction.

When it comes to carrier mobility, an important property for potential transistor applications, there are a

number of contradicting results. From a basic theoretical perspective, electrons in bulk and multilayer TMD flakes can only travel through the outermost van der Waals layers as they are blocked by the gaps between them (Figure 2.20). Monolayer flakes do not have this issue, but are limited by channel width, W. Nanoscrolls effectively increase this current density by allowing carriers to flow through all layers in a more compact form. In addition to reporting a higher mobility in their nanoscrolls than multilayer or monolayer flakes (200-700 $cm^2V^{-1}s^{-1}$ versus 10-20 $cm^2V^{-1}s^{-1}$, Cui et al. [78] found that the monolayer flake based transistors they produced were more sensitive to degradation of mobility from exposure to air while the nanoscroll transistors were self-protecting. Thus, their work is highly encouraging for the development of TMD nanoscroll-based transistors. However, this is not well corroborated by other literature. Wang et al. [80] find a nearly 4 times lower carrier mobility for MoS_2 nanoscrolls compared to sheets at only 9.7 $cm^2V^{-1}s^{-1}$ versus 37.5 $cm^2V^{-1}s^{-1}$. These results are incredibly different from one another and provoke one to question the methodological differences that could lead to such disparity. Although it is hard to know exactly what mechanisms lead to these changes, the most suspect difference is in the fabrication of the nanostructures themselves, whereby Wang et al. most likely had far greater contamination of the materials. While Cui et al. had only ethanol applied once over the whole process, Wang et al. used PMMA, deionized water, three applications of acetone, and isopropyl alcohol, creating far more possibilities of contaminating their results. This is not the cause of the difference for certain, but it is nonetheless something that has been kept in mind for choosing the scrolling method applied later in this work.

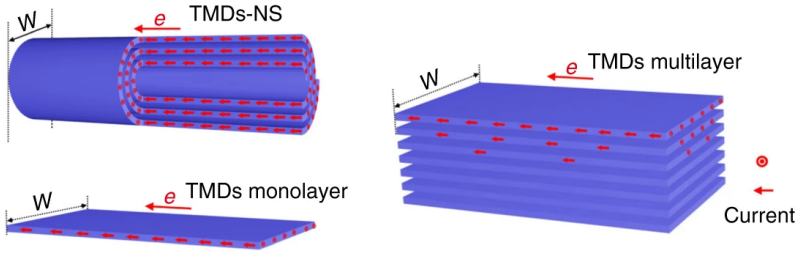


Figure 2.20: Diagram of the theoretical current (e) of TMD nanoscrolls (NS), monolayers, and multilayers. Figure reproduced with permission from [78].

2.4. Motivation for the Thesis

Having thoroughly reviewed the available scientific literature regarding TMDs, their properties, and their fabrication, it can be seen that there is significant potential for their further study. Particularly, recent advances in strain-based tunability of properties such as bandgap, photoluminescence, and the emergence of in-plane polarization textures have opened an avenue for developing techniques for precise control of non-uniformly strained morphologies. Specifically, with regard to complex polarization fields and vortices, little is still known about the conditions for their formation. While theoretical models predict in-plane polarization in strictly non-inversion symmetric materials like heterostructures, hBN, and multilayers [70], the experimental evidence is inconclusive on the matter. Some reports, like that of Sangers et al. [8], corroborate this finding in their complex multilayer TMD structure; however, the idea is contradicted by Tsang et al.'s [73] bilayer MoS_2 structure. Based on the available evidence, it does seem that uniquely non-uniformly strained morphologies with no inversion symmetry have the greatest potential to exhibit these effects. Thus, in combination, there is great motivation to explore morphologies such as heterostructure nanoscrolls, which could be key to understanding these effects. Since nanoscrolls produce highly unique strain fields due to the combination of curvature, layering, and spiral-like cross-section, it is clear that understanding the morphological factors that contribute to their final structure and its properties is paramount. Therefore, it is highly valuable to focus on the fabrication of nanoscrolls, correlating and comparing pre- and post-scrolled morphology, and creating avenues for the development of heterostructure scrolls.

The following chapter will explain the methodologies chosen for the goals of this work and provide the remaining necessary background for understanding the mechanisms that play the most significant roles in the obtained results.

3

Methodology

Having established a fundamental basis for the properties and emergent phenomena that make the study of TMD nanoscroll fabrication particularly motivating, this chapter serves to introduce the theory of CVD. It will also explore the fabrication and characterization that will be most significantly utilized in this thesis. Because this project involves a large number of synthesis trials with many systematic parameter changes, a description of the core CVD methodology in this work will be described.

3.1. 2D Fabrication of TMDs

While various methodologies exist to directly grow 1D TMD structures [93, 94], in the case of nanoscrolls, one must necessarily start with a flat 2D structure that can be "rolled up". Due to the large body of research into 2D TMDs over the last decade, there are many effective methods to achieve this goal; however, some are more suitable for the goal of nanoscrolling than others. One key parameter of this is the thickness of flakes. The thinner a TMD nanosheet/flake is, the lower its bending stiffness is, allowing it to be rolled more efficiently and without breaking [75]. Additionally, the rolling process is more energetically favorable for thin sheets as their scrolling activation energy is lower [95]. Fabrication methods of TMD flakes and sheets can be broken down into top-down and bottom-up approaches. Top-down methods are characterized by moving from bulk crystal to 2D, i.e., removing a small amount of the desired material from a large premade source. These consist of methods such as mechanical and liquid phase exfoliation [96, 97, 98]. Bottom-up methods, on the other hand, are those that fabricate the needed amount or morphology of a material starting from precursor compounds, with examples being chemical vapor deposition (CVD) and physical vapor deposition (PVD) [99, 100]. This project focuses on the CVD method of growth, which can be used to produce thin, high-quality, and contamination-free TMD flakes [101] and has been successfully used as the basis of nanoscrolling in several published works [75, 78, 80, 102].

3.1.1. Chemical Vapor Deposition

Chemical vapor deposition (CVD) is a bottom-up material growth process in which gaseous precursor materials react with each other either in the vapor phase or directly on the surface of a substrate to form the desired solid product [103]. Generally, reactions in CVD are activated by heat, plasma, or photons, with high temperatures being by far the most common and simplest procedure.

The basic process of CVD consists of a few important steps, which can be seen in Figure 3.1. To begin, precursors are introduced into the heated reaction chamber either via gaseous pumping or a crucible of solid reactant. In the case of solid reactants, the precursors must sublimate to the vapor phase within the reaction chamber. At this point, the vapor phase reactants are transferred towards the growth substrate via a flow of gas (often inert, e.g., Ar), which is assumed to be laminar. During this time, reactions between the precursors may occur, creating intermediate reactants or byproducts [104]. The interface between the stationary substrate surface and the flowing gas leads to the formation of a boundary layer. The reactants must diffuse through this layer to reach the substrate and adsorb to it, at which point surface reactions can proceed, leading to the formation of solid products. Finally,

byproducts from these surface reactions will diffuse back through the boundary layer, where they will be carried out of the chamber [104, 105, 106].

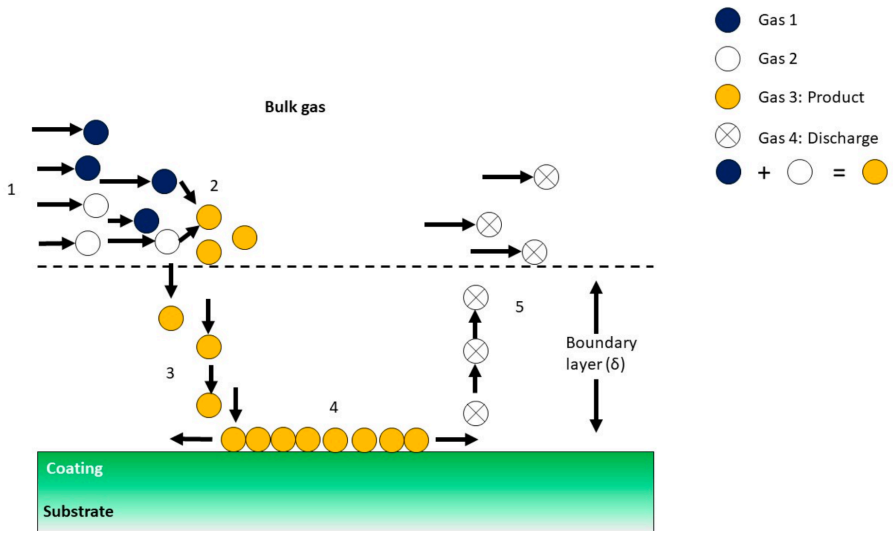


Figure 3.1: Schematic structure of CVD process. 1. Precursor vapors are transported downstream by the carrier gas. 2. Initial reactions for gaseous products. 3. Both precursors and initial products diffuse through the boundary layer and reach the substrate. 4. Surface reactions take place, forming solid products. 5. Secondary reaction products diffuse once again through the boundary layer and are carried out of the furnace. Figure reproduced from [1].

One of the most important stages in the previously explained process is that of nucleation on the substrate surface and the growth mechanisms that follow. Once the reactants have adsorbed to the substrate, they diffuse across the surface and nucleate at sites where it is energetically favorable, such as defects or surface impurities. This diffusion is driven by the thermal energy of the atoms can vary greatly by not just temperature, but also by the interplay between the energy possessed and the barrier to either create a new nucleation site or join an existing crystal lattice. This will ultimately affect the nucleation density and, eventually, whether the CVD process results in many small crystal growths, large flakes, or solid sheets. The presence of favorable nucleation sites and the diffusion rate of the adatoms will also impact the locational distribution of growth on the substrate. Generally, CVD growth of materials occupies one of two domains: kinetic or thermodynamic. In the kinetically controlled regime, reactants at the substrate surface are plentiful due to good mass transport through the boundary layer. However, these reactants are limited by their ability to diffuse to the optimal lattice locations and are more likely to nucleate into new crystal structures [51, 106]. Additionally, this increases the number of defects present on the grown crystals. In the case of the thermodynamically controlled regime, mass transfer across the boundary layer is a limiting factor, and the reactants that arrive at the surface have sufficient time to diffuse to the most energetically favorable lattice positions. This leads to the growth of larger and more stable crystal domains with uniform edges [51, 106].

As can be seen, the process of CVD is governed by thermodynamics and is, thus, highly dependent on a set of growth parameters which make up a CVD “recipe.” These parameters include temperature, time, gas flow rate, pressure, substrate choice, and both precursor composition and amount [103]. How these parameters interact with one another is also dependent on the unique chemical species being grown and the precursors’ properties [106]. This is why, now, the state of the art in fabrication of MoS_2 and $MoSe_2$ will be examined.

Growth of MoS_2 and $MoSe_2$

In contrast to the bottom-up approaches which have already been discussed, CVD growth of MoS_2 and $MoSe_2$ allows for far greater control of the size, shape, and thickness of the resultant material [101]. CVD has, thus, emerged as one of the most well-studied methods for obtaining high-quality, high-yield flakes and sheets of MoS_2 and $MoSe_2$ [107, 108].

There are two methods common in the literature for TMD CVD growth: two-step and one-step (vapor

phase). The former of these methods is the direct chalcogen inclusion into a predeposited transition metal film, while the latter involves utilizing both transition metal and chalcogenide precursors in the CVD reaction furnace [1]. Generally, the two-step method is employed to create large continuous sheets of MoS_2, rather than the separated crystal flakes seen with vapor phase techniques [109, 110]. Both can be potentially viable for producing 2D MoS_2 which can be rolled up into high-quality nanoscrolls; however, the two-step approach is generally preferable due to its ability to reproducibly create monolayer flakes and overall more uniform results [103].

As mentioned, the vapor phase synthesis of MoS_2 required the use of an individual precursor for both Mo and Se. Some studies have been done on the use of gaseous precursors such as $MoCl_5$, $Mo[Co]_6$, and $[C_2H_5]_2S$ with success in producing large monolayer MoS_2 sheets [111, 112]. However, CVD systems capable of using gaseous precursors are highly complex and require precise and expensive instrumentation to maintain safety and control. Instead, solid precursors are far more common [1]. In the case of S and Se, solid elemental powders and pellets of 99.5% or higher purity are almost exclusively used, while the transition metal precursors have much more variety. They are most often oxides, like MoO_3 powder, but can also be chlorides, foils, or aqueous oxide solutions painted on the substrate [103]. The main complexity associated with utilizing these solid precursors is the need to precisely control the temperatures they are brought to and held at during the growth. This is largely because the vapor pressure of solids is sensitive to temperature [103]. Furthermore, unlike with gaseous delivery, one must be aware of the various melting points of the materials used and where in a CVD furnace they must be placed to achieve control over the amount of vapor carried by the laminar carrier gas flow [1]. In the case of MoO_3 and S(Se), the melting point of the former is 759ºC while the latter's is 114ºC(221ºC). This means it is often considered best practice to separate them thermally. This can be done in two ways in a standard quartz tube furnace. The less specialized method involves using a single heating source in line with the growth substrate that reaches a set maximum temperature, with a temperature gradient being formed in the tube due to imperfect heat isolation. This method leads to less exact control of the temperature reached by the chalcogen, but has nonetheless been successfully used for the fabrication of both MoS_2 and $MoSe_2$ [113]. The more common method involves two- or three-zone CVD furnaces where each zone has its own heating element, which can be controlled individually [1, 105, 114, 115]. S/Se is placed upstream of MoO_3 and heated to a value above its melting point. The oxide is placed next to or under the substrate and heated to a temperature in the range of 700ºC to 900ºC.

The chemistry of the unassisted MoS_2 vapor phase reaction is widely accepted to consist of a two-part process that can be described via the Equations 3.1 and 3.2.

$$MoO_3 + \frac{x}{2}S \rightarrow MoO_{3-x} + \frac{x}{2}SO_2 \tag{3.1}$$

$$MoO_{3-x} + \frac{7-x}{2}S \rightarrow MoS_2 + \frac{3-x}{2}SO_2 \tag{3.2}$$

This can be simplified to Equation 3.3. However, due to non-ideal conditions in most CVDs, incomplete reactions often occur with intermediary products being flushed out of the furnace before ending up as solid MoS_2 [101].

$$2MoO_3(v) + 7S(v) \rightarrow 2MoS_2(s) + 3SO_2(v) \tag{3.3}$$

One can imagine a similar set of equations for the synthesis of $MoSe_2$, however, this mechanism has as of yet only been successfully observed in one study [116]. Nevertheless, growing $MoSe_2$ flakes by CVD with various promoting mechanisms is a well-explored method to obtain high-quality and controlled morphology [12, 18, 113, 114, 117]. The reason for this difference for seemingly chemically similar materials is that the process is more difficult due to the less chemically reactive nature of Se. As a result, CVD growths of $MoSe_2$ mainly differ from that of MoS_2 in that they often have higher temperatures and longer reaction times. Additionally, supplementary chemical agents are used in some fashion to improve the growth process. Most often, hydrogen gas is utilized (in mixture with Ar) to act as a reducing agent [12, 113, 114]. This reduction reaction is represented by Equation 3.4, where H_2 gas acts as an

invaluable reducing agent. The literature suggests H_2 is necessary for the growth of high-quality $MoSe_2$ films (at least below 820ºC), however, the gas is highly flammable and expensive, and well-maintained safety systems must be in place to work with it [12]. This creates a burden in utilizing this method and has prompted some researchers to experiment with CVD growth in pure Ar environments [12].

$$MoO_3 + xH_2 \rightarrow MoO_{3-x} + xH_2O \tag{3.4}$$

An alternative method for encouraging the growth of $MoSe_2$ by simpler means is via the use of NaCl as a promoter for MoO_3. This works by NaCl reacting with metal oxides to form chlorine oxides, which have lower melting temperatures and, thus, can selenize more efficiently [12]. Equation 3.5 shows one pathway possibly occurring in the CVD proposed by Zhao et al. [12].

$$MoO_3 + NaCl \rightarrow Na_2MoO_4 + xMoO_xCl_y \tag{3.5}$$

Incorporating salts is an easy, cost-effectively, and minimally harmful method by which $MoSe_2$ monolayer flakes can be grown in atmospheric pressure CVD (APCVD) furnaces without the need to reach temperature ranges (800ºC+) often outside the capabilities of standard equipment. However, successfully synthesizing $MoSe_2$ in the vapor phase without any promoters is still a relatively unexplored area in the literature that could benefit from additional research.

Effect of CVD Parameters on Vapor Phase Synthesis of MoS_2 and $MoSe_2$

Having discussed the overarching mechanisms and most common precursors of MoS_2 and $MoSe_2$ CVD growth, each parameter's effect on resulting growths and properties can be examined. Since many parameters interact with one another and can be related (especially in the case of solid precursor recipes), this review attempts to simplify the parameters into the most individually controllable ones (gas flow rate, substrate temperature, chalcogen temperature, and reaction time). This is followed by a discussion of how others may be affected by those included as part of a "recipe." Before reading further, it is important to keep in mind that it is nearly impossible to define a set of objective correlations between specific parameters and resulting crystal growths. This is because the nature of each CVD furnace is highly unique, and exact replication is not feasible. Instead, one can look to the following literature to get an understanding of the relative effects as certain parameters are varied.

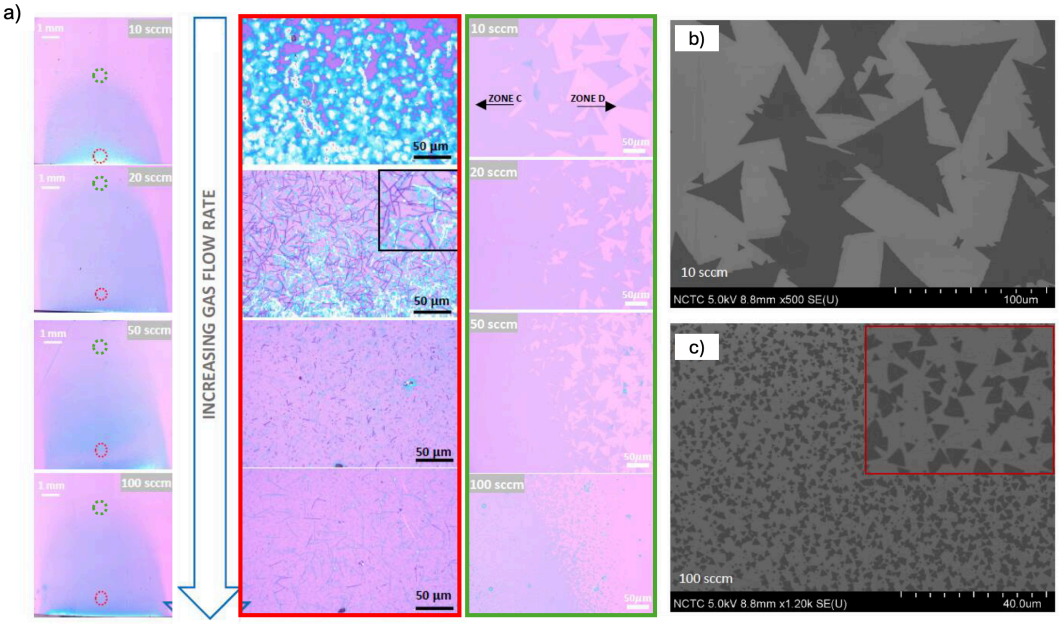


Figure 3.2: a) OM images of MoS_2 grown at varying Ar flow rates taken near the upstream edge (red) and at the film interface (green). b) & c) SEM images of the edge structure of flakes grown with 10 and 100 sccm. Figure adapted for use with permission from [101].

Gas Flow Rate In CVD growth of MoS_2 and $MoSe_2$ without H_2, the Ar carrier gas flow rate strongly influences flake morphology and concentration. For MoS_2, Chiawchan et al. [101] showed that low flow rates produce dense, thick flakes concentrated near the upstream edge of the substrate, while higher rates (e.g., 100 sccm vs. 20 sccm) yield smaller, more uniformly distributed flakes (Figure 3.2). This reflects the shift from a thermodynamically controlled regime, where limited mass transport favors large, stable domains, to a kinetically controlled regime, where abundant reactants promote rapid nucleation and more defects [51, 106]. Senkić et al. [118] demonstrated that increasing flow rate can actually enhance crystal size, but only within the thermodynamic regime. Beyond this, kinetic effects dominate, producing smaller, more irregular or serrated flakes. Similarly, Cao et al. [119] observed a morphological transition from multilayer dendritic to monolayer triangular flakes as the flow rate decreased.

For $MoSe_2$, similar trends exist but with subtler effects due to selenium's lower reactivity. Zhao et al. [12] found that, for NaCl-assisted growth, higher Ar flow rates favored hexagonal and multifaceted domains, while lower rates yielded triangular flakes (Figure 3.3). This difference likely arises because $MoSe_2$ remains thermodynamically controlled over a wider flow range. The resulting morphology is linked to changes in the Mo:Se ratio, whereby lower flow rates create Mo-rich conditions and favor Mo-terminated edges [50]. As the flow rate increases and the Mo:Se reaches near-stoichiometric ratios, both edges form, and hexagonal flakes are grown. This observed pattern over the same flow rate ranges as studied for MoS_2 suggested that high-quality $MoSe_2$ can form at higher flow rates than MoS_2.

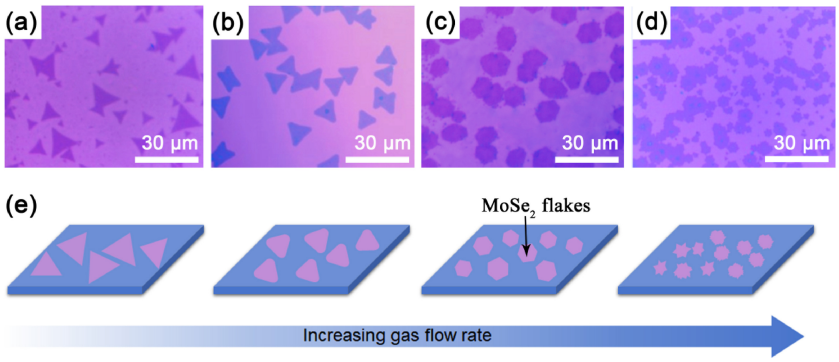


Figure 3.3: Effect of Argon flow rate on the morphology of CVD grown $MoSe_2$ flakes at a) 50 sccm, b) 75 sccm, c) 100 sccm, d) 125 sccm, and e) Diagram of morphological change. Reproduced with permission from [12].

Substrate Temperature In most CVD setups, the growth substrate and Mo precursor are heated together, making substrate temperature a key factor controlling both vaporization and reaction kinetics [103]. Temperature affects not only precursor vapor pressure but also gas flow behavior and mass transport [120]. For Mo-based TMDs, sufficient precursor vaporization begins near 600ºC for MoO_2 and 350ºC for MoO_3, though complete sulfurization typically requires >700ºC [108, 121]. At higher temperatures, reactions become kinetics-limited and precursor depletion accelerates [103]. However, as mentioned in Section 3.1.1, using precursors with lower melting points can reduce the needed growth temperature, something that can also work for MoS_2 [121].

Experimentally, growth temperature determines both flake size and morphology. For MoS_2, increasing temperature from 650ºC to 750ºC enlarges triangular domains (to ∼50 μm) while lowering nucleation density [120, 122]. Beyond about 750 °C, flakes thicken and develop truncated or hexagonal shapes, often with improved crystallinity but reduced uniformity (Figures 3.4). At even higher temperatures (>800ºC), thermal stress during cooling from high temperatures may induce cracks due to mismatch between MoS_2 and the SiO_x substrate [120, 123]. Additionally, at these high temperatures, intermediate Mo–oxide phases can form [108], as enhanced MoO_3 diffusion locally lowers the S:Mo ratio. The diffusion of MoO_3 vapor can be expressed as [124]:

$$n(x,t) = n(0,t)\exp\left\{-\frac{x^2}{4Dt}\right\} \tag{3.6}$$

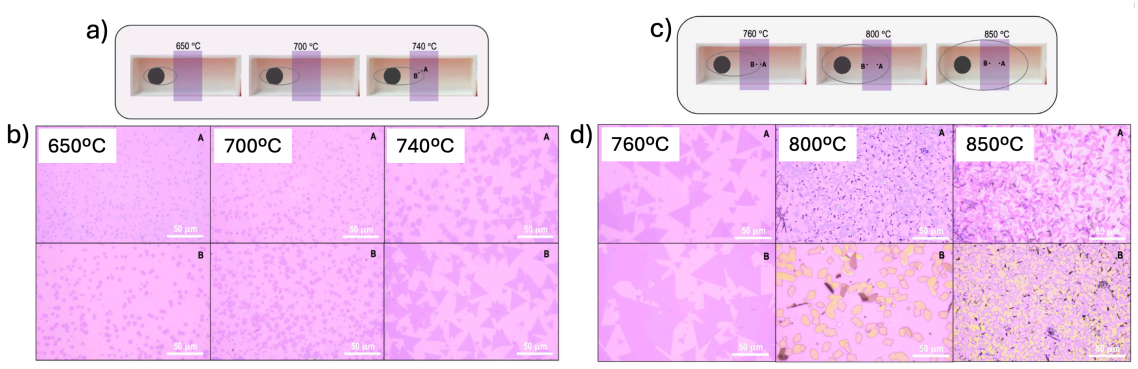


Figure 3.4: a) & c) Diagram of location of Mo precursor (black circle) and substrate b) & d) Optical images showing the morphological evolution of MoS_2 flakes upon increasing the growth temperature from 650ºC to 850ºC. Adapted with permission from [108].

where $n(x,t)$ is the concentration of the gas at a distance x away from the source, D is the diffusion constant, and t is the time the gas spends in the reaction chamber. The diffusion constant, approximated for a hard-sphere model, follows [124]

$$D \approx \sqrt{\frac{k^3}{\pi^3 m}} \frac{T^{\frac{3}{2}}}{Pa^2} \tag{3.7}$$

Since the process of APCVD occurs at 1 atm, increasing temperature directly raises D, thereby enhancing MoO_3 diffusion and precursor concentration across the substrate. Consequently, temperature can dominate precursor supply dynamics, sometimes outweighing even the initial powder mass ratio in determining growth outcomes.

$MoSe_2$ growth follows similar trends to MoS_2 but requires slightly higher temperatures due to Se's lower reactivity. Zhao et al. [12] reported increasing domain size and reduced nucleation from 700ºC to 850ºC, followed by thicker multilayer growth above this range (Figure 3.5). The transition is attributed to Mo enrichment at flake edges, stabilizing multilayer formation. Thus, optimal temperatures for monolayer $MoSe_2$ growth are typically higher than for MoS_2 but governed by the same thermodynamic–kinetic balance.

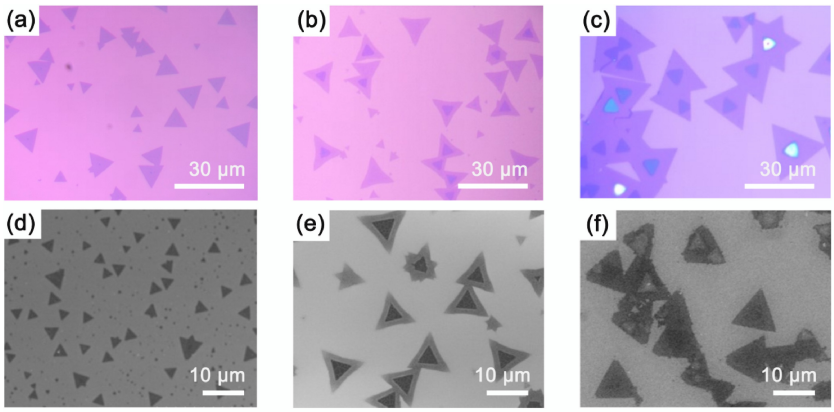


Figure 3.5: Effect of substrate temperature on the morphology of CVD grown $MoSe_2$ flakes. Reproduced with permission from [12].

Chalcogen Temperature Since many CVD processes are performed with only one temperature-controlled zone [12, 18, 122], the effect of chalcogen temperature is not often studied. However, there are a small number of studies that vary the temperature in a small range. Senkić et al. [118] investigated the morphological changes when heating sulfur powder in the range from 135ºC to 170ºC. They

found that higher sulfurization temperatures logically lead to an increase in sulfur concentration at the reaction site. This skew towards S results in the development of star-like shapes (Figure 3.6).

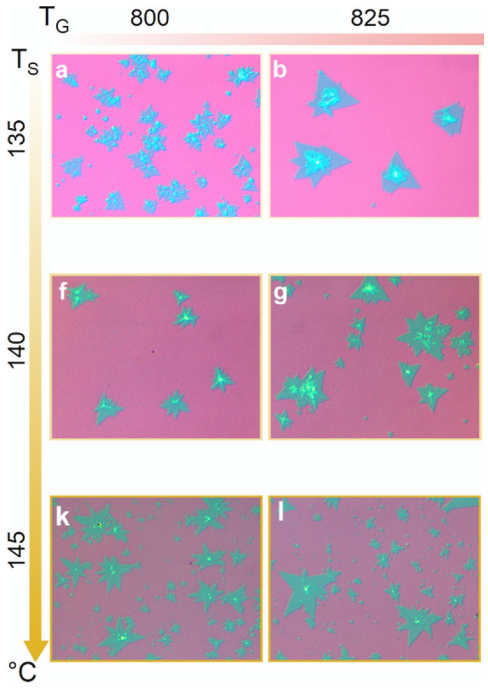


Figure 3.6: Optical images showing the morphology evolution of MoS_2 flakes as sulfurization temperature (T_s) is varied. Reproduced with permission from [118].

While the lack of specific further studies on this matter hinders the ability to understand the mechanisms of chalcogen temperature on the growth of MoS_2 and $MoSe_2$, the average values of heating can still be addressed. In the case of MoS_2, successful mono and few-layer growths can be found from temperatures as low as 135ºC [118] to as high as 220ºC [1], though, in some cases [125], the value of sulfurization is not reported due to unknown heating gradients in a single zone furnace. For Se, even less is reported in the literature regarding the effect of changing its vaporization temperature. When no hydrogen is used, Se has been heated anywhere from 300ºC [12] to 780ºC [18], and some reports, again, do not mention the temperature at all [116]. Since other parameters are quite different in these studies, it is extremely difficult to make conclusions about what temperature leads to the best reactivity of Se. Thus, the takeaway in these circumstances is that S and Se have a wide range of temperatures over which they can be successfully vaporized and supplied to the growth substrate. Additionally, this can be identified as a gap in the literature and could be investigated to gain a fuller picture of ideal CVD parameters.

Precursor Mass The masses of Mo and chalcogen precursors directly affect TMD crystal growth, as higher precursor quantities increase the vapor-phase concentration available for reaction. The most crucial aspect is creating the right balance between the two precursors [118]. Although MoS_2 and $MoSe_2$ are stoichiometrically 1:2 (Mo:S(Se)), effective vapor phase ratios must be much higher in chalcogen due to long transport distances and limited surface reaction probabilities [126]. Consequently, molar ratios of S:Mo around 30:1 are commonly used for MoS_2, though often without detailed justification. Han et al. [122] systematically varied both MoO_3 and S precursor masses and found MoO_3 strongly determines nucleation density. Too little yields sparse flakes, while excess produces dense deposits and small dark particles, which have been attributed by others to MoO_x or $MoOS_2$ phases from insufficient sulfur [126, 127]. Excess MoO_3 can further promote oxide crystal growth, particularly at lower temperatures (<750ºC) [127]. Conversely, excessive S leads to morphological changes such as concave triangle formation (Figure 3.7).

For $MoSe_2$, hydrogen-assisted CVD typically employs similar or slightly lower chalcogen ratios than MoS_2, reflecting selenium's higher molecular weight [113, 114, 116, 128]. However, in NaCl-assisted,

H_2-free processes, reported MoO_3 masses are much lower (2 mg), raising the Se:Mo ratio to roughly 100:1 [12, 18]. While data on varying these masses are limited, the results found suggest a highly chalcogen-rich environment is even more critical for $MoSe_2$ than for MoS_2. Future experimental work should explore this parameter space to clarify its impact on growth outcomes.

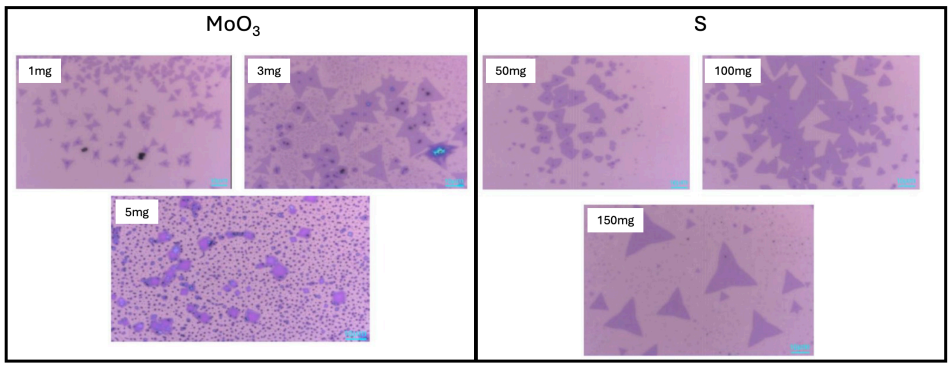


Figure 3.7: Optical images of flakes grown with varying levels of MoO_3 (left) and S (right). Adapted with permission from [122].

Reaction Time Reaction time is a surprisingly understudied element of CVD growth from MoS_2 and $MoSe_2$. It is generally understood that under the same conditions otherwise, increased growth time will lead to more growth, but in what way is less predictable [103]. This is because the importance of time hinges directly on the amount of it spent under a certain growth condition. For example, flakes of MoS_2 can continue to grow either larger or thicker if the substrate continues to receive the correct ratio of all precursors at the same growth temperature. However, if a needed condition is disturbed, like the precursor is evaporated fully and flushed from the tube, the growth cannot proceed any further. In some cases, the growth will simply stall, but flakes can also shrink or disappear if enough time at high temperature is spent. Hammett [129] found that with 80 mg of S, 10-30mg of MoO_3, and a temperature of 700ºC, after 3 minutes of holding at growth temperature, the size of the flakes produced decreased. The reasoning for this is not well reported as MoS_2 and $MoSe_2$ have been found to be stable compounds at temperatures up to 1000ºC, but desorption of S can be seen at CVD growth temperatures with increased amounts of oxygen present in the environment [130]. Of particular interest to $MoSe_2$ growth is an apparent etching mechanism that is possible via the introduction of NaCl as a promoter. It was found by Oh et al. [131] that, especially under reduced Ar flow conditions, the sodium droplets that help reduce the energy of formation for MoS_2, also induced etching at particular edge defects. However, this etching was found to mainly lead to shape changes in the CVD-grown crystals, creating either more convex or concave triangles and not entirely removing the flake growth. Considering the ease with which reaction time can be varied in a CVD experiment, it is not entirely understandable why more literature exploring the topic was not able to be found. The few sources found were very small and did not properly document the parameters used compared to studies on factors like flow rate and temperature. The most important takeaway from this is, thus, that attention should be paid to time at peak temperature and not allowing it to be longer than the lifetime of the precursors added to the furnace. Reporting findings on the time of growth could also be valuable for the literature.

Other Considerations

The choice of substrate for the vapor phase CVD of MoS_2 (and other TMDs) is highly important to the growth mechanisms that arise. It, for instance, can be leveraged to achieve phase control in the fabrication of 1T or to increase the electrocatalytic nature of MoS_2 [132]. Additionally, the interfacial interaction of MoS_2 with the substrate plays a significant role in qualitative aspects of scientific study. Substrates like SiO_2 and sapphire are extremely popular choices for 2H MoS_2 and $MoSe_2$ growth [101, 108, 115, 118, 133, 134, 135, 136, 137]. These substrates are often chosen specifically for their lack of strong adhesion with MoS_2, which allows for the easy transfer of flakes to other substrates or inspection apparatuses. This also reduces the amount of influence substrates have on optoelectronic measurements, which take place on the growth substrate, such as Raman spectroscopy [75]. Furthermore, the most common choice of substrate, SiO_2/Si, has the distinct advantage of possessing great optical contrast with thin MoS_2 flakes, allowing for efficient and easy observation of relative thickness and size

[125]. However, the use of (C-plane) sapphire has been reported to enhance the alignment of TMD flakes by encouraging epitaxial growth and decreasing the amount of grain boundaries present on a nanosheet [138]. This creates a favorable middle ground between two-step and one-step approaches, where large nanosheet growth can be achieved while maintaining the uniform few-layer growth of vapor phase methods. Finally, to further enhance ease of characterization, some work has been done on growing TMDs directly on amorphous Si_3N_4 membranes as part of prefabricated transmission electron microscopy (TEM) grids [1, 105]. This eliminates the need to transfer the flakes for TEM inspection, but does present challenges to other forms of characterization.

Substrates do not have to be simply platforms for the fabrication of single species TMDs, though. Presently, an increasing amount of work is being done on the direct growth of 2D heterostructures via the use of other van der Waals materials as substrates [99, 139, 140]. As discussed in Section 2.2.5, heterostructures have great potential for designer tuning of properties, and their orientation and alignment with one another play a crucial role in this. So far, two-step CVD heterostructure growth has most often been performed in the context of growth on graphene and hexagonal boron nitride (hBN), which is necessitated due to the vastly different growth conditions for these materials compared to TMDs [139, 141]. Few papers have reported work in TMD only stacked heterostructures grown via multiple CVD processes, usually instead preferring to grow the combinations (e.g., WS_2/MoS_2, WSe_2, and $MoS_2/MoSe_2$) as one-step processes with all precursors present in the furnace simultaneously [33, 99, 115, 142]. However, Gong et al. developed a methodology in 2015 for growing epitaxial $WS_2/MoSe_2$ heterostructures via a two-step process [140]. In this method, $MoSe_2$ grown via vapor phase reaction with Se and MoO_3 as precursors. The substrate containing this growth is then placed into a different CVD where a similar CVD process (optimized for WSe_2 growth with a WO_3 powder precursor) is carried out. Gong et al. report that no special treatments are needed for the substrate in between these processes as the high temperature environment removes H_2O and O_2 molecules that may be present on the edges of the $MoSe_2$ flakes due to air exposure. It is found that, under these conditions, WS_2 preferentially grows from the edges of the $MoSe_2$ flakes, Figure 3.8, growing both outward (in-plane) and upward (stacked). As growth time is extended, the WS_2 flakes eventually cover the entire surface of the $MoSe_2$ and surround it from all sides (other than the bottom, which is in contact with the original SiO_2/Si substrate).

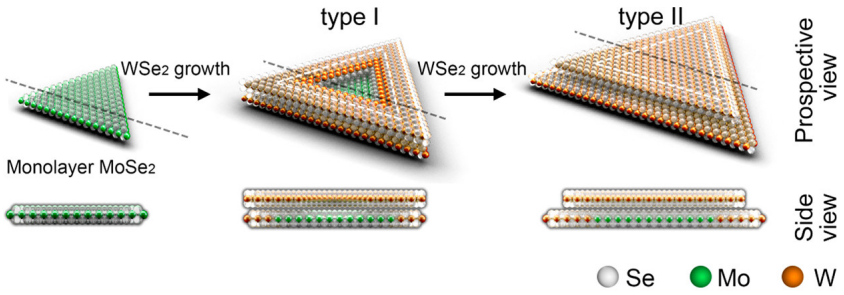


Figure 3.8: Morphology of $WS_2/MoSe_2$ heterostructures grown via two-step CVD method. Reproduced with permission from [140].

These heterostructures indeed saw some of the emergent properties expected, such as a new PL peak corresponding to an exciton transition that appears due to the coupling effect between WS_2 and $MoSe_2$ and the establishment of a p-n junction [140]. What sets this particular methodology for growth apart from the one-step methods most commonly used is the apparent lack of interatomic mixing between the two materials. Analysis of both the TMDs and their interfaces showed no W inclusions in the $MoSe_2$ regions or vice versa, which is almost always seen in one-step vapor phase growth [142]. This makes two-step CVD growth of TMD heterostructures an extremely promising field of study with little exploration as of the present day.

3.2. Methodology of the Study

CVD growth of TMDs is a well-explored and controllable process that produces thin, uniform, and replicable flakes. It is also a platform for directly growing heterostructures without the inconsistencies

of mechanical stacking methods. This makes it the ideal platform for answering the research questions presented in Chapter 1. While CVD growth of MoS_2 is a mature field, there were some specific gaps found. Most notably, the effect of changing chalcogen temperature has not been well documented compared to growth temperature. This is most likely due to the wide use of single-zone furnaces, which make adjusting this temperature more difficult. However, by having access to a multi-zone furnace, the effects of adjusting chalcogen temperature can be systematically assessed.

Additionally, it is noted that, compared to MoS_2, a significant gap in the literature specifically exists in the context of facile CVD growth approaches for $MoSe_2$. Currently, the only feasible approaches for any CVD growth of $MoSe_2$ structures is to use a reaction assistant (H_2 gas or NaCl) to increase the reactivity. While NaCl is a harmless additive, the use of H_2 gas comes with substantial risk factors, including dangers to the health of those working in the laboratory and potential for explosions and fire. It also increases the cost and complexity of the setup needed for fabrication. This means that finding a simple alternative, ideally one which does not require any species other than the Mo and Se precursors and the inert Ar carrier gas, is highly desirable. Beyond the desire to create easier growth methods, however, this literature review has revealed a lack of holistic understanding in the scientific community in the conditions needed for vapor phase $MoSe_2$ synthesis in APCVD. Due to CVD systems being highly individual, combined with the vastly different research goals and methods used across groups, it is nearly impossible to say with certainty what values of temperature, flow rate, and timing will result in successful $MoSe_2$ growth. While some papers have reported success while Se temperature as low as 300ºC [12], others require upwards of 800ºC [18] with little indication of what leads to this vast difference. As a result, attempting to synthesize $MoSe_2$ while focusing on a range of parameters from across the literature would be an extremely valuable avenue of study. Since the lab hosting this thesis project has never fabricated $MoSe_2$ by CVD before, doing so would also open up an opportunity for its study in conjunction with the more well-explored MoS_2. By stacking these two well-matched materials together, inversion symmetry would be broken, further enhancing the potential for polarization studies.

Thus, the methodology of this thesis will be made up of three parts:

1. Growing MoS_2 flakes while tuning CVD parameters to produce varying morphologies.
2. Characterizing the structures of the obtained flakes before and after scrolling.
3. Attempting to develop a $MoSe_2$ flake CVD recipe for eventual use in nanoscrolling and heterostructure fabrication.

3.2.1. Example Growth of MoS_2 as a Template for the Experimental Work

The approach used for CVD growth in this thesis relies on a three-zone quartz tube furnace as seen in Figure 3.9. This furnace can be fitted with various diameters of tubes that can be interchanged to prevent contamination between the different chalcogens. Using the furnace controller and software, the user can set the target temperature, ramping rate, and dwell time for each zone individually. This allows for precursors and substrates to be precisely controlled during the growth process. The CVD furnace is attached to a gas system that supplies pure Ar gas through a gas flowmeter that can be adjusted from 50 sccm to 1000 sccm. Gas expelled from the tube is passed through a glass bubbler, which is filled with paraffin oil before being flushed out via an exhaust pump. The bubbler prevents unintentional backflow of air (particularly oxygen) into the CVD system during a synthesis.

During a vapor phase growth of MoS_2, a 1 cm by 1 cm Si chip that has been coated with with 285 nm of SiO_2 is used a growth substrate. Before the synthesis, the substrate is cleaned via HNO_3. It is placed on a flat crucible and loaded into the center zone, known as Zone 2 (Z2), of the CVD furnace (quartz tube diameter of 3.5 cm) 36 cm from the entrance. Then, 10 mg of MoO_3 powder (99.95% Alfa Aesar) in a alumina boat is loaded 0.5 cm away from the substrate crucible (also in Z2). Finally, 500 mg of Sulfur powder (99.5% Alfa Aesar), also in an alumina boat, is placed 16 cm from the entrance of the furnace in the third heating zone (Zone 3, Z3). It is important to clarify that Ar gas enters first through Z3 of the CVD before traveling through Z2, then Z1 (unused throughout this project), and finally exiting to the bubbler. Thus, the terms upstream and downstream will heretofore refer to closer to the gas entrance and further from the gas entrance, respectively. This set-up is diagrammed in Figure 3.10.

Before any heating is begun, Ar gas is flushed through the system for 30 minutes at 1000 sccm to remove any oxygen from the reaction. After this, Z2 is ramped from room temperature to 750ºC at

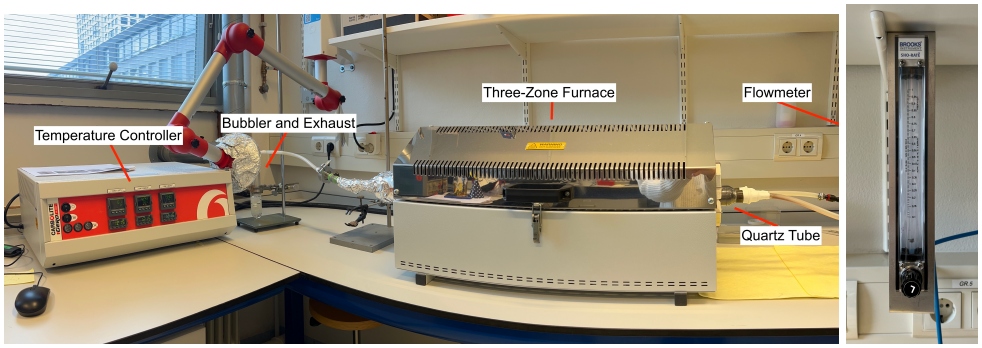


Figure 3.9: a) CVD furnace equipment used for growing materials in the project, and b) the flowmeter.

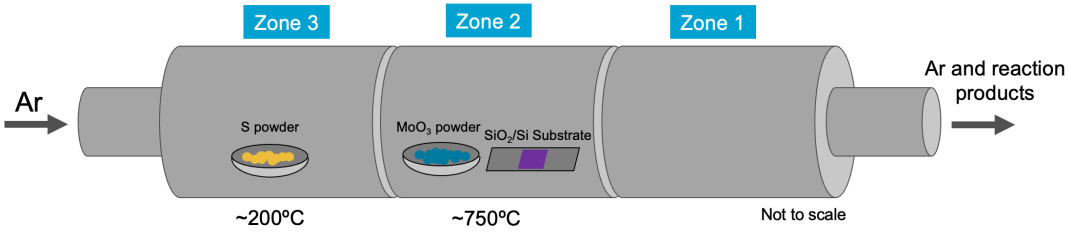


Figure 3.10: Diagram of parameters for MoS_2 vapor phase CVD growth.

10ºC/min. When 500ºC is reached, the Ar flow is reduced to the reaction flow rate of 100 sccm. Z3, which contains the sulfur powder, is not ramped until Z2 has reached the target temperature of 750ºC. When that occurs, the controller is instructed to hold zone 2 at the target temperature, and the ramping of Z3 is turned on also to a rate of 10ºC/min with a set point of 200ºC. When both zones have reached their target temperature, they are held for 5 minutes, after which the furnace is turned off and the tube is allowed to cool down naturally to 100ºC before the Ar flow is turned off and the sample removed. Figure 3.11a displays a temperature profile of the two zones during the entire heating and cooling process. It can be noticed here that due to heat transfer from Z2 to Z3 during the ramping phase, Z3 already measures about 160ºC when zone 2 reaches the setpoint. This means that ramping the rest of the way to 200ºC only takes about 4 minutes. The effects of this will be discussed in the following chapter.

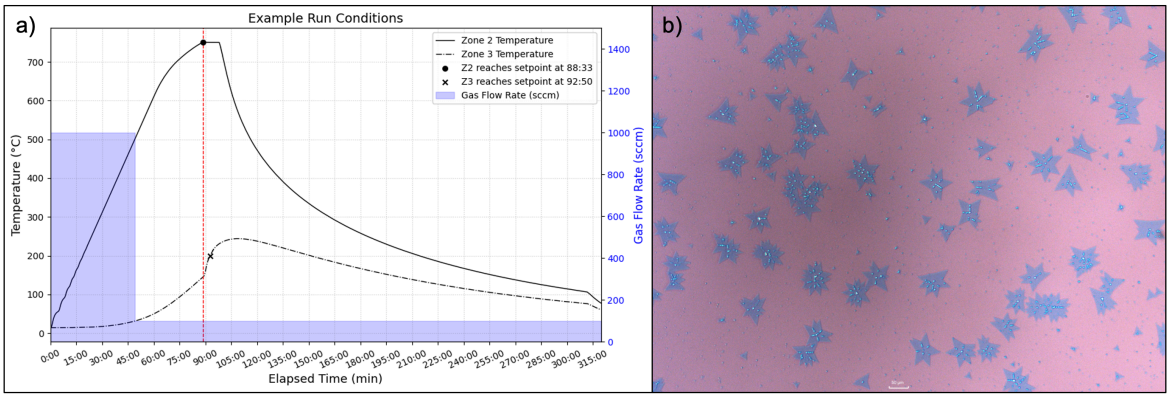


Figure 3.11: a) Temperature and gas flow profile plot for the initial method of vapor phase MoS_2 growth. 30-minute Ar flush phase not shown b) MoS_2 flakes grown via the initial vapor phase CVD recipe.

Flakes grown via this method are representatively displayed in Figure 3.11b and are of the general sample morphology that has, up until this study, been used within the lab. In the next chapter, this recipe and the flakes and nanoscrolls it produces will be examined. Furthermore, the actions taken to optimize the recipe for improved scroll morphology will be detailed.

3.3. Scrolling Flakes via Volatile Organic Solvents

Various methods have been employed in the literature to convert 2D TMDs into 1D structures via scrolling. Some examples include external strain-induced scrolling [82], vortex flow device [143], supercritical fluid [144], and solvent-assisted [78]. Among these, volatile organic solvent–assisted scrolling has proven the most reproducible and widely adopted approach. This method exploits the strain introduced in CVD-grown flakes during cooling, which arises from thermal expansion mismatch between the TMD and substrate [78]. When a volatile solvent—such as ethanol, methanol, or N-methyl-2-pyrrolidone is applied, it intercalates at the flake–substrate interface, weakening adhesion and initiating delamination. As the solvent rapidly evaporates, capillary flow lifts the flake edge, allowing van der Waals attraction to pull it upward into a rolled nanoscroll [102, 145]. This process is visualized in Figure 3.12.

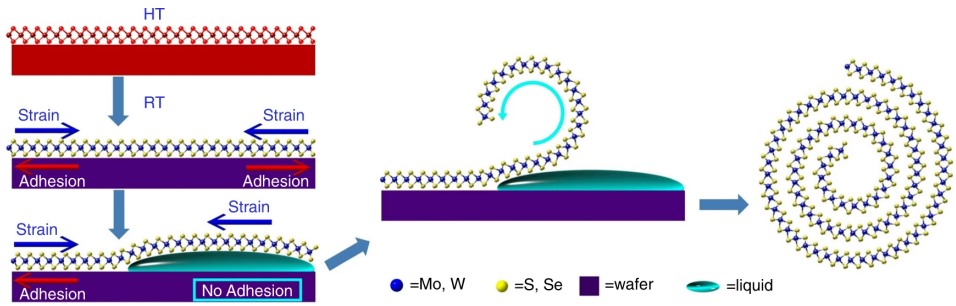


Figure 3.12: Diagram of the process of inducing scrolling in CVD growth flakes via application of a volatile organic solvent. Reproduced with permission from [78].

The ability for the solvent to penetrate between the flake and the substrate can be found by looking at the solid-liquid interfacial energy γ_{sl}, which can be expressed via the equation [91]

$$\gamma_{sl} = \gamma_{sg} - \gamma_{lg} \cos\theta_C \tag{3.8}$$

where γ_{sg} and γ_{lg} are the solid-gas and liquid-gas interfacial energies, respectively, and θ_C is the contact angle of equilibrium. It can be noted that γ_{sg} does not change with differing solvents and, thus, γ_{sl} can be minimized by maximizing the term $\gamma_{lg} \cos\theta_C$. Halim et al. [146] performed an analysis for an ethanol water solution on SiO_2 and found that γ_{sl} is minimized when the ratio of ethanol:water is about 1:3. This value has been utilized in the literature [91] along with other concentrations like pure ethanol [75, 102] and a 2:1 ratio mixture [78]. It is well agreed across these sources that the volatile organic solvent-assisted rolling method is quite efficient when applied to CVD-grown flakes. However, the reported efficiencies for different concentrations vary widely, likely due to differences in flake thickness and morphology, highlighting the need to optimize the solvent ratio empirically for each system.

Some of the largest drawbacks of solvent-assisted scrolling come from the residue that is often left behind on the nanoscrolls and in between their layers. This is difficult to fully remove without damaging the scrolls [91]. Additionally, it is reported that this method can lead to larger diameter nanoscrolls or flakes, which remain partially unscrolled and stuck to the substrate [147]. Nevertheless, the advantages of this technique, including the large coverage area, quick effect, low complexity and cost, and general efficiency, are highly compelling for this technique. This makes it understandable why it has risen to be the most widely used method since its first publication in 2018 [78]. It should also be noted that solvent-assisted scrolling has been successfully utilized in the hosting lab group [75].

3.3.1. Technique for this Study

The procedure for scrolling in this thesis is as follows: After a CVD growth has been completed, the substrate with MoS_2 flakes that are intended to be scrolled is allowed to come fully to room temperature. It is then placed under an optical microscope in order to see and document the scrolling process live. A small amount of clean ethanol (CH_3CH_2OH, EtOH) is decanted into a clean beaker. Using a clean glass pipette, two to five drops of EtOH ($\sim$150 µL) are then dispensed onto the surface of the substrate, ensuring it is completely covered but that no EtOH is spilled over the edge. The EtOH is then allowed to

evaporate over the course of about 10 minutes. During this time, the process described in Section 3.3 occurs, causing the flakes to release at their edges and roll up into the scrolled morphology. While this is happening, some scrolls become fully detached from the surface of the SiO_2 and float in EtOH subject to the flow caused by the evaporation. Most often, these scrolls are collected in a large mass of material that forms as the EtOH evaporates from the edges first, forming a bubble that decreases in size over time. Other scrolls remain fully or partially stuck to the surface for the entire process, making them much easier to inspect and characterize. This process is diagrammed in Figure 3.13.

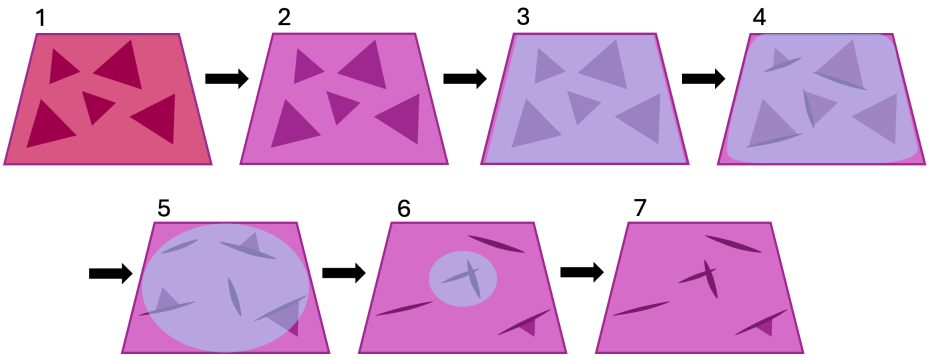


Figure 3.13: Diagram of the nanoscrolling process for TMD flakes. 1. Substrate with flakes comes out of the CVD at an elevated temperature 2. Substrate is cooled to room temperature 3. EtOH is dropped on surface 4. Evaporation begins, causing initial scrolling 5. Scrolling continues as EtOH pulls away from the edges 6. The majority of scrolls have formed as EtOH creates a bubble on the surface, carrying detached scrolls 7. EtOH is fully evaporated, leaving behind partially and fully formed scrolls.

3.4. Raman Spectroscopy for Characterization

While some characterization techniques are used in this thesis for the purposes of understanding the structure of the materials fabricated, Raman spectroscopy is the one most specialized for TMDs and for which the understanding of its theory is most vital to its use in the work. Thus, this section will give a brief overview and explain the elements of the technique that allow it to be powerful for gaining information on the composition, thickness, and lattice strain of TMD materials.

Raman spectroscopy non-destructive technique, utilizes scattering of focused laser light to probe the vibrational modes, or phonons, in a material. When photons from the laser interact with a material, the majority of them are elastically scattered; a small amount, however, are inelastically scattered (known as Raman scattering) via interaction with the molecular vibrations in the system. As a result, the energy of the scattered photon is higher or lower than the incident photons from the laser. This change is observed as a change in measured photon wavelength and is reported as a wavenumber, in cm^{-1}, called “Raman shift” [148].

Since the vibrational modes of individual materials are largely unique, and TMDs like MoS_2 exhibit changing susceptibility to polarization under atomic vibration, Raman spectroscopy can be used to determine if CVD-grown flakes are in fact the species desired. Additionally, TMDs’ vibrational modes are sensitive to the thickness of the sample. This allows Raman spectroscopy to additionally be used to probe the number of layers grown [149].

Hexagonal MoS_2 exhibits four active Raman modes that can be used to define its signal. The characteristic wavenumbers of these modes are: E^2_{2g}=32 cm^{-1}, E_{1g}=286 cm^{-1}, E^1_{2g}=383 cm^{-1}, and A_{1g}=408 cm^{-1}. The names of these modes are correlated to an irreducible representation of the vibration in line with the point group on the molecule being studied [150]. In the case of MoS_2, A_{1g} is the only mode correlating to an out-of-plane vibration, while E_{1g}, E^1_{2g}, and E^2_{2g} are in-plane modes. Furthermore, it is generally the A_{1g}, E_{1g}, and E^1_{2g} modes which are investigated in literature due to their prominence under the 488nm and 514nm lasers most often used in Raman spectrometers. In the case of E_{1g}, it is often considered a “forbidden” mode because it is only visible when the laser is not perpendicular to the basal plane. This is usually only possible in the case of vertical MoS_2 crystal growths and can be an indicator of such. Figure 3.15 presents some example Raman spectra for horizontal MoS_2 flakes.

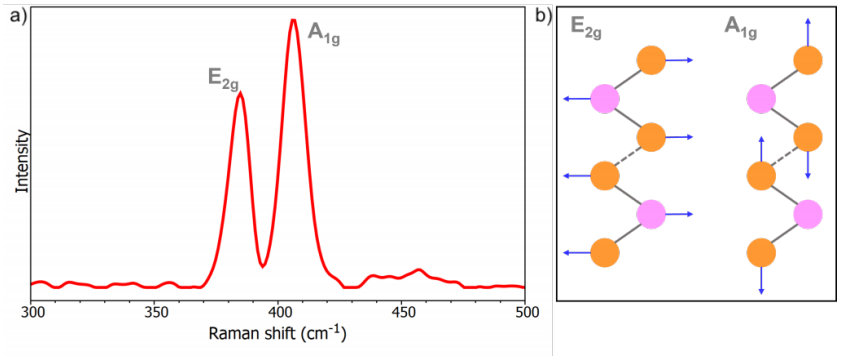


Figure 3.14: a) Example Raman spectra of MoS_2 b) diagram of vibrational movement in MoS_2 Raman modes. Reproduced from [151].

As stated before, beyond just confirming the presence of MoS_2 or $MoSe_2$, Raman spectroscopy techniques are valuable for confirming the thickness of flakes and the presence of strain or doping. When the bulk crystal is reduced to just a few layers, the intensity of the out-of-plane A_{1g} mode is reduced (Figure 3.15a). Theoretically, this should result in a 1:1 height ratio between the two most prominent modes; however, this is rarely the case in experiment and is, thus, not a good methodology for determining thickness. A more effective method can be seen in Figure 3.15b. By measuring the spacing in between the A_{1g} and $E^1{}_{2g}$ modes, one can determine the approximate number of layers present due to the red (blue) shift present in the A_{1g} ($E^1{}_{2g}$) mode.

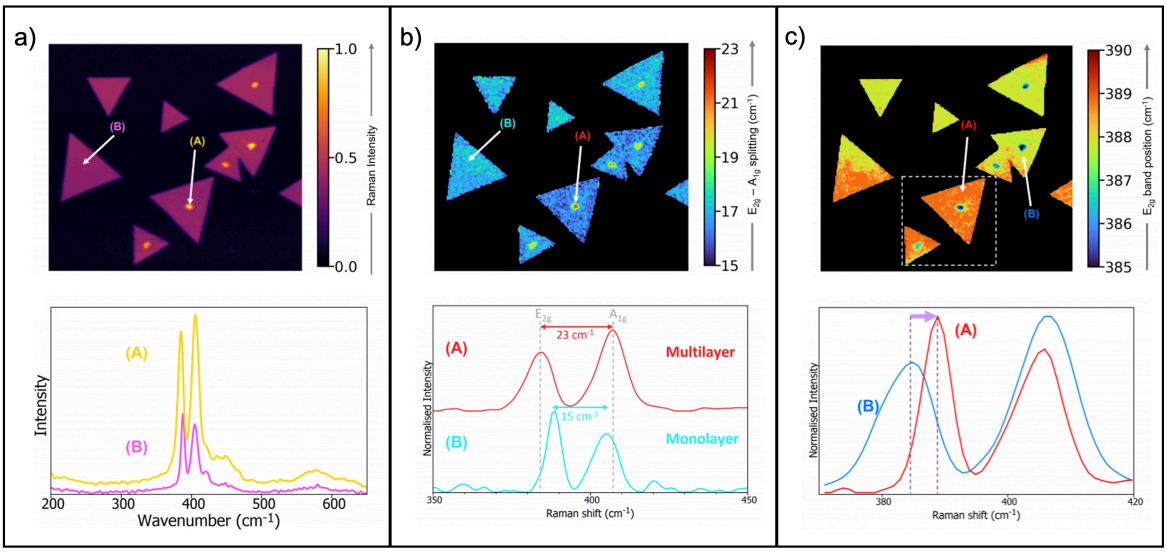


Figure 3.15: Example Raman spectra which highlight the impact of a) thickness on intensity, b) thickness on wavenumber gap, and c) strain on wavenumber. Adapted from [151].

Many other factors can contribute to changes to TMD Raman modes that are potentially present in nanoscrolled structures. As more layers come into proximity of one another, the van der Waals interaction is enhanced. This increase has been shown to result in frequency stiffening for certain Raman modes since it raises the restoring force that pulls atoms back to their equilibrium position in vibrational motion [78, 152]. As a result, the out-of-plane A_{1g} mode of nanoscrolled (or other rolled) TMDs is observed to increase in frequency compared to flat CVD-grown flakes [75]. Strain can also affect the Raman shift of TMDs due to the tension/compression that occurs in a strained lattice. The in-plane vibrational modes, like $E^1{}_{2g}$, are sensitive to this lattice strain and result in a small change in their frequency, thus changing the results of Raman analysis [153]. Furthermore, electrostatic interactions can affect in-plane modes, which are substantially present in nanoscrolls as discussed in Section 2.3.2. While experiments observing the Raman spectra of various nanoscrolls with different morphologies (length, diameter, layer number, and interlayer spacing) have been done in the context of heterostructures [154],

this area remains poorly understood and could benefit from a more detailed analysis. However, without the addition of special equipment, Raman spectroscopy is often limited by a resolution of about 1 µm. This can present limitations to its use in structures like nanoscrolls, which have dimensions below this value. The nature of the equipment and the accuracy of the results from it must thus be assessed when probing nanoscale structures.

4

Optimization of CVD Grown MoS_2 for Nanoscrolling

4.1. Characterizing Flakes Grown with Unoptimized Procedure

To begin the study, MoS_2 flakes were grown multiple times via the described method in Section 3.2.1 to gain an understanding of the morphology produced via the current method. Example results taken from a single growth substrate are displayed in Figure 4.1. By observing the substrate visually under an optical microscope, it can be seen that the vast majority of flakes grown possess a multi-point star shape rather than the idealized triangle. Additionally, the more reflective lines and triangles visible within the blue-looking flakes signify potential areas of increased thickness and vertical growth. Beyond this, the first trend noticeable about the sample as a whole is the size and density gradient that exists laterally from upstream to downstream of the Ar flow. The flakes grown more upstream and, thus, closer to the S precursor are larger than those grown further away. These differences were assessed qualitatively in Table 4.1, finding that there is a 2.6 times decrease in size from one side of the substrate to the other and a nearly 10 times increase in density. Thus, there is a lack of uniformity in MoS_2 flakes grown via this CVD recipe.

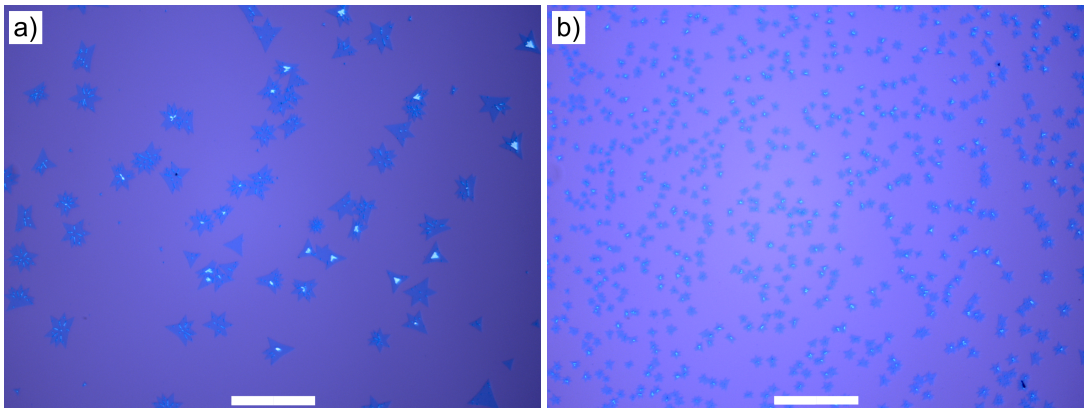


Figure 4.1: Optical microscopy of flakes grown using method 1 taken from a) upstream, b) downstream (scale bar 200 µm).

	Upstream Region	**Downstream Region**
Outer Diameter (µm)	70.4	26.3
Inner Diameter (µm)	42.6	16.2
Density (# of flakes/mm)	60	576

Table 4.1: Table of measured flake sizes and nucleation density from sample pictured in Figure 4.1.

At higher magnifications, the nature of the brighter regions becomes clearer. Two morphologies present on the flakes produced using this recipe are seen in Figure 4.2. Starting with Figure 4.2a; in this case, it can be seen that what appeared as lines in lower magnifications are actually a collection of small triangular flakes (about 1 to 2 µm wide) which have begun growing on the surface of the larger flake. These seem to mostly congregate in lines that connect the center of the flake with the inner corners of the points. Figure 4.2b, on the other hand, displays a flake with a more uniform second layer of MoS_2 growth. However, closer inspection reveals once again a collection of smaller individual flakes, but in this case growing with a more dendritic structure. Furthermore, the high magnification reveals rough edges on both samples and very small serrated features reminiscent of those seen from high Ar flow rates in the literature [119]. To quantify this mixed growth pattern, in the upstream region, about 59% of the flakes have the ”line” morphology, 24% have the dense secondary growth, and the other 17% of flakes either show neither or are too small to categorize. In the downstream region, there is an increased amount of dense central growths with 41% of the flakes possessing it, 52% of them having the lines, and 7% with something in between the two. Almost no flakes were discovered in the downstream region without some type of secondary growth, indicating that, overall, MoS_2 prefers to grow on top of previous layers rather than outward at this location.

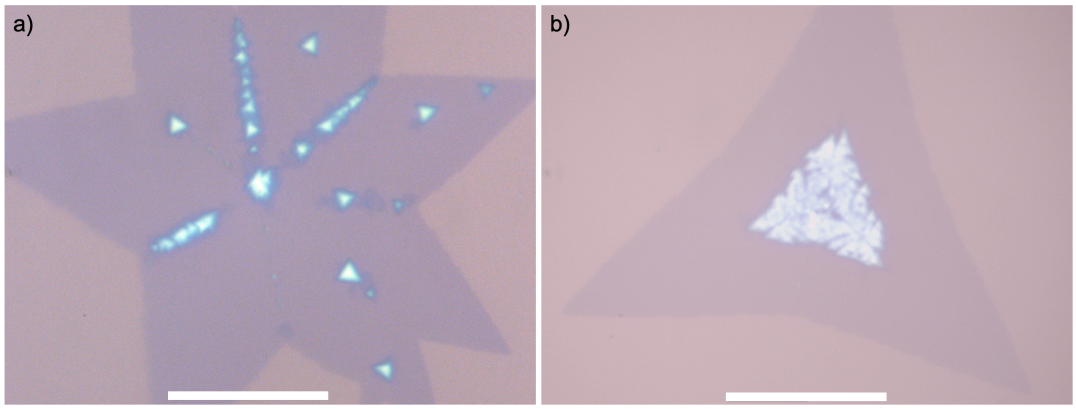


Figure 4.2: Optical microscopy of multilayer flakes with two different central growth patterns (scale bar 10 µm).

This leads directly to the next physical parameter of interest. As discussed in Section 2.2.3, the z-dimension plays a highly significant role in the properties of TMDs. While several methods exist to probe thickness in 2D materials, as described in Section 3.4, Raman spectroscopy is an especially effective and simple procedure for obtaining this value for TMDs like MoS_2.

4.1.1. Raman Spectroscopy Thickness Analysis

Raman spectra were taken for flakes with multiple visual contrasts to highlight the thickness differences observed on one sample. Representative spectra fitted via a simple Voigt profile and OM images are visible in Figure 4.3. Because the flakes are grown on SiO_x/Si substrates, there is a clear peak at 520 cm^{-1} corresponding to the Raman signature of Si. This peak is used to ensure correct calibration of the data. Figure 4.3a is an example of one of the points of a star which, by contrast against the SiO_2 substrate, appears to be the thinnest area of the flake, Figure 4.3b is a center reflective region common among the sample flakes, and Figure 4.3c is a small triangular flake. Table 4.2 displays the fitted wavenumbers of the A_{1g} and $E^1{}_{2g}$ peaks for each location as well as the distances between them. The brighter contrast regions show a gap of $\Delta\omega = (25.33 \pm 1.56)\,cm^{-1}$ which correlates most closely with the bulk or 4-layer spectra in the literature [152]. On the points of the flakes, the gap of $\Delta\omega = (20.84 \pm 0.51)\,cm^{-1}$ indicates a bi-layer sample. This confirms the optical contrast-based assumption of multiple thicknesses both across the sample and within individual flakes. Previous studies on the fabrication of TMD nanoscrolls generally address uniformly monolayer flakes [78, 80], the reasoning behind which will be speculated on in Section 4.4.

Using the information gathered up to this point, it is possible to make some hypotheses about the flakes' scrolling potential and what changes to the flake morphology may be preferable. To start, the lack of uniformity across the substrate is the first hindrance to scrolling, as it will lead to scrolls with various sizes

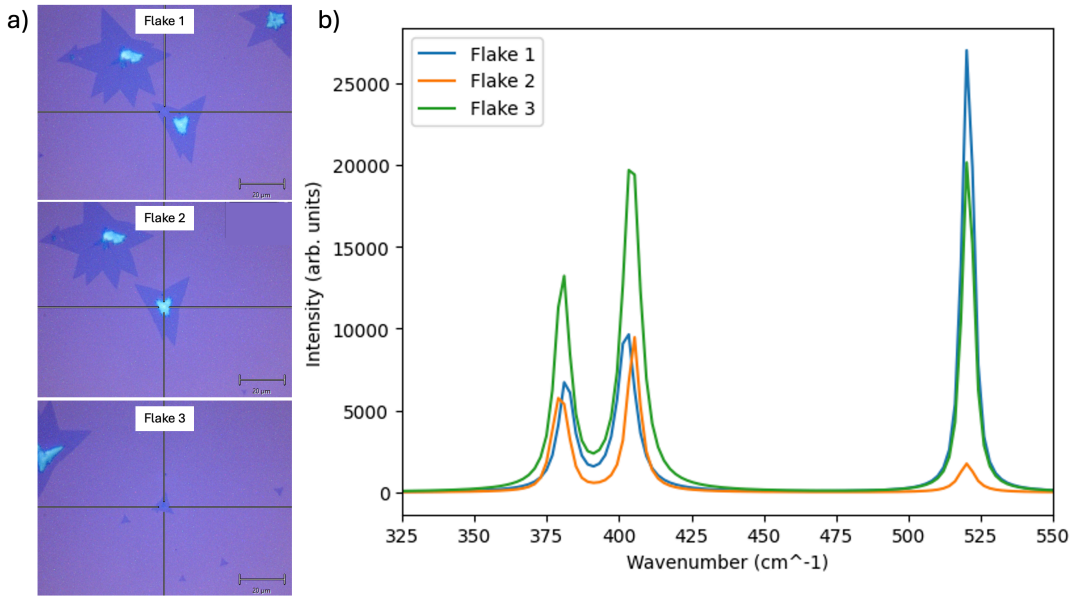


Figure 4.3: Raman spectra for flakes from initial CVD recipe.

	Flake 1	**Flake 2**	**Flake 3**
$\mathbf{E^1_{2g}}$ (cm^{-1})	381.67 ± 0.43	379.67 ± 0.18	380.40 ± 0.19
$\mathbf{A_{1g}}$ (cm^{-1})	402.51 ± 0.08	405.00 ± 1.38	404.27 ± 0.04
$\Delta\omega$ (cm^{-1})	20.84 ± 0.51	25.33 ± 1.56	23.87 ± 0.23

Table 4.2: Fitted Raman mode peaks for flakes pictured in Figure 4.3

and potential properties. Achieving a substrate with flakes that are more similar in size and shape would increase the productive yield of scrolling and allow for more concrete conclusions to be drawn about the properties of scrolls produced by a particular CVD recipe. Focusing more closely on the individual flakes, the star shape is likely to present challenges to scrolling. As discussed in Section 2.3.1,MoS_2 flakes have an energetic preference for rolling from a ZZ edge. In the case of a triangular morphology, this allows for the whole flake to be rolled into the nanoscroll structure. However, with a multi-pointed star structure, there are theoretically multiple edges from which the scrolling can begin. This could result in incompletely formed scrolls and more complex structures. Finally, the secondary growth over the flakes means that a fully scrolled structure will have a non-uniform amount of layers across the scroll. This would mean that certain regions would have different electronic properties than others on the same scroll, and makes predicting those properties very difficult due to the various locations of the multilayer stacks.

The main goals for improving the starting morphology of the MoS_2 flakes should thus be to obtain more uniformity across both the substrate, even thickness across the individual flakes, and a smoother triangular shape.

4.2. Increased Control Over Temperature Profile

As mentioned in Section 3.2.1, using the baseline vapor phase CVD recipe results in Z3 naturally reaching about 160ºC when Z2 reaches the growth temperature of 750ºC. This is above the melting point of sulfur (about 115ºC); however, it is at the lower end of values used for CVD, and vaporization should be relatively limited up until this point of the ramp where its vapor pressure maximizes at 0.0004 atm [1, 155]. However, by looking again at the temperature profile of the recipe (Figure 3.11b), one should also note that using this recipe leads to the overshooting of the target temperature of 200ºC. Instead of the temperature holding at the set point for the 5 minutes of growth (as the controller is set for), the heat leakage from 750ºC Z2 causes Z3 to continue increasing in temperature for the next 17 minutes (note that this is 12 minutes past when all heating is turned off), eventually reaching a peak of

about 248ºC. This poor control of Z3's temperature over the course of the growth recipe is a concern for the development of flakes with the best morphology for scrolling. As it has been seen in the literature, flake morphology is highly dependent on the amount of precursor reaching the substrate at a certain time with a certain energy. Thus, it is possible to hypothesize that the varying sulfurization temperature throughout the reaction time could be contributing to both the non-uniformity of the flakes as well as the shape. While the Ar flow remains the same throughout the synthesis, a higher temperature sulfur powder could be leading to faster vaporization than desired and, as a result, a higher S:Mo ratio than is desired for triangular growth. Thus, steps should be taken to create a new recipe that improves this uncontrolled variable.

The first step in gaining better control over the temperature within the furnace during a synthesis is increasing the isolation between the zones. This was done by increasing the amount of fiberglass insulation material that acts as padding between the furnace and the inserted quartz tube. By filling any potential air gaps within the closed furnace, heat leakage is more controlled. It was also determined through testing that allowing the ramping of Z3 to begin (at a lower rate of 5ºC/min) during the ramping of Z2 further limited the amount of overshooting as the PID controller could more accurately limit the heating elements when both zones were ramping at once. This change is a significant one, but is supported as a viable growth strategy due to the many reports of single-zone furnace use in TMD growth [80, 122, 136]. As a byproduct, this change is that it allows Z3 to reach the target temperature at the same time Z2 does, leading to more precise knowledge of where the recorded reaction begins. To achieve this synced ramp, a test heating cycle is performed to determine the time taken to reach the growth temperature set point of 750ºC from room temperature. The results of this showed a total ramp time of 77 minutes, which is used throughout the rest of the syntheses in this chapter to ensure that the Z3 ramp is started at the right moment. Altogether, the adjusted methodology has the same physical setup as seen in Figure 3.10, but, after the initial 30-minute Ar flush at 1000 sccm, the heating process proceeds in the following manner. First, the Z2 ramp is initiated at 10ºC/min. Then, about 41 minutes later, the Z3 ramp began at 5ºC/min. As before, when Z2 reaches 500ºC, the Ar flow is reduced to 100 sccm. When both zones reach the target temperature, a dwell for 5 minutes is commenced, after which all heating is turned off and the furnace is allowed to naturally cool under the same Ar flow until 100ºC is reached.

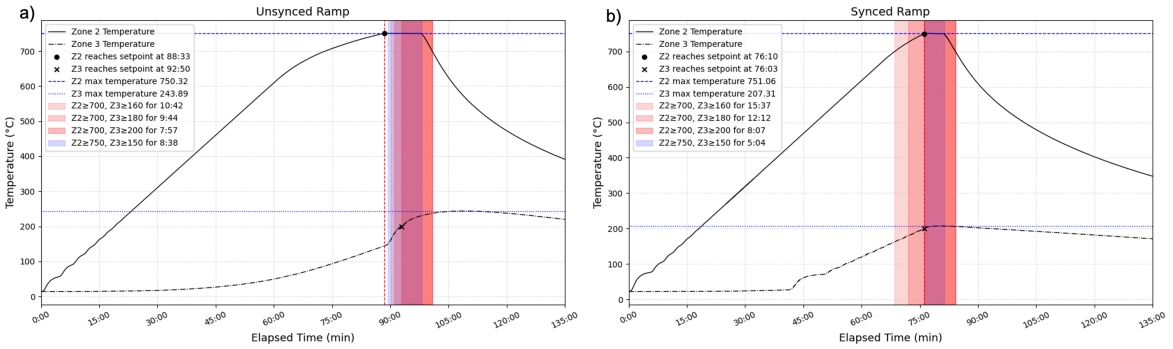


Figure 4.4: Plot of temperature profile with highlighted regions indicating time spent in particular temperature zones. a) original method, b) adjusted CVD methodology with synced Z2 and Z3 heating.

The new resulting temperature curve is displayed in comparison to that from the original method in Figure 4.4 where it can be seen that the max of temperature of the sulfur zone is now only about 207ºC which is far more controlled than the previous method and that the increased insulation of the furnace has allowed Z2 to come to the set-point temperature in a faster and more linear way. The plots also highlight the time spent in various temperature regions. These regions are established based on the theory of the vapor phase reactions involving S and MoO_3. Based on the available literature, 160ºC is the lower end of temperatures used for S powder in CVD MoS_2 synthesis [156]. In the case of MoO_3, as mentioned in Section 3.1.1, 700ºC is generally the lowest temperature used for vapor phase synthesis, below which little MoO_3 is available for reaction. An interesting aspect of the temperature profiles to note is the shifted periods of heating. In the original heating method, since Z3 stays just below 160ºC until it is turned on, before this moment, both zones are never simultaneously in a growth-favorable temperature regime. On the other hand, the synced method results in these *possible* growing conditions

occurring before the specified reaction point is reached. This leads to the new method spending more time overall in the range of Z2 $\geq$ 700ºC and Z3 $\geq$ 160ºC. However, one particular zone experiences the reverse effect when implementing the new method. That is the Z2 $\geq$ 750ºC and Z3 $\geq$ 160ºC zone. While before these conditions are met for almost 8 minutes, in the new synced method, they are held for the same amount as the specified dwell time. It can be hypothesized that the synchronized ramping will reduce excessive sulfurization, yielding fewer serrated edges, a more triangular shape, and a more uniform thickness. Growths will thus be performed for the new method, and the results with regard to these factors will be investigated.

4.3. Optimization of MoS_2 Flakes

Growing MoS_2 with the new method produces flakes which are much smaller than those seen previously. As highlighted in Figure 4.5a, visibility of these flakes under optical microscopy was highly limited, rendering the method unable to distinguish the edge morphology. Thus, scanning electron microscopy (SEM) was employed to better assess the flakes, Figure 4.5b. The flakes in this image, representative of those across the sample, were measured to be about 1 µm across at the longest point. Looking at the upstream and downstream edges (Figure 4.5c & d), it can be seen that this size remains quite uniform across the sample with an average size of 0 µm compared to 0 µm. However, there is a slight reduction in density as one moves further away from the precursor flow.

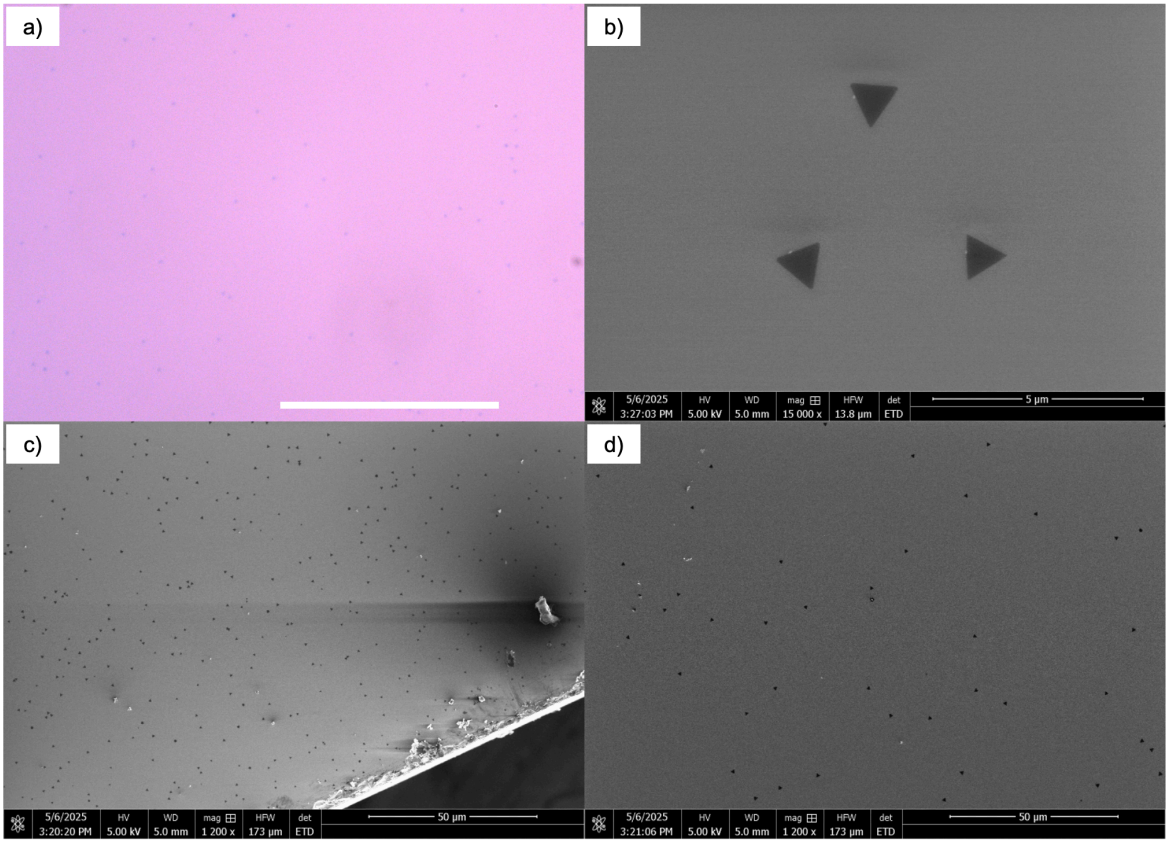


Figure 4.5: a) Optical microscopy (scale bar 50 µm and b) SEM images of MoS_2 flakes grown via the adjusted CVD method. c) & d) SEM images highlighting the nucleation density of the upstream and downstream edges, respectively.

4.3.1. Thickness Measurements

Once again, Raman measurements were used to probe the thickness of the flakes grown. Raman was performed on the MoS_2 flakes, which were grown with a sulfurization temperature of 200ºC as seen in Figure 4.5. Multiple flakes on the surface of the substrate with various levels of opaqueness were tested in order to see the average thickness across the sample. Figure 4.6 shows the Raman spectra of three flakes taken from the sample, and Table 4.3 highlights, as before, the position of their E^1_{2g}

and A_{1g} modes as well as the gap between them. Images of the flakes measured can be found in Figure A.1. Comparing these to the literature once again, it can be seen that the flakes were found with gaps that correlate to 1, 2, and 3 layers. The fact that a potentially monolayer flake was found is highly promising, as such uniformly thin flakes were not able to be found via the original method.

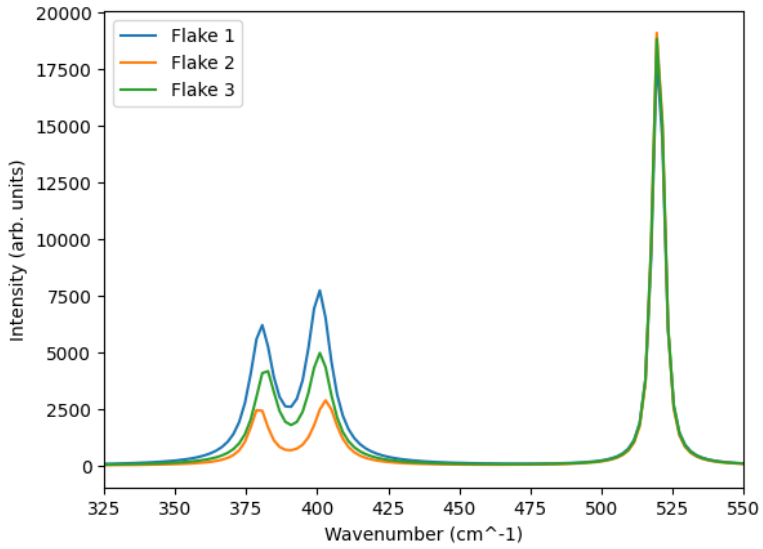


Figure 4.6: Fitted Raman peaks for three flakes growing via the synced ramped method.

Raman Mode (cm^{-1})	**Flake 1**	**Flake 2**	**Flake 3**
$\mathbf{E^1_{2g}}$	380.27 ± 0.18	379.53 ± 0.12	381.69 ± 0.44
$\mathbf{A_{1g}}$	400.72 ± 0.11	402.96 ± 0.31	401.00 ± 0.05
Gap	20.45 ± 0.29	23.43 ± 0.43	19.31 ± 0.49

Table 4.3: Fitted Raman mode peaks for flakes pictured in Figure 4.6

However, due to the very small size of the flakes grown with the synced furnace methodology approaching the resolution limit of the Raman spectroscope, the confidence in the thickness measurement is reduced. Thus, atomic force microscopy (AFM) was employed to gain a more accurate assessment of a flake sample from both the original method and the synced ramp method. These are both displayed in Figure 4.7 along with line profiles from their edges. In the case of the flake produced via the synced ramp method, the line profile taken indicates a thickness of about 0.7 nm which, accounting for the noise in the measurement, is in line with one layer of MoS_2 (0.65 nm). It also shows clearly that there are no additional layers anywhere else on the flake, thus it is a uniform monolayer. As for the larger flake from the original method, since the flakes are quite large, an AFM image was taken just from the edge of one arm of a star-like formation. The line scan average of this section shows a thickness of about 0.4 nm. This is smaller than should be possible, however the sample used was older, so oxide growth or other contamination may have developed on the surface of the sample with preference towards the uncovered SiO_2 substrate, or that degradation to the MoS_2 flake has occurred over time due to exposure to oxygen and water (though the sample was stored under vacuum when not being characterized) [157].

Beyond the thickness of the flakes, these AFM scans also highlight the difference in the edge structure of the two flakes. While the smaller flake has a perfectly straight edge, the larger flake grown with the original method again shows signs of a serrated growth pattern.

Before moving on to the scrolling of these flakes, it is desirable to optimize the method of growth to ensure the most ideal results are obtained. Since the effects of adjusting sulfur temperature are not well understood in the literature, and because early sulfurization due to synced ramping could affect the results obtained for the growths, a study was performed regarding the morphological changes experienced by different sulfur temperatures during the reaction time.

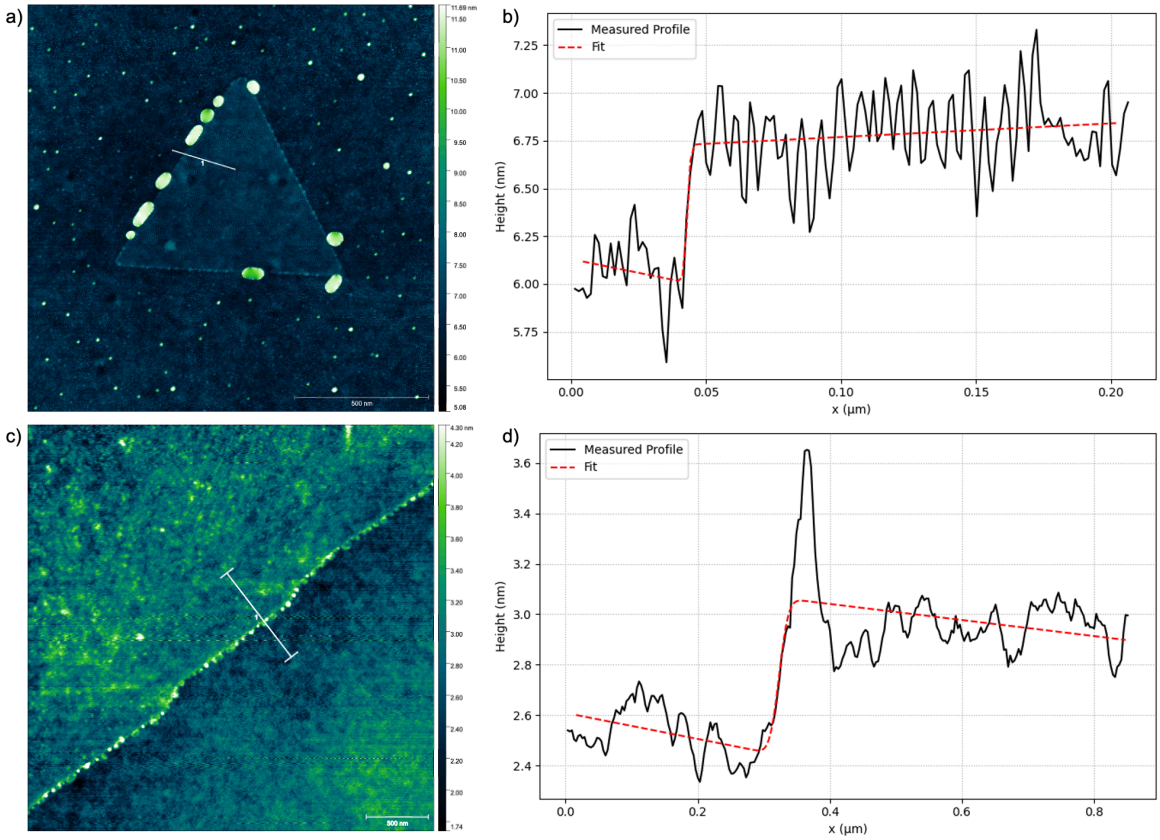


Figure 4.7: a) AFM image of flake grown using the synced ramp method with Z3 at 200ºC. b) Height profile taken from the line depicted on a). c) AFM image of the edge of the flake grown using the original unsynced method. d) Height profile taken from the line depicted on c).

4.3.2. Effects of Sulfurization Temperature

To test the effects of the changing sulfur precursor temperature and the limits at which MoS_2 flake growth is still possible, a series of growths was performed over a range of temperatures (160ºC, 180ºC, 200ºC, and 220ºC). All other parameters were kept the same. Z2 of the CVD furnace (containing the substrate and the MoO_3 precursor) is heated to 750ºC, the reaction time is 5 minutes at the target temperatures, and the flow rate of Ar gas during the reaction is held at 100 sccm with a pressure of 1 atm.

The results of these four different temperatures are displayed in Figure 4.8. At the lower temperatures of 160ºC and 180ºC, it can be seen that the growth is more chaotic and the sizes are highly non-uniform. The 160ºC sample in particular displayed flakes with a much larger size range than seen in any other growth (from about 500 nm up to 10 µm across. Flakes on the 180ºC sample are overall smaller and cover a range of about 200 nm to 1 µm. At 200ºC, the sizes are uniformly about 1 µm as discussed in the previous section. While growth essentially ceases at 220ºC, with the structure pictured in Figure 4.8d being the only one found in SEM. Beyond the sizes, there is also a clear trend of higher to lower nucleation density as the temperature is increased. It is not initially apparent why this is the case, as one might assume the higher sulfur concentration would simply lead to more growth. Instead, this effect could be the result of a surface-reaction-limited growth process. More than enough S is reaching the substrate, to an increased overall time spent with vapor sulfur available for the reaction, possibly leading to a diffusion-dominant system where S atoms have enough time to find the most energetically favorable lattice positions and reducing individual nucleation sites [51, 106]. However, at a certain point somewhere before 220ºC, it is possible that the temperature of the Mo precursor is not high enough when the sulfur is readily vaporizing, and by the time it is, the energy of the sulfur is so high that it desorbs from the substrate as quickly as it adsorbs. In this case, growth of MoS_2 is no longer possible. Additionally, it is possible that during the ramping to 220ºC, sulfur is reacting with the MoO_3 near the crucible rather than at the substrate, leaving little to no Mo available for reaction during the growth window [158]. This, if occurring, could also contribute to the decreasing nucleation density seen as temperature is increased. The discussion of sulfur prevalence can be furthered by looking at the precursor pre- and post-reaction. Having all begun with an initial mass of 500 mg of S powder. After each of the 160ºC, 180ºC, 200ºC, and 220ºC reactions was complete, the S precursor boats were found to have a mass decrease of 11.96%, 15.68%, 27.32%, and 43.51%, respectively. As can be seen, this is not a linear increase in usage. This is reasonable since higher temperatures must, by virtue of the synced ramping method, spend additional time at elevated temperatures below the target but above the sulfurization low end of 160ºC. The result confirms that a higher overall flux is occurring at higher temperatures, but that it does not necessarily correlate to more MoS_2 growth.

While flakes grown with sulfur at 160ºC and 200ºC generally maintain their triangle shape, those at 180ºC develop a more truncated morphology with significantly rounder edges. These truncated triangles share similarities with the hexagonal growth formations seen when the available precursor ratio is close to 1:2 [51], which supports the hypothesis that the sulfurization temperature is directly tied to the amount of sulfur vapor available during the reaction. Furthermore, because equilateral triangle shapes emerge both below and above 180ºC, it indicates an inflection point at this temperature, where at 160ºC there is a Mo-ZZ edge dominance and at 200ºC there is S-ZZ edge dominance.

4.3.3. Ideal flakes for scrolling

To obtain the best potential nanoscroll results and obtain the strongest/clearest comparison to the original MoS_2 flakes after scrolling. A few conditions are placed on the flakes chosen for future use.

- Size and shape should be highly uniform without many significant outliers
- Thickness should be uniform and preferably less than 3 layers
- Shape should be triangular
- Edges should be straight and smooth

On reviewing the flakes obtained via all four sulfurization temperatures, 200ºC was decided to be the best candidate for scrolling. Because little to no growth was observed using 220ºC, the three remaining options are 160ºC, 180ºC, and 200ºC. Triangular morphologies with sharp vertices theoretically encourage scrolling from just one edge and limit defects that may cause early termination of the motion. Addi-

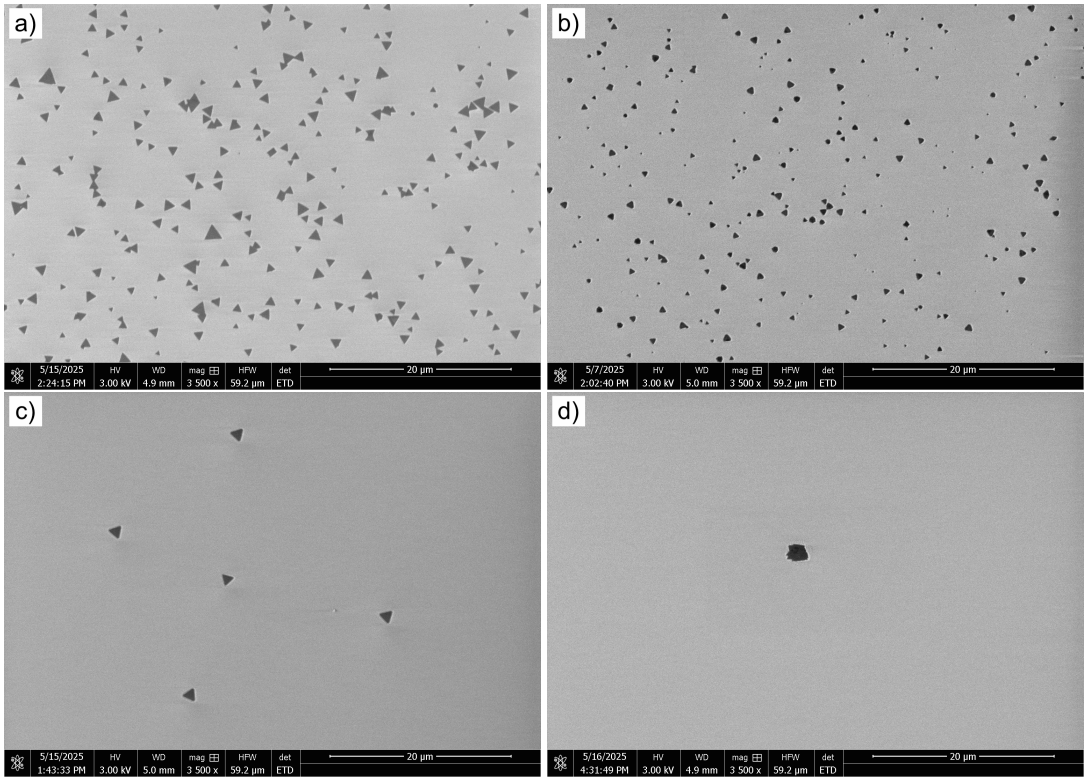


Figure 4.8: SEM image of MoS_2 flakes grown with sulfurization temperature of a) 160ºC, b) 180ºC, c) 200ºC, and d) 220ºC.

tionally, it is desirable to scroll with a sample that has uniformly sized flakes across the substrate so that the resulting scrolls can be better correlated to their original morphology. The samples made at 180ºC are not uniform in size and shape, and many of the flakes possess rounded and non-triangular shapes. While the 160ºC samples possess nicely triangular flakes, they are even less uniform in size. This leaves the uniformly 1 µm triangular 200ºC sulfurized samples as the most theoretically ideal based on the information gathered from the literature review.

4.4. Scrolling MoS_2 Flakes

The procedure for scrolling, detailed in Section 3.3.1, was replicated on flakes obtained both in Section 4.1 and Section 4.3. An example result for the larger flakes from the original un-synced heating method is shown over time in Figure 4.9. Upon adding the EtOH, it generally took anywhere from 5 to 10 minutes to see the first signs of scrolling, which usually appeared as the EtOH layer began to noticeably evaporate. From there, as seen in the images, full scrolling occurred over the course of the next minute or two. While it was expected that the larger star-shaped flakes would scroll mainly from the sides of the points, it was observed that the center of the flake often split, and scrolling began from the center. This can be further correlated with the lines of secondary growth on the flakes, but that was not always the case. For example, at the 42-second mark in Figure 4.9, in the lower large flake scrolling originates from a tear between the bottom two star points, where there does not seem to be a clear line of secondary growth. A further example of how the star morphology influences the scroll shape is seen in Figure 4.10a. In this case, the flakes possessed multilayer central regions which were inhibited from scrolling as predicted in Section 4.1.1. Because the center remained intact during the process, the arms of the stars scrolled inward from both sides and created interconnected scrolls with an uneven external texture, as seen by the difference in reflection.

This type of scrolling, however, was not the only type exhibited. Compared to the literature, which reports anywhere from an 80 to 100% efficiency rate for scrolling [78, 146], in this study, several samples were found to scroll only a small amount before the EtOH completely evaporated (Figure 4.10b & c). Referencing Equation 3.8 and the theory of the volatile organic solvent scrolling method, it can be

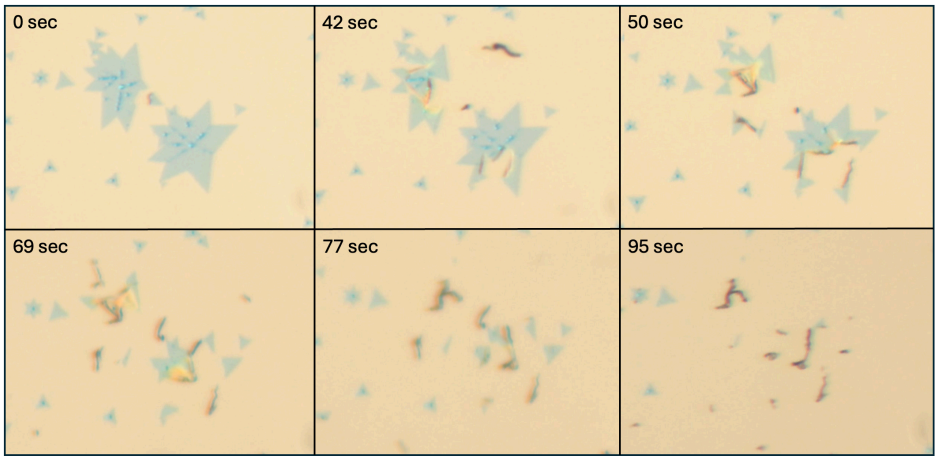


Figure 4.9: Optical microscopy images of flakes grown from the original method scrolling with labels indicating the time since the first image, which was taken right as the first sign of scrolling began, about 10 minutes after the EtOH was applied.

concluded that the adhesion forces, or the interfacial energy, between the flake and the SiO_2 substrate must be higher than the penetration of the EtOH. However, the ethanol:water ratio did not seem to be the cause of this inefficiency, as samples were both successfully and unsuccessfully scrolled with the same ratio. Instead, there is some other factor leading to this lack of reproducibility. Some potential variables could be related to the surface chemistry of the substrate, such as the amount of time since cleaning or exposure to variable air conditions. For example, humidity has been found to affect the adhesion of MoS_2 to SiO_2 with films in higher humidity environments experiencing more peeling from external forces [157]. It is possible that different days had varying levels of humidity or that there was an unaccounted-for difference in the amount of time certain substrates spent in open air before being used in a CVD synthesis. Furthermore, MoS_2 is known to have higher adhesion to SiO_2 than other 2D materials due to the attraction between positively charged sulfur atoms and negatively charged oxygen [159]. It is possible that this effect was more present in the flakes that failed to scroll, perhaps due to more or less oxidation occurring in the time since acid cleaning.

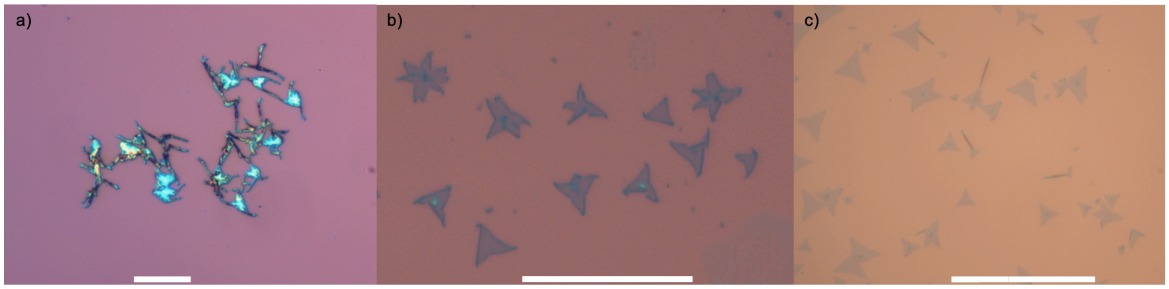


Figure 4.10: Optical microscopy images of a) scrolled and b) & c) partially scrolled flakes after EtOH application. Scale bars 50 µm

4.4.1. Scrolling Small Flakes

The disadvantage of the 1 µm MoS_2 flakes obtained via the synced ramping method is that they are too small to observe during scrolling with optical microscopy. As a result of this limitation, the EtOH scrolling procedure needed to be carried out "blindly," after which SEM was employed to observe the results. During the first attempt at scrolling the 1 µm MoS_2 flakes obtained from the synced ramp method, it was discovered that the action of ethanol evaporation is too violent for the extremely small and thin flakes. As can be seen in Figure 4.11, it appears that, upon the intercalation of the ethanol, the entire scrolled flake lifts from the substrate and begins to follow the flow of the evaporating ethanol. This was an effect observed for smaller flakes in the original method; however, the uniformity of these samples seems to lead to this happening to nearly all of the flakes. Once the scrolls have lifted, the

surface tension of the ethanol causes it to collect in droplets on the substrate as it evaporates, and the nanoscrolls collect in an increasingly dense area. This process, shown in Figure 4.11 c, results in the maceration of the MoS_2 material and the formation of a slurry that is left behind when the bubble of ethanol fully evaporates.

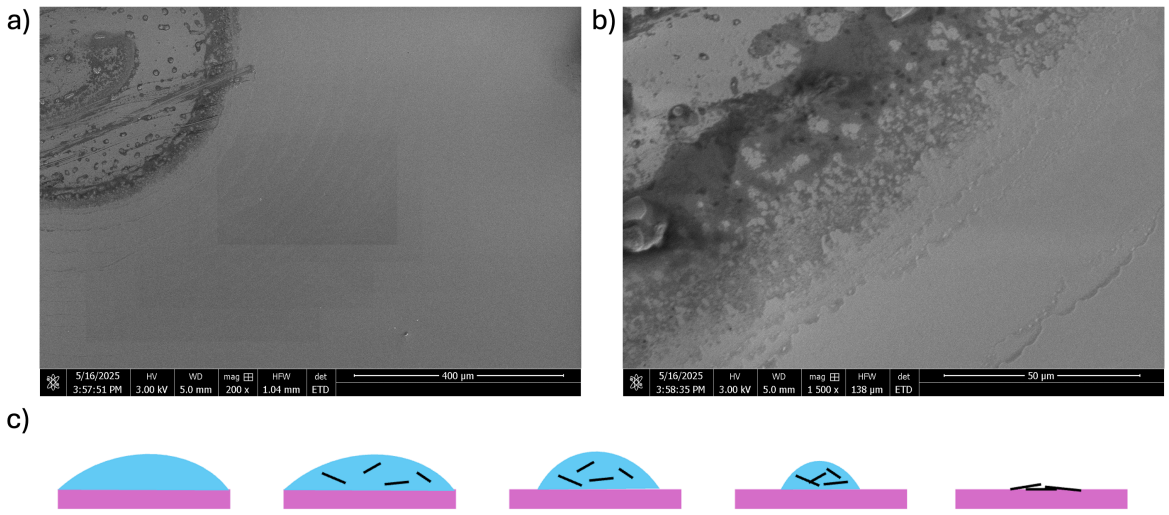


Figure 4.11: a) & b) SEM images of MoS_2 residue left behind from ethanol evaporation during the scrolling procedure. c) Diagram of the theorized scroll destruction mechanism.

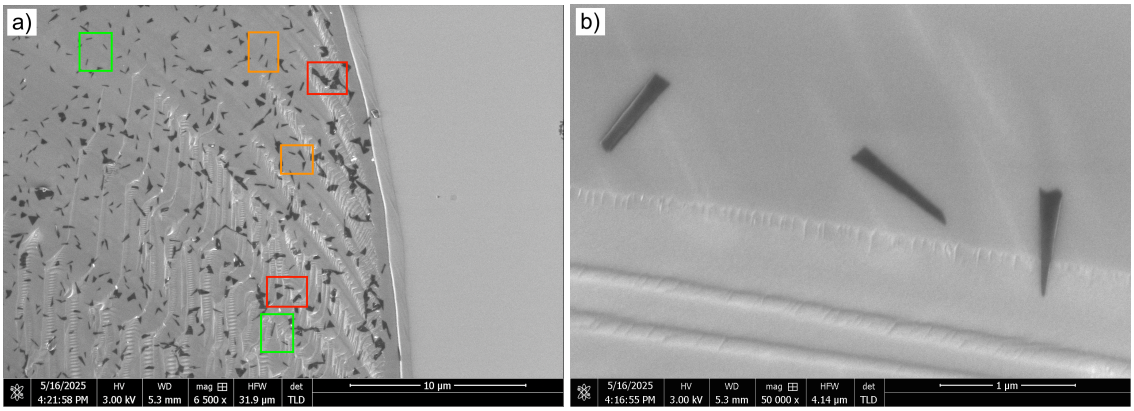


Figure 4.12: a) SEM image of MoS_2 scrolls collected on the chipped surface of the SiOx/Si substrate. b) Zoomed in SEM image of MoS_2 scrolls of conical and cylindrical shape.

As mentioned (and seen clearly in Figure 4.11a, virtually all flakes on the surface of the substrates for which the scrolling was attempted are fully delaminated and destroyed, leading to an effective scrolling yield of close to 0%. However, in one sample, some formed nanoscrolls were able to remain in their place due to a chip in the substrate, creating an uphill geometry. These nanoscrolls (and misshapen flakes) collected on the ridges created in the chips are seen in Figure 4.12a. Based on the area of this region compared to the rest of the substrate, a roughly estimated scrolling yield of less than 0.5% was calculated. It can be seen in this image that not all the flakes have scrolled fully, with three distinct formations visible and highlighted: unscrolled (red), conically scrolled (orange), and neatly scrolled (green). Since these nanoscrolls were formed on an uneven Si surface, it is difficult to make robust conclusions about the formation mechanisms for them. However, the significant presence of well-formed scrolls like those seen in Figure 4.12b indicates that the small triangular nature of these flakes allowed for ideal scrolling from a singular edge. Unfortunately, beyond this sample, no other successful scrolling attempts were able to be obtained for flakes produced via the synced ramping method.

4.4.2. Characterizing the Scrolls

With scrolls obtained from both CVD methodologies, a direct comparison of their morphologies can be conducted. The length and outer diameter of representatives from both are measured in Figure 4.13. The large scroll from a star shaped flake has a length of about 23 µm and an outer diameter of 300 nm, this is compared to the 1.2 µm length and 70 nm outer diameter of the scroll from a small triangular flake.

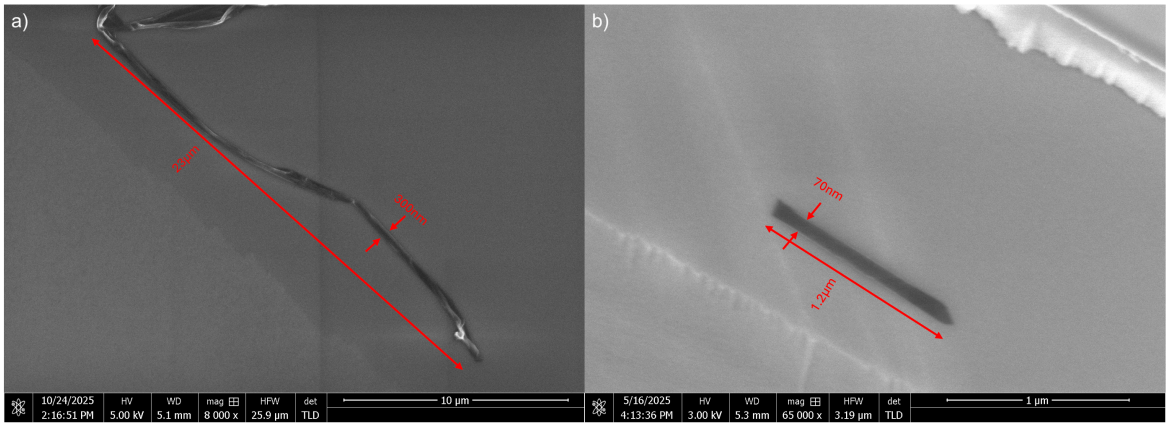


Figure 4.13: SEM images of MoS_2 scrolls fabricated via a) original unsynced CVD ramping method and b) synced ramping method, measured along their length and outer diameter.

To get an even closer look at the structure of the scrolls, transmission electron microscopy (TEM) was used. The large scrolls were able to be transferred onto a holey carbon copper grid during the scrolling process by swiping the grid across the bubble of EtOH after scrolling occurred, but before the solvent was fully evaporated. It should be kept in mind that this methodology may favor the capture of slightly smaller scrolls than average, since they will necessarily be detached and floating in the EtOH. The STEM images for one example multi-armed scroll can be seen in Figure 4.14a, with b displaying a zoomed-in image of the bottom left scroll end. Looking at the close-up image, some important details about the nanoscroll morphology can be ascertained. To begin with, it is clear that this is a chiral scroll due to the stark change in layer number from the left side of the image to the right. At the densest part of the scroll, at least 18 layers can be counted on the upper side, though it is hard to distinguish which layers are from full turns of the MoS_2 and which are from folding or overlapping. On the bottom side of the scroll, a much clearer 8 layers can be counted. This lack of matching on opposite sides indicates this scroll was formed from two edges scrolling into each other, and is further confirmed by the two separate open edges seen in the center of the scroll. The interlayer spacing of the scroll is also non-uniform but possesses an interesting pattern. Focusing on the bottom 8 layers, the distance alternates between a smaller and larger number (about 2.9 nm and 3.7 nm). This pattern is indicative of the original flake possessing a bilayer and highlights the kind of asymmetries that can arise from nanoscrolling flakes, which are not monolayers. The outer diameter of the scroll is 315 nm at its largest point, and the inner diameter is about 150 nm at the point seen in the image.

Figure 4.15 shows a cross-sectional TEM image of a scroll made from the synced ramping method. Scrolls produced via this method could not be transferred whole to the TEM grid using the same method as the larger scrolls; however, a lamella was able to be made with a Focused Ion Beam. This lamella can be seen in Figure 4.15. It is first important to note that the scroll has most likely collapsed from the deposition of platinum on top of it as a necessary step in the lamella-making process. This is further confirmed by the uniform flattening, which is visible, and the fact that the innermost layers appear to be broken where the curvature induced was the highest. Nevertheless, it is still possible to gain useful information from the cross-section. The outer most dimensions of the scroll are 54 nm by 10 nm, while the inner most are 40 nm by about 0.65 nm (or one MoS_2 interlayer distance). Knowing that this was once a hollow spiral shape and making critical assumptions that the shape was nearly circular before a highly uniform collapse, these dimensions can be used to estimate the original inner and outer diameter by conservation of circumference. Taking C as 80 nm would indicate a circular diameter of about 25 nm. For the out diameter, a less accurate (due to increased curvature) assumption of 80 nm leads to a

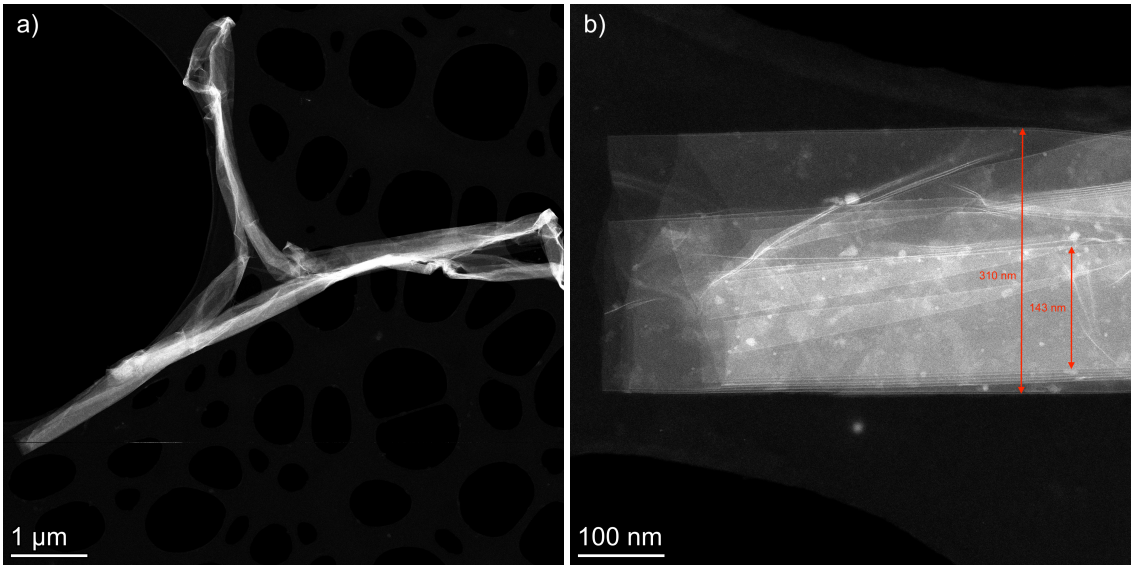


Figure 4.14: a) STEM image of large multi-armed MoS_2 scroll b) Zoom in of the bottom left arm end.

reconstructed value of 38 nm. Additionally, it is possible to count the layers visible to determine N_{turns} for this particular scroll. While human error is involved due to the somewhat poor contrast of the image, it seems there are somewhere between 5-6 layers.

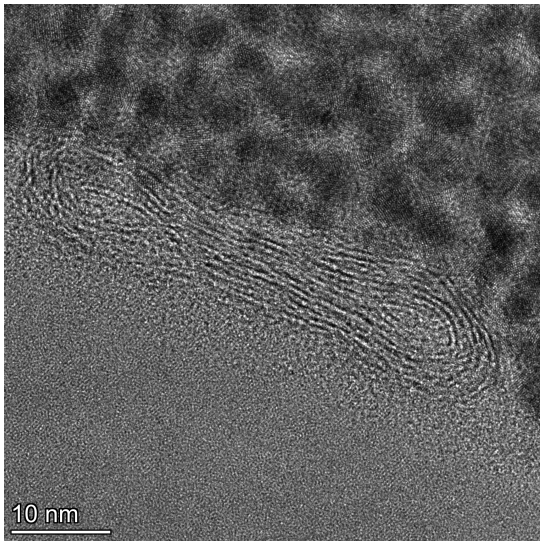


Figure 4.15: TEM cross-section image of MoS_2 scroll from synced ramping method.

Unfortunately, it is much more difficult to assume the interlayer distance in the scroll, as the platinum could have forced them into the close vdW contact seen in the TEM image. Recalling, though, Equation 2.2 and the fact that flakes from this CVD recipe have a highly uniform length of 1 µm, the parameters that are known can allow for the determination of the estimated average d_{in}.

$$d_{in} \approx \frac{L - 2\pi r_{in} N_{turn}}{\pi N_{turn}^2} = \frac{(1000 \pm 100) - 2\pi \cdot (25 \pm 1) \cdot N_{turn}}{\pi \cdot N_{turn}^2} \tag{4.1}$$

Assuming an N_{turn} value of 6 and accounting for the errors associated with the other values, the result for d_{in} is approximately (0.5 ± 9.0) nm. While using 5 turns gives a result of (3 ± 1) nm. Of course, the value can not be any less than about 0.65; however, both cases indicate a scroll that is just about as tightly rolled as the larger ones. Moreover, when factoring in the significantly smaller outer-to-inner

diameter ratio of these scrolls, it is apparent that a tighter, more uniform nanoscroll is achieved via the optimized CVD procedure.

Finally, since no TEM cross-section was obtained for the larger scrolls, AFM was once again used to get a better understanding of the diameter of the scroll and to understand more about its profile morphology. As can be seen in the images presented in Figure 4.16, the scrolls do not possess the expected thickness profile for either a hollow or collapsed cylinder. Instead, it seems there is an irregular shape arising from the scrolling process itself. In Figure 4.16a, the left side of the scroll is more tightly wound than the right side, and in the middle, there appears to be a portion of flake which has folded in both directions, creating a twisted shape. Figure 4.16b, on the other hand, looks more clearly like a scroll which has formed via the rolling of two sides of a star point, with the right side scrolling more quickly and tightly than the left. Furthermore, the thinnest regions on either of these scrolls were found to be around 25 nm, which is nearly 40 times the thickness of a single layer. Since it is clear that 20 turns is not possible in these structures, and it is known that the thickness of these flakes was between 1 and 3 layers, this indicates significant open space in these less scrolled regions.

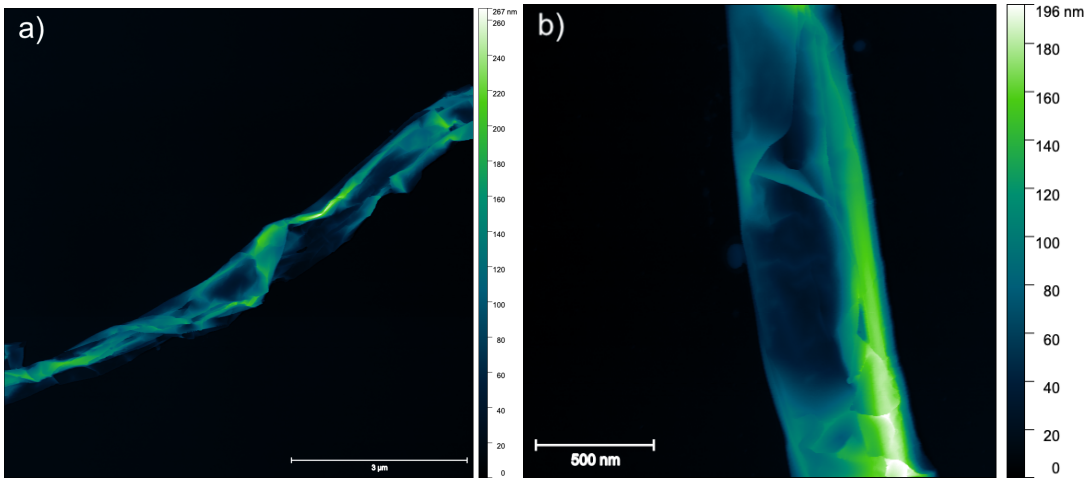


Figure 4.16: AFM images of two scrolls fabricated with flakes from the original CVD methodology.

For the bigger scrolls, Raman was used to assess the baseline strain in the structure. Recalling from the literature, scrolls are expected to experience shifts outside of those normally expected for increased layer amounts; in the A_{1g} due to increased vdW interactions and in $E^1{}_{2g}$ due to lattice strain. As can be seen in Table 4.4, which compares the positions of the Raman peaks of the scrolls to that of a single-layer flake from Table 4.2, there is a significantly larger shift in the $E^1{}_{2g}$ mode than A_{1g}. This indicates that there is more contribution from strain in the MoS_2 lattice in Raman effects than there is in increased vdW interactions, i.e., there is significant strain present in the scrolls, and they are not tightly wound. The other characterization methods employed confirm the lack of tight scrolling and, thus, more confidence can be had in concluding that strain is playing a role in the $E^1{}_{2g}$ shift present.

	Thin Flake	**Scroll 1**	**Scroll 2**
$\mathbf{E^1{}_{2g}}$ (cm^{-1})	381.67 ± 0.43	378.77 ± 0.05	377.47 ± 0.15
$\mathbf{A_{1g}}$ (cm^{-1})	402.51 ± 0.08	403.76 ± 0.01	402.22 ± 0.03
$\Delta\omega$ (cm^{-1})	20.84 ± 0.51	24.99 ± 0.06	24.75 ± 0.18

Table 4.4: Fitted Raman mode peaks for scrolls pictured in Figure 4.17 and a thin flake originally from Table 4.2

4.5. Conclusions Regarding MoS_2 Optimization

In this chapter, it was found that using the initial CVD recipe for growing MoS_2 flakes, which involved allowing the growth zone to come fully to 750ºC before beginning the heating ramp of the sulfur precursor zone, leads to the development of multilayer star-shaped flakes with sizes from around 20 to 80 µm. By increasing thermal insulation in the CVD and adjusting the recipe to allow for the temperature in the two zones to reach their setpoint at the same time, much smaller, uniformly triangular flakes were

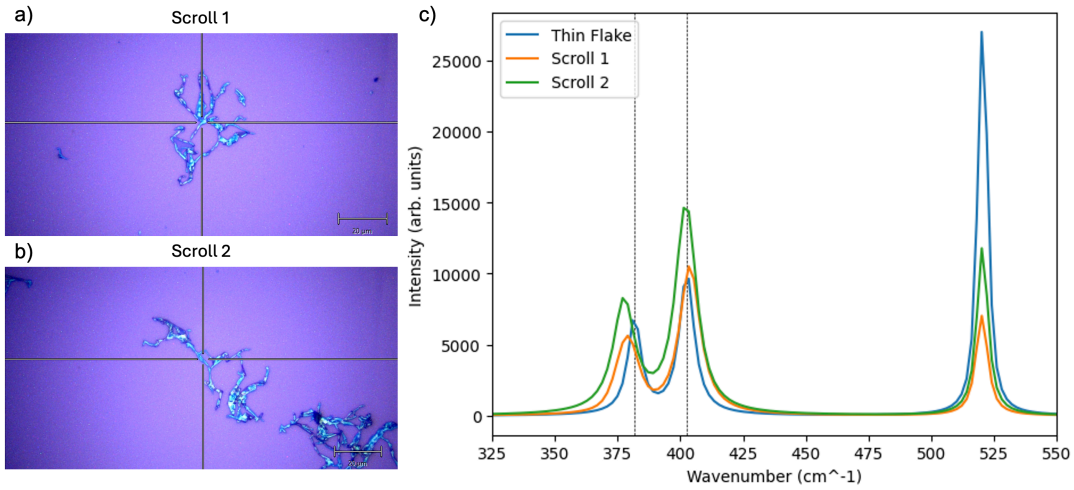


Figure 4.17: a) & b) OM images of the scrolls measured with Raman spectroscopy. c) Plot comparing the Raman shift of scrolls with a thin flake.

grown with much higher repeatability. Using the temperature profiles of the two methodologies, it can be concluded that the main factor contributing to the change in size is the amount of time the precursors spend simultaneously in the ideal growth temperature range, while the shape most probably relates to the lowered maximum temperature of the sulfur. This is because the star-shaped morphology can be linked to an excessive amount of sulfur atoms reaching the reaction surface. Furthermore, by assessing the effect that sulfur temperature had on the new reaction method, it was found that 200ºC remains the ideal Z3 temperature for growing uniform triangular flakes, and 180ºC is near the inflection point of 2:1 S:Mo stoichiometry.

Upon scrolling flakes obtained via the two different methods, unsynced and synced ramping, a number of the hypotheses regarding their morphologies were confirmed. Flakes grown with the unsynced method suffered from their star-like shapes, with scrolling often initiating from multiple edges at once and often ripping apart or tangling in the process. Additionally, the multilayer flakes did seem to separate to some extent during scrolling, producing nanoscrolls with highly uneven interlayer spacing and complex internal scrolling. On the other hand, the synced ramping flakes did in fact produce tighter, more uniform scrolls, which appeared to initiate from one singular edge.

However, there were a number of outcomes that were not initially predicted. The most significant of these was concerning the adhesion of flakes to the SiO_2 substrate. In the case of the unsynced method flakes, many of the samples had issues fully detaching from the substrate, leading to a larger number of only partial scrolls. The opposite was true for the synced method flakes, which completely delaminated from the substrate and became unusable as a result. This strongly highlights that morphology is not the only factor to consider in optimizing flakes for nanoscrolling. Because area has a direct correlation with adhesion force, one should aim to strike a balance between size and shape to obtain the highest quality scrolls with the highest usable yields. This would be the main avenue for continued research in MoS_2 scroll morphology optimization, adjusting CVD parameters to slightly increase size without impacting triangular shape. A recommended first parameter change would be to increase the reaction time in small increments.

Having successfully gained a deeper understanding of the relationship between flake and nanoscroll morphology via the MoS_2 flakes already grown in this CVD, the foundations are laid for attempting the growth of $MoSe_2$ for eventual use in scrolling. This set of experiments is explored in the next chapter.

5

Attempted CVD Fabrication of $MoSe_2$

To construct MoS_2/$MoSe_2$ heterostructures through a bottom-up approach, it is essential first to establish reliable growth conditions for $MoSe_2$. Since this material had not yet been synthesized in the lab hosting this project, the optimized MoS_2 CVD process was adopted as a starting point and adapted to accommodate the lower reactivity and higher vaporization temperature of selenium (Se). The process of this attempted growth was guided by literature reports and optimized via trial and error within the unique furnace setup. The objective was to realize few-layer $MoSe_2$ flakes suitable for subsequent scrolling and integration into van der Waals heterostructures.

While multiple CVD routes for $MoSe_2$ have been reported and are discussed in Chapter 3, they can be separated into two major categories: low-temperature Se and high-temperature Se growth. In the former, Se powder or pellets are placed in a cooler zone than the Mo precursor [12, 113], while in the high-temperature method, Se powder is placed near or at the growth temperature (around 750 - 900ºC) usually with closer physical proximity to the Mo precursor and growth substrate [18, 114, 160]. The low-temperature approach is largely the same as that used in the MoS_2 growths described in this work; however, the Se zone temperature is set higher, usually around 300ºC, since Se has a higher melting point than S at 221ºC [12, 113].

As discussed in the theoretical framework of $MoSe_2$ CVD growth, Se has a significantly lower chemical reactivity than S, which is a direct hindrance to the synthesis of $MoSe_2$. Numerous studies report that hydrogen gas acts as an indispensable reducing agent in APCVD $MoSe_2$ growth [113]. However, alternative approaches have demonstrated that sodium chloride (NaCl) can effectively promote selenization under hydrogen-free conditions [12, 18]. Even more interesting is the single report found of $MoSe_2$ flakes growing without either hydrogen or a salt-based promoter [116]. The uncertainty surrounding these mechanisms, along with the absence of H_2 supply in the accessible CVD system, motivated the strategies explored in this chapter. Therefore, a direct analogue to the MoS_2 growth process was first attempted, using pure argon (Ar) as the carrier gas with no additional promoting agents, followed by the introduction of NaCl to facilitate selenium activation.

5.1. Developing a Vapor Phase CVD Recipe for $MoSe_2$ Flakes

To avoid sulfur cross-contamination from previous MoS_2 growths, the CVD set-up was modified by replacing the 3.5 cm quartz tube with a clean double-tube configuration, each with a diameter of 4.2 cm. This is diagrammed in Figure 5.1. In all experiments described here, only the front tube was used for the growth, while the rear tube remained empty. To compensate for the resulting parallel gas flow, all Ar flow rates are doubled relative to the flowmeter reading, i.e., a 100 sccm flow rate is equivalent to a 200 sccm total flow. This is with the exception of the purge flow rate of 1000 sccm, which remains at this value due to it being the maximum setting. Beyond these described changes, the arrangement for loading the CVD is much the same as in the MoS_2 growths and can also be seen in Figure 5.1. An acid-cleaned 1 cm by 1 cm SiO_2/Si chip is placed on a flat crucible and loaded in the center zone (Z2) of the furnace 36 cm from the entrance. As a starting point, 10 mg of the same MoO_3 powder

(99.95% Alfa Aesar) is placed in a alumina boat 0.5 cm away, and 500 mg of now selenium powder (99.5% Sigma-Aldrich) is loaded in Z3 12 cm from the entrance.

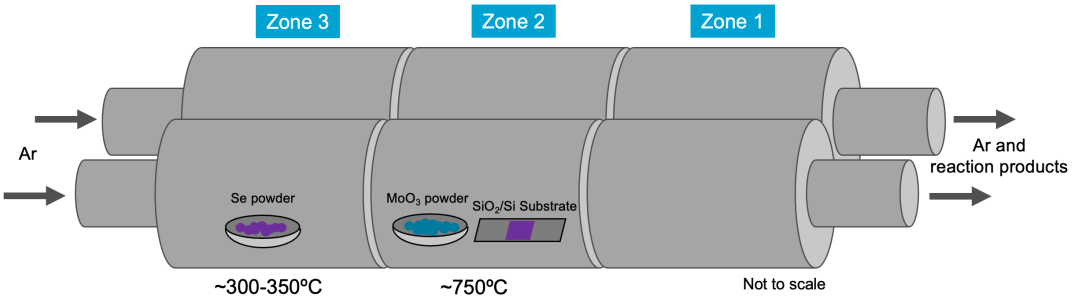


Figure 5.1: Photo of CVD furnace used for growing materials in the project.

The methodology used for heating will be the synced zone ramping detailed in Section 4.2. However, the temperature of the zones must be determined. When it comes to growth temperature, the lack of existing literature regarding promoter-free syntheses means that the value will need to be chosen based on assumptions from the work that is available. In the context of all APCVD recipes found in the literature, the range of growth temperatures used is between 700ºC and 1200ºC [117, 161] though the most common temperatures are 750 - 850ºC [12, 18, 113, 128]. While temperatures above 800ºC seem to be preferable for the unassisted methods [116], values reaching 800ºC were found to be practically impossible to achieve with a reasonable amount of time due to the limitations of the furnace equipment. Thus, 750ºC was chosen as the default growth temperature. Concerning the selenization temperature (the target temperature for Z3), 300ºC was by far the most commonly seen in literature, with some reports up to 350ºC [12, 113, 128]. Since this range was fully accessible to the CVD furnace, experiments were conducted with the goal of optimizing this temperature.

5.1.1. Selenization Temperature

Initially, a target of 300ºC was selected for the selenium heating zone. This temperature was attempted with a flow rate of 100 sccm for a reaction time of 5, 15, and 20 minutes as a baseline for determining time moving forward. Upon inspection of the 5-minute sample, there were no features visible; however, the results of the 15 and 20 minute growths can be seen in Figure 5.2. Even with the longer reaction times, little to no evidence of growth was found with these parameters. By looking closely, one can see small dot-like features that are not present on clean SiO_2/Si substrates. These dots are between 10 and 100 nm across and seem to be distributed on the sample with a higher density upstream. While they were the only structure found on the 15-minute reaction time sample, the 20-minute trial also possessed a few relatively larger dots seen in Figure 5.3, some of which took on an “island” structure where the dark circle surrounds a light square object. Due to the increased reaction, 20 minutes was the chosen reaction time for the remaining two temperatures of 325ºC and 350ºC. The collected SEM images of the results can be seen in Figure 5.4a & b.

As can be seen from the images, the pattern of small circular growths continues in the higher temperature samples as well, with the 350ºC selenized sample possessing the largest-sized features (up to 250 nm in diameter). Looking at the types of growths obtained thus far, it is apparent that the triangular or hexagonal $MoSe_2$ flakes expected are not found. Closer inspection of the largest spots on the 350ºC sample reveals a concentric pattern with a darker center (inset Figure 5.4b). Figure 5.5 displays a temperature profile plot for the synced ramping of a run with temperatures of 750ºC and 350ºC. Profiles for the other combinations can be found in Figure A.2 & A.3 and Table A.1.

High-Temperature Selenization

As the maximum low temperature value seen in the literature had been reached, a CVD run was also performed with the Se powder placed just upstream of the MoO_3 powder within the high temperature growth zone in order to replicate the studies utilizing this higher temperature methodology. For the sake of consistency, all other parameters were kept the same, and Z3 was still heated (empty) to 350ºC. As can be observed in the collected SEM image (Figure 5.4c), the multi-sized dot formations remain with

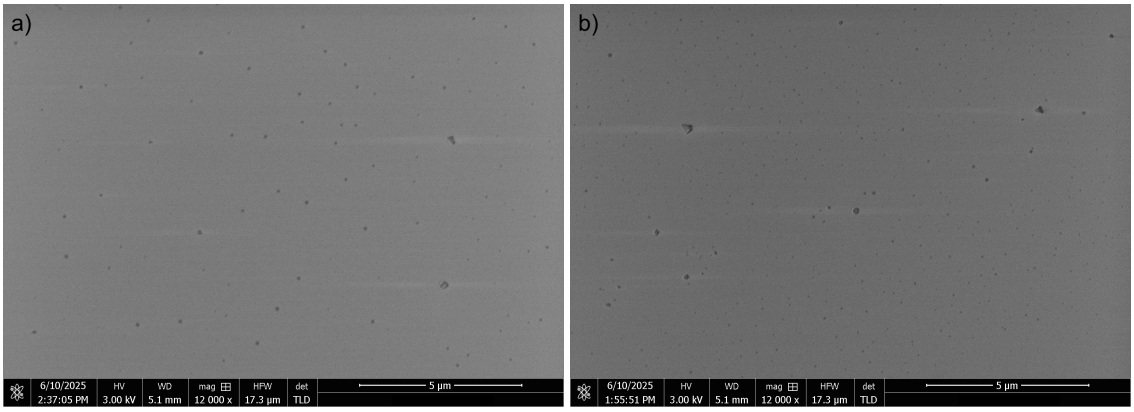


Figure 5.2: SEM image of $MoSe_2$ flakes grown with a selenization temperature of 300ºC with a reaction time of a) 15 min, and b) 20 min.

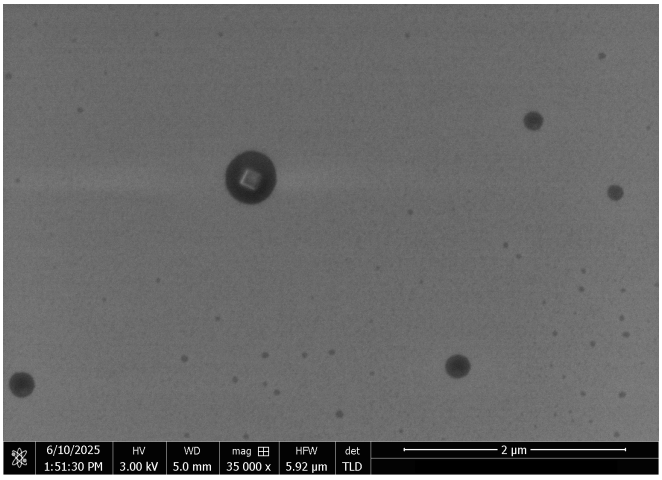


Figure 5.3: SEM image of $MoSe_2$ flakes from a growth of 300ºC for 20 minutes, zoomed in on a small oxide island with $MoSe_2$ growing around it.

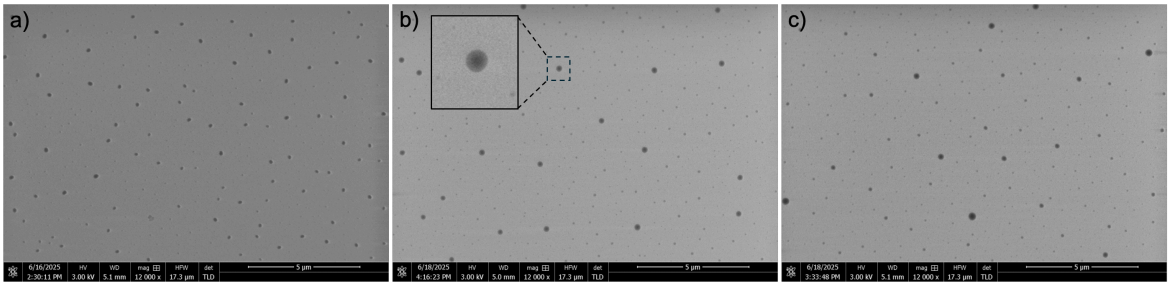


Figure 5.4: SEM images of $MoSe_2$ flakes growth with a selenization temperature of a) 325ºC, b) 350ºC, and c) 750ºC. Inset b) is a digitally zoomed image of a circular feature.

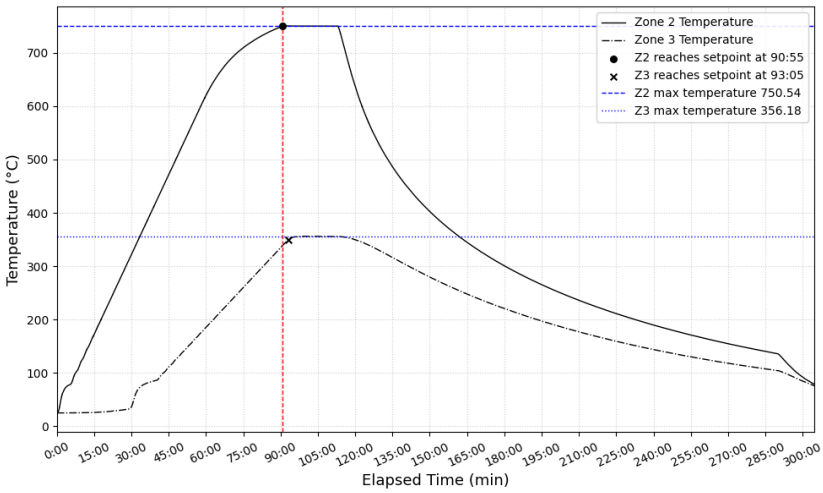


Figure 5.5: Temperature profile of the furnace zones when performing a CVD synthesis with a selenization temperature of 350ºC.

nearly the same visual characteristics. These experiments, and their failure to form the expected $MoSe_2$ morphologies, invoke the need to determine the composition of these features and their mechanism of growth.

Spectroscopic and Compositional Analysis

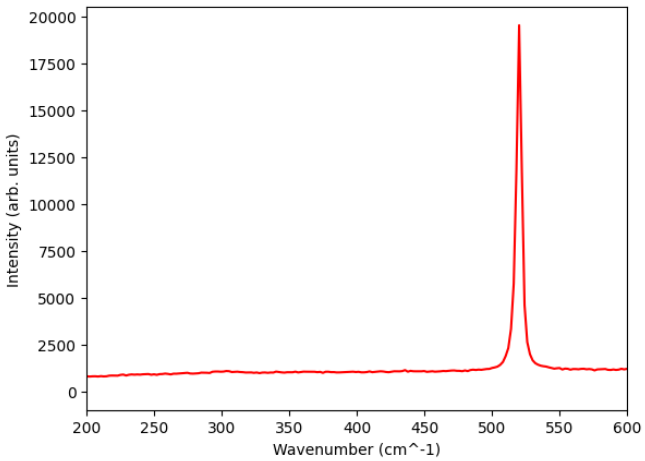


Figure 5.6: Raw Raman spectrum data of a circular spot from the first set of attempted $MoSe_2$ growths.

If $MoSe_2$ is present on the samples, Raman spectroscopy should be similarly effective as it is for MoS_2, thus this method of characterization was employed first. As with MoS_2, the A_{1g} and $E^1{}_{2g}$ vibrational modes for $MoSe_2$ are expected to be excited, but with shifted wavenumber positions of 241 cm^{-1} and 282 cm^{-1}, respectively [162]. Although the features of interest are even smaller than those probed in Section 4.3.1, the measurements were attempted by positioning the small circles as close to the center of the laser spot as possible and repeating the measurements several times. However, no vibrational modes outside of those from the substrate were found (see Figure 5.6). This result could indicate the lack of $MoSe_2$ or any other Raman sensitive material, but, as discussed in the last chapter, the resolution limitations mean this is not conclusive. To gain more resolution, SEM based point EDX was also used. This technique utilizes X-ray emissions produced by the elementally unique shell transitions that occur when an electron fills a vacancy left by the SEM beam interactions with the atom [163]. While not able to provide information about crystallography or directly confirm the presence of a TMD like $MoSe_2$, EDX does allow for an elemental composition to be determined. In the case of these dots, EDX confirmed only the presence of Mo and O. Table 5.1 displays the compositional results of several spots tested

covering a range of sizes. It should be noted that some of the largest outlier spots were measured due to a lack of signal from smaller spots.

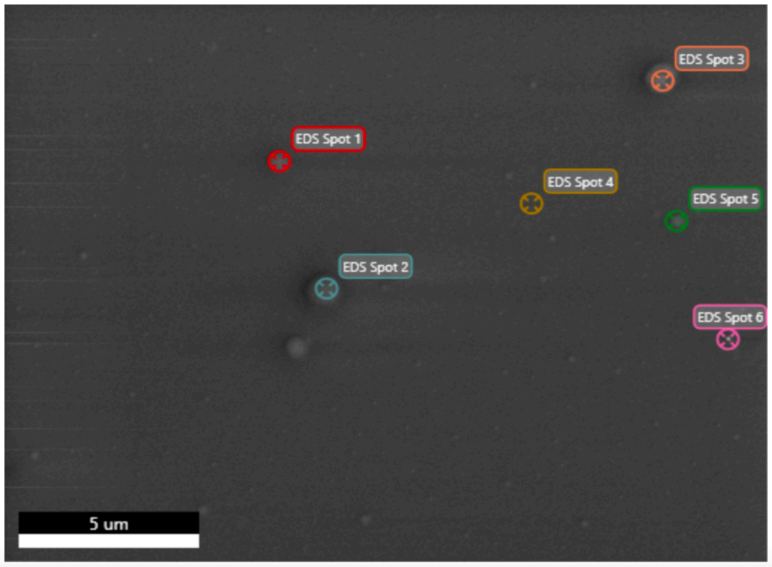


Figure 5.7: SEM image of points taken for EDX measurement.

Element (at %)	**Spot 1** (350 nm)	**Spot 2** (600 nm)	**Spot 3** (700 nm)	**Spot 5** (200 nm)	**Spot 6** (100 nm)	**Spot 4** (Background)
Si	51.81	48.19	55.70	61.07	59.40	59.07
O	46.06	47.88	42.75	38.93	40.60	40.93
Mo	1.59	2.74	1.03	0	0	0
Other	0.54	1.19	0.53	0	0	0

Table 5.1: Atomic percentages found via EDX of various-sized spots

None of the spots tested showed any evidence of Se, however, the largest ones did show the presence of Mo. While the background is composed of SiO_2 and Si, the largest samples also showed a relatively higher percentage of O atoms, indicating the dots also contain oxygen, though it is unclear if any specific oxide has formed. However, by assuming the same background composition of 40.93:59.07 O:Si, a rough calculation on Spot 2 reveals a possible Mo:O composition of 1:5.37. This ratio is not a stoichiometric composition for molybdenum oxide, which can form with a maximum ratio of 1:3. Since oxygen is a light element, the EDX may have inaccurately calculated its value. It is also possible that oxygen is present via a different composition entirely. For example, the molybdic acid $MoO_3 \cdot 2H_2O$ is a common hydrated form of molybdenum oxide with an atomic ratio similar to that found via EDX [164] and which could have formed in these circumstances due to the incorporation of water molecules from air exposure during the cooling phase of the CVD. Given the absence of Se on the substrate, it seems that the MoO_3 successfully vaporized and adsorbed to the surface, but, without a reaction with Se, potentially gathered in droplets as the substrate cooled down. While these theories cannot be confirmed by the characterization steps performed, what is certain is that the $MoSe_2$ formation reaction is not occurring under the conditions which have so far been used. Thus, experiments were performed varying two other parameters: Ar reaction flow rate and substrate orientation.

5.1.2. Argon Flow Rate

Since varying the selenization temperature did not yield $MoSe_2$ formation, attention was next directed to the carrier-gas flow rate, a parameter known to influence the vapor transport of Mo and Se species. Previous studies on the optimization of CVD-grown $MoSe_2$ have shown that excessive Argon flow rates can contribute to fewer triangular flakes due to a lack of Mo in the reaction environment [12]. In contrast, however, it is also reported that “particles” can appear at insufficient Ar flow rates, which are the result of low selenization, an effect seen in Figure 5.8. Because these features resemble those found in the

previous experiments, both higher and lower flow rates are investigated to assess their influence on growth.

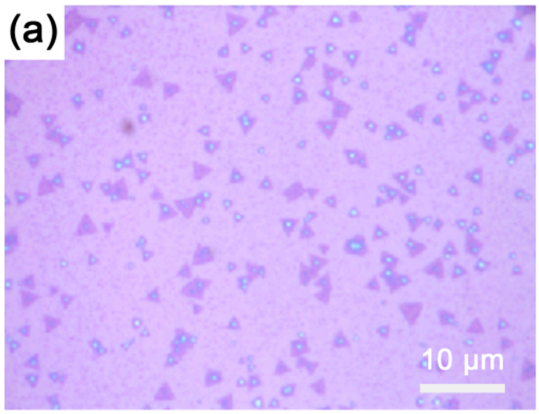


Figure 5.8: OM image of $MoSe_2$ flakes growth with flow rate of 15sccm and demonstrating "particles" between flakes due to low selenization. Reproduced with permission from [12].

Figure 5.9 shows the results of the samples made with reaction flow rates of 50 sccm and 150 sccm. These again possessed almost identical results visually to those with 100 sccm at the selenization temperatures of 350ºC and 750ºC. The only notable difference is seen in the 50 sccm sample at 350ºC, which contains a region of much larger droplet formations on the upstream edge of the sample. These droplets each surround a globule-like particle and have a clear amorphous shape.

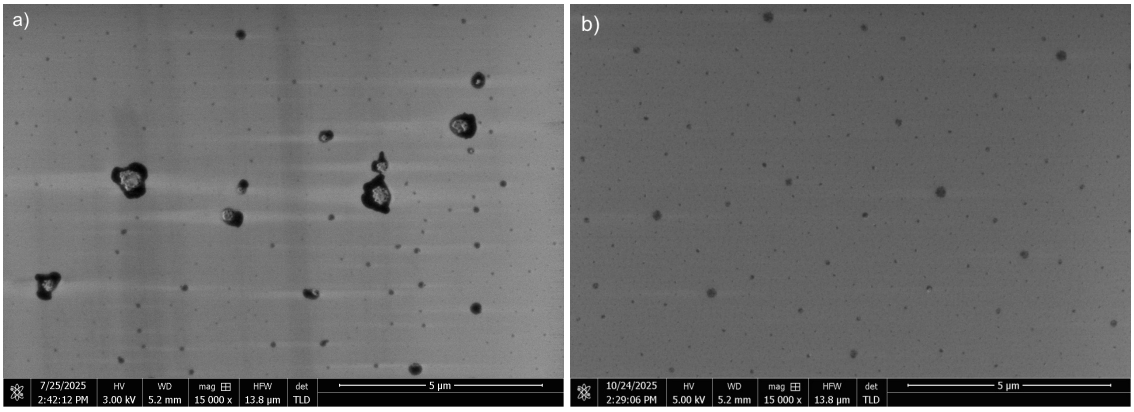


Figure 5.9: SEM image of $MoSe_2$ flakes grown with a selenization temperature of 350ºC at a) 50 sccm and b) 150 sccm Ar flow rate.

5.1.3. Substrate Orientation

Since varying the argon flow rate also did not promote $MoSe_2$ formation, the substrate orientation was examined. Many successful $MoSe_2$ CVD growth reports employ a configuration in which the substrate is positioned upside down above the MoO_3 powder as diagrammed in Figure 5.10 [113, 114, 165]. This was therefore also attempted, allowing the substrate to be much closer to the precursors and, in theory, creating an environment more conducive to reactions happening on the surface.

Using a selenization temperature of 750ºC, the upside-down substrate produced a unique result displayed in Figure 5.11. On the upstream side of the sample, many rectangular and vertically oriented crystals were grown. It was also noticed that while the small circular formations remained, the density of their formation was greatly reduced. Finally, large amorphous droplets, as in Figure 5.9c, were again seen but without the accompanying particles within them. These were significantly larger as well, with sizes around 3 µm across. The emergence of the thin vertical growths is interesting as it confirms the theory that some reactions taking place closer to the precursors are no longer happening with enough frequency near the separately placed substrate to lead to any growth.

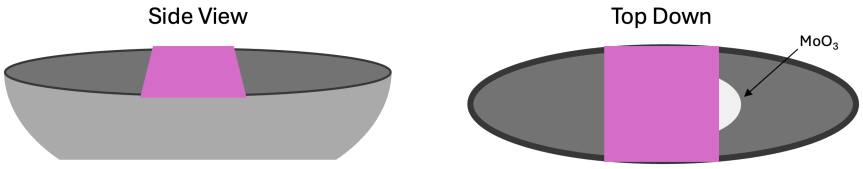


Figure 5.10: Diagram of substrate positioned over Mo precursor from side and top down view.

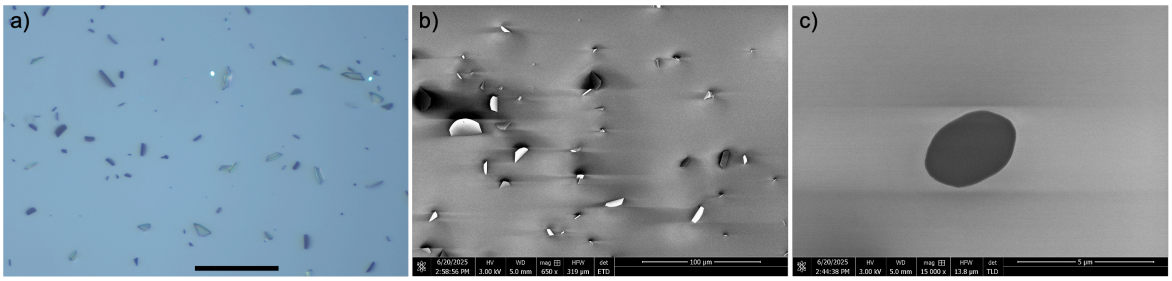


Figure 5.11: a) OM (Scale bar 50 µm) and b) SEM image of substrate grown upside down over Mo precursor with a selenization temperature of 750ºC. c) SEM image of an amorphous dark feature on the substrate.

While vertical $MoSe_2$ flakes can take on a similar shape to the flakes seen in Figure 5.11b [166], these are usually only a few hundred nanometers across. The relatively large size of the ones found in this experiment (up to 50 µm) and their angular edges support their characterization a molybdenum oxides, which have formed during the cooldown process between 600ºC and 700ºC [167]. This was confirmed by EDX, which detected no presence of Se on any of the vertically oriented flakes. Without the Se equivalent reaction of Equation 3.3 taking place, and with the proximity afforded by the changed substrate orientation, it seems the vapor phase molybdenum oxides are able to nucleate and grow in a stable phase on the surface of the substrate.

This section has detailed just a selection of the most relevant CVD syntheses performed when exploring the parameter space of selenization temperature, Ar flow rate, and substrate positioning. Table A.1 contains the full list of trials along with basic notes concerning their outcome. Among all the trials, no confirmable $MoSe_2$ was able to be grown. While a range of parameters were tested, which are in line with those found in the literature, the presence of Mo oxidation states on the substrate without any Se indicates that there was a failure of the $MoSe_2$ synthesis reaction to proceed. This work does support the idea that a reducing agent or promoter may be essential for the growth of $MoSe_2$ via APCVD. Since the goal of this thesis is to develop the simplest and safest approach to growing $MoSe_2$ flakes for nanoscrolling, NaCl will thus be introduced over a reducing agent like H_2.

5.2. Introducing NaCl as a Promoter

Building upon this rationale, NaCl is introduced to assist the $MoSe_2$ synthesis reaction under hydrogen-free conditions. While NaCl and related alkali halides are well-known promoters of $MoSe_2$ CVD growth [117], only a few studies have examined their use without hydrogen gas [12, 18]. Thus, these reports will serve as a guide for the changes to the CVD procedure going into this section.

The synced ramping procedure is retained, as one-zone furnaces are also used in the referenced methods. The growth temperatures are in the same range as those reported in the literature, where well-developed flakes are typically obtained between 750ºC to 800ºC. However, both high- and low-temperature Se configurations have been used successfully, allowing flexibility in this parameter. In all reports, the SiO_2 substrate has been placed face-down over the MoO_3 powder as in Figure 5.10, and this orientation is therefore selected for the present experiments.

The only parameter which is unable to be replicated in the CVD furnace used by this project is the ramping rates. The two studies referenced use 25-50ºC/min temperature ramps, but 10ºC/min is the highest safely achievable for the set-up introduced in Section 3.2.1. Thus, along with the already

showcased 5ºC/min Z3 ramp, a 10ºC/min version is also used. This results in a temperature profile like that seen in Figure 5.12. Finally, the Ar flush and cool-down procedure remains the same as the rest of the experiments discussed thus far.

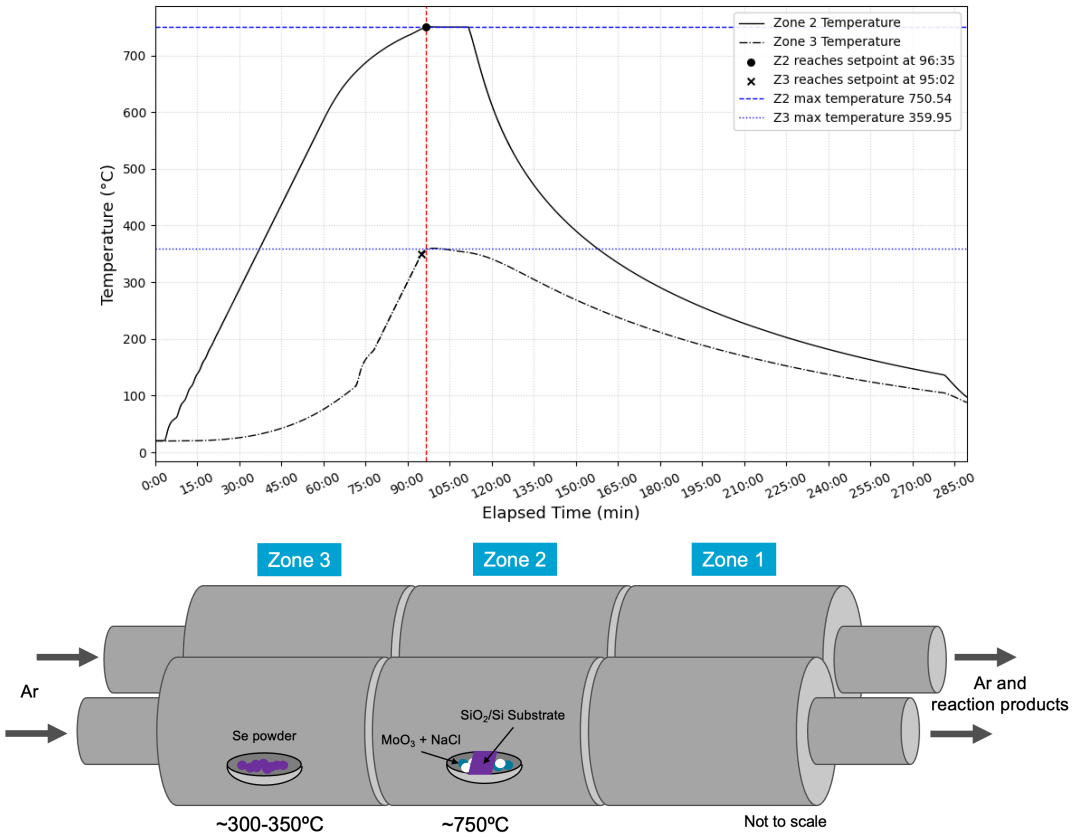


Figure 5.12: a) Example temperature profile of CVD synthesis for NaCl-assisted $MoSe_2$ growth with higher Z3 ramp rate. b) Diagram of CVD furnace for NaCl-assisted growths.

With regard to the NaCl incorporation, a choice must be made between directly mixing the MoO_3 and NaCl powders together and creating a deionized water NaCl solution, which is then added to the MoO_3 powder. Since the NaCl available for use (99.0% Sigma-Aldrich) has large granules (between 500 µm and 1 mm), it was determined that creating a solution would allow for more even distribution of the compound with the MoO_3 powder. The solution used for these experiments is 0.5 wt% NaCl [12]. Once the solution was made, a micro-pipette was used to dispense the desired amount of solution (1 µL for every 1 mg) onto the MoO_3, which was already measured into the boat. This was then delicately mixed with the end of the pipette tip before the substrate was placed on top.

Growth runs were performed with the selenium powder heated to 300ºC (as reported in [12]) and 350ºC (as used in the previous section), as well as with a range of MoO_3 + NaCl amounts from 2 mg + 2 µL to 10 mg + 10 µL. The optical results for the extreme ends of these ranges are shown in Figure 5.13. Compared with the non-NaCl-assisted growths, the most evident feature across all trials is the substantial increase in the size and visibility of the small circular formations that were previously only barely seen at the maximum magnification of the optical microscope. While in non-NaCl assisted growth these dots were measured to be less than 0.5 µm across (Figure 5.4), there are now a significant number of them clearly distinguishable on the substrate with diameters of 1 µm plus. These features support the proposed mechanism that NaCl acts to lower the melting point of MoO_3 (by forming new compounds) and increasing the amount of vapor/liquid reactant reaching the surface of the sample. As can be seen from the upstream edge of the selected samples, the substrate exposed to the higher amounts of MoO_3 and lower temperature (Figure 5.13a) grew beads more densely packed than the substrate which was exposed to less MoO_3 at a higher temperature (Figure 5.13b). This comparison is quantified in Table 5.2. This could be related to more coalescence and evaporation occurring at higher temperatures,

while the increased precursor mass leads to the continuous adsorption of Na_2MoO_4 or MoO_3 vapor to the substrate surface throughout the whole reaction period.

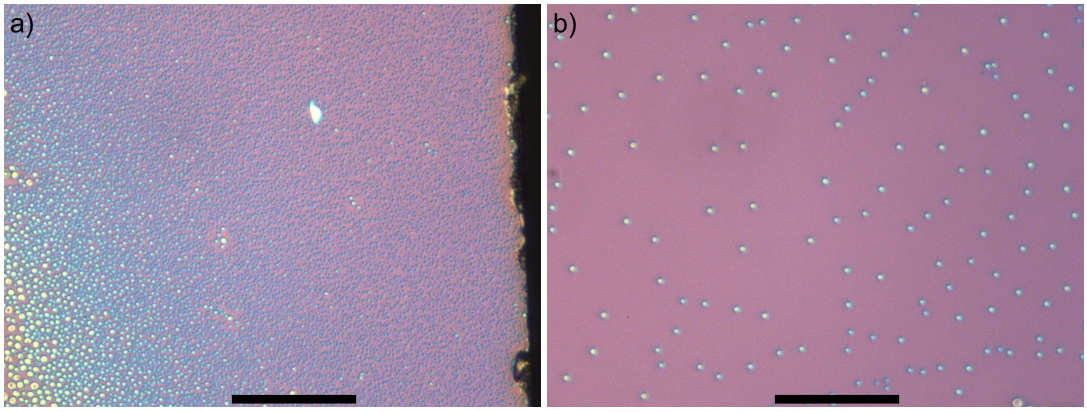


Figure 5.13: Optical microscopy images of the upstream edge of substrates produced at a) 300ºC selenization with 10 mg + 10 µL MoO_3 + NaCl and b) 350ºC selenization with 2 mg + 2 µL MoO_3 + NaCl. Scale bars 30 µm

	300ºC 10 mg + 10 µL	**350ºC 2 mg + 2 µL**
Bead Diameter (µm)	∼0.5 - 2.0	∼1.5
Average Density(#/100 µm^2)	33	1.2

Table 5.2: Atomic percentages found via EDX of various-sized spots

It is also important to consider whether the composition differs in the composition of the droplets compared to that found in Section 5.1.1. Based on the proposed reaction in Equation 3.5, Na_2MoO_4 and MoO_xCl_y are expected to form during the heating of the MoO_3 and NaCl and to be transported to the substrate via the Ar flow. Kim et al. [168] reported similar droplets in the halide-assisted CVD growth of various TMDs. Using NaOH as the promoter with MoO_3 and annealing at 800ºC for 15 minutes without any Se present in the furnace, they found that beads were formed on the surface of the SiO_2 substrate with the composition of Na_2MoO_4. Some of these beads, with further time at high temperature, react with Si in the substrate to form a stable Na–Mo–Si–O compound. It is thought that both the Na–Mo–Si–O compound and Na_2MoO_4 act as an additional stable source of Mo for the MoS_2 or $MoSe_2$ reaction [168].

EDX analysis on the beads in this project (pictured in Figure 5.15a and included in Table 5.3) found a small signal peak at 1.04 keV, corresponding to the Kα emission of energy of Na [169]. However, the detected Na intensity is below the threshold of quantitative reliability, preventing definitive conclusions about the elemental ratios or whether Na_2MoO_4 has been formed. This weak signal is consistent with the low overall Mo content (1.61 at.%) and is likely due to the small thickness of the beads, whose elemental X-ray emissions are partially overwhelmed by those of the underlying SiO_2 substrate.

In addition to the familiar bead structures, on the edges of the substrates (where there was direct contact with the crucible), a much more chaotic region of growth was found (Figure 5.14). The substrate in this area was covered with a rainbow surface coloration reminiscent of thin film interference [170] and flakes possessing a layered structure, that bared some resemblance to bulk $MoSe_2$, but could not be identified simply by eye. These visuals indicate a unique effect happening only at the interface between the crucible and the substrate, the reasoning of which will become clearer in Section 5.2.1.

EDX measurements were also made on these features along with Raman spectroscopy. Figure 5.15 shows the other spots tested, while Table 5.3 displays the compositional results of EDX. While it was more difficult to see the interference coloration in SEM than in OM, an attempt was made to measure a point in the ”film” region (Spot 5) as well as a normally colored substrate region (Spot 6). No new elements were detected in the discolored region; however, there was a significant change in the ratio of Si:O. While in the normal background region, the ratio is about 7:3, Spot 5’s ratio is measured as 3:2, constituting a 10% increase in oxygen atoms.

The larger beads present in this region show a much stronger Mo and Na signal. As can be seen from the atomic percentage values, there are more Mo atoms than Na. Since Na_2MoO_4 should contain a 2:1 Na:Mo atomic ratio, the EDX measurements signify that the beads cannot be purely this compound.

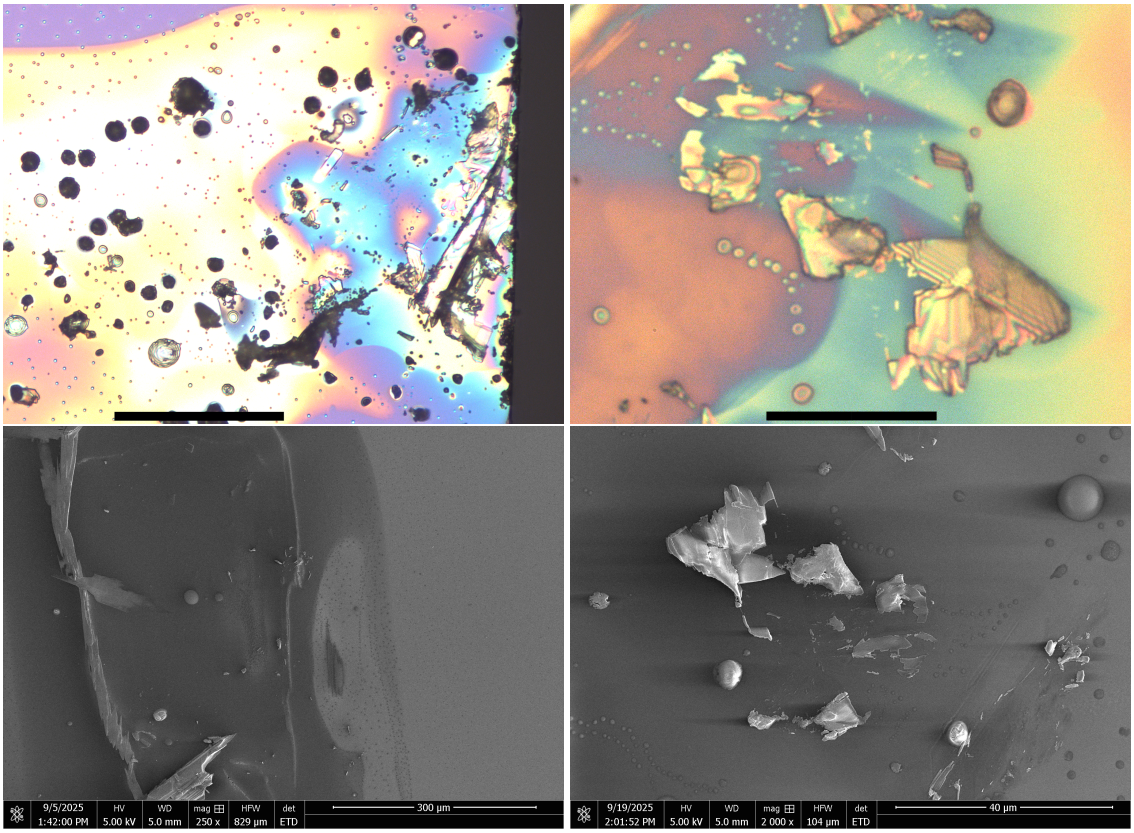


Figure 5.14: Top: OM images (left scale bar 100 µm, right scale bare 20 µm) and Bottom: SEM images of chaotic region of growth and film formation near edges of substrates which were placed upside down over MoO_3 + NaCl.

	Spot 1	**Spot 2**	**Spot 3**	**Spot 4**	**Spot 5**	**Spot 6**
Si (at %)	65.32	3.43	10.76	8.10	59.10	70.88
O (at %)	33.08	50.70	64.96	55.94	40.90	29.12
Mo (at %)	1.61	27.75	24.28	19.86	0	0
Na (at %)	–	18.12	0	16.10	0	0

Table 5.3: Atomic percentages found via EDX of spots labeled in Figure 5.15. The dashed lines indicate that the element was detected without an atomic percentage estimation.

In terms of Raman spectroscopy, the thin films show no identifiable signal. However, the layered flake shows the characteristic signal of orthorhombic MoO_3 [171]. More uniquely, however, the beads do demonstrate a slight shoulder in the range from about 150 cm^{-1} to 450 cm^{-1}, with a potential fitted peak at $(300.8400 \pm 0.7608)\,cm^{-1}$. Unfortunately, this signal is extremely weak compared to the SiO_2 background, which is a direct limitation of the resolution of this Raman instrument. Thus, to potentially gain crystallographic information, XRD on the surface of the most densely packed beads (visible by eye without a microscope) was carried out. No Bragg peaks were found, which indicates an amorphous crystal, something in line with the visual evidence gathered thus far and further explaining the lack of Raman signal for either MoO_3 or Na_2MoO_4.

5.2.1. Direct Placement on Substrate

In other reports of Na_2MoO_4 based assisted growth, the precursor mixture is sometimes placed directly on the substrate [168]. This technique was also attempted with the diagrammed setup seen in Figure 5.17. All other methods of growth are kept the same, and detailed parameters can be found in

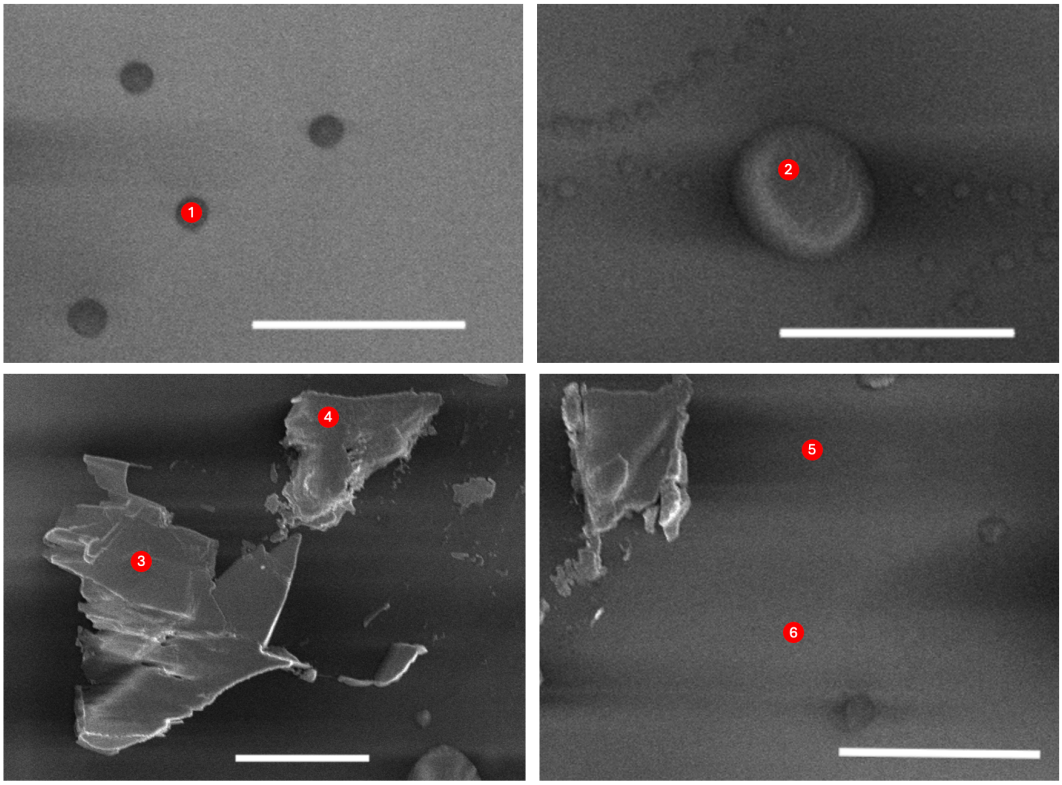


Figure 5.15: Positions correlating to the EDX composition measurements in Figure 5.3. Scale bar 10 µm.

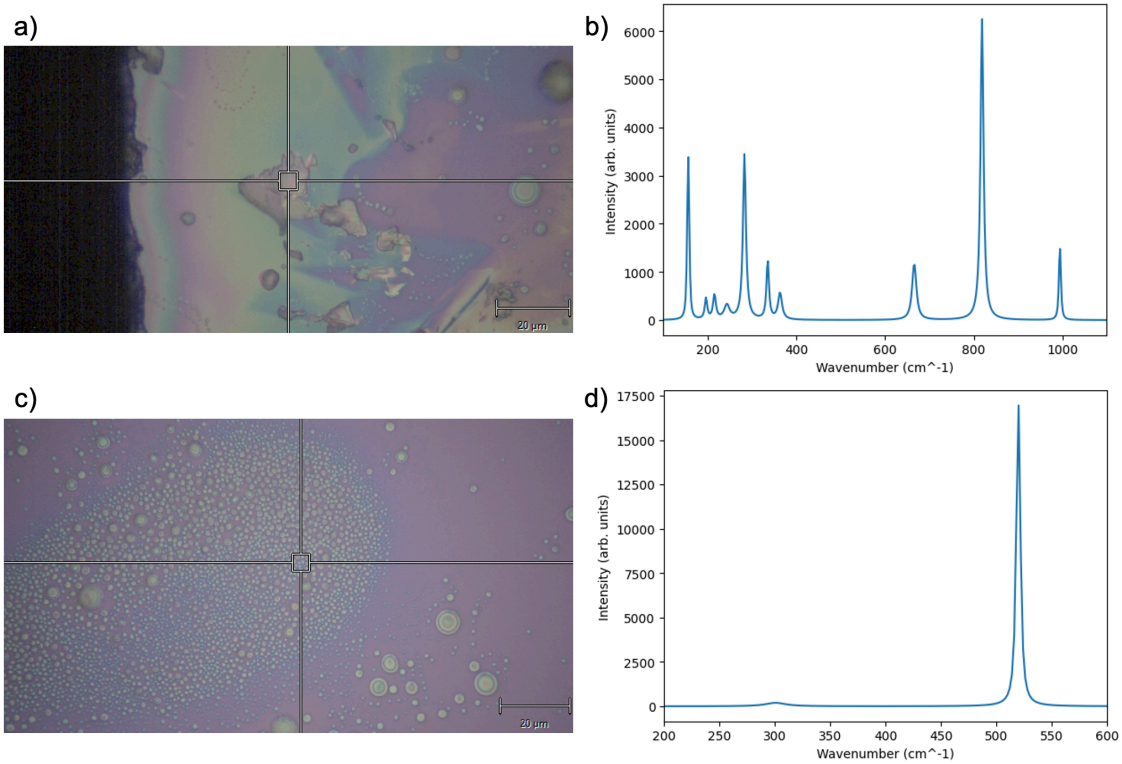


Figure 5.16: Raman spectra of two features found on NaCl-assisted CVD growths.

Table A.2. In this case, NaCl crystals were used to allow for the piling of the precursors on the substrate without loss over the edges.

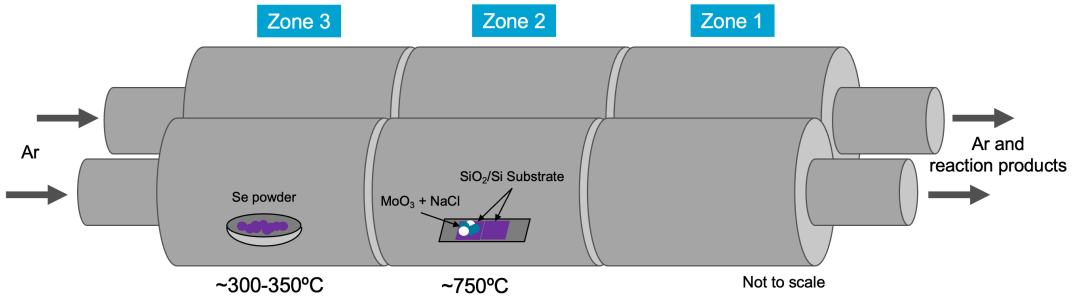


Figure 5.17: Diagram of CVD furnace for growths where NaCl was placed directly on the substrate.

As can be seen by the optical images (Figure 5.18) of the substrates after the CVD process, the main features were: the already observed blue colored beads, significantly more thin-film interference on the surface, and the new development of large semi-transparent domes centered around the location where the MoO_3 + NaCl pile was made. Based on this observation, it can be reasoned that interference coloring on the substrate, both in these trials and the previous ones, is a result of direct contact with the molten MoO_3 + NaCl. In the case of the substrates upside down on the precursor boat, the walls of the crucible must create a capillary effect on the liquid solution, pulling it up towards the substrate over time. Because there is no Raman signal for these films, it cannot be said exactly their composition, but once again EDX showed only a signal for Si and O atoms. This time the ratio of Si:O was 67.74% to 32.26% (Table 5.4), which is much more in line with the regular background measurements, leaving these films still a mystery. A closer look at the unknown domed structures in SEM reveals a rough surface texture on some domes and the development of thin crystals on the largest smooth beads.

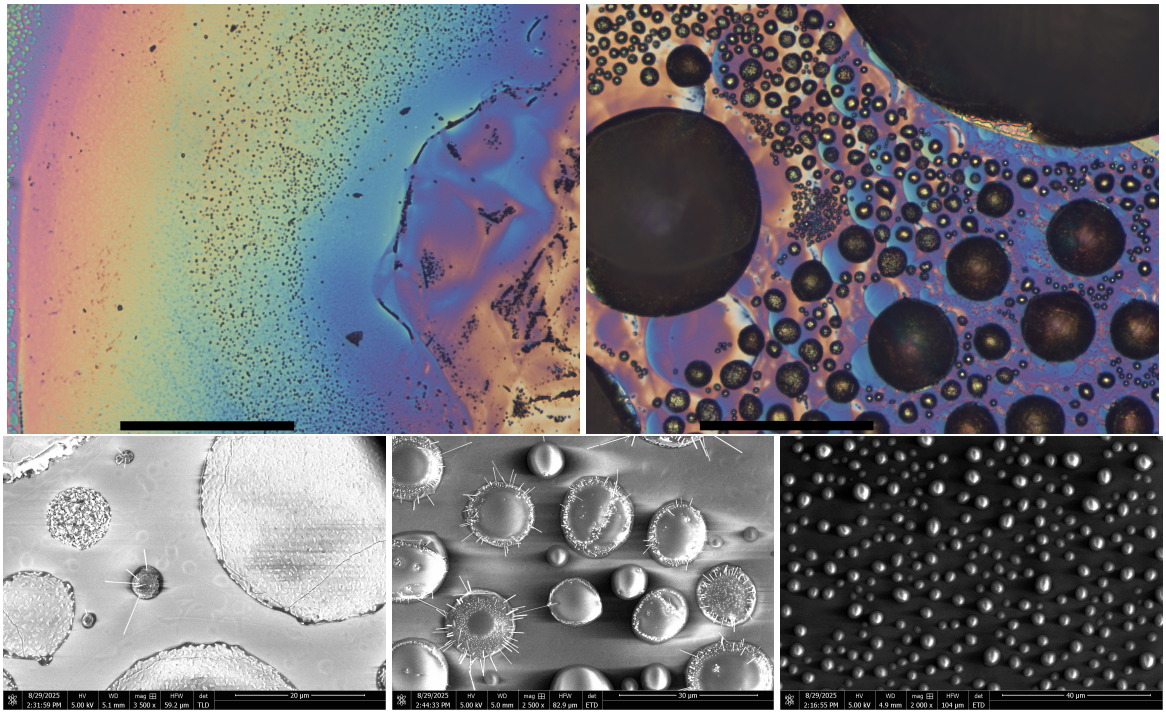


Figure 5.18: Top: OM images of the substrate after CVD where the MoO_3 + NaCl was piled (left scale bar 100 µm, right scale bare 20 µm). Bottom: SEM images of various circular morphologies present on the same sample.

Via EDX (Figure 5.19 and Table 5.4), it was found that the smooth texture dome (Spot 1) possessed relatively more Na and less Mo than the textured one (Spot 3). Additionally, Cl atoms were detected in the smooth dome, but not the textured one. However, these differences were quite minimal, especially

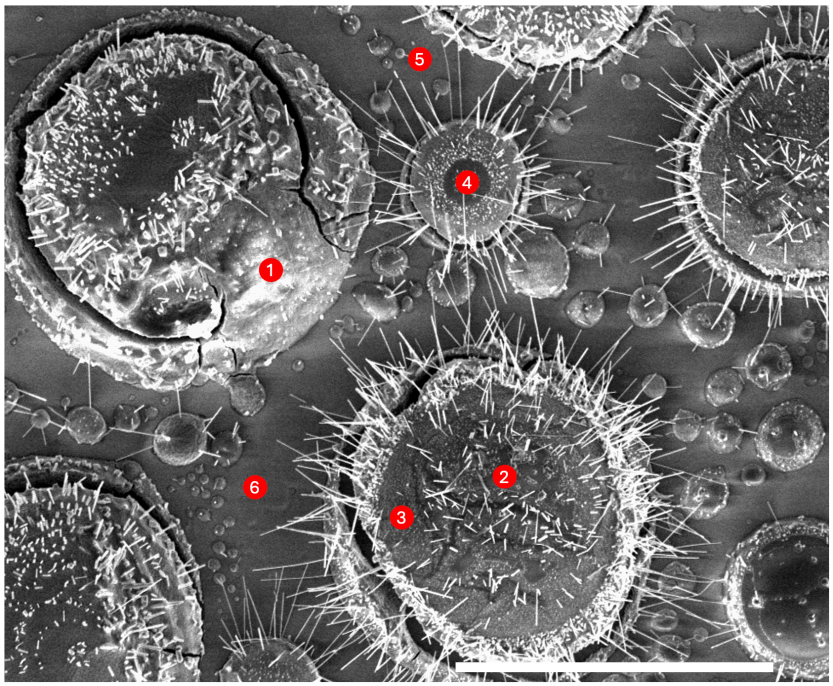


Figure 5.19: SEM images with red numbered spots indicating the location of EDX analysis reported in Table 5.4.

when compared with Spot 2, which has values somewhere between 1 and 3. Furthermore, trace amounts of Se were in fact detected on the domes, something not the case for any other methodology used. However, the calculated value is too low to make any assumptions about its incorporation as $MoSe_2$ or otherwise. Its presence simply indicates that there is potentially some benefit to more NaCl closer to the substrate, but under the conditions presented, the use of it directly on the substrate has not led to any significant $MoSe_2$ synthesis.

Element (at %)	**Spot 1**	**Spot 2**	**Spot 3**	**Spot 4**	**Spot 5**	**Spot 6**
Si	0.71	0.63	1.07	0.68	56.59	67.74
O	58.75	60.78	56.47	63.59	37.45	32.26
Mo	18.91	20.56	32.09	20.98	3.72	0
Na	19.99	17.71	10.09	13.62	2.24	0
Cl	1.36	0	0	0.82	0	0
Se	0.27	0.31	0.27	0.31	0	0

Table 5.4: Atomic percentages found via EDX of spots labeled in Figure 5.19.

In addition to the most relevant CVD attempts discussed in this chapter, a large number of runs were performed with various parameters, including changing the flow rate, orientation of the substrate, reaction time, and more. None of these attempts succeeded in producing identifiable $MoSe_2$ nor any unique morphologies/effects outside of what is detailed and characterized in these sections. For a full list of the parameter space, please once again refer to Table A.2.

These experiments have shown once again a failure to produce $MoSe_2$ without the assistance of hydrogen. While the best attempts were made to replicate the conditions reported in the most relevant literature of successful NaCl-promoted APCVD $MoSe_2$ fabrication, similar results were not achieved. It has been shown that NaCl has the intended effect of increasing the vaporization rate of MoO_3 and creating more viable nucleation sites for Se atoms. However, Se continues to bypass the sample and synthesis reaction. With the information gathered thus far, it is difficult to say exactly how the fabrication fails. The main condition that could not be directly achieved in this CVD furnace is the significantly higher temperature ramping rates. Some pre-reactions might take place before the target temperature is reached, which reduces the favorability of the $MoSe_2$ synthesis reaction, but no data was gathered

during this thesis, which allows that conclusion to be drawn with any confidence. Furthermore, one significant potential hindrance to growth is the possibility of oxygen contamination in the system.

5.3. Mo-film Based Two-Step Growth Approach

After a failure to produce $MoSe_2$ flakes via one-step vapor phase growth, attempts were made to grow vertical $MoSe_2$ with a two-step method. These techniques have been used with success for the growth of MoS_2 by using a pre-deposited Mo layer on a SiO_x/Si substrate [1], and there is also literature with a very similar procedure for $MoSe_2$ [166]. The theory behind the two-step growth is that one of the precursors, that of Mo, is predeposited on the growth substrate via a different fabrication method before CVD. In the case of both the cited studies and this project, that method is sputtering. Work in the two-step growth of MoS_2 has shown a correlation between the thickness of the sputtered seed layer and the orientation of the TMD grown. In the case of thin layers (below 5 nm, horizontal flakes of MoS_2 grow, while thicker layers lead to vertical growth and, as thickness increases, conversion of the Mo layer into MoS_2 [1]. However, the two-step method is less effective than the vapor phase approach for obtaining horizontal MoS_2 as the grain structure of deposited Mo can limit the lateral growth of the flakes [1]. This is the reasoning behind opting for an attempt at growing vertical $MoSe_2$ (v-$MoSe_2$). Even though vertical sheets are not optimal for the end goal of scrolling, achieving $MoSe_2$ in any form without the assistance of H_2 or NaCl would give invaluable insight into how to begin modifying its morphology for use.

Thus, the methodology for the following experiments in two-step growth is as follows. A clean 1 cm by 1 cm Si wafer is cleaned and a 1 µm Mo thin film is deposited via AC magnetron sputtering. This substrate is then placed on a flat alumina crucible and placed in the furnace at the center of Z2, while 500 mg of Se powder is loaded in the center of Z3. For the ramping, the synced strategy is used with an example temperature profile shown in Figure 5.20. Z2 is ramped only to 700ºC as it is the most optimal value seen in the literature [1, 166]; however, Z3 remains at 350ºC to ensure adequate Se reaches Z2 during the reaction. Three reaction times were used: 50 minutes, 35 minutes, and 20 minutes. These were chosen in an attempt to pick the highest temperature that would be sufficient to convert almost all of the Mo to $MoSe_2$ without risking it delaminating [156] with subsequent lower times to potentially see partial selenization.

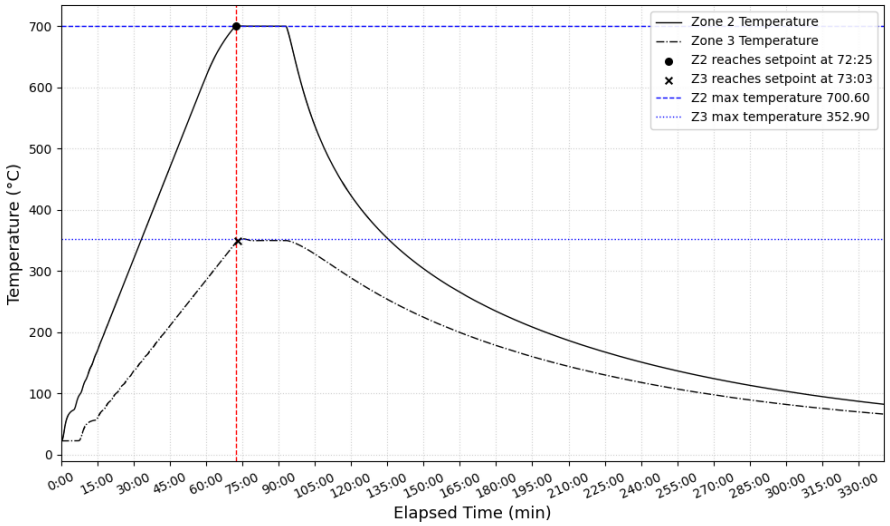


Figure 5.20: Example temperature profile of two-step CVD synthesis for vertical $MoSe_2$ held at target temperatures for 20 minutes.

Figure 5.21 displays the look of the Mo-coated wafer both before and after going through the CVD synthesis process. As can be seen in the images, the longer the films were exposed at high temperature, the more of the SiO_2 was revealed from the edges, indicating the evaporation of the film. It is important to note that this effect was visible as soon as the furnace was opened, rather than potential growths "falling off" due to delamination as was seen in previous work [156]. Additionally, the films darken in

color and become matte in appearance, with the 50-minute sample developing a polycrystalline texture visible by eye. The lower reaction time samples also exhibit a lighter gray ”halo” effect near their edges, which is not as visible in the captured images but is apparent by eye. These visuals confirm that some reaction has indeed taken place.

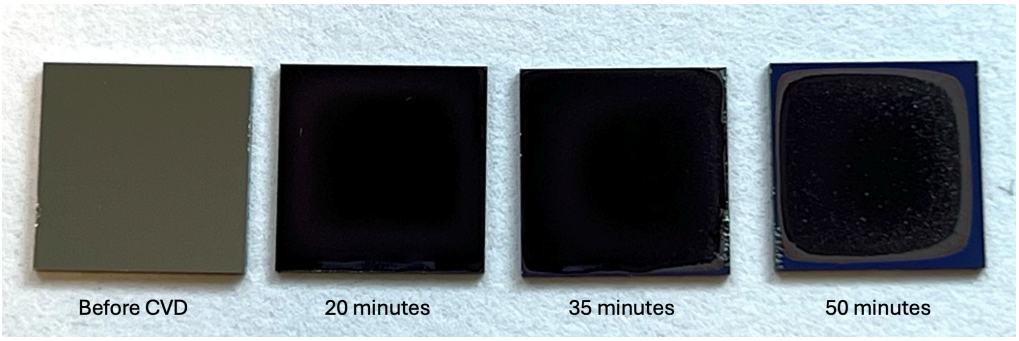


Figure 5.21: Photograph of a fresh Mo-coated wafer along with the three two-step samples after the CVD process.

Looking closer at the samples with SEM gives deeper insight into what has taken place and serves as a qualitative examination of the results before moving on to quantitative characterization methods. The first region of interest is the edges of the samples near the exposed substrate. In the 50-minute sample (Figure 5.22 top), a texture highly similar to the dots found on the vapor phase samples is visible; however, the circular formations are denser and larger than those found before. At the film-substrate transition, the dots transform into three-dimensional bubbles of up to 3 µm diameter, and some take on oblong shapes. These large beads are seen again in the edges of both the 35-minute and 20-minute samples, with less significant presence of the flat dots. As the samples only have a difference in the amount of time spent at high temperature, it can be seen how vaporization of the film progresses from the edge of the sample inward, with the solid uniform film first breaking apart into islands before individually evaporating. Where the film does still exist, seen in the right column of Figure 5.22, it is clear that the molybdenum metal has reacted to form a different material. In the 35 and 50-minute samples, this material has an organic plate-like structure, while the 20-minute sample shows filamentary growth with both large elongated crystals and thin needle structures.

Moving inward on the three samples reveals some unique morphologies growing on the surface of the films. On the 35 and 50 minute samples, a dark region of interconnected plates is encountered first (Figure 5.23 left). Growing between these plates are thin needle crystals similar to those seen at the edge of the 20-minute sample. Closer inspection of these needles (Figure 5.23 bottom) reveals that they are layered crystals with each discernible layer being 10 nm or thinner. When the sample is inspected even closer to the center, the dark background changes to a much more granular one and rectangular growths on the surface are revealed (Figure 5.23 right). In the 35-minute growth, small versions up to 6 µm are seen, while larger crystals up to 20 µm form in flower-like patterns on the 50-minute sample.

In contrast to the longer growth samples, the 20-minute growth does not possess the dark region highlighted in Figure 5.23. However, in the same relative location on the sample, crystals can be found (Figure 5.24) which grow with a similar pattern and size to those on the 50-minute sample but with a noticeably different morphology. These are better referred to as flakes since they are flatter and have sharp, pointed edges. By taking a closer look at Figure 5.24b, one can also notice the emergence of the thin needle crystals seen in the two other samples growing from these unique formations. Furthermore, it was noticed that their texture somewhat resembles that of the region where these needles grow on the samples heated for a longer time. This will be revisited in the following sections.

Finally, the central region of the substrates is observed via SEM in Figure 5.25. In all three regions, dark layered crystals are seen with the same texture and shape. However, when measured along their longest axis, a clear trend emerges in their average size (Table 5.5). As reaction time is increased, so is the average size of these structures. Also notable is the increased standard deviation of these averages, highlighting how structures as small as 4 µm are still seen on the higher reaction time samples. The presence of these smaller crystals could signify that active nucleation is happening up to and possibly past the 50-minute mark.

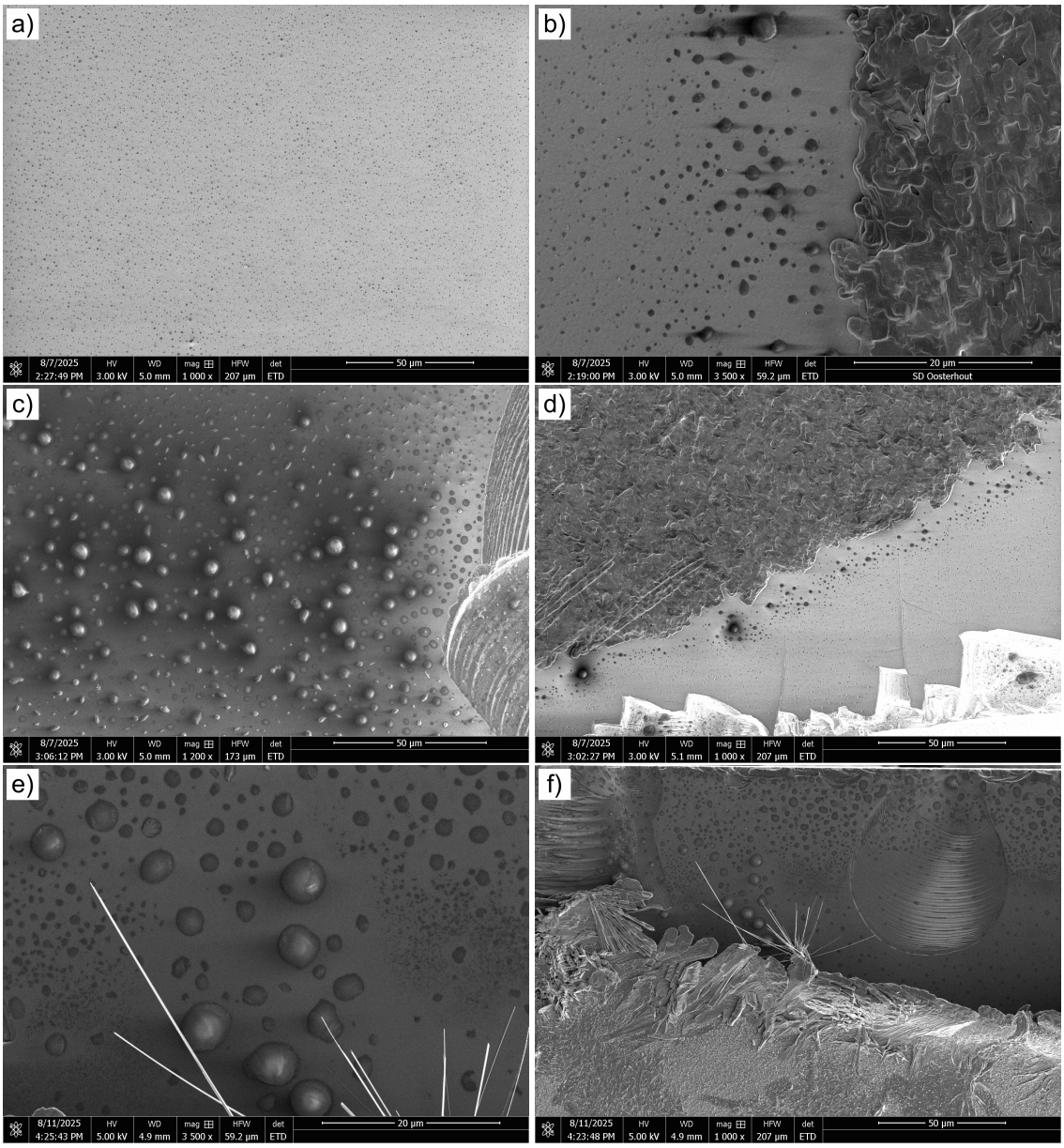


Figure 5.22: SEM images of the edge of samples with 1 µm Mo sputtered coating after a) & b) 50 minutes, c) & d) 35 minutes, and e) & f) 20 minutes of selenization.

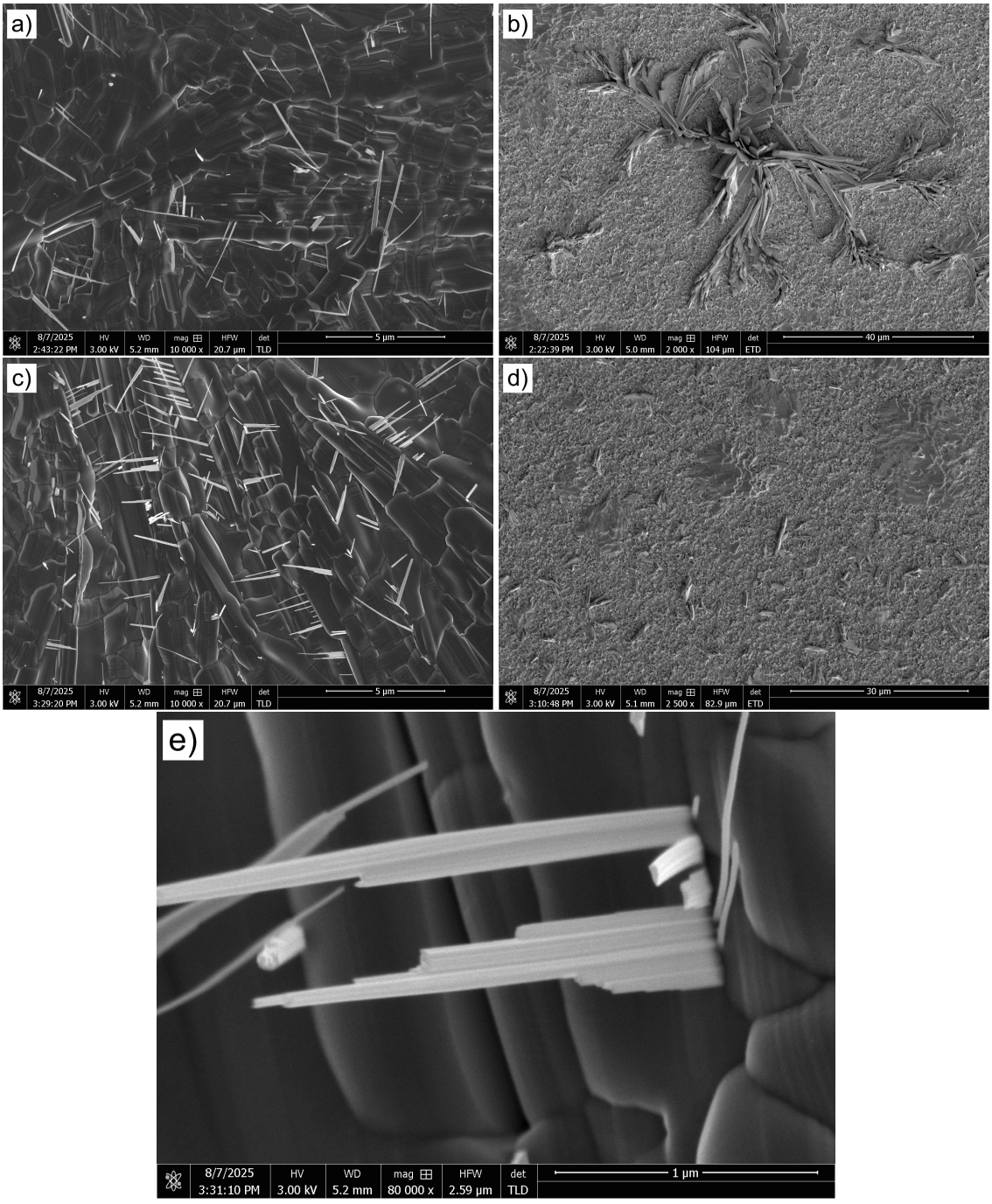


Figure 5.23: SEM image of samples with Mo sputtered coating after a) & b) 50 minutes and c), d) & e) 35 minutes of selenization, showcasing structures found between the edge and center regions.

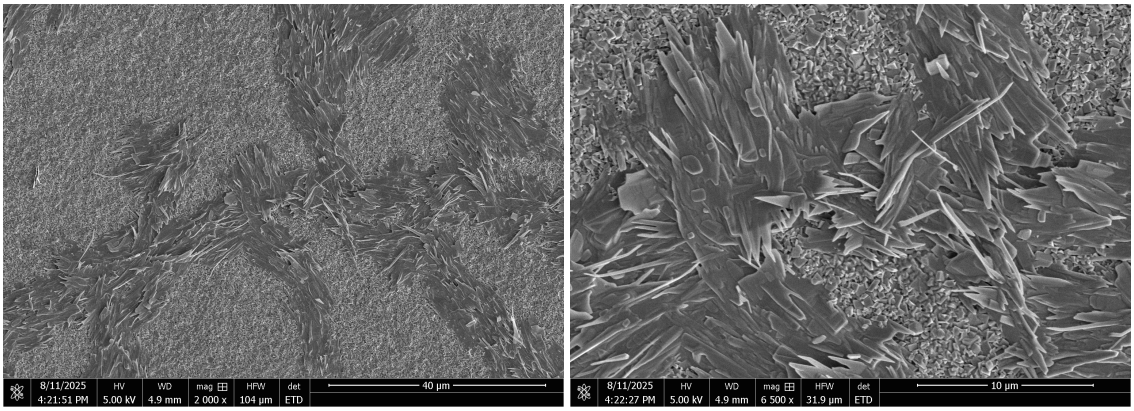


Figure 5.24: SEM images of sample after 20 minutes of selenization showcasing the unique crystal growth seen between the edge and center regions.

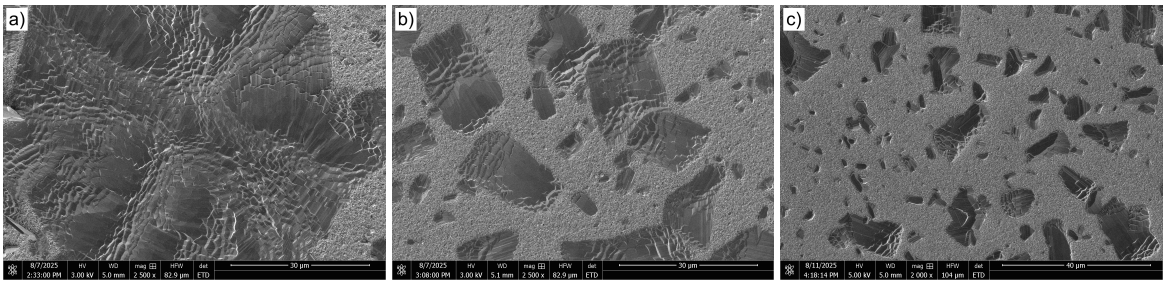


Figure 5.25: SEM image of the center of samples with 1 µm Mo sputtered coating after a) 50 minutes, b) 35 minutes, and c) 20 minutes of selenization.

Using increased magnification, a detailed view of the microstructure of the background was obtained and is showcased in Figure 5.26. Using ImageJ software, statistics were obtained regarding the size of these grains (excluding the large surface crystals). It was found that they have an average area of 0.042 µm with quite isotropic x and y sizes of 0.246 µm and 0.241 µm, respectively.

Reaction Time (min)	**20**	**35**	**50**
Average Length (µm)	5.9	11.9	16.4
Standard Deviation (µm)	4.3	7.8	15.5

Table 5.5: Table of average measured crystal sizes from each sample pictured in Figure 5.25.

While it still remains to be seen exactly the composition of the different structures found on the three substrates, none of those found seem to resemble the hexagonal layered crystal expected of $MoSe_2$. To confirm this and potentially gain insight into what materials are present, compositional characterization steps were performed.

5.3.1. Characterization of Crystals

First, the various identified morphologies were examined with EDX. Since multiple measurements were taken over many regions of the sample, Figure 5.27 was made to create an overview of the positions tested for reference. The compositional results for each structure are displayed in Table 5.6.

As can be seen in the table, only the structures closest to the edge of the sample showed any Si presence. Because the penetration depth for 15kV SEM EDX is about 1 µm, this indicates that the remaining film (even in the 50-minute sample) is not significantly reduced in thickness due to the CVD process. Otherwise, the EDX results show only Mo and O, with occasionally some additional elements (like K and Ne) whose values are below the error margins to be considered accurately detected. Se atoms were not detected at any of the points tested. This in itself confirms the failure of $MoSe_2$ to be synthesized via these two-step experiments. However, analysis can be performed on the apparent molybdenum

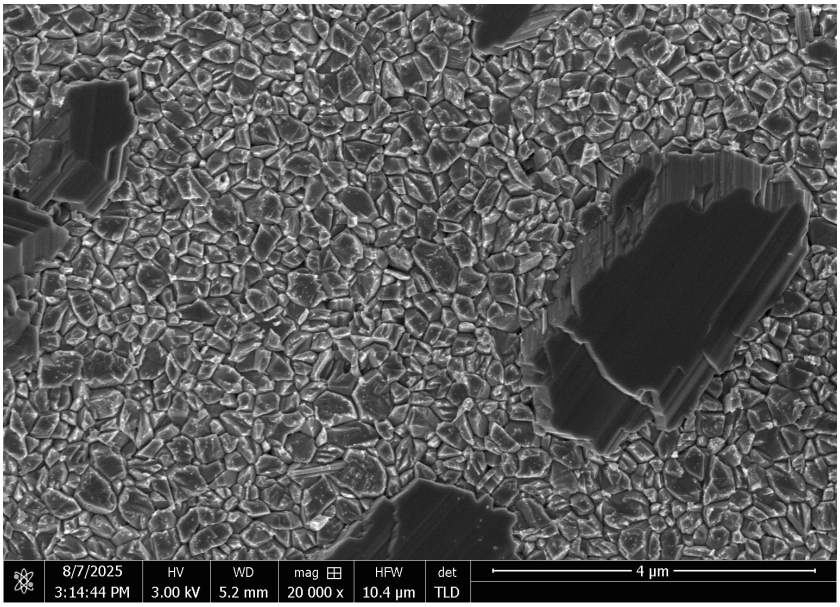


Figure 5.26: High magnification SEM image of region shown in Figure 5.25

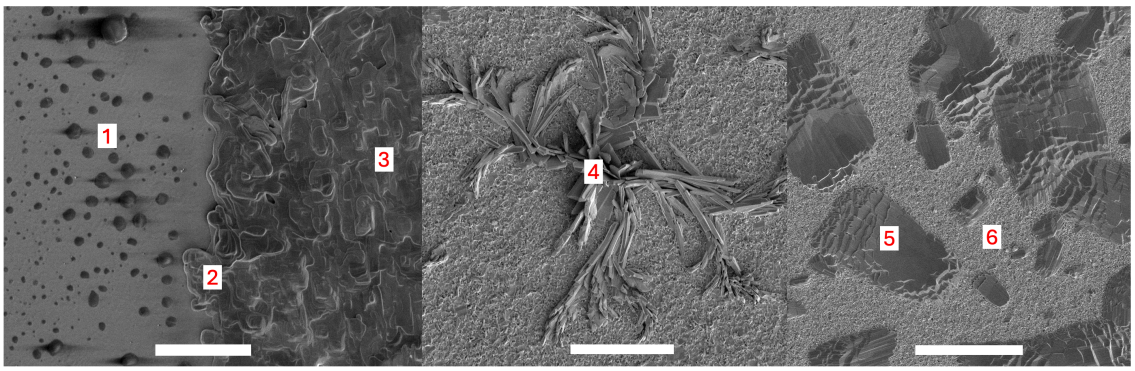


Figure 5.27: Reconstructed reference for the morphologies measured using SEM-EDX. Scale bars (from left to right) 10 µm, 20 µm, 15 µm.

	Region 1	Region 2	Region 3	Region 4	Region 5	Region 6
Si (at %)	57.2	12.6	0	0	0	0
O (at %)	38.6	69.7	73.2	82.5	78.23	69.6
Mo (at %)	2.6	17.8	25.7	15.8	21.8	30.4
Other (at %)	1.6	0	1.2	1.7	0	0
O:Mo Ratio	3.7±0.8	3.6±0.3	2.8±0.2	5.2±0.4	3.5±0.3	2.3±0.2

Table 5.6: Atomic percentages found via EDX of structures labeled in Figure 5.27. The last row displays the calculated Mo:O ratio when corrected for the presence of SiO_X.

oxides to relate their stoichiometry to the physical observations made via SEM in Section 5.3.

This analysis is done using the facile approach of comparing the Mo:O atomic ratio at each measured point. For the two regions nearest the edge (the beads and film edge) where Si was also detected, a background EDX measurement was used to determine the substrate Si:O ratio and then subtract it from the Mo:O ratio. When looking at these results (also displayed in Table 5.27) it can be seen that regions 1, 2, 3, and 5 have ratios somewhere between 1:3 and 1:4, while region 6 has a ratio near 1:2, and region 4 has a ratio near 1:5. Molybdenum has independent stable oxide phases of MoO_2 and MoO_3 [164], so there is evidence to support that the structures seen in Figure 5.22 and the dark flakes in Figure 5.25 are composed of MoO_3. Similarly, the surface grains in Figure 5.26 appear to be MoO_2. The only outlier result is that from the dendritic structures from region 4 and seen in the right column of Figure 5.23. EDX analysis measured an oxygen ratio of about 5 atoms to every one molybdenum. While the molybdic acid $MoO_3{\cdot}2H_2O$ was presented as a possibility for this ratio seen in the vapor phase obtained structures, the highly crystalline nature of the features seen on the two-step samples reduces the possibility of this theory. Instead, one possible explanation for the inflated oxygen presence may be the fact that the crystals are thin and sit on top of a mixture of MoO_2 and empty space. Because EDX analysis assumes a uniform bulk sample for accurate measurements, the odd morphology may be affecting the accuracy of the EDX measurement. To solidify the results of this compositional analysis and clarify the composition of region 4, Raman was once again employed.

As discussed in previous chapters, TMDs have distinctive Raman spectra that can be used to identify them. However, the molybdenum oxides also show strong Raman peaks, which makes it a highly effective technique for understanding the materials present on these samples. To ensure the best possibility of detecting $MoSe_2$ if it exists somewhere not found with EDX, a 488 nm laser source was used, and it was, as before, calibrated to a 520 cm^{-1} Si peak.

To begin, the morphologies identified as region 3 and 4 in Figure 5.7, had strong fitted peaks for at the positions 667 cm^{-1}, 823 cm^{-1}, and 996 cm^{-1} (seen in Figure 5.28 which highly correlate to the octahedral stretching modes of MoO_3 [171, 172]. This confirms the results obtained via EDX in region 3 and helps to clarify the composition of the dendritic crystals, which most likely suffered from an error or contamination in measurement. Unfortunately, the beads as well as the material just on the edge of the film showed no Raman signal besides the Si background peak, most likely indicating either that the structure is amorphous or simply not large enough for proper scattering to occur.

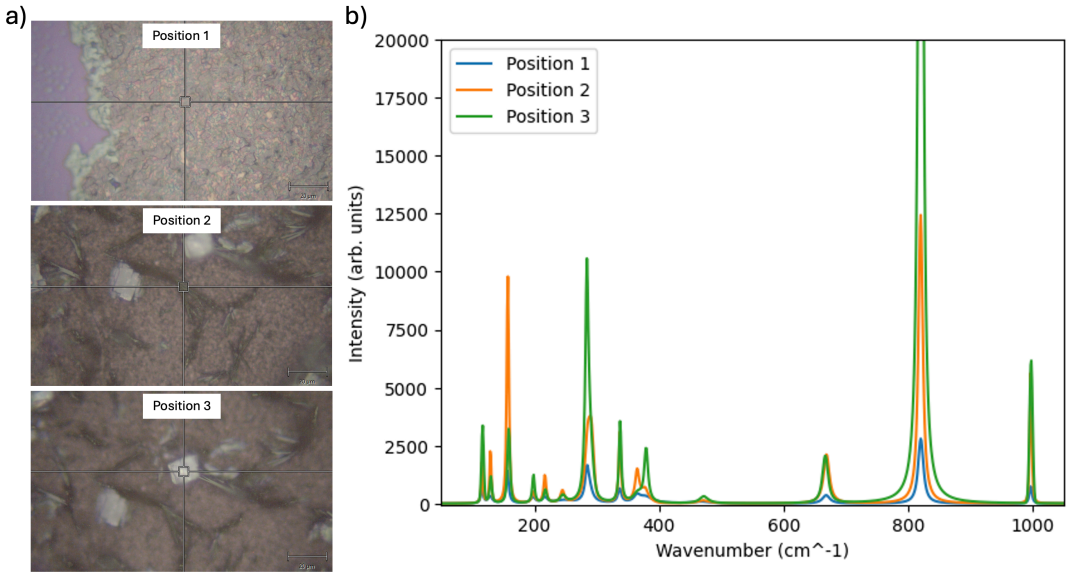


Figure 5.28: a) OM images of positions used for Raman spectroscopy fitted and plotted in b) demonstrating the presence of MoO_3.

Furthermore, the surface grains identified as MoO_2 by EDX, also show correlation to this material's Raman modes as seen in literature [173], though not quite as strongly as seen in the previous crystals.

This slightly worse fit (seen in Figure 5.29 may be caused by the lower number of counts obtained from these measurements. However, by combining the results from both characterization methods, it can be concluded that the material is most likely MoO_2.

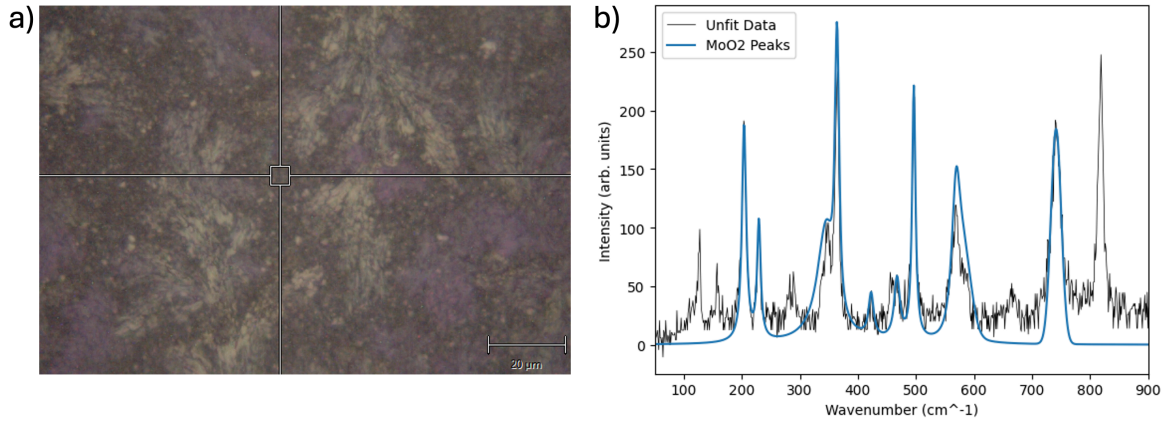


Figure 5.29: a) OM image of the region in the center of a 35-minute two-step $MoSe_2$ attempted growth process. b) Raman spectrum of position in a) fitted for MoO_2.

Finally, a unique result was obtained from the crystals seen at EDX region 5. While these quite closely matched the stoichiometric ratio of MoO_3 elementally, their Raman spectra, at first glance, did not correlate with that found in the bulk of the literature. Deeper research, though, led to the discovery that the three highest wave number peaks match those of the monoclinic phase of MoO_3 [171]. However, the peaks located at lower wave numbers (which represent the bending, deformation, and lattice modes) do not match either phase of MoO_3 [171]. This most likely indicates a mixed-phase, though further characterization steps would be needed to verify this, which are outside the scope of this thesis.

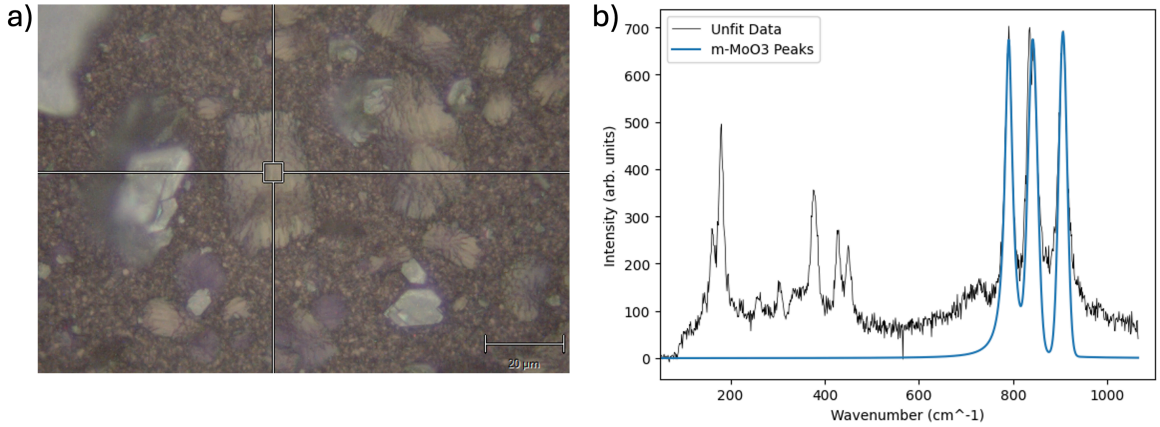


Figure 5.30: a) OM image of the region in the center of a 35-minute two-step $MoSe_2$ attempted growth process. b) Raman spectrum of position in a) fitted for peaks at 776 cm^{-1}, 848 cm^{-1}, and 905 cm^{-1} corresponding to monoclinic MoO_3 [171].

Utilizing all of the information gained via the two-step growth experiments, a picture of the growth mechanisms taking place can begin to be put together. While it is clear from the characterization that synthesis of $MoSe_2$, vertical or otherwise, was not achieved, the transition from pure Mo to MoO_X was observed. The three different reaction times, combined with the apparent edge favored heat distribution, help elucidate the over time transformation of the 1 µm Mo film. In the center of the substrate (Figure 5.26), it can be seen what is likely the first transformation to occur, grain growth of the Mo under high-temperature annealing and oxidation to MoO_2 [174]. This is the prime stage where the $MoSe_2$ synthesis reaction should occur, as has been seen in vertical MoS_2 growths previously [156]. However, this does not occur under the conditions of this experiment and, thus, further oxidation begins. Most clearly seen in Figure 5.25, MoO_3 crystals nucleate and, as further time is spent at high temperature,

grow in size. These dark crystals possess at least a partial phase of monoclinic MoO_3, which could be the result of their development from MoO_2, which is also a monoclinic crystal.

This process occurs across the whole substrate; however, the edges seem to experience all stages first. As evidenced by the 20-minute sample, these monoclinic crystals transition into fully orthorhombic MoO_3 and grow large enough to join together into a continuous layer (seen in the left column of Figure 5.23). At the same time, thin-layered needle-like crystals nucleate between the grain boundaries of the larger MoO_3. These layered crystals are visually reminiscent of α-MoO_3 [175], which is a topic further explored in Chapter 6. Longer time spent at 700ºC additionally seems to encourage the development of the dendritic MoO_3 crystals seen in the right column of Figure 5.23, which are not present on the 20-minute sample. The final stage of the film is a transition of the orthorhombic MoO_3 to amorphous MoO_X before complete evaporation (shown in Figure 5.22). This description of the full oxidation process is summarized as a diagram in Figure 5.31.

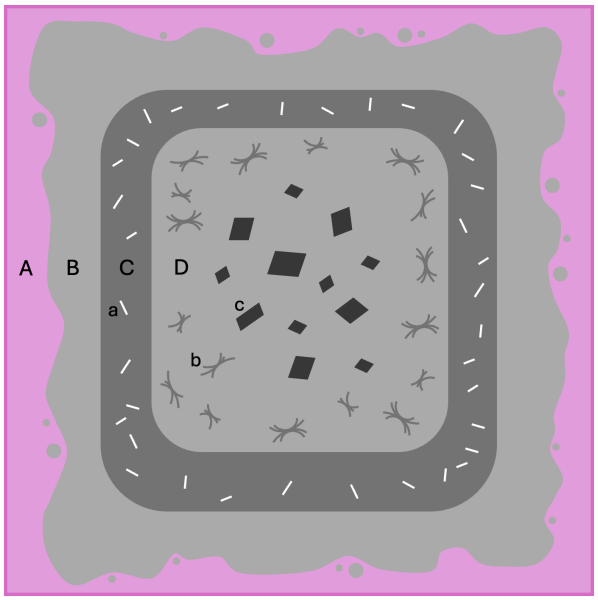


Figure 5.31: Diagram of the various morphologies on the two-step growth substrates after CVD processing. A: SiO2 with Mo-O droplets, B: MoO_3 amorphous layer, C: MoO_3, D: MoO2, a: MoO_3 nanowires, b: MoO_3, c: m-MoO_3. Diagram not to scale.

These phase assignments explain the observed morphologies and inform the following analysis of oxidation pathways and the rationale behind growth failure.

5.4. Discussion of Oxidation States and Failure of Growth

The combined structural and compositional analyses provide a coherent picture of the chemical pathways governing these CVD experiments. In all configurations, vapor-phase, NaCl-assisted, and two-step growth, the Mo precursor was found to undergo progressive oxidation rather than selenization. This indicates that, under the available furnace conditions, the kinetics of Mo oxidation and the volatility of Se favor the formation of Mo-O phases instead of Mo-Se compounds.

In the vapor-phase experiments, the results confirm that MoO_3 effectively vaporizes and reaches the substrate even in the absence of NaCl. However, unlike S in Chapter 4, the low reactivity of Se prevents it from reacting with Mo to form $MoSe_2$ under otherwise comparable conditions (apart from higher chalcogen-zone temperature). Variations in reaction time, Ar carrier-gas flow rate, Se temperature, and substrate orientation did not produce a significant change in the substrate. Upon the addition of NaCl to the MoO_3 precursor, a noticeable increase in the amount of Mo present on the substrate was observed; however, $MoSe_2$ growth was still not achieved. EDX analysis supported the mechanism described in the literature of Na-Mo compounds forming and coalescing on the surface, but the lower boiling point of these materials did not have the effect of increasing the reaction rate of the Se with Mo.

Finally, regarding the two-step Mo-film-based experiments without NaCl assistance, rather than see-

ing a conversion of the seed layer to $MoSe_2$ as is expected from the literature, the films underwent significant oxidation and, eventually, evaporation. While reduction of MoO_3 to MoO_{3-x} is an important pathway in vapor-phase $MoSe_2$ growth [101], Mo-film-based growths seen in literature wish to avoid oxidation in favor of direct Mo-S reaction employing oxygen-free environments during synthesis [156]. Since the precautions for gas isolation described in Section 3.2.1 were employed throughout the experiments, it raises the question of where the oxygen in this system is coming from. The SiO_2 substrate used should not decompose and release significant amounts of oxygen below 800ºC [176]. This was also previously verified in the CVD system used in this thesis [156]. Thus, it is possible that there is some amount of oxygen from the air leaking into the system. If this is the case, it could be the result of either backflow or inflow failures somewhere in the gas line system. To rule this out or fix the issue, experiments should be done to test for unwanted oxygen contamination. Additionally, the use of the double-tube in these experiments inherently leads to more potential failure points in the system, creates controlling the gas flow less precise due to the doubling of the flow needed, and reduces certainty in the evenness of sample and precursor heating. It would be desirable to repeat the experiments reported in this chapter in a furnace set-up more similar to that used in Chapter 4.

6

Self-Assembled α-MoO_3 Nanobelts: A Byproduct of $MoSe_2$ CVD

During the period of attempted $MoSe_2$ CVD syntheses, the quartz double tube developed a noticeable pattern of material build-up on its inner walls (pictured in Figure 6.1). Although initially regarded as residue from the repeated growth trials, close inspection revealed that these deposits possessed distinct crystalline morphologies, including elongated belt-like structures.

The aggregation of chalcogen, previously S and here Se, is expected due to the large amounts of precursor being used and the temperature gradient that exists outside of the heated zones. When unreacted Se vapor reaches cooler regions of the tube, it condenses on the inner walls, leaving behind a dark layer with the characteristic inky color of the bulk crystal. However, unlike in the case of the tube used for MoS_2 synthesis, a secondary white layer also developed inside the tube. This layer is observed in regions closer to the growth zone, correlating to places with higher temperature than where the Se is seen, but not heated to as high as Z2. Due to its location and white coloration, it is hypothesized to be MoO_3. Its appearance here and not in the MoS_2 tube can be at least partially explained by the failure of the Mo/Se reaction and its increased vaporization due to the NaCl promoter. However, these thin coatings were not the only material found growing inside the tube.

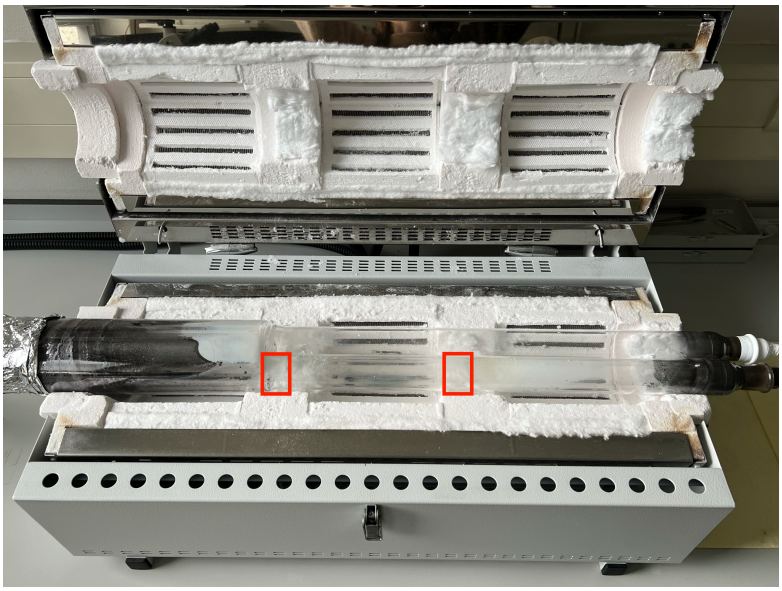


Figure 6.1: Photo of quartz double tube used for $MoSe_2$ synthesis attempts after experiments were finished. The dark material inside the tube on the far left and right is Se.

6.1. Synthesis of Unidentified Crystals

After several attempted CVD growths using MoO_3 with NaCl, filamentary crystals were found to be growing on the inner surface of the quartz tube in the areas between the heating zones, in Figure 6.1. These structures, pictured in Figure 6.2a, were visually unlike the molybdenum oxides often seen in MoS_2 and $MoSe_2$ CVD studies [12, 122, 126], or those seen in Chapter 5. The crystal growths appear to be partially translucent and highly rectangular by eye, though their sizes varied widely, with observed lengths ranging from 10 µm to multiple millimeters and widths from 100 µm down to only 50 nm. Due to the fact that the synthesis process is isolated from air and the only precursors used are MoO_3, Se, and NaCl, it is probable to believe that the crystals are some combination of these elements. One study, by Yadav et al. [177], grew visually similar crystals in their study also along the inner wall of a quartz tube, and identified them as $MoSe_2$. However, due to the lack of similar structures elsewhere in the CVD literature and their lack of dark $MoSe_2$ coloration, characterization methods should be used to identify the material.

A notable feature of the smaller crystals under optical imaging is the stark variations in contrast, which are separated by straight lines. This is highlighted in Figure 6.2a, which shows an example of a crystal with two distinct color sections.

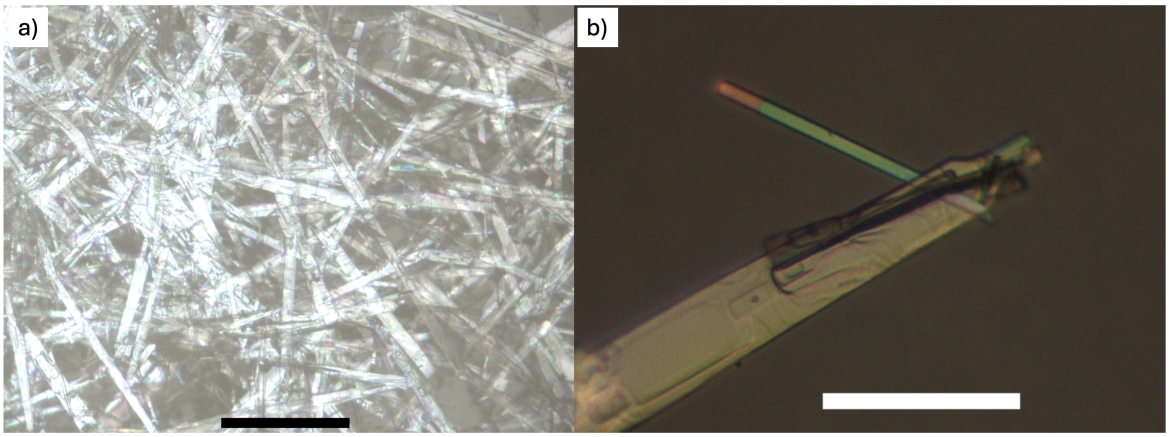


Figure 6.2: Optical microscopy image of a) the pile of crystals extracted from the CVD furnace. Scale bar 300 µm b) Crystalline material with a clear difference in optical contrast marked by color change. Scale bar 50 µm

These contrast variations are directly related to the material's thickness and are often used to estimate thickness in transparent thin materials like epoxy resins [178] or 2D materials like graphene, hBN, and TMDs [179, 180, 181] via a technique known as optical contrast spectroscopy. The method is based on the Fresnel equations, which describe the reflection and transmission of light at the boundaries of two media [182]. When incident light reaches the boundary between air and the thin material, part of the wave is reflected at the same angle as incidence, while the remainder propagates through the material with a refracted path due to the change in refractive index. Upon reaching the opposite interface, a portion of this refracted wave is again reflected at the second interface. The two reflected light waves will, thus, experience a phase shift from one another due to the extra distance traveled by the initially refracted light. This path length is defined by the equation [182]:

$$\Delta L = 2nd\cos\theta \tag{6.1}$$

where n is the index of refraction of the material and d is the thickness of the film. If λ is the initial wavelength of the light in air, then the values of this path length difference that will lead to either constructive or destructive interference are $m\lambda$ and $(m+\frac{1}{2})\lambda$, respectively. So, the thickness of the sample in these cases can be solved for as

$$d_c = \frac{m\lambda}{2n\cos\theta} \tag{6.2}$$

$$d_d = \frac{(m + \frac{1}{2})\lambda}{2n \cos\theta} \tag{6.3}$$

This relationship allows the interference wavelengths to be derived for a given film thickness and angle of incidence. While the refractive index of the material is not yet known, it is well documented that for materials whose index of refraction is close to 1.5 (that of glass, certain plastics, and some transparent crystals), a well-defined color spectrum emerges seen in Figure 6.3 [178, 182]. The colors in this chart, used for determining thickness in microtomed samples, resemble those seen in the smallest of the filamentary flakes (Figure 6.2b). From the contrast in this image, the orange region at the tip of the needle-like structure appears thinner than the adjacent green region. Furthermore, the abrupt color transition suggests a sudden change in thickness, providing initial evidence that the crystals possess a layered morphology.

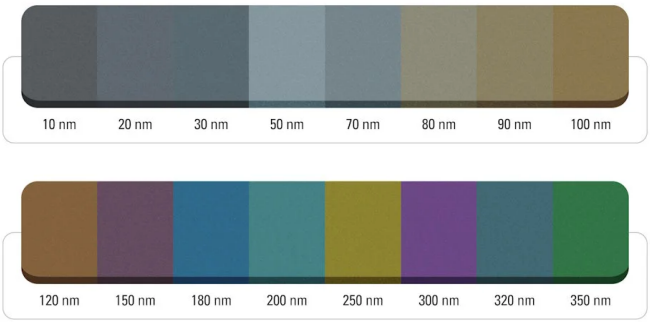


Figure 6.3: Guideline for the determination of thickness based on interference color of thin materials with n ≈ 1.5 [178].

6.2. Determination of Chemical Composition and Characterization

To understand the elemental composition of the synthesized crystals and characterize their structure, some of the flakes were transferred onto a copper and holey carbon TEM grid. This was done by manually placing a small amount of the crystals on a clean glass slide with forceps and subsequently gently sliding the grid against the glass slide. The adhesion forces naturally lead to the smallest and thinnest specimens becoming stuck to the grid. The thin growths were examined with both STEM and HR-TEM. The crystals were found to be highly elongated. For the specimen shown in Figure 6.4, the length to width ratio is 54 (18.9 µm by 350 nm). By imaging at a higher resolution, displayed in Figure 6.4b, the layered structure of the crystal becomes clear. At near-atomic resolution achieved by HR-TEM, it can be seen that the thinnest regions at the edge of the specimen can be as thin as just a few atomic layers. Thus, while the morphology may not match any TMD, a bulk-vdW material seems to have been grown. It can also be said from these observations that the structures are not symmetrical radially as a nanowire would be, and are thus better described as ”nanobelts.”

To determine the composition of the unknown material, TEM-based EDX spectroscopy was performed at various locations across multiple specimens that were present on the grid. This showed an elemental composition of $\sim$25% Mo and $\sim$75% of O, with trace amounts of Cu, C, and K. This confirms that no Se is present in the structures and they are most likely a phase of MoO_3. Although these measured structures appear visually distinct from the MoO_3 crystals seen throughout this work, the orthorhombic phase known as α-MoO_3 is a well-known stable layered vdW oxide and the thermodynamically most stable form of molybdenum oxide [183].

Furthermore, two types of crystal diffraction were carried out on the specimens. For the individual nanobelts observed via TEM, a selected area diffraction (SAD) pattern was obtained from the fast Fourier transform (FFT) of an atomic resolution HR-TEM image filtered for noise from the grid (Figure 6.5). The spot pattern shows agreement with the rectangular shape expected from a molybdenum oxide known as α-MoO_3 taken with a zone axis of [011]. Using simulated diffraction software and tables, the pattern was indexed as seen in Figure 6.5b. Using averaged line intensity profiles over the HR-TEM

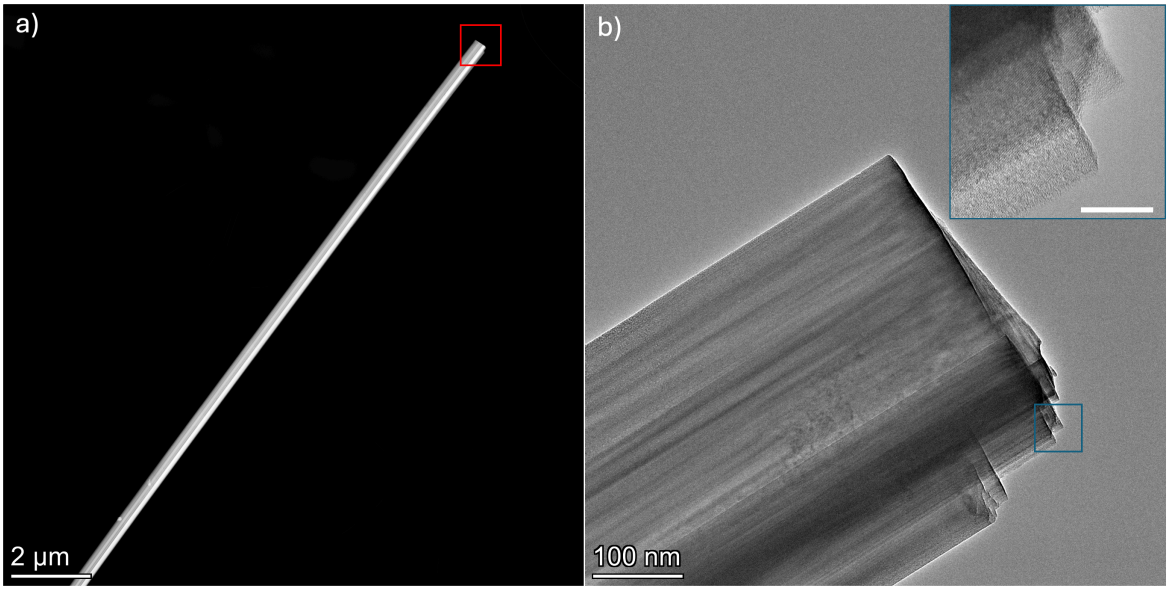


Figure 6.4: a) STEM image of thin nanobelt b) TEM image of area highlighted in red, inset: HR-TEM image of region highlighted in blue, scale bar 20 nm.

image, the distance between the planes was measured as 0.39 nm and 0.37 nm, which correlates very well with the α-MoO_3 reference and allows for the labeling of the axes on the image [184]. If one looks closely at Figure 6.5a, it is also possible to notice that while the crystal lattice is of very high quality in the [001] direction, there are some noticeable edge dislocations in the planes parallel to [100]. This is hard to discern with great accuracy at this scale, though, and it should be noted that the FFT diffraction pattern is still very strong, indicating a well-formed lattice.

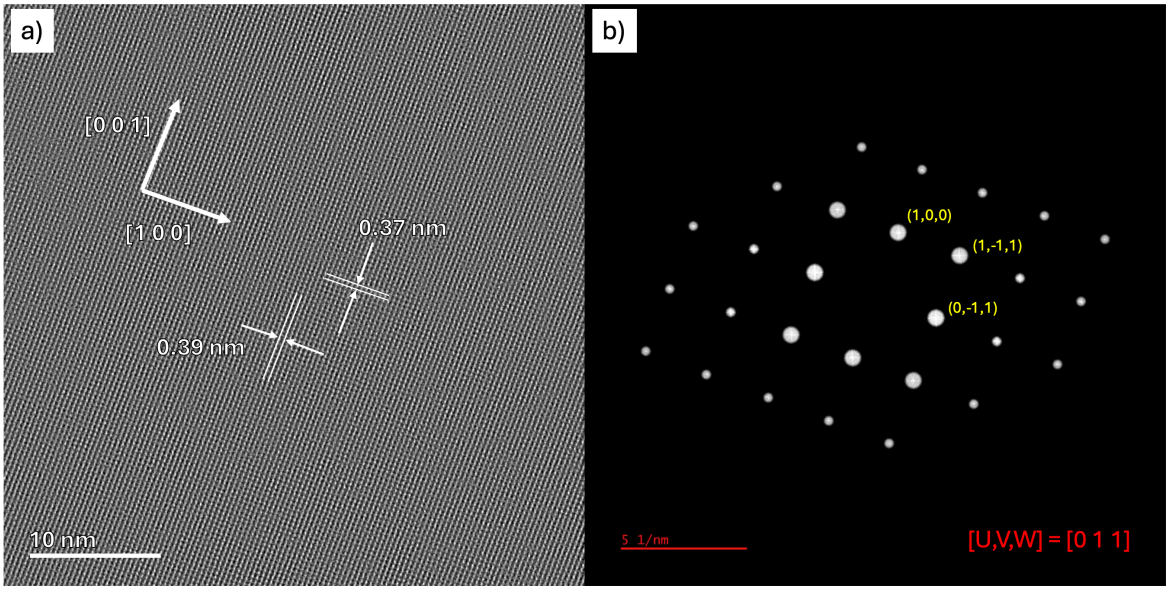


Figure 6.5: a) Filtered HR-TEM image showing the crystal planes and their distances. b) Filtered selected area diffraction pattern with identified zone axis [011].

In addition to the SAD data obtained via TEM, an X-ray diffraction (XRD) measurement was performed on a Si substrate coated with a dense layer of bulk crystals. The resulting spectrum, displayed in Figure 6.6, exhibits strong diffraction peaks at $2\alpha = 12.75°$, 25.68°, and 38.94° which correlate to the (020), (040), and (060) planes in the JCPDS card no. 05-0508 for α-MoO_3 [183]. Other peaks that are present in the powder diffraction for this material are $2\alpha = 23.7°$ and 27.2° which represent the

(110) and (021) planes, respectively. These peaks are not seen in the XRD, most likely due to the fact that the sample was not a uniformly distributed powder and that the crystals are highly anisotropic. In this case, only the planes parallel to (010) showed a strong signal. However, these peaks are sharp, indicating high-quality crystals.

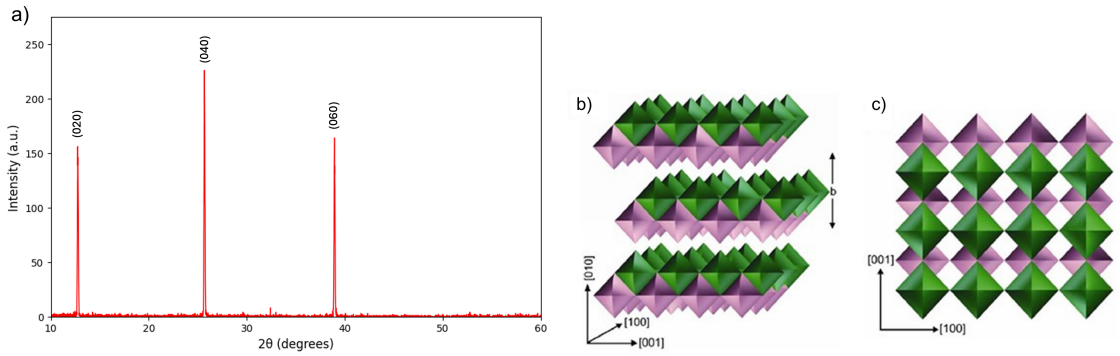


Figure 6.6: a) XRD pattern of the bulk crystal sample. b) Diagram of α-MoO_3 crystal structure as viewed perpendicular to the vdW layers and b) from above a single layer [183].

Looking at the crystal structure of α-MoO_3 (Figure 6.6b & c), which consists of edge- and corner-sharing MoO_6 octahedra, it can be seen that these planes are parallel to the vdW layers and, recalling the TEM images, are the vast majority of surface area. Overall, the characterization methods of EDX, TEM-SAD, and XRD demonstrate with high confidence that α-MoO_3 has been grown on the quartz surface of the CVD.

6.3. Electronic Properties of α-MoO_3 Nanobelts

The final experiment conducted with the sample was measurement via electron energy loss spectroscopy (EELS). EELS is a technique unique to (S)TEM that works by mapping the energy-loss distribution of electrons that have passed through the sample material, creating spectra of the amount of electrons detected with certain energy loss values [105]. EELS is a powerful technique for probing both structural and electronic properties of materials. In particular, it is possible to calculate the bandgap from the low-loss EELS region [185].

To begin, the EELS spectrum taken from the region highlighted in Figure 6.7a was plotted against a high-quality α-MoO_3 reference spectrum (Figure 6.7b) [186]. As can be seen from the low-loss region (<22 eV), the CVD flake sample has very good agreement with the reference in regards to feature location at 7 eV and 12.5 eV. These low-loss features are strongly tied to crystal structure and interband electron transitions, providing even more conclusive evidence for the characterization of the CVD-grown structures [186].

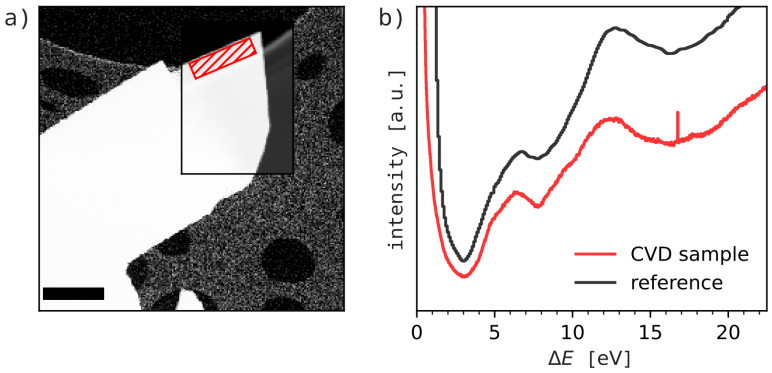


Figure 6.7: a) TEM image of α-MoO_3 sample with red shaded box indicating region of EELS acquisition. b) EELS spectrum with α-MoO_3 reference from [186].

Knowing concretely that the material is α-MoO_3, the EELS data can additionally be used to calculate

a few other interesting properties. Utilizing the methodology described in Iakoubovskii et al. [187], the thickness of the sample observed was found to be 23.61 nm. This indicates a crystal with around 17 vdW layers, as the lattice parameter in the [010] direction is 1.386 nm. It also confirms that the assessment of the structures as nanobelts is indeed a good descriptor of their morphology since their thickness is significantly smaller than their width.

Finally, the low-loss EELS region contains information about the electronic bandgap of the material; however, the zero-loss-peak (ZLP) interferes with the extraction of this data. The ZLP can be subtracted via means that are outside the scope of this thesis, and the bandgap fitted. The result for the data gathered for the CVD grown α-MoO_3 samples is in the range of 3.4 - 3.8 eV. This is a somewhat reasonable value compared to that found in the literature of 3.2 eV [188], given that the fitting used has a wide confidence interval and the relatively thick nature of the sample. Generally, α-MoO_3 is considered a wide bandgap n-type semiconductor. This makes it highly interesting for applications in optoelectronics, specifically in contexts where 2D materials would be useful (flexibility, tunability, etc.) but where a slightly higher bandgap than in materials like TMDs is desired [189]. Due to its layer structure, α-MoO_3 has also been widely studied for its potential use as both a cathode and an anode material in lithium-ion batteries [190, 191]. This is especially true in recent years for nanostructure morphologies, which have increased contact area between the electrode and electrolyte, improved strain relaxation, and efficient 1D electron transport pathways [190]. Beyond this, however, α-MoO_3 in unique nanoscale morphologies are a promising direction in the applications of gas sensing, photodetectors, solar cells, and many others [192].

6.4. Discussion

As an unexpected result of the CVD methodology used for $MoSe_2$ synthesis attempts, the growth of high-quality α-MoO_3 crystals which nucleated on the inner wall of the quartz tube is still an intriguing avenue of study. While α-MoO_3 belts have been synthesized via CVD before [193], these techniques are mostly used to produce morphologies similar to those seen in Figure 5.11, with dome-like shapes attached directly to the substrate [194]. By far the most common method for the nanobelt morphology is that of hydrothermal synthesis, which includes dispersing a precursor chemical like peroxomolybdic acid or molybdenyl acetylacetonate in a solvent and placing it in an autoclave at around 200ºC for at least 24 hours [190, 191]. While these methods produce much more uniform nanoscale products than those found in the CVD, there is a high chance of contamination from the solvent, and cleaning procedures must be used. Beyond this, isolating single nanobelts is much more difficult with these techniques, whereas the α-MoO_3 grown in this project were easily isolated via mechanical methods.

Due to the nature of their unplanned synthesis, some hypotheses must be made regarding the synthesis pathway that has led to the growth of the α-MoO_3 crystals. One reasoning behind why this has not been seen previously, over the large number of MoS_2 growths carried out in the same CVD furnace, is the lack of NaCl promoter. Na_2MoO_4 has been used as a precursor along with HCl in hydrothermal reactions to form nanoribbons [195]; however, NaCl on itself has only been used as a capping agent in these reactions in combination with other solvents [196]. Jung et al. [193] were able to produce high-quality α-MoO_3 nanobelts in CVD from MoO_3 powder without the assistance of any promoter, but a temperature of 900ºC was required. In the case of this project, the addition of NaCl and the increased vaporization of Na_2MoO_4 may be the reason this reaction was seen at a significantly lower temperature. Furthermore, the development of α-MoO_3 in this manner is often observed as a vapor-solid growth, which consists of sublimation of solid MoO_3 and its subsequent recrystallization [193]. This mechanism could explain why significant growth occurred only over the course of multiple CVD runs. The polycrystalline white coating on the inner tube is potentially the initial source of recrystallization into the high-quality belts that were characterized.

However, to truly gain insight into the formation mechanism of these crystals, controlled studies should be done on the growth conditions used to produce them. These include assessing the effect of removing Se powder, changing the NaCl:MoO_3 ratio, and attempting to isolate the nucleation phase by using individual quartz substrates. While methods used to produce crystals in this thesis are not practical for use in larger-scale study of α-MoO_3, the potential for NaCl to be used as an enhancing agent for current CVD-based growth strategies without significant contamination is a worthwhile path for research in this domain.

7

Conclusion and Outlook

This thesis explored the synthesis, transformation, and structural control of TMDs, with a focus on understanding how fabrication conditions influence their resulting morphologies and potential for nanoscroll formation. Through the optimization of MoS_2 CVD growth, it was demonstrated that the synchronization of temperature ramps between precursor zones has a decisive effect on flake uniformity and size. By allowing both zones to reach their set points simultaneously, more control was gained over the time spent at peak temperature conditions, and overshooting of sulfur temperature was reduced drastically. As a result, growth conditions favored the formation of smaller, mono/bilayer triangular flakes with improved uniformity across the substrate. These were in contrast to the multilayered, star-shaped structures obtained via the original unsynchronized ramping method. Subsequent scrolling experiments confirmed that these more uniform flakes yield tighter and more controlled nanoscrolls, validating the hypothesis that flake morphology directly governs scrolling behavior. However, the findings also revealed the crucial role of substrate adhesion on scrolling yield. In the case of the original flakes, high adhesion resulted in many unformed and half-formed scrolls, but the optimized flakes suffered the opposite issue. Too little adhesion to the substrate caused nearly 100% of the flakes to wash away and become destroyed during the scrolling process, highlighting that optimal scroll formation requires balancing flake size, shape, and adhesion strength to achieve high yields and structural integrity. Future work in this regard should focus on adjusting parameters to increase flake size without affecting the highly triangular and smooth-edged morphology. One avenue to take in this regard would be to increase the reaction time of the synced ramp procedure, ideally maintaining the relative amounts of Mo and S in the growth zone, but for a longer period. Alternatively, different scrolling procedures could be explored, e.g., altering the solvent used to increase intercalation. Whichever path is taken, after obtaining a recipe for scrolls with much higher and consistent yields, further experiments should be done to probe the properties of these scrolls, such as strain, bandgap, and possibly evidence of polarization.

The exploration of $MoSe_2$ growth via CVD emphasized the challenges inherent to extending sulfur-based synthesis methodologies to selenium systems. Despite multiple approaches including direct vapor phase synthesis, NaCl-assisted reactions, and a two-step process using pre-deposited Mo film, $MoSe_2$ growth was not achieved. The results, however, still provide valuable insight into the reaction mechanisms taking place under the hydrogen-free conditions. The detection of Mo particles on the substrate indicated that the precursor was successfully reaching the substrate, but the apparent low reactivity of selenium prevented chalcogenization. This result remained through the adjustment of selenization temperature, reaction time, carrier gas flow rate, and substrate positioning. EDX characterization confirmed that Se was not adhering to the substrate in any detectable quantities, ruling out the possibility of other solid products or Mo-O-Se compounds forming. The addition of NaCl as a promoter increased Mo deposition on the substrate, likely through the formation of volatile Na–Mo species. This provided more nucleation sites for $MoSe_2$ growth, but did not result in any observable synthesis. These findings underscore the difficulty of hydrogen-free $MoSe_2$ APCVD growth and draw attention to the potential differences in this study over those in the literature who have found success. The main differences observed are the reported high ramping rates, which are not possible in the system used

in this thesis. This is theoretically the most impactful for high-temperature selenization runs, where, if ramping is slow, the Se supply may be depleted by the time the growth temperature is reached. It is recommended that continued experiments to achieve $MoSe_2$ growth in this system should attempt intermediate temperature ranges for Se heating. Moreover, obtaining a small diameter, single tube and increasing insulation would help to create conditions for higher achievable growth temperatures (800ºC+), which could further encourage Se reaction.

Two-step attempted growth of vertical $MoSe_2$ flakes proved similarly ineffective as vapor phase, but gave rise to an insightful study of the oxidation states of Mo in high temperature conditions. Using trials performed over a range of dwell times, a "map" of MoO_X phases was developed. This section of experimentation is a unique visual exploration into oxidation and recrystallization pathways of Mo, highlighting the versatility of the material, which produced many different micro- and nanoscale structures within close proximity to one another. While this result was not an explicit goal of the thesis, it nevertheless provides a wealth of information for continued work on growing $MoSe_2$ flakes. For example, it seems from the observed trends that the Mo oxidation reaction is dominant over the $MoSe_2$ synthesis reaction in the conditions tested, highlighting the need to control and limit unfavorable pathways. One should consider performing the same growth procedure with a Mo film deposited over a pure Si substrate and assessing if any differences in oxidation occur.

Unexpectedly, the unsuccessful $MoSe_2$ synthesis experiments led to the discovery of α-MoO_3 nanobelts forming on the inner wall of the quartz tube. These crystals, produced unintentionally under CVD conditions with NaCl present, exhibited high structural quality and were easily isolated, offering a new and efficient route for free-standing α-MoO_3 nanobelt growth. The evidence suggests that NaCl may have facilitated the sublimation and recrystallization of MoO_3 at lower temperatures, indicating a vapor-solid mechanism distinct from traditional high-temperature or hydrothermal methods. This serendipitous finding not only broadens the understanding of molybdenum oxide chemistry in CVD systems but also reveals a promising direction for producing clean, high-aspect-ratio nanostructures without solvent contamination.

It is also important to recognize the limitations and possible shortcomings of the work presented in this thesis. Two of the largest uncontrolled factors in the experiments are the relative time the SiO_2 substrates spent outside of a clean room environment and/or in vacuum isolation since cleaning was performed and the general presence of environmental contamination. While the literature does not report on the effect small amounts of dust and debris have on MoS_2 and $MoSe_2$ growth, it is possible that this could have affected the results presented here. This is particularly noticeable in the original MoS_2 growths, which had inconsistencies in their flake-substrate adhesion. Additionally, the precursors used for the $MoSe_2$ experiments presented in Chapter 5 were not freshly purchased for this project and were of unknown age and history. Although no clear signs of contamination appeared throughout the investigation, it would be recommended for future work to acquire new Se and NaCl powders of quality in line with that reported in the literature.

Continuing the discussion of possible contamination, the presence of oxygen inside the CVD furnace is a concern that should be addressed in any future work done with the system. It is clear from both the work of this thesis and previous projects in the same lab that the reactivity of S is such that any undesired oxygen is not a hindrance to the successful formation of MoS_2. However, the two-step $MoSe_2$ growth attempts show significant oxidation without it being an elemental component of any precursor used. This is an indication of one or more isolation steps failing. It is crucial that controlled tests be carried out to determine the cause of unwanted oxidation before more $MoSe_2$ synthesis attempts are made.

Finally, as with any experiment, human error must be acknowledged, especially with regard to how it affects the CVD parameters reported throughout the work. These include differences in precursor masses up to 5% and small timing mistakes in the heating procedure. Precautions were taken throughout the project to ensure accuracy and consistency wherever possible.

Overall, this work undoubtedly fulfills the first goal it set out to achieve of gaining insights into the relationship between CVD-grown 2D morphologies of TMD flakes and their resulting scrolled nanostructure. Regarding the second goal of the thesis, while success was not found in developing a non-hydrogen-based synthesis technique of $MoSe_2$ flakes for heterostructure nanoscrolling, important information

was gained for future researchers who may wish to continue developing a recipe in the same furnace. With many avenues for continued study in any of the three main areas of experimentation reported, MoS_2 scroll optimization, $MoSe_2$ synthesis, and molybdenum oxide structures, this work has found unique crossroads of 2D nanoscale fabrication.

References

[1] Maarten Bolhuis. “Exploring van der Waals Materials From Nanofabrication to Strain Mapping using Transmission Electron Microscopy”. PhD thesis. Delft University of Technology, 2025. URL: https://doi.org/10.4233/uuid:35d1c57b-8f79-4e37-85e4-65bf95f471c4.

[2] K. S. Novoselov et al. “Electric Field Effect in Atomically Thin Carbon Films”. In: *Science* 306.5696 (Oct. 2004), pp. 666–669. DOI: 10.1126/science.1102896. URL: https://www.science.org/doi/10.1126/science.1102896 (visited on 09/15/2025).

[3] Robert W Keyes. “Physical limits of silicon transistors and circuits”. en. In: *Reports on Progress in Physics* 68.12 (Sept. 2005), p. 2701. ISSN: 0034-4885. DOI: 10.1088/0034-4885/68/12/R01. URL: https://dx.doi.org/10.1088/0034-4885/68/12/R01 (visited on 04/14/2025).

[4] Wafer World Inc. *Band Gap in Semiconductors: All You Need to Know*. en. URL: https://www.waferworld.com/post/band-gap-in-semiconductors-all-you-need-to-know (visited on 10/08/2025).

[5] Sajedeh Manzeli et al. “2D transition metal dichalcogenides”. en. In: *Nature Reviews Materials* 2.8 (June 2017), pp. 1–15. ISSN: 2058-8437. DOI: 10.1038/natrevmats.2017.33. URL: https://www.nature.com/articles/natrevmats201733 (visited on 02/07/2025).

[6] Leo J. McGilly et al. “Visualization of moiré superlattices”. en. In: *Nature Nanotechnology* 15.7 (July 2020), pp. 580–584. ISSN: 1748-3395. DOI: 10.1038/s41565-020-0708-3. URL: https://www.nature.com/articles/s41565-020-0708-3 (visited on 04/22/2025).

[7] Sabrya E. van Heijst et al. “Heterostrain-Driven Bandgap Increase in Twisted WS2: A Nanoscale Study”. en. In: *Advanced Functional Materials* 34.8 (2024), p. 2307893. ISSN: 1616-3028. DOI: 10.1002/adfm.202307893. URL: https://onlinelibrary.wiley.com/doi/abs/10.1002/adfm.202307893 (visited on 04/10/2025).

[8] Jeroen J.M. Sangers, Abel Brokkelkamp, and Sonia Conesa-Boj. “Strain-Induced Moiré Polarization Vortices in Twisted-Multilayer WSe2”. en. In: *Small* n/a.n/a (2025), p. 2503363. ISSN: 1613-6829. DOI: 10.1002/smll.202503363. URL: https://onlinelibrary.wiley.com/doi/abs/10.1002/smll.202503363 (visited on 08/20/2025).

[9] Jeonghyeon Na et al. “Indirect Band Gap in Scrolled MoS2 Monolayers”. en. In: *Nanomaterials* 12.19 (Jan. 2022), p. 3353. ISSN: 2079-4991. DOI: 10.3390/nano12193353. URL: https://www.mdpi.com/2079-4991/12/19/3353 (visited on 09/03/2025).

[10] Daniel Bennett and Benjamin Remez. “On electrically tunable stacking domains and ferroelectricity in moiré superlattices”. en. In: *npj 2D Materials and Applications* 6.1 (Jan. 2022), p. 7. ISSN: 2397-7132. DOI: 10.1038/s41699-021-00281-6. URL: https://www.nature.com/articles/s41699-021-00281-6 (visited on 08/26/2025).

[11] Songzhan Li et al. “Heterojunction engineering of MoSe2/MoS2 with electronic modulation towards synergetic hydrogen evolution reaction and supercapacitance performance”. In: *Chemical Engineering Journal* 359 (Mar. 2019), pp. 1419–1426. ISSN: 1385-8947. DOI: 10.1016/j.cej.2018.11.036. URL: https://www.sciencedirect.com/science/article/pii/S1385894718322708 (visited on 04/30/2025).

[12] Yajuan Zhao et al. “NaCl-assisted chemical vapor deposition growth of MoSe2 and MoSe2/h-BN heterostructure”. In: *Vacuum* 224 (June 2024), p. 113182. ISSN: 0042-207X. DOI: 10.1016/j.vacuum.2024.113182. URL: https://www.sciencedirect.com/science/article/pii/S0042207X24002288 (visited on 01/21/2025).

[13] Department of Materials Science and Engineering. *2D Materials*. URL: https://www.matse.psu.edu/2d-materials (visited on 01/14/2025).

[14] Penghong Ci et al. “Quantifying van der Waals Interactions in Layered Transition Metal Dichalcogenides from Pressure-Enhanced Valence Band Splitting”. In: *Nano Letters* 17.8 (Aug. 2017), pp. 4982–4988. ISSN: 1530-6984. DOI: 10.1021/acs.nanolett.7b02159. URL: https://doi.org/10.1021/acs.nanolett.7b02159 (visited on 02/03/2025).

[15] Akanksha R. Urade, Indranil Lahiri, and K. S. Suresh. “Graphene Properties, Synthesis and Applications: A Review”. en. In: *JOM* 75.3 (Mar. 2023), pp. 614–630. ISSN: 1543-1851. DOI: 10.1007/s11837-022-05505-8. URL: https://link.springer.com/article/10.1007/s11837-022-05505-8 (visited on 04/29/2025).

[16] Saju Joseph et al. “A review of the synthesis, properties, and applications of 2D transition metal dichalcogenides and their heterostructures”. In: *Materials Chemistry and Physics* 297 (Mar. 2023), p. 127332. ISSN: 0254-0584. DOI: 10.1016/j.matchemphys.2023.127332. URL: https://www.sciencedirect.com/science/article/pii/S0254058423000408 (visited on 04/14/2025).

[17] *Graphite - Structures - (CCEA) - GCSE Combined Science Revision - CCEA Double Award*. en-GB. URL: https://www.bbc.co.uk/bitesize/guides/z7h6kmn/revision/5 (visited on 07/16/2025).

[18] Hui Yan et al. “Synthesis of large-area monolayer and few-layer MoSe 2 continuous films by chemical vapor deposition without hydrogen assistance and formation mechanism”. en. In: *Nanoscale* 13.19 (2021), pp. 8922–8930. DOI: 10.1039/D1NR00552A. URL: https://pubs.rsc.org/en/content/articlelanding/2021/nr/d1nr00552a (visited on 01/21/2025).

[19] Shiv Dutta Lawaniya et al. “Functional nanomaterials in flexible gas sensors: recent progress and future prospects”. In: *Materials Today Chemistry* 29 (Apr. 2023), p. 101428. ISSN: 2468-5194. DOI: 10.1016/j.mtchem.2023.101428. URL: https://www.sciencedirect.com/science/article/pii/S2468519423000551 (visited on 02/03/2025).

[20] Manish Chhowalla et al. “The chemistry of two-dimensional layered transition metal dichalcogenide nanosheets”. en. In: *Nature Chemistry* 5.4 (Apr. 2013), pp. 263–275. ISSN: 1755-4349. DOI: 10.1038/nchem.1589. URL: https://www.nature.com/articles/nchem.1589 (visited on 04/16/2025).

[21] Yao Li et al. “Structural semiconductor-to-semimetal phase transition in two-dimensional materials induced by electrostatic gating”. en. In: *Nature Communications* 7.1 (Feb. 2016), p. 10671. ISSN: 2041-1723. DOI: 10.1038/ncomms10671. URL: https://www.nature.com/articles/ncomms10671 (visited on 04/29/2025).

[22] Intek Song, Chibeom Park, and Hee Cheul Choi. “Synthesis and properties of molybdenum disulphide: from bulk to atomic layers”. en. In: *RSC Advances* 5.10 (Dec. 2014), pp. 7495–7514. ISSN: 2046-2069. DOI: 10.1039/C4RA11852A. URL: https://pubs.rsc.org/en/content/articlelanding/2015/ra/c4ra11852a (visited on 04/10/2025).

[23] Xiaofeng Fan et al. “Modulation of electronic properties from stacking orders and spin-orbit coupling for 3R-type MoS2”. en. In: *Scientific Reports* 6.1 (Apr. 2016), p. 24140. ISSN: 2045-2322. DOI: 10.1038/srep24140. URL: https://www.nature.com/articles/srep24140 (visited on 04/11/2025).

[24] Maria S. Sokolikova and Cecilia Mattevi. “Direct synthesis of metastable phases of 2D transition metal dichalcogenides”. en. In: *Chemical Society Reviews* 49.12 (June 2020), pp. 3952–3980. ISSN: 1460-4744. DOI: 10.1039/D0CS00143K. URL: https://pubs.rsc.org/en/content/articlelanding/2020/cs/d0cs00143k (visited on 04/29/2025).

[25] Shangli Shi, Zhuxing Sun, and Yun Hang Hu. “Synthesis, stabilization and applications of 2-dimensional 1T metallic MoS2”. en. In: *Journal of Materials Chemistry A* 6.47 (Dec. 2018), pp. 23932–23977. ISSN: 2050-7496. DOI: 10.1039/C8TA08152B. URL: https://pubs.rsc.org/en/content/articlelanding/2018/ta/c8ta08152b (visited on 04/29/2025).

[26] *Molybdenite*. URL: https://www.mindat.org/min-2746.html (visited on 04/16/2025).

[27] Robert L Fusaro. *Lubrication and Failure Mechanisms of MolybdenumDisulfideFilms*. en. 1978. URL: https://ntrs.nasa.gov/api/citations/19790004988/downloads/19790004988.pdf.

[28] O Madelung, U Rössler, and M Schulz. “MoS2: crystal structure, physical properties”. In: *Landolt-Börnstein - Group III Condensed Matter 41D*. Springer Materials, 2000. URL: 10.1007/10681735_690.

[29] Megan Cowie et al. “How high is a MoSe2 monolayer?” en. In: *Nanotechnology* 33.12 (Dec. 2021), p. 125706. ISSN: 0957-4484. DOI: 10.1088/1361-6528/ac40bd. URL: https://dx.doi.org/10.1088/1361-6528/ac40bd (visited on 08/13/2025).

[30] Miao Jiang et al. “Synthesis of 1T-MoSe2 ultrathin nanosheets with an expanded interlayer spacing of 1.17 nm for efficient hydrogen evolution reaction”. en. In: *Journal of Materials Chemistry A* 4.39 (Oct. 2016), pp. 14949–14953. ISSN: 2050-7496. DOI: 10.1039/C6TA07020E. URL: https://pubs.rsc.org/en/content/articlelanding/2016/ta/c6ta07020e (visited on 08/13/2025).

[31] *Materials Data on MoSe2 by Materials Project*. English. Tech. rep. mp-1634. LBNL Materials Project; Lawrence Berkeley National Laboratory (LBNL), Berkeley, CA (United States), May 2020. DOI: 10.17188/1191826. URL: https://www.osti.gov/biblio/1191826 (visited on 08/13/2025).

[32] Saurav Sachin et al. “Twist-engineered tunability in vertical MoS2/MoSe2 heterostructure”. en. In: *Applied Physics A* 129.1 (Dec. 2022), p. 46. ISSN: 1432-0630. DOI: 10.1007/s00339-022-06282-6. URL: https://doi.org/10.1007/s00339-022-06282-6 (visited on 08/15/2025).

[33] Nan Zhang. “Electronic properties of MoS2/MoSe2 van der Waals heterostructures”. PhD. Toulouse, France: Toulouse University, 2020. URL: https://theses.hal.science/tel-03185900v2/file/2020NanZhang.pdf.

[34] Liping Ji et al. “Theoretical prediction of high electron mobility in multilayer MoS2 heterostructured with MoSe2”. In: *The Journal of Chemical Physics* 148.1 (Jan. 2018), p. 014704. ISSN: 0021-9606. DOI: 10.1063/1.4998672. URL: https://doi.org/10.1063/1.4998672 (visited on 07/17/2025).

[35] Asha Rani et al. “Electronic Characteristics of MoSe2 and MoTe2 for Nanoelectronic Applications”. In: *IEEE transactions on electron devices* 13 (2018). ISSN: 0018-9383. DOI: https://doi.org/10.1109/NMDC.2018.8605918. URL: https://www.ncbi.nlm.nih.gov/pmc/articles/PMC7673224/ (visited on 07/17/2025).

[36] Nasser Alidoust et al. “Observation of monolayer valence band spin-orbit effect and induced quantum well states in MoX2”. en. In: *Nature Communications* 5.1 (Aug. 2014), p. 4673. ISSN: 2041-1723. DOI: 10.1038/ncomms5673. URL: https://www.nature.com/articles/ncomms5673 (visited on 07/17/2025).

[37] Z. Y. Zhu, Y. C. Cheng, and U. Schwingenschlögl. “Giant spin-orbit-induced spin splitting in two-dimensional transition-metal dichalcogenide semiconductors”. In: *Physical Review B* 84.15 (Oct. 2011), p. 153402. DOI: 10.1103/PhysRevB.84.153402. URL: https://link.aps.org/doi/10.1103/PhysRevB.84.153402 (visited on 07/17/2025).

[38] Qing Hua Wang et al. “Electronics and optoelectronics of two-dimensional transition metal dichalcogenides”. en. In: *Nature Nanotechnology* 7.11 (Nov. 2012), pp. 699–712. ISSN: 1748-3395. DOI: 10.1038/nnano.2012.193. URL: https://www.nature.com/articles/nnano.2012.193 (visited on 07/17/2025).

[39] Rik V. Mom et al. “In situ observations of an active MoS2 model hydrodesulfurization catalyst”. en. In: *Nature Communications* 10.1 (June 2019), p. 2546. ISSN: 2041-1723. DOI: 10.1038/s41467-019-10526-0. URL: https://www.nature.com/articles/s41467-019-10526-0 (visited on 07/30/2025).

[40] Damien Voiry et al. “Conducting MoS2 Nanosheets as Catalysts for Hydrogen Evolution Reaction”. In: *Nano Letters* 13.12 (Dec. 2013), pp. 6222–6227. ISSN: 1530-6984. DOI: 10.1021/nl403661s. URL: https://doi.org/10.1021/nl403661s (visited on 07/30/2025).

[41] Long Zhang et al. “Twist-angle dependence of moiré excitons in WS2/MoSe2 heterobilayers”. en. In: *Nature Communications* 11.1 (Nov. 2020), p. 5888. ISSN: 2041-1723. DOI: 10.1038/s41467-020-19466-6. URL: https://www.nature.com/articles/s41467-020-19466-6 (visited on 04/23/2025).

[42] Ding-Rui Chen et al. “Edge-dominated hydrogen evolution reactions in ultra-narrow MoS2 nanoribbon arrays”. en. In: *Journal of Materials Chemistry A* 11.29 (July 2023), pp. 15802–15810. ISSN: 2050-7496. DOI: 10.1039/D3TA01573D. URL: https://pubs.rsc.org/en/content/articlelanding/2023/ta/d3ta01573d (visited on 07/30/2025).

[43] Habib Rostami, Reza Asgari, and Francisco Guinea. “Edge modes in zigzag and armchair ribbons of monolayer MoS2”. en. In: *Journal of Physics: Condensed Matter* 28.49 (Oct. 2016), p. 495001. ISSN: 0953-8984. DOI: 10.1088/0953-8984/28/49/495001. URL: https://dx.doi.org/10.1088/0953-8984/28/49/495001 (visited on 08/07/2025).

[44] Miguel Tinoco, Louis Maduro, and Sonia Conesa-Boj. “Metallic edge states in zig-zag vertically-oriented MoS2 nanowalls”. en. In: *Scientific Reports* 9.1 (Oct. 2019), p. 15602. ISSN: 2045-2322. DOI: 10.1038/s41598-019-52119-3. URL: https://www.nature.com/articles/s41598-019-52119-3 (visited on 08/06/2025).

[45] Miguel Tinoco et al. “Strain-Dependent Edge Structures in MoS2 Layers”. In: *Nano Letters* 17.11 (Nov. 2017), pp. 7021–7026. ISSN: 1530-6984. DOI: 10.1021/acs.nanolett.7b03627. URL: https://doi.org/10.1021/acs.nanolett.7b03627 (visited on 08/07/2025).

[46] Xihong Peng, Qun Wei, and Andrew Copple. “Strain-engineered direct-indirect band gap transition and its mechanism in two-dimensional phosphorene”. In: *Physical Review B* 90.8 (Aug. 2014), p. 085402. DOI: 10.1103/PhysRevB.90.085402. URL: https://link.aps.org/doi/10.1103/PhysRevB.90.085402 (visited on 08/07/2025).

[47] Jakob Kibsgaard et al. “Engineering the surface structure of MoS2 to preferentially expose active edge sites for electrocatalysis”. en. In: *Nature Materials* 11.11 (Nov. 2012), pp. 963–969. ISSN: 1476-4660. DOI: 10.1038/nmat3439. URL: https://www.nature.com/articles/nmat3439 (visited on 08/07/2025).

[48] Hui Pan and Yong-Wei Zhang. “Edge-dependent structural, electronic and magnetic properties of MoS2 nanoribbons”. en. In: *Journal of Materials Chemistry* 22.15 (Mar. 2012), pp. 7280–7290. ISSN: 1364-5501. DOI: 10.1039/C2JM15906F. URL: https://pubs.rsc.org/en/content/articlelanding/2012/jm/c2jm15906f (visited on 08/24/2025).

[49] Wei Fu et al. “Toward Edge Engineering of Two-Dimensional Layered Transition-Metal Dichalcogenides by Chemical Vapor Deposition”. In: *ACS Nano* 17.17 (Sept. 2023), pp. 16348–16368. ISSN: 1936-0851. DOI: 10.1021/acsnano.3c04581. URL: https://doi.org/10.1021/acsnano.3c04581 (visited on 08/24/2025).

[50] Yeonjoon Jung et al. “Recent Progresses in the Growth of Two-dimensional Transition Metal Dichalcogenides”. English. In: *Journal of the Korean Ceramic Society* 56.1 (Jan. 2019), pp. 24–36. ISSN: 1229-7801, 2234-0491. DOI: 10.4191/kcers.2019.56.1.12. URL: http://jkcs.or.kr/journal/view.php?doi=10.4191/kcers.2019.56.1.12 (visited on 08/23/2025).

[51] Shanshan Wang et al. “Shape Evolution of Monolayer MoS2 Crystals Grown by Chemical Vapor Deposition”. In: *Chemistry of Materials* 26.22 (Nov. 2014), pp. 6371–6379. ISSN: 0897-4756. DOI: 10.1021/cm5025662. URL: https://doi.org/10.1021/cm5025662 (visited on 08/23/2025).

[52] Katsuyoshi Kobayashi and Jun Yamauchi. “Electronic structure and scanning-tunneling-microscopy image of molybdenum dichalcogenide surfaces”. In: *Physical Review B* 51.23 (June 1995), pp. 17085–17095. DOI: 10.1103/PhysRevB.51.17085. URL: https://link.aps.org/doi/10.1103/PhysRevB.51.17085 (visited on 08/15/2025).

[53] Andrea Splendiani et al. “Emerging Photoluminescence in Monolayer MoS2”. In: *Nano Letters* 10.4 (Apr. 2010), pp. 1271–1275. ISSN: 1530-6984. DOI: 10.1021/nl903868w. URL: https://doi.org/10.1021/nl903868w (visited on 10/28/2025).

[54] Thomas Mueller and Ermin Malic. “Exciton physics and device application of two-dimensional transition metal dichalcogenide semiconductors”. en. In: *npj 2D Materials and Applications* 2.1 (Sept. 2018), p. 29. ISSN: 2397-7132. DOI: 10.1038/s41699-018-0074-2. URL: https://www.nature.com/articles/s41699-018-0074-2 (visited on 08/15/2025).

[55] Kristen Kaasbjerg, Kristian S. Thygesen, and Karsten W. Jacobsen. “Phonon-limited mobility in n-type single-layer MoS${}_{2}$ from first principles”. In: *Physical Review B* 85.11 (Mar. 2012), p. 115317. DOI: 10.1103/PhysRevB.85.115317. URL: https://link.aps.org/doi/10.1103/PhysRevB.85.115317 (visited on 07/17/2025).

[56] Hyejoo Lee et al. “High-Responsivity Multilayer MoSe2 Phototransistors with Fast Response Time”. en. In: *Scientific Reports* 8.1 (Aug. 2018), p. 11545. ISSN: 2045-2322. DOI: 10.1038/s41598-018-29942-1. URL: https://www.nature.com/articles/s41598-018-29942-1 (visited on 07/17/2025).

[57] Jixiang Zhong et al. “Vacancy-driven resistive switching behavior based on wafer-scale MoSe2 artificial synapses”. In: *Applied Surface Science* 678 (Dec. 2024), p. 161050. ISSN: 0169-4332. DOI: 10.1016/j.apsusc.2024.161050. URL: https://www.sciencedirect.com/science/article/pii/S016943322401763X (visited on 07/17/2025).

[58] B. S. Kim et al. “Possible electric field induced indirect to direct band gap transition in MoSe2”. en. In: *Scientific Reports* 7.1 (July 2017), p. 5206. ISSN: 2045-2322. DOI: 10.1038/s41598-017-05613-5. URL: https://www.nature.com/articles/s41598-017-05613-5 (visited on 07/17/2025).

[59] Sefaattin Tongay et al. “Thermally Driven Crossover from Indirect toward Direct Bandgap in 2D Semiconductors: MoSe2 versus MoS2”. In: *Nano Letters* 12.11 (Nov. 2012), pp. 5576–5580. ISSN: 1530-6984. DOI: 10.1021/nl302584w. URL: https://doi.org/10.1021/nl302584w (visited on 07/17/2025).

[60] Kin Fai Mak et al. “Atomically Thin ${\mathrm{MoS}}_{2}$: A New Direct-Gap Semiconductor”. In: *Physical Review Letters* 105.13 (Sept. 2010), p. 136805. DOI: 10.1103/PhysRevLett.105.136805. URL: https://link.aps.org/doi/10.1103/PhysRevLett.105.136805 (visited on 08/15/2025).

[61] Arend M. van der Zande et al. “Grains and grain boundaries in highly crystalline monolayer molybdenum disulphide”. en. In: *Nature Materials* 12.6 (June 2013), pp. 554–561. ISSN: 1476-4660. DOI: 10.1038/nmat3633. URL: https://www.nature.com/articles/nmat3633 (visited on 08/15/2025).

[62] Heather M. Hill et al. “Observation of Excitonic Rydberg States in Monolayer MoS2 and WS2 by Photoluminescence Excitation Spectroscopy”. In: *Nano Letters* 15.5 (May 2015), pp. 2992–2997. ISSN: 1530-6984. DOI: 10.1021/nl504868p. URL: https://doi.org/10.1021/nl504868p (visited on 08/15/2025).

[63] Jun Xiao et al. “Excitons in atomically thin 2D semiconductors and their applications”. en. In: *Nanophotonics* 6.6 (Nov. 2017), pp. 1309–1328. ISSN: 2192-8614. DOI: 10.1515/nanoph-2016-0160. URL: https://www.degruyterbrill.com/document/doi/10.1515/nanoph-2016-0160/html?lang=en (visited on 08/15/2025).

[64] Peng Lu et al. “Strain-dependent electronic and magnetic properties of MoS2 monolayer, bilayer, nanoribbons and nanotubes”. en. In: *Physical Chemistry Chemical Physics* 14.37 (Aug. 2012), pp. 13035–13040. ISSN: 1463-9084. DOI: 10.1039/C2CP42181J. URL: https://pubs.rsc.org/en/content/articlelanding/2012/cp/c2cp42181j (visited on 08/24/2025).

[65] Yinghui Sun, Rongming Wang, and Kai Liu. “Substrate induced changes in atomically thin 2-dimensional semiconductors: Fundamentals, engineering, and applications”. In: *Applied Physics Reviews* 4.1 (Jan. 2017), p. 011301. ISSN: 1931-9401. DOI: 10.1063/1.4974072. URL: https://doi.org/10.1063/1.4974072 (visited on 08/24/2025).

[66] Yeung Yu Hui et al. “Exceptional Tunability of Band Energy in a Compressively Strained Trilayer MoS2 Sheet”. In: *ACS Nano* 7.8 (Aug. 2013), pp. 7126–7131. ISSN: 1936-0851. DOI: 10.1021/nn4024834. URL: https://doi.org/10.1021/nn4024834 (visited on 04/10/2025).

[67] Luojun Du et al. “Moiré photonics and optoelectronics”. In: *Science* 379.6639 (Mar. 2023), eadg0014. DOI: 10.1126/science.adg0014. URL: https://www.science.org/doi/10.1126/science.adg0014 (visited on 08/24/2025).

[68] Yuan Cao et al. “Unconventional superconductivity in magic-angle graphene superlattices”. en. In: *Nature* 556.7699 (Apr. 2018), pp. 43–50. ISSN: 1476-4687. DOI: 10.1038/nature26160. URL: https://www.nature.com/articles/nature26160 (visited on 08/25/2025).

[69] Ponor. *Moire of twisted bilayer graphene*. 2023. URL: https://commons.wikimedia.org/wiki/File:Moire_of_twisted_bilayer_graphene.svg.

[70] Daniel Bennett et al. “Polar meron-antimeron networks in strained and twisted bilayers”. en. In: *Nature Communications* 14.1 (Mar. 2023), p. 1629. ISSN: 2041-1723. DOI: 10.1038/s41467-023-37337-8. URL: https://www.nature.com/articles/s41467-023-37337-8 (visited on 04/10/2025).

[71] Jiamin Quan et al. “Quantifying Strain in Moiré Superlattice”. In: *Nano Letters* 23.24 (Dec. 2023), pp. 11510–11516. ISSN: 1530-6984. DOI: 10.1021/acs.nanolett.3c03115. URL: https://doi.org/10.1021/acs.nanolett.3c03115 (visited on 04/10/2025).

[72] Lei Li and Menghao Wu. “Binary Compound Bilayer and Multilayer with Vertical Polarizations: Two-Dimensional Ferroelectrics, Multiferroics, and Nanogenerators”. In: *ACS Nano* 11.6 (June 2017), pp. 6382–6388. ISSN: 1936-0851. DOI: 10.1021/acsnano.7b02756. URL: https://doi.org/10.1021/acsnano.7b02756 (visited on 08/26/2025).

[73] Chi Shing Tsang et al. “Polar and quasicrystal vortex observed in twisted-bilayer molybdenum disulfide”. In: *Science* 386.6718 (Oct. 2024), pp. 198–205. DOI: 10.1126/science.adp7099. URL: https://www.science.org/doi/10.1126/science.adp7099 (visited on 08/26/2025).

[74] S. J. Magorrian et al. “Multifaceted moir\’e superlattice physics in twisted ${\mathrm{WSe}}_{2}$ bilayers”. In: *Physical Review B* 104.12 (Sept. 2021), p. 125440. DOI: 10.1103/PhysRevB.104.125440. URL: https://link.aps.org/doi/10.1103/PhysRevB.104.125440 (visited on 08/26/2025).

[75] Christina Sfetsou. “From 2D to 1D Nanostructures: Rolling van der Waals Materials Fabrication and Characterization of Nanoscrolls”. PhD thesis. Delft, NL: Technische Universiteit Delft, 2024.

[76] Ankush D. Sontakke and Mihir K. Purkait. “A brief review on graphene oxide Nanoscrolls: Structure, Synthesis, characterization and scope of applications”. In: *Chemical Engineering Journal* 420 (Sept. 2021), p. 129914. ISSN: 1385-8947. DOI: 10.1016/j.cej.2021.129914. URL: https://www.sciencedirect.com/science/article/pii/S1385894721014984 (visited on 08/31/2025).

[77] Sikandar Aftab, Muhammad Zahir Iqbal, and You Seung Rim. “Recent Advances in Rolling 2D TMDs Nanosheets into 1D TMDs Nanotubes/Nanoscrolls”. In: *Small* 19.1 (Jan. 2023), p. 2205418. ISSN: 1613-6810. DOI: 10.1002/smll.202205418. URL: https://onlinelibrary.wiley.com/doi/10.1002/smll.202205418 (visited on 01/14/2025).

[78] Xueping Cui et al. “Rolling up transition metal dichalcogenide nanoscrolls via one drop of ethanol”. en. In: *Nature Communications* 9.1 (Apr. 2018), p. 1301. ISSN: 2041-1723. DOI: 10.1038/s41467-018-03752-5. URL: https://www.nature.com/articles/s41467-018-03752-5 (visited on 03/19/2025).

[79] Thaar M. D. Alharbi. “Fast fabrication of High-Yield WS2 nanoscrolls via ultrasound sonication”. In: *Arabian Journal of Chemistry* 17.7 (July 2024), p. 105819. ISSN: 1878-5352. DOI: 10.1016/j.arabjc.2024.105819. URL: https://www.sciencedirect.com/science/article/pii/S1878535224002211 (visited on 04/10/2025).

[80] Zegao Wang et al. “Self-scrolling MoS2 metallic wires”. en. In: *Nanoscale* 10.38 (Oct. 2018), pp. 18178–18185. ISSN: 2040-3372. DOI: 10.1039/C8NR04611E. URL: https://pubs.rsc.org/en/content/articlelanding/2018/nr/c8nr04611e (visited on 04/25/2025).

[81] Shilong Yu et al. “Centrifugal Force-Assisted Preparation of Closely Packed Transition Metal Dichalcogenide Nanoscrolls for Enhanced Optoelectronic Performance”. In: *ACS Applied Nano Materials* 7.16 (Aug. 2024), pp. 18801–18810. DOI: 10.1021/acsanm.4c02307. URL: https://doi.org/10.1021/acsanm.4c02307 (visited on 09/01/2025).

[82] Xuefei Zhou et al. “Rolling up MoSe2 Nanomembranes as a Sensitive Tubular Photodetector”. en. In: *Small* 15.42 (2019), p. 1902528. ISSN: 1613-6829. DOI: 10.1002/smll.201902528. URL: https://onlinelibrary.wiley.com/doi/abs/10.1002/smll.201902528 (visited on 04/24/2025).

[83] Lin Wang et al. “Scrolling bilayer WS2/MoS2 heterostructures for high-performance photo-detection”. en. In: *Nano Research* 13.4 (Apr. 2020), pp. 959–966. ISSN: 1998-0000. DOI: 10.1007/s12274-020-2725-9. URL: https://link.springer.com/article/10.1007/s12274-020-2725-9 (visited on 04/24/2025).

[84] Mohsen Khaledian, Razali Ismail, and Elnaz Akbari. “Band structures of graphene nanoscrolls and their dispersion relation near the Fermi point”. en. In: *RSC Advances* 6.45 (Apr. 2016), pp. 38753–38760. ISSN: 2046-2069. DOI: 10.1039/C5RA27789B. URL: https://pubs.rsc.org/en/content/articlelanding/2016/ra/c5ra27789b (visited on 08/31/2025).

[85] Xinghua Shi, Nicola M. Pugno, and Huajian Gao. “Tunable Core Size of Carbon Nanoscrolls”. In: *Journal of Computational and Theoretical Nanoscience* 7.3 (Mar. 2010), pp. 517–521. DOI: 10.1166/jctn.2010.1387.

[86] Christian Thomsen and Stephanie Reich. “Raman Scattering in Carbon Nanotubes”. en. In: *Light Scattering in Solid IX*. Ed. by Manuel Cardona and Roberto Merlin. Berlin, Heidelberg: Springer, 2007, pp. 115–234. ISBN: 978-3-540-34436-0. DOI: 10.1007/978-3-540-34436-0_3. URL: https://doi.org/10.1007/978-3-540-34436-0_3 (visited on 10/28/2025).

[87] Mohammed Sayyad et al. “Strain Anisotropy Driven Spontaneous Formation of Nanoscrolls from 2D Janus Layers”. en. In: *Advanced Functional Materials* 33.42 (2023), p. 2303526. ISSN: 1616-3028. DOI: 10.1002/adfm.202303526. URL: https://onlinelibrary.wiley.com/doi/abs/10.1002/adfm.202303526 (visited on 09/14/2025).

[88] Sagnik Chatterjee et al. “Twists and turns: stacking and structure-dependent optical response in MoS2 nanoscrolls”. en. In: *2D Materials* 12.4 (July 2025), p. 045005. ISSN: 2053-1583. DOI: 10.1088/2053-1583/ade9d8. URL: https://dx.doi.org/10.1088/2053-1583/ade9d8 (visited on 09/14/2025).

[89] Z. Khalitov, A. Khadiev, and D. Pashin. “Electron diffraction patterns from scroll nanotubes: interpretation peculiarities”. en. In: *Journal of Applied Crystallography* 48.1 (Feb. 2015), pp. 29–36. ISSN: 1600-5767. DOI: 10.1107/S1600576714024005. URL: https://journals.iucr.org/j/issues/2015/01/00/nb5130/ (visited on 09/14/2025).

[90] Nobuyuki Fukui et al. “Moir\’e image patterns on double-walled carbon nanotubes observed by scanning tunneling microscopy”. In: *Physical Review B* 79.12 (Mar. 2009), p. 125402. DOI: 10.1103/PhysRevB.79.125402. URL: https://link.aps.org/doi/10.1103/PhysRevB.79.125402 (visited on 09/12/2025).

[91] Bei Zhao et al. “High-order superlattices by rolling up van der Waals heterostructures”. en. In: *Nature* 591.7850 (Mar. 2021), pp. 385–390. ISSN: 1476-4687. DOI: 10.1038/s41586-021-03338-0. URL: https://www.nature.com/articles/s41586-021-03338-0 (visited on 03/19/2025).

[92] Ci Lin et al. “Direct Band Gap in Multilayer Transition Metal Dichalcogenide Nanoscrolls with Enhanced Photoluminescence”. In: *ACS Materials Letters* 4.8 (Aug. 2022), pp. 1547–1555. DOI: 10.1021/acsmaterialslett.2c00162. URL: https://doi.org/10.1021/acsmaterialslett.2c00162 (visited on 09/14/2025).

[93] Jiashuo Yan et al. “Controlled growth, characterization and field emission properties of high-quality WS2 nanowires by chemical vapor deposition”. In: *Vacuum* 208 (Feb. 2023), p. 111725. ISSN: 0042-207X. DOI: 10.1016/j.vacuum.2022.111725. URL: https://www.sciencedirect.com/science/article/pii/S0042207X22008478 (visited on 08/12/2025).

[94] Lei Yang et al. “Properties, Preparation and Applications of Low Dimensional Transition Metal Dichalcogenides”. en. In: *Nanomaterials* 8.7 (July 2018), p. 463. ISSN: 2079-4991. DOI: 10.3390/nano8070463. URL: https://www.mdpi.com/2079-4991/8/7/463 (visited on 08/12/2025).

[95] Denis Salikhyanov, Ivan Kamantsev, and Nikolay Michurov. “Technological Shells in Rolling Processes of Thin Sheets from Hard-to-Deform Materials”. en. In: *Journal of Materials Engineering and Performance* 32.22 (Nov. 2023), pp. 10085–10102. ISSN: 1544-1024. DOI: 10.1007/s11665-023-07834-4. URL: https://doi.org/10.1007/s11665-023-07834-4 (visited on 08/18/2025).

[96] Yangang Li et al. “Recent progress on the mechanical exfoliation of 2D transition metal dichalcogenides”. en. In: *Materials Research Express* 9.12 (Dec. 2022), p. 122001. ISSN: 2053-1591. DOI: 10.1088/2053-1591/aca6c6. URL: https://dx.doi.org/10.1088/2053-1591/aca6c6 (visited on 06/05/2025).

[97] Panwad Chavalekvirat et al. “Liquid Phase Exfoliation of 2D Materials and Its Electrochemical Applications in the Data-Driven Future”. In: *Precision Chemistry* 2.7 (July 2024), pp. 300–329. DOI: 10.1021/prechem.3c00119. URL: https://doi.org/10.1021/prechem.3c00119 (visited on 06/06/2025).

[98] Ali Raza et al. “Advances in Liquid-Phase and Intercalation Exfoliations of Transition Metal Dichalcogenides to Produce 2D Framework”. en. In: *Advanced Materials Interfaces* 8.14 (2021), p. 2002205. ISSN: 2196-7350. DOI: 10.1002/admi.202002205. URL: https://onlinelibrary.wiley.com/doi/abs/10.1002/admi.202002205 (visited on 06/13/2025).

[99] Yu Zhang et al. “Recent Progress in CVD Growth of 2D Transition Metal Dichalcogenides and Related Heterostructures”. en. In: *Advanced Materials* 31.41 (2019), p. 1901694. ISSN: 1521-4095. DOI: 10.1002/adma.201901694. URL: https://onlinelibrary.wiley.com/doi/abs/10.1002/adma.201901694 (visited on 08/19/2025).

[100] C. Muratore et al. “Continuous ultra-thin MoS2 films grown by low-temperature physical vapor deposition”. In: *Applied Physics Letters* 104.26 (July 2014), p. 261604. ISSN: 0003-6951. DOI: 10.1063/1.4885391. URL: https://doi.org/10.1063/1.4885391 (visited on 08/12/2025).

[101] Tinna Chiawchan et al. “CVD Synthesis of Intermediate State-Free, Large-Area and Continuous MoS2 via Single-Step Vapor-Phase Sulfurization of MoO2 Precursor”. en. In: *Nanomaterials* 11.10 (Oct. 2021), p. 2642. ISSN: 2079-4991. DOI: 10.3390/nano11102642. URL: https://www.mdpi.com/2079-4991/11/10/2642 (visited on 08/13/2025).

[102] Xiangru Fang et al. “Transforming Monolayer Transition-Metal Dichalcogenide Nanosheets into One-Dimensional Nanoscrolls with High Photosensitivity”. In: *ACS Applied Materials & Interfaces* 10.15 (Apr. 2018), pp. 13011–13018. ISSN: 1944-8244. DOI: 10.1021/acsami.8b01856. URL: https://doi.org/10.1021/acsami.8b01856 (visited on 09/15/2025).

[103] Zhengyang Cai et al. “Chemical Vapor Deposition Growth and Applications of Two-Dimensional Materials and Their Heterostructures”. In: *Chemical Reviews* 118.13 (July 2018), pp. 6091–6133. ISSN: 0009-2665. DOI: 10.1021/acs.chemrev.7b00536. URL: https://doi.org/10.1021/acs.chemrev.7b00536 (visited on 02/19/2025).

[104] Luzhao Sun et al. “Chemical vapour deposition”. en. In: *Nature Reviews Methods Primers* 1.1 (Jan. 2021), pp. 1–20. ISSN: 2662-8449. DOI: 10.1038/s43586-020-00005-y. URL: https://www.nature.com/articles/s43586-020-00005-y (visited on 02/24/2025).

[105] Sabrya van Heijst. “Fingerprinting the Properties of WS2 Nanostructures using Advanced Transmission Electron Microscopy Techniques”. PhD thesis. Netherlands: Technische Universiteit Delft, 2024.

[106] Hugh O. Pierson and Hugh O. Pierson. *Handbook of chemical vapor deposition*. en. 2nd ed. Norwich, NY: Noyes Publications, 1999. ISBN: 978-0-8155-1432-9.

[107] Yi-Hsien Lee et al. “Synthesis of Large-Area MoS2 Atomic Layers with Chemical Vapor Deposition”. In: *Advanced Materials* 24.17 (2012), pp. 2320–2325. ISSN: 1521-4095. DOI: 10.1002/adma.201104798. URL: https://onlinelibrary.wiley.com/doi/abs/10.1002/adma.201104798 (visited on 08/13/2025).

[108] Ratchanok Somphonsane et al. “CVD Synthesis of MoS2 Using a Direct MoO2 Precursor: A Study on the Effects of Growth Temperature on Precursor Diffusion and Morphology Evolutions”. en. In: *Materials* 16.13 (Jan. 2023), p. 4817. ISSN: 1996-1944. DOI: 10.3390/ma16134817. URL: https://www.mdpi.com/1996-1944/16/13/4817 (visited on 08/13/2025).

[109] Nitin Choudhary et al. “Growth of Large-Scale and Thickness-Modulated MoS2 Nanosheets”. In: *ACS Applied Materials & Interfaces* 6.23 (Dec. 2014), pp. 21215–21222. ISSN: 1944-8244. DOI: 10.1021/am506198b. URL: https://doi.org/10.1021/am506198b (visited on 08/19/2025).

[110] Yongjie Zhan et al. “Large-Area Vapor-Phase Growth and Characterization of MoS2 Atomic Layers on a SiO2 Substrate”. In: *Small* 8.7 (2012), pp. 966–971. ISSN: 1613-6829. DOI: 10.1002/smll.201102654. URL: https://onlinelibrary.wiley.com/doi/abs/10.1002/smll.201102654 (visited on 08/19/2025).

[111] Yifei Yu et al. “Controlled Scalable Synthesis of Uniform, High-Quality Monolayer and Few-layer MoS2 Films”. en. In: *Scientific Reports* 3.1 (May 2013), p. 1866. ISSN: 2045-2322. DOI: 10.1038/srep01866. URL: https://www.nature.com/articles/srep01866 (visited on 08/19/2025).

[112] Kibum Kang et al. “High-mobility three-atom-thick semiconducting films with wafer-scale homogeneity”. en. In: *Nature* 520.7549 (Apr. 2015), pp. 656–660. ISSN: 1476-4687. DOI: 10.1038/nature14417. URL: https://www.nature.com/articles/nature14417 (visited on 08/19/2025).

[113] C. González et al. “Shape-controlled monolayer MoSe2 flakes by chemical vapor deposition towards tuning the photoluminescence emission”. In: *Applied Surface Science* 605 (Dec. 2022), p. 154742. ISSN: 0169-4332. DOI: 10.1016/j.apsusc.2022.154742. URL: https://www.sciencedirect.com/science/article/pii/S016943322202270X (visited on 01/18/2025).

[114] Xingli Wang et al. “Chemical Vapor Deposition Growth of Crystalline Monolayer MoSe2”. In: *ACS Nano* 8.5 (May 2014), pp. 5125–5131. ISSN: 1936-0851. DOI: 10.1021/nn501175k. URL: https://doi.org/10.1021/nn501175k (visited on 08/19/2025).

[115] Binjie Zheng and Yuanfu Chen. “Controllable Growth of Monolayer MoS2 and MoSe2 Crystals Using Three-temperature-zone Furnace”. en. In: *IOP Conference Series: Materials Science and Engineering* 274.1 (Dec. 2017), p. 012085. ISSN: 1757-899X. DOI: 10.1088/1757-899X/274/1/012085. URL: https://dx.doi.org/10.1088/1757-899X/274/1/012085 (visited on 08/15/2025).

[116] Jing Xia et al. “CVD synthesis of large-area, highly crystalline MoSe 2 atomic layers on diverse substrates and application to photodetectors”. en. In: *Nanoscale* 6.15 (2014), pp. 8949–8955. DOI: 10.1039/C4NR02311K. URL: https://pubs.rsc.org/en/content/articlelanding/2014/nr/c4nr02311k (visited on 08/19/2025).

[117] Mehmet Bay et al. “Catalytic strategies for uniform monolayer MoSe2 growth in CVD processes”. In: *Materials Science in Semiconductor Processing* 180 (Sept. 2024), p. 108551. ISSN: 1369-8001. DOI: 10.1016/j.mssp.2024.108551. URL: https://www.sciencedirect.com/science/article/pii/S1369800124004475 (visited on 09/04/2025).

[118] Ana Senkić et al. “Effects of CVD growth parameters on global and local optical properties of MoS2 monolayers”. In: *Materials Chemistry and Physics* 296 (Feb. 2023), p. 127185. ISSN: 0254-0584. DOI: 10.1016/j.matchemphys.2022.127185. URL: https://www.sciencedirect.com/science/article/pii/S0254058422014912 (visited on 03/05/2025).

[119] Yingjie Cao et al. “Influences of carrier gas flow rate on the morphologies of MoS2 flakes”. In: *Chemical Physics Letters* 631-632 (July 2015), pp. 30–33. ISSN: 0009-2614. DOI: 10.1016/j.cplett.2015.05.001. URL: https://www.sciencedirect.com/science/article/pii/S0009261415003097 (visited on 08/23/2025).

[120] Zusong Zhu et al. “Influence of growth temperature on MoS2 synthesis by chemical vapor deposition”. en. In: *Materials Research Express* 6.9 (July 2019), p. 095011. ISSN: 2053-1591. DOI: 10.1088/2053-1591/ab2c19. URL: https://dx.doi.org/10.1088/2053-1591/ab2c19 (visited on 09/09/2025).

[121] Xiangwei Huang et al. “Low-Temperature Chemical Vapor Deposition Growth of Monolayer MoS2 Using a Dual-Assisted Approach”. In: *ACS Omega* 10.16 (Apr. 2025), pp. 16257–16264. DOI: 10.1021/acsomega.4c10312. URL: https://doi.org/10.1021/acsomega.4c10312 (visited on 09/09/2025).

[122] Tao Han et al. “Research on the Factors Affecting the Growth of Large-Size Monolayer MoS2 by APCVD”. In: *Materials* 11.12 (Dec. 2018), p. 2562. ISSN: 1996-1944. DOI: 10.3390/ma11122562. URL: https://www.ncbi.nlm.nih.gov/pmc/articles/PMC6316495/ (visited on 09/09/2025).

[123] Krishnamoorthy Ponnusamy, Santhosh Durairaj, and S. Chandramohan. “Effect of growth temperature on the morphology control and optical behavior of monolayer MoS2 on SiO2 substrate”. en. In: *Journal of Materials Science: Materials in Electronics* 33.12 (Apr. 2022), pp. 9549–9557. ISSN: 1573-482X. DOI: 10.1007/s10854-021-07547-1. URL: https://doi.org/10.1007/s10854-021-07547-1 (visited on 09/09/2025).

[124] Daniel Dobkin and M. K. Zuraw. *Principles of Chemical Vapor Deposition*. en. Springer Science & Business Media, Apr. 2003. ISBN: 978-1-4020-1248-8.

[125] Tao Han et al. “Probing the Optical Properties of MoS2 on SiO2/Si and Sapphire Substrates”. In: *Nanomaterials* 9.5 (May 2019), p. 740. ISSN: 2079-4991. DOI: 10.3390/nano9050740. URL: https://www.ncbi.nlm.nih.gov/pmc/articles/PMC6566663/ (visited on 08/19/2025).

[126] Aditya Singh, Monika Moun, and Rajendra Singh. “Effect of different precursors on CVD growth of molybdenum disulfide”. In: *Journal of Alloys and Compounds* 782 (Apr. 2019), pp. 772–779. ISSN: 0925-8388. DOI: 10.1016/j.jallcom.2018.12.230. URL: https://www.sciencedirect.com/science/article/pii/S0925838818347868 (visited on 09/16/2025).

[127] V. Senthilkumar et al. “Direct vapor phase growth process and robust photoluminescence properties of large area MoS2 layers”. en. In: *Nano Research* 7.12 (Dec. 2014), pp. 1759–1768. ISSN: 1998-0000. DOI: 10.1007/s12274-014-0535-7. URL: https://doi.org/10.1007/s12274-014-0535-7 (visited on 09/17/2025).

[128] Jonathan C. Shaw et al. “Chemical vapor deposition growth of monolayer MoSe2 nanosheets”. en. In: *Nano Research* 7.4 (Apr. 2014), pp. 511–517. ISSN: 1998-0000. DOI: 10.1007/s12274-014-0417-z. URL: https://doi.org/10.1007/s12274-014-0417-z (visited on 08/19/2025).

[129] Breanne Hammett. *Optimizing growth conditions for 2D MoS 2*. Tech. rep. Golden, Colorado: National Renewable Energy Laboratory, 2017. URL: https://www.nrel.gov/docs/libraries/careers/cci-project-report-breanne-hammett.pdf.

[130] Shuhong Li et al. “Experimental verification of SO2 and S desorption contributing to defect formation in MoS2 by thermal desorption spectroscopy”. en. In: *Nanoscale Advances* 5.2 (Jan. 2023), pp. 405–411. ISSN: 2516-0230. DOI: 10.1039/D2NA00636G. URL: https://pubs.rsc.org/en/content/articlelanding/2023/na/d2na00636g (visited on 09/19/2025).

[131] Jehyun Oh et al. “Real-Time Observation for MoS2 Growth Kinetics and Mechanism Promoted by the Na Droplet”. In: *ACS Nano* 18.29 (July 2024), pp. 19314–19323. ISSN: 1936-0851. DOI: 10.1021/acsnano.4c05586. URL: https://doi.org/10.1021/acsnano.4c05586 (visited on 09/18/2025).

[132] Xinmao Yin et al. “Recent developments in 2D transition metal dichalcogenides: phase transition and applications of the (quasi-)metallic phases”. en. In: *Chemical Society Reviews* 50.18 (Sept. 2021), pp. 10087–10115. ISSN: 1460-4744. DOI: 10.1039/D1CS00236H. URL: https://pubs.rsc.org/en/content/articlelanding/2021/cs/d1cs00236h (visited on 08/19/2025).

[133] In Soo Kim et al. “Influence of Stoichiometry on the Optical and Electrical Properties of Chemical Vapor Deposition Derived MoS2”. In: *ACS Nano* 8.10 (Oct. 2014), pp. 10551–10558. ISSN: 1936-0851. DOI: 10.1021/nn503988x. URL: https://doi.org/10.1021/nn503988x (visited on 04/10/2025).

[134] Seon Kyeong Kang and Hyun Seok Lee. “Study on Growth Parameters for Monolayer MoS2 Synthesized by CVD Using Solution-based Metal Precursors”. en. In: *Applied Science and Convergence Technology* 28.5 (Sept. 2019), pp. 159–163. DOI: 10.5757/ASCT.2019.28.5.159. URL: https://www.e-asct.org/journal/view.html?doi=10.5757/ASCT.2019.28.5.159 (visited on 03/07/2025).

[135] Lulu Kang et al. “Epitaxial growth of highly-aligned MoS2 on c-plane sapphire”. In: *Surface Science* 720 (June 2022), p. 122046. ISSN: 0039-6028. DOI: 10.1016/j.susc.2022.122046. URL: https://www.sciencedirect.com/science/article/pii/S0039602822000310 (visited on 08/19/2025).

[136] Jiaojie Yue et al. “Growth of Single-Layer MoS2 by Chemical Vapor Deposition on sapphire substrate”. en. In: *IOP Conference Series: Materials Science and Engineering* 592.1 (Aug. 2019), p. 012044. ISSN: 1757-899X. DOI: 10.1088/1757-899X/592/1/012044. URL: https://dx.doi.org/10.1088/1757-899X/592/1/012044 (visited on 03/05/2025).

[137] Sajeevi S. Withanage and Saiful I. Khondaker. “CVD Growth of Monolayer MoS2 on Sapphire Substrates by using MoO3 Thin Films as a Precursor for Co-Evaporation”. en. In: *MRS Advances* 4.10 (Feb. 2019), pp. 587–592. ISSN: 2059-8521. DOI: 10.1557/adv.2018.657. URL: https://doi.org/10.1557/adv.2018.657 (visited on 08/19/2025).

[138] Liang Chen et al. “Step-Edge-Guided Nucleation and Growth of Aligned WSe2 on Sapphire via a Layer-over-Layer Growth Mode”. In: *ACS Nano* 9.8 (Aug. 2015), pp. 8368–8375. ISSN: 1936-0851. DOI: 10.1021/acsnano.5b03043. URL: https://doi.org/10.1021/acsnano.5b03043 (visited on 08/19/2025).

[139] Jakub Sitek et al. “Substrate-Induced Variances in Morphological and Structural Properties of MoS2 Grown by Chemical Vapor Deposition on Epitaxial Graphene and SiO2”. In: *ACS Applied Materials & Interfaces* 12.40 (Oct. 2020), pp. 45101–45110. ISSN: 1944-8244. DOI: 10.1021/acsami.0c06173. URL: https://doi.org/10.1021/acsami.0c06173 (visited on 08/19/2025).

[140] Yongji Gong et al. “Two-Step Growth of Two-Dimensional WSe2/MoSe2 Heterostructures”. In: *Nano Letters* 15.9 (Sept. 2015), pp. 6135–6141. ISSN: 1530-6984. DOI: 10.1021/acs.nanolett.5b02423. URL: https://doi.org/10.1021/acs.nanolett.5b02423 (visited on 08/19/2025).

[141] Shanshan Wang, Xiaochen Wang, and Jamie H. Warner. “All Chemical Vapor Deposition Growth of MoS2:h-BN Vertical van der Waals Heterostructures”. In: *ACS Nano* 9.5 (May 2015), pp. 5246–5254. ISSN: 1936-0851. DOI: 10.1021/acsnano.5b00655. URL: https://doi.org/10.1021/acsnano.5b00655 (visited on 08/19/2025).

[142] Yongji Gong et al. “Vertical and in-plane heterostructures from WS2/MoS2 monolayers”. en. In: *Nature Materials* 13.12 (Dec. 2014), pp. 1135–1142. ISSN: 1476-4660. DOI: 10.1038/nmat4091. URL: https://www.nature.com/articles/nmat4091 (visited on 08/19/2025).

[143] Kasturi Vimalanathan et al. “Vortex fluidic mediated transformation of graphite into highly conducting graphene scrolls”. en. In: *Nanoscale Advances* 1.7 (July 2019), pp. 2495–2501. ISSN: 2516-0230. DOI: 10.1039/C9NA00184K. URL: https://pubs.rsc.org/en/content/articlelanding/2019/na/c9na00184k (visited on 09/16/2025).

[144] Pitchai Thangasamy, Jeyaraman Anandha Raj, and Marappan Sathish. “Transformation of multilayer WS2 nanosheets to 1D luminescent WS2 nanostructures by one-pot supercritical fluid processing for hydrogen evolution reaction”. In: *Materials Science in Semiconductor Processing* 119 (Nov. 2020), p. 105167. ISSN: 1369-8001. DOI: 10.1016/j.mssp.2020.105167. URL: https://www.sciencedirect.com/science/article/pii/S1369800120302663 (visited on 09/01/2025).

[145] Xu Xie et al. “Controlled Fabrication of High-Quality Carbon Nanoscrolls from Monolayer Graphene”. In: *Nano Letters* 9.7 (July 2009), pp. 2565–2570. ISSN: 1530-6984. DOI: 10.1021/nl900677y. URL: https://doi.org/10.1021/nl900677y (visited on 09/15/2025).

[146] Udayabagya Halim et al. “A rational design of cosolvent exfoliation of layered materials by directly probing liquid–solid interaction”. en. In: *Nature Communications* 4.1 (July 2013), p. 2213. ISSN: 2041-1723. DOI: 10.1038/ncomms3213. URL: https://www.nature.com/articles/ncomms3213 (visited on 09/15/2025).

[147] Shilong Yu et al. “Transition Metal Dichalcogenides Nanoscrolls: Preparation and Applications”. en. In: *Nanomaterials* 13.17 (Jan. 2023), p. 2433. ISSN: 2079-4991. DOI: 10.3390/nano13172433. URL: https://www.mdpi.com/2079-4991/13/17/2433 (visited on 09/15/2025).

[148] Ewen Smith and Geoffrey Dent. *Modern Raman Spectroscopy: A Practical Approach*. en. John Wiley & Sons, Apr. 2019. ISBN: 978-1-119-44055-0.

[149] Philipp Tonndorf et al. “Photoluminescence emission and Raman response of monolayer MoS_2, $MoSe_2$, and WSe_2”. EN. In: *Optics Express* 21.4 (Feb. 2013), pp. 4908–4916. ISSN: 1094-4087. DOI: 10.1364/OE.21.004908. URL: https://opg.optica.org/oe/abstract.cfm?uri=oe-21-4-4908 (visited on 07/17/2025).

[150] David Tuschel. “Practical Group Theory and Raman Spectroscopy, Part I: Normal Vibrational Modes”. en. In: *Spectroscopy*. Spectroscopy-02-01-2014 29(2).14 (Feb. 2014). URL: https://www.horiba.com/fileadmin/uploads/Scientific/Documents/Raman/Specy_Workbench-DT-Practical_Group_Theory__Raman_Spectroscopy-part_1.pdf (visited on 07/30/2025).

[151] Edinburgh Intruments. *MoS2 Raman Imaging: Characterizing 2D Materials*. en-GB. URL: https://www.edinst.com/resource/high-resolution-raman-pl-imaging-of-mos2/ (visited on 07/30/2025).

[152] Hong Li et al. “From Bulk to Monolayer MoS2: Evolution of Raman Scattering”. en. In: *Advanced Functional Materials* 22.7 (2012), pp. 1385–1390. ISSN: 1616-3028. DOI: 10.1002/adfm.201102111. URL: https://onlinelibrary.wiley.com/doi/abs/10.1002/adfm.201102111 (visited on 08/07/2025).

[153] Xiao Hu Wang, Chang Cheng Zheng, and Ji Qiang Ning. “Influence of curvature strain and Van der Waals force on the inter-layer vibration mode of WS2 nanotubes: A confocal micro-Raman spectroscopic study”. en. In: *Scientific Reports* 6.1 (Sept. 2016), p. 33091. ISSN: 2045-2322. DOI: 10.1038/srep33091. URL: https://www.nature.com/articles/srep33091 (visited on 08/17/2025).

[154] Zhikang Wu et al. “Decorating MoS2 Nanoscrolls with Solution-Processed PbI2 Nanocrystals for Improved Photosensitivity”. In: *ACS Applied Nano Materials* 5.10 (Oct. 2022), pp. 15892–15901. DOI: 10.1021/acsanm.2c04113. URL: https://doi.org/10.1021/acsanm.2c04113 (visited on 09/03/2025).

[155] James R. Lyons. “An estimate of the equilibrium speciation of sulfur vapor over solid sulfur and implications for planetary atmospheres”. In: *Journal of Sulfur Chemistry* 29.3-4 (Aug. 2008), pp. 269–279. ISSN: 1741-5993. DOI: 10.1080/17415990802195615. URL: https://doi.org/10.1080/17415990802195615 (visited on 10/27/2025).

[156] Maarten Bolhuis. “Synthesis of horizontal and vertical molybdenum disulphide nanosheets using chemical vapour deposition”. PhD thesis. Delft University of Technology, 2019.

[157] Prachi Budania et al. “Long-term stability of mechanically exfoliated MoS2 flakes”. en. In: *MRS Communications* 7.4 (Dec. 2017), pp. 813–818. ISSN: 2159-6859, 2159-6867. DOI: 10.1557/mrc.2017.105. URL: https://www.cambridge.org/core/journals/mrs-communications/article/longterm-stability-of-mechanically-exfoliated-mos2-flakes/E702460BE9E38BBF176FCCB07FB6FC5D (visited on 10/17/2025).

[158] Yan Jiang et al. “Effects of Strategically Placed Water Droplets on Monolayer Growth of Molybdenum Disulfide”. en. In: *Journal of Nanomaterials* 2018.1 (2018), p. 6192532. ISSN: 1687-4129. DOI: 10.1155/2018/6192532. URL: https://onlinelibrary.wiley.com/doi/abs/10.1155/2018/6192532 (visited on 10/28/2025).

[159] Jorge Torres et al. “Adhesion Energies of 2D Graphene and MoS2 to Silicon and Metal Substrates”. en. In: *physica status solidi (a)* 215.1 (2018), p. 1700512. ISSN: 1862-6319. DOI: 10.1002/pssa.201700512. URL: https://onlinelibrary.wiley.com/doi/abs/10.1002/pssa.201700512 (visited on 10/18/2025).

[160] Chulseung Jung et al. “Highly Crystalline CVD-grown Multilayer MoSe2 Thin Film Transistor for Fast Photodetector”. en. In: *Scientific Reports* 5.1 (Oct. 2015), p. 15313. ISSN: 2045-2322. DOI: 10.1038/srep15313. URL: https://www.nature.com/articles/srep15313 (visited on 10/20/2025).

[161] Mahima Tyagi et al. “Systematic study of CVD-growth parameters in NaCl-assisted growth of MoSe 2 nanostructures: nanoribbons, dendrites and spirals”. en. In: *Materials Advances* 6.14 (2025), pp. 4833–4846. DOI: 10.1039/D5MA00121H. URL: https://pubs.rsc.org/en/content/articlelanding/2025/ma/d5ma00121h (visited on 10/20/2025).

[162] Alireza Taghizadeh et al. “A library of ab initio Raman spectra for automated identification of 2D materials”. en. In: *Nature Communications* 11.1 (June 2020), p. 3011. ISSN: 2041-1723. DOI: 10.1038/s41467-020-16529-6. URL: https://www.nature.com/articles/s41467-020-16529-6 (visited on 09/24/2025).

[163] Antonis Nanakoudis. *EDX Analysis with SEM: How Does it Work?* en-US. Nov. 2019. URL: https://www.thermofisher.com/blog/materials/edx-analysis-with-sem-how-does-it-work/ (visited on 10/21/2025).

[164] Isabela Alves de Castro et al. “Molybdenum Oxides – From Fundamentals to Functionality”. In: *Advanced Materials* 29.40 (Oct. 2017), p. 1701619. ISSN: 0935-9648. DOI: 10.1002/adma.201701619. URL: https://advanced.onlinelibrary.wiley.com/doi/10.1002/adma.201701619 (visited on 10/21/2025).

[165] Chengtao Shen et al. “Controllable Selenization Transformation from MoO2 to MoSe2 by Gas Pressure-Mediated Chemical Vapor Deposition”. en. In: *physica status solidi (a)* 219.14 (2022), p. 2200044. ISSN: 1862-6319. DOI: 10.1002/pssa.202200044. URL: https://onlinelibrary.wiley.com/doi/abs/10.1002/pssa.202200044 (visited on 09/26/2025).

[166] Simin Tao et al. “Effect of selenation temperature on the structure and electrocatalytic properties of MoSe2”. In: *International Journal of Hydrogen Energy* 58 (Mar. 2024), pp. 829–838. ISSN: 0360-3199. DOI: 10.1016/j.ijhydene.2023.12.093. URL: https://www.sciencedirect.com/science/article/pii/S0360319923063930 (visited on 08/14/2025).

[167] Xiaoshuang Chen et al. “Vertical MoSe2–MoOx p–n heterojunction and its application in optoelectronics”. en. In: *Nanotechnology* 29.4 (Dec. 2017), p. 045202. ISSN: 0957-4484. DOI: 10.1088/1361-6528/aa9d4f. URL: https://doi.org/10.1088/1361-6528/aa9d4f (visited on 10/21/2025).

[168] Hyun Kim et al. “Role of alkali metal promoter in enhancing lateral growth of monolayer transition metal dichalcogenides”. en. In: *Nanotechnology* 28.36 (Aug. 2017), 36LT01. ISSN: 0957-4484. DOI: 10.1088/1361-6528/aa7e5e. URL: https://dx.doi.org/10.1088/1361-6528/aa7e5e (visited on 09/04/2025).

[169] Jeffrey B. Kortright and Albert C. Thompson. *X-Ray Emission Energies*. URL: https://xdb.lbl.gov/Section1/Sec_1-2.html.

[170] Harvard University. *Thin Film Interference*. 2014. URL: https://sciencedemonstrations.fas.harvard.edu/presentations/thin-film-interference.

[171] L Seguin et al. “Infrared and Raman spectra of MoO3 molybdenum trioxides and MoO3 · *x*H2O molybdenum trioxide hydrates”. In: *Spectrochimica Acta Part A: Molecular and Biomolecular Spectroscopy* 51.8 (July 1995), pp. 1323–1344. ISSN: 1386-1425. DOI: 10.1016/0584-8539(94)00247-9. URL: https://www.sciencedirect.com/science/article/pii/0584853994002479 (visited on 10/23/2025).

[172] M. A. Py, Ph. E. Schmid, and J. T. Vallin. “Raman scattering and structural properties of MoO3”. en. In: *Il Nuovo Cimento B (1971-1996)* 38.2 (Apr. 1977), pp. 271–279. ISSN: 1826-9877. DOI: 10.1007/BF02723496. URL: https://doi.org/10.1007/BF02723496 (visited on 08/21/2025).

[173] R. Narro-García et al. “Effect of the Substrate Temperature on the Structural and Morphological Properties of MoO2 Thin Films Obtained by Pulsed Injection MOCVD”. In: *International Journal of Electrochemical Science* 12.5 (Feb. 2017), pp. 3907–3915. ISSN: 1452-3981. DOI: 10.20964/2017.05.51. URL: https://www.sciencedirect.com/science/article/pii/S1452398123107942 (visited on 08/22/2025).

[174] Victor Rejón et al. “The CdS/CdTe solar cell protected by ITO/Mo bilayer at improved back contact”. In: *2014 IEEE 40th Photovoltaic Specialist Conference (PVSC)*. June 2014, pp. 1696–1698. DOI: 10.1109/PVSC.2014.6925247. URL: https://ieeexplore.ieee.org/document/6925247 (visited on 10/23/2025).

[175] Lichuan Wang et al. “MoO3 nanobelts for high-performance asymmetric supercapacitor”. en. In: *Journal of Materials Science* 54.21 (Nov. 2019), pp. 13685–13693. ISSN: 1573-4803. DOI: 10.1007/s10853-019-03836-7. URL: https://doi.org/10.1007/s10853-019-03836-7 (visited on 10/01/2025).

[176] M. Liehr, J. E. Lewis, and G. W. Rubloff. “Kinetics of high□temperature thermal decomposition of SiO2 on Si(100)”. In: *Journal of Vacuum Science & Technology A* 5.4 (July 1987), pp. 1559–1562. ISSN: 0734-2101. DOI: 10.1116/1.574564. URL: https://doi.org/10.1116/1.574564 (visited on 10/25/2025).

[177] Vinay Kumar Yadav, Priya Pradeep Kumar, and Vinod Singh. “Effect of different precursors on morphology of CVD synthesized MoSe2”. In: *Materials Today: Proceedings*. First International Conference on Design and Materials 56 (Jan. 2022), pp. 3786–3789. ISSN: 2214-7853. DOI: 10.1016/j.matpr.2022.01.127. URL: https://www.sciencedirect.com/science/article/pii/S2214785322001559 (visited on 09/29/2025).

[178] Jenna Brownrout and Robert Kirmse. *High Quality Sectioning in Ultramicrotomy*. en. White Paper. Leica Microsystems, Mar. 2024. URL: https://www.leica-microsystems.com/science-lab/life-science/high-quality-sectioning-in-ultramicrotomy/ (visited on 10/04/2025).

[179] Dan Bing et al. “Optical contrast for identifying the thickness of two-dimensional materials”. In: *Optics Communications*. Optoelectronics and Photonics Based on Two-dimensional Materials 406 (Jan. 2018), pp. 128–138. ISSN: 0030-4018. DOI: 10.1016/j.optcom.2017.06.012. URL: https://www.sciencedirect.com/science/article/pii/S0030401817304789 (visited on 10/04/2025).

[180] Z. H. Ni et al. “Graphene Thickness Determination Using Reflection and Contrast Spectroscopy”. In: *Nano Letters* 7.9 (Sept. 2007), pp. 2758–2763. ISSN: 1530-6984. DOI: 10.1021/nl071254m. URL: https://doi.org/10.1021/nl071254m (visited on 10/04/2025).

[181] Huanping Yang et al. “Rapid and non-destructive identification of graphene oxide thickness using white light contrast spectroscopy”. In: *Carbon* 52 (Feb. 2013), pp. 528–534. ISSN: 0008-6223. DOI: 10.1016/j.carbon.2012.10.005. URL: https://www.sciencedirect.com/science/article/pii/S0008622312008184 (visited on 10/04/2025).

[182] Koutsogiannis Panagiotis. “Standardization of the Use of the Ultramicrotome for Inorganic and Hybrid Transmission Electron Microscopy Samples and Applications”. PhD thesis. Thessaloniki: Aristotle University of Thessaloniki, 2017. URL: https://ikee.lib.auth.gr/record/294663/files/Thesis%20Panagiotis%20K..pdf.

[183] C. V. Ramana, A. Mauger, and C. M. Julien. “Growth, characterization and performance of bulk and nanoengineered molybdenum oxides for electrochemical energy storage and conversion”. In: *Progress in Crystal Growth and Characterization of Materials* 67.3 (Aug. 2021), p. 100533. ISSN: 0960-8974. DOI: 10.1016/j.pcrysgrow.2021.100533. URL: https://www.sciencedirect.com/science/article/pii/S0960897421000127 (visited on 10/26/2025).

[184] Du Xiang et al. “Gap States Assisted MoO3 Nanobelt Photodetector with Wide Spectrum Response”. en. In: *Scientific Reports* 4.1 (May 2014), p. 4891. ISSN: 2045-2322. DOI: 10.1038/srep04891. URL: https://www.nature.com/articles/srep04891 (visited on 10/01/2025).

[185] Luiz H. G. Tizei et al. “Exciton Mapping at Subwavelength Scales in Two-Dimensional Materials”. In: *Physical Review Letters* 114.10 (Mar. 2015), p. 107601. DOI: 10.1103/PhysRevLett.114.107601. URL: https://link.aps.org/doi/10.1103/PhysRevLett.114.107601 (visited on 08/20/2025).

[186] L. Lajaunie et al. “Strong anisotropic influence of local-field effects on the dielectric response of $\ensuremath{\alpha}$-MoO${}_{3}$”. In: *Physical Review B* 88.11 (Sept. 2013), p. 115141. DOI: 10.1103/PhysRevB.88.115141. URL: https://link.aps.org/doi/10.1103/PhysRevB.88.115141 (visited on 10/04/2025).

[187] K. Iakoubovskii et al. “Thickness measurements with electron energy loss spectroscopy”. en. In: *Microscopy Research and Technique* 71.8 (2008), pp. 626–631. ISSN: 1097-0029. DOI: 10.1002/jemt.20597. URL: https://onlinelibrary.wiley.com/doi/abs/10.1002/jemt.20597 (visited on 10/30/2025).

[188] P. F. Carcia and E. M. McCarron. “Synthesis and properties of thin film polymorphs of molybdenum trioxide”. In: *Thin Solid Films* 155.1 (Dec. 1987), pp. 53–63. ISSN: 0040-6090. DOI: 10.1016/0040-6090(87)90452-4. URL: https://www.sciencedirect.com/science/article/pii/0040609087904524 (visited on 10/30/2025).

[189] Kihyun Ma et al. “Mechanical and electrical properties of α-MoO3 belts under strain for flexible electronics applications”. In: *Applied Surface Science* 681 (Feb. 2025), p. 161512. ISSN: 0169-4332. DOI: 10.1016/j.apsusc.2024.161512. URL: https://www.sciencedirect.com/science/article/pii/S016943322402227X (visited on 10/30/2025).

[190] Liang Zhou et al. “α-MoO3 Nanobelts: A High Performance Cathode Material for Lithium Ion Batteries”. In: *The Journal of Physical Chemistry C* 114.49 (Dec. 2010), pp. 21868–21872. ISSN: 1932-7447. DOI: 10.1021/jp108778v. URL: https://doi.org/10.1021/jp108778v (visited on 10/26/2025).

[191] Zhiyu Wang, Srinivasan Madhavi, and Xiong Wen (David) Lou. “Ultralong α-MoO3 Nanobelts: Synthesis and Effect of Binder Choice on Their Lithium Storage Properties”. In: *The Journal of Physical Chemistry C* 116.23 (June 2012), pp. 12508–12513. ISSN: 1932-7447. DOI: 10.1021/jp304216z. URL: https://doi.org/10.1021/jp304216z (visited on 10/26/2025).

[192] Haoqi Ren et al. “Synthesis, Functional Modifications, and Diversified Applications of Molybdenum Oxides Micro-/Nanocrystals: A Review”. In: *Crystal Growth & Design* 18.10 (Oct. 2018), pp. 6326–6369. ISSN: 1528-7483. DOI: 10.1021/acs.cgd.8b00894. URL: https://doi.org/10.1021/acs.cgd.8b00894 (visited on 10/26/2025).

[193] Hayoung Jung et al. “Direct and fast growth of highly single crystalline α-MoO3 nanosheets on various substrates and its electrochemical activities”. In: *Materials Letters* 204 (Oct. 2017), pp. 173–176. ISSN: 0167-577X. DOI: 10.1016/j.matlet.2017.06.034. URL: https://www.sciencedirect.com/science/article/pii/S0167577X17309229 (visited on 10/26/2025).

[194] Wenxian Wei et al. “Preparation of recyclable MoO3 nanosheets for visible-light driven photocatalytic reduction of Cr(VI)”. en. In: *RSC Advances* 9.49 (Sept. 2019), pp. 28768–28774. ISSN: 2046-2069. DOI: 10.1039/C9RA05644K. URL: https://pubs.rsc.org/en/content/articlelanding/2019/ra/c9ra05644k (visited on 10/26/2025).

[195] Liang Cheng et al. “Single-Crystalline Molybdenum Trioxide Nanoribbons: Photocatalytic, Photoconductive, and Electrochemical Properties”. In: *Chemistry – A European Journal* 15.10 (Feb. 2009), pp. 2310–2316. ISSN: 0947-6539. DOI: 10.1002/chem.200802182. URL: https://chemistry.europe.onlinelibrary.wiley.com/doi/full/10.1002/chem.200802182 (visited on 10/26/2025).

[196] Xiaofei Yang et al. “synthesis of high-quality crystalline α-MoO3 nanobelts”. en. In: *Crystal Research and Technology* 46.4 (2011), pp. 409–412. ISSN: 1521-4079. DOI: 10.1002/crat.201100061. URL: https://onlinelibrary.wiley.com/doi/abs/10.1002/crat.201100061 (visited on 10/26/2025).

A

Supplementary Data & Images

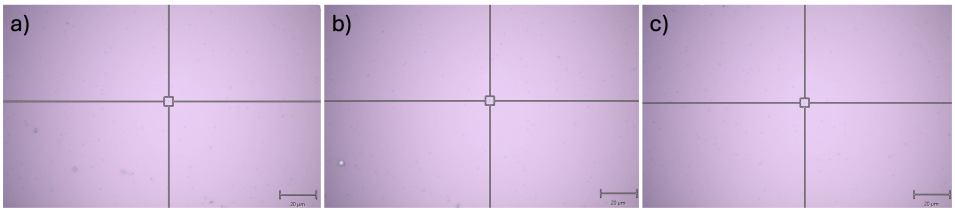


Figure A.1: OM images of flakes used for obtaining raman peaks in Table 4.3 a) Flake 1, b) Flake 2, c) Flake 3.

A.1. $MoSe_2$ CVD Parameters and Temperature Profiles

Run #	Growth Temp (ºC)	Selenization Temp (ºC)	Ar Flow Rate (sccm)	Reaction Time (min)	Substrate Position
1	750	300	100	5	D
2	750	300	100	15	D
3	750	300	100	20	D
4	750	325	100	20	D
5	750	350	100	20	D
6	750	750	100	20	D
7	750	350	100	20	A
8	750	350	50	20	D
9	750	750	50	20	D
10	750	750	150	20	D
11	750	750	50	20	D
12	750	350	50	20	D
13	750	350	100	20	D
14	800	350	100	10	D

Table A.1: CVD synthesis parameters for all runs of attempted vapor phase $MoSe_2$ growth without NaCl. D indicates a substrate positioned “downstream” of MoO_3, while A indicates being upside down “above” the MoO_3.

Run #	Growth Temp (ºC)	Selenization Temp (ºC)	Ar Flow Rate (sccm)	Reaction Time (min)	NaCl Form	NaCl Amount	Substrate Position
1	750	350	150	15	Crystals	2 mg	D
2	750	350	150	15	Crystals	2 mg	B
3	750	350	150	15	Crystals	2 mg	B
4	750	750	150	0	Crystals	2 mg	B
5	750	350	75	15	Solution	15 µL	A
6	750	350	75	15	Solution	15 µL	A
7	750	350	75	15	Solution	15 µL	A
8	750	350	75	15	Solution	10 µL	A
9	750	350	25	15	Solution	8 µL	A
10	750	350	38	15	Solution	5 µL	A
11	750	350	38	15	Solution	2 µL	A
12	750	350	38	30	Solution	4 µL	A
13	750	350	38	30	Solution	2 µL	A
14	750	350	38	5	Solution	2 µL	A
15	750	350	100	15	Solution	2 µL	A
16	750	350	13	15	Solution	2 µL	A

Table A.2: CVD synthesis parameters for all runs of attempted vapor phase $MoSe_2$ growth with NaCl. D indicates a substrate positioned “downstream” of MoO_3, B indicates the MoO_3 + NaCl was placed on top of the substrate, and A indicates being upside down “above” the MoO_3.

Run #	Growth Temp (ºC)	Selenization Temp (ºC)	Ar Flow Rate (sccm)	Reaction Time (min)	Substrate Type
1	700	300	100	50	1 µm Mo
2	700	300	100	35	1 µm Mo
3	700	300	100	20	1 µm Mo

Table A.3: CVD synthesis parameters for all runs of attempted two-step $MoSe_2$ growth.

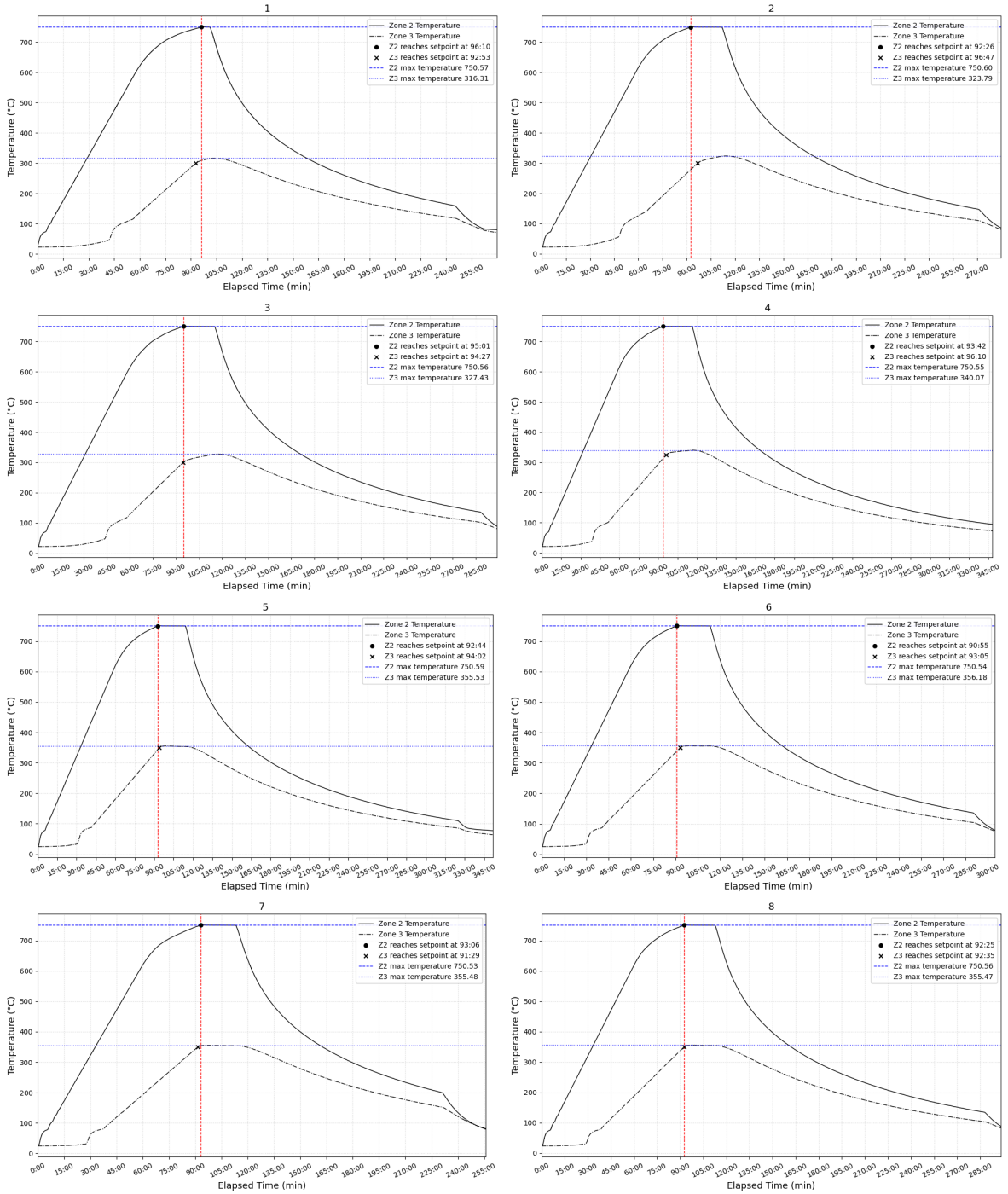


Figure A.2: Additional temperature profiles for runs listed in Table A.1.

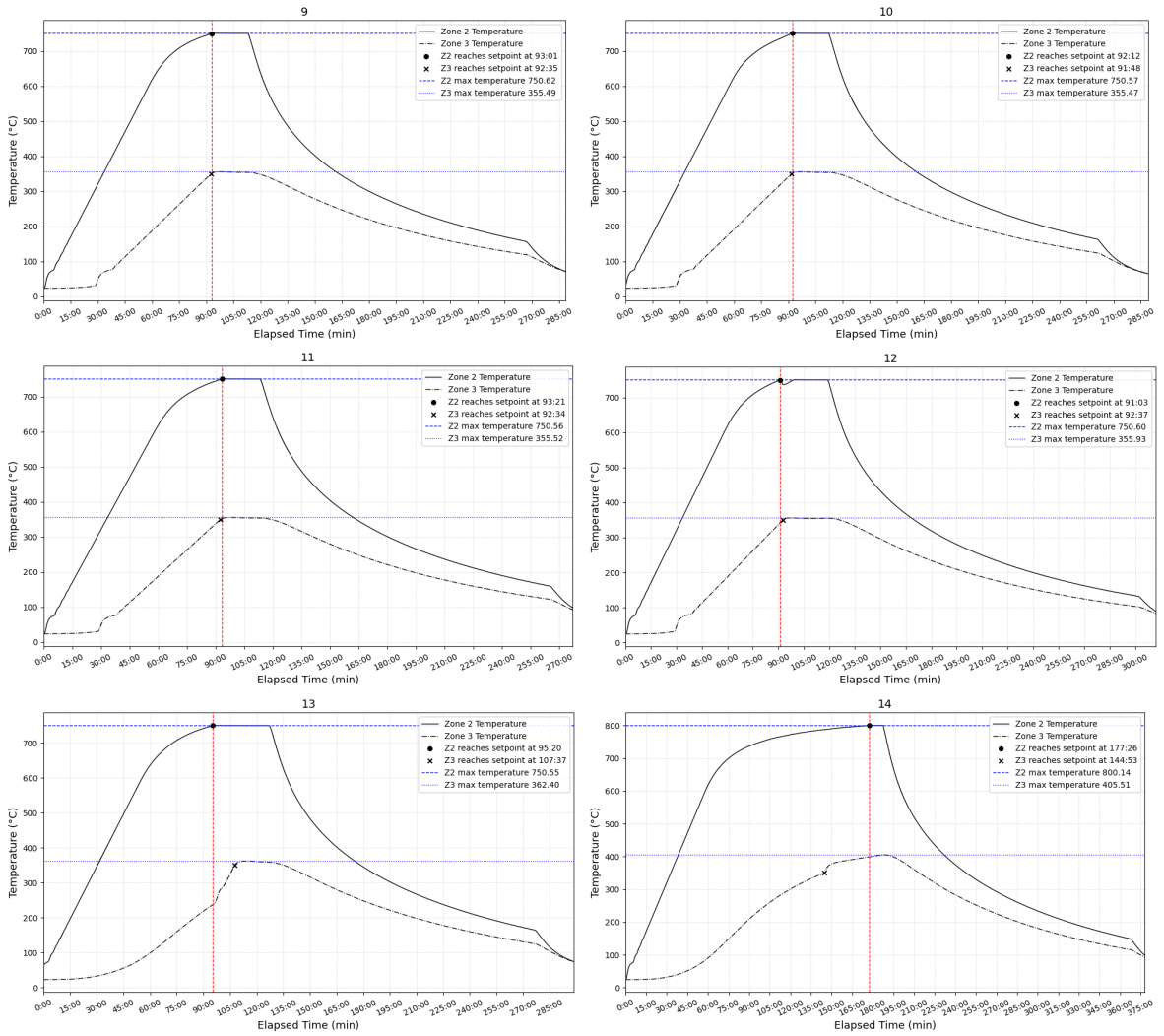


Figure A.3: Additional temperature profiles for runs listed in Table A.1.

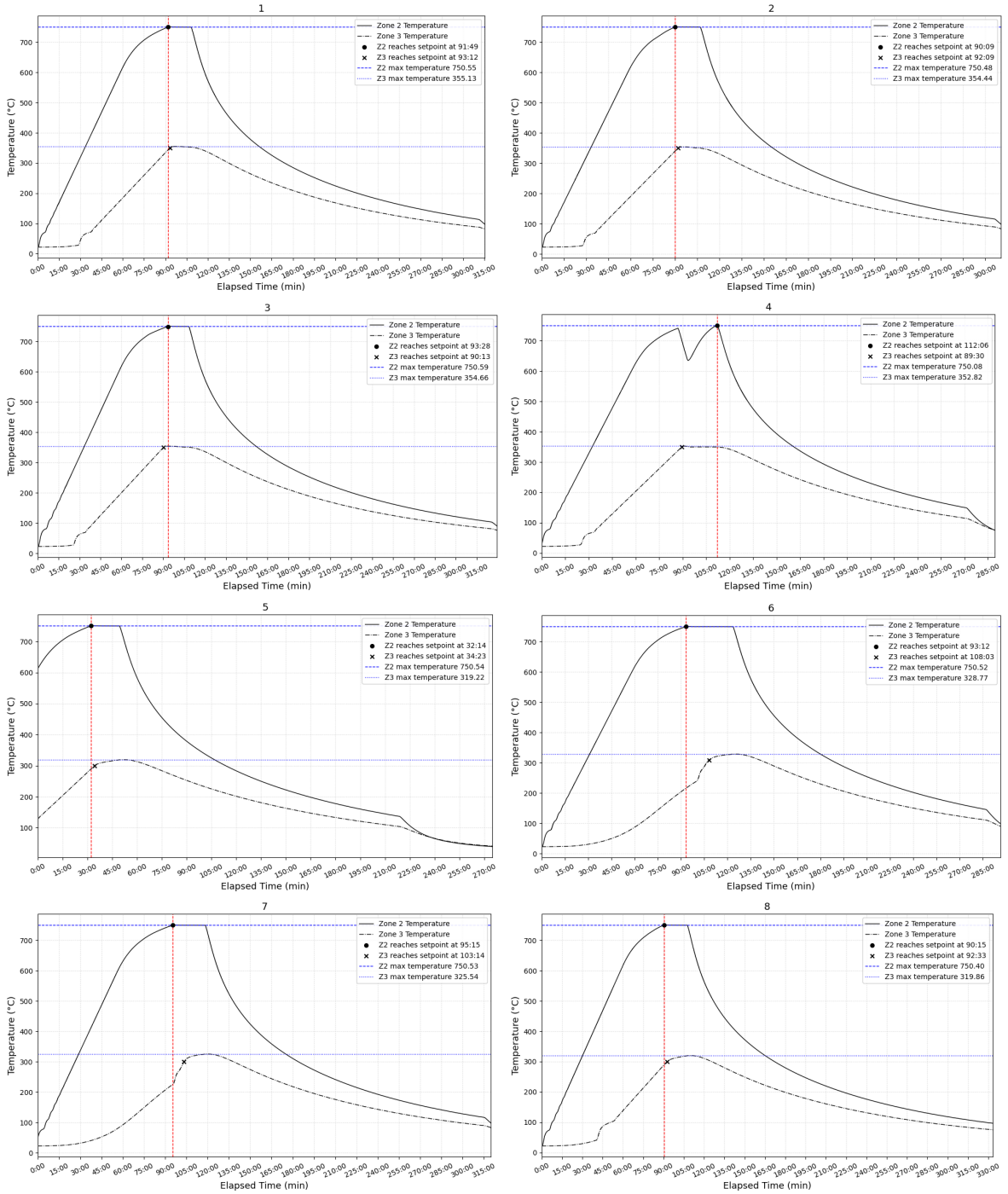


Figure A.4: Additional temperature profiles for runs listed in Table A.2.

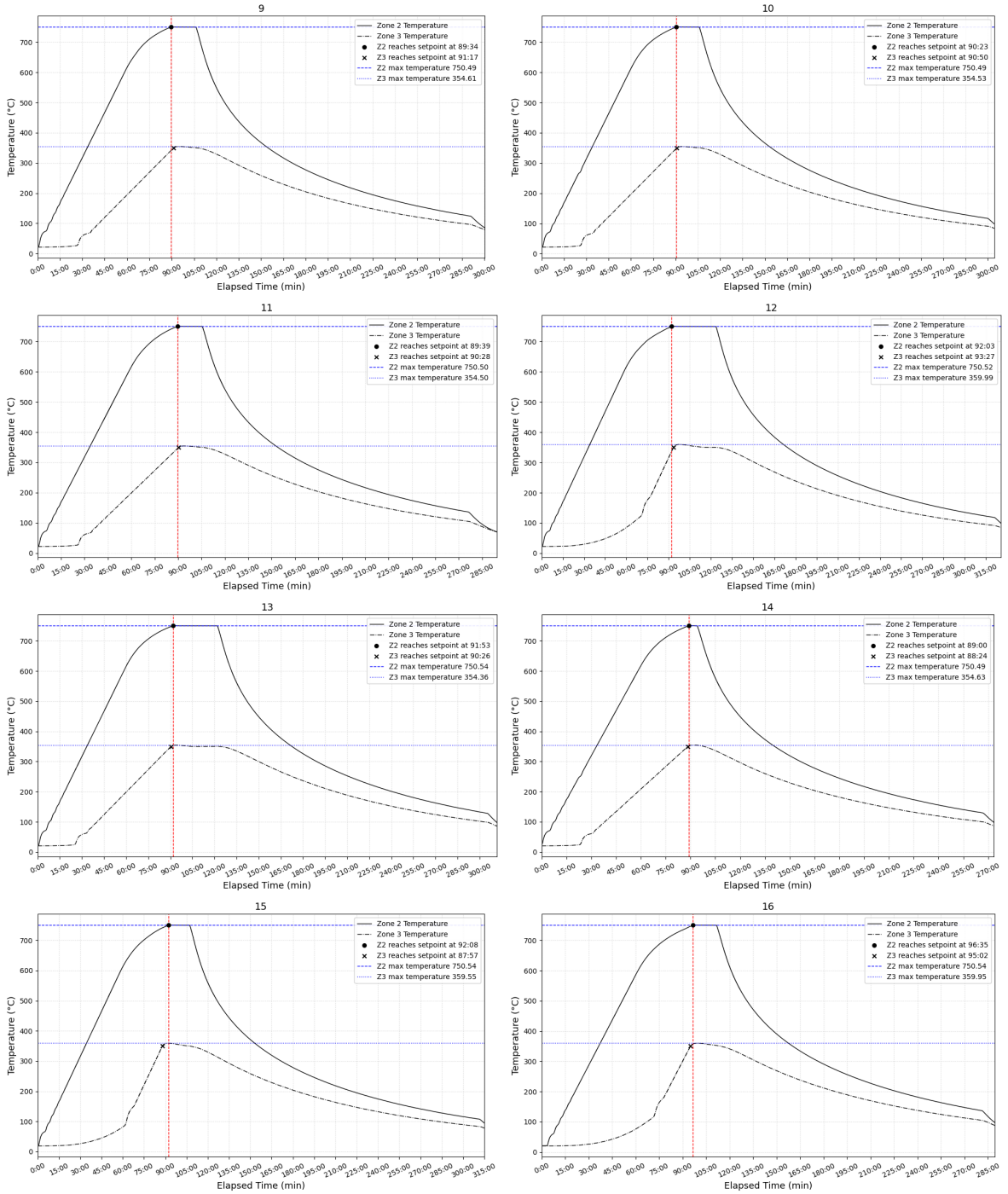


Figure A.5: Additional temperature profiles for runs listed in Table A.2.

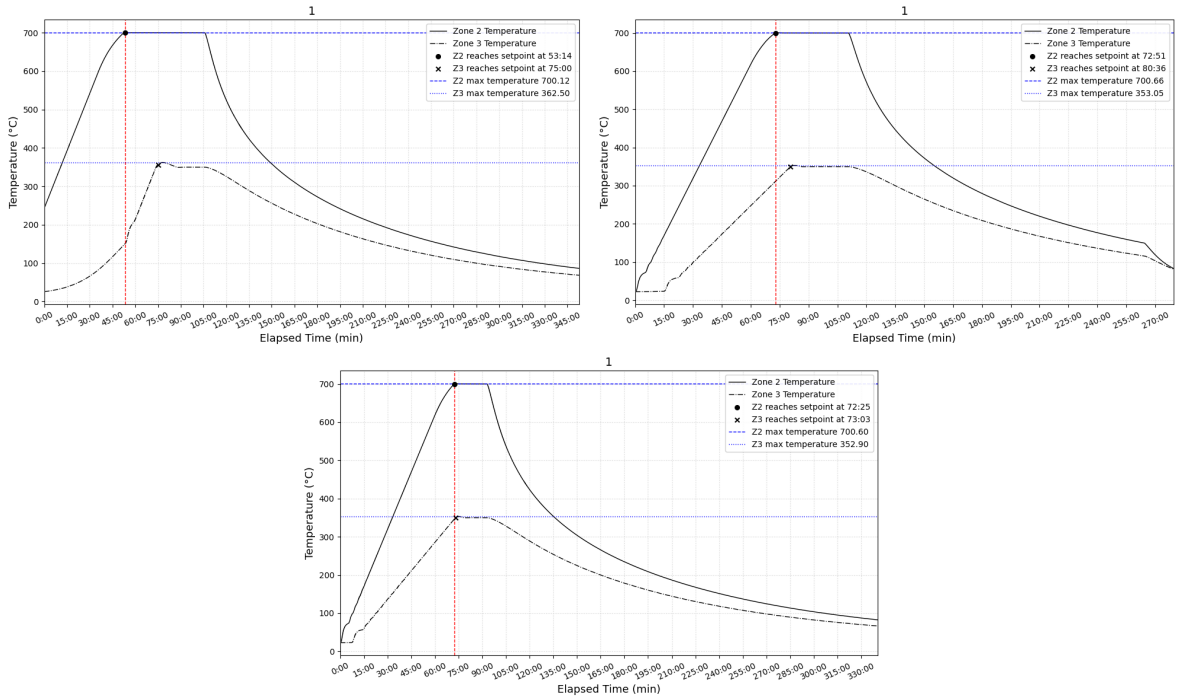


Figure A.6: Additional temperature profiles for runs listed in Table A.3.